Die approbierte Originalversion dieser Dissertation ist in der Hauptbibliothek der Technischen Universität Wien aufgestellt und zugänglich.
http://www.ub.tuwien.ac.at

The approved original version of this thesis is available at the main library of the Vienna University of Technology.

http://www.ub.tuwien.ac.at/eng

TECHNISCHE
UNIVERSITÄT
WIEN
Vienna University of Technology

Cavity quantum electrodynamics with non-transversal photons

DISSERTATION

zur Erlangung des akademischen Grades

Doktor der Naturwissenschaften

eingereicht von

Christian Junge
Matrikelnummer 1029552
Hießgasse 2 / 9, 1030 Wien

an der
Fakultät für Physik der Technischen Universität Wien

Betreuung: Prof. Dr. Arno Rauschenbeutel, E141 – Atominstitut

Diese Dissertation haben begutachtet:

(Prof. Dr. Arno Rauschenbeutel)

(Prof. Dr. Jean-Michel Raimond)

Wien, 18.12.2013

(Christian Junge)

TECHNISCHE
UNIVERSITÄT
WIEN
Vienna University of Technology

Cavity quantum electrodynamics with non-transversal photons

DISSERTATION

submitted in partial fulfillment of the requirements for the degree of

Doktor der Naturwissenschaften

by

Christian Junge
Registration Number 1029552
Hießgasse 2 / 9, 1030 Wien

to the Faculty of Physics
at the Vienna University of Technology

Advisor: Prof. Dr. Arno Rauschenbeutel, E141 – Atominstitut

The dissertation has been reviewed by:

(Prof. Dr. Arno Rauschenbeutel)

(Prof. Dr. Jean-Michel Raimond)

Wien, 18.12.2013

(Christian Junge)

Abstract

In most physical situations, light is correctly described as a fully transversally polarized wave, i.e., the electric field vector is always orthogonal to the direction of propagation. However, photons confined in dielectric structures such as optical waveguides or whispering-gallery-mode microresonators can have strong longitudinal polarization components whose presence fundamentally alters the interaction between light and matter. In the present thesis, this phenomenon is investigated experimentally and theoretically in the context of cavity quantum electrodynamics for single Rubidium 85 atoms coupled to a whispering-gallery-mode microresonator.

To date, these resonators have been exclusively treated as conventional ring resonators with two linearly polarized, counter-propagating optical modes. By contrast, the analysis in this thesis shows that in the evanescent field of whispering-gallery-mode resonators the longitudinal component fundamentally links the propagation direction of the light with its polarization. Thus, whispering-gallery-mode resonators have to be recognized as a new class of optical resonators for which the current description of light–matter interaction is substantially incomplete. The experimental results are in good agreement with a new theoretical model developed in the thesis and show that the longitudinal polarization component decisively alters the atom–light coupling.

Based on these findings a highly efficient switch for light controlled by a single atom is realized. The key element of the experiment is the whispering-gallery-mode microresonator, which is coupled to a single atom and interfaced by two optical fibers. This configuration allows one to control the light flux between the two fibers depending on the presence of a single atom in the evanescent field of the resonator. In the thesis, the performance of this optical one-atom-switch is studied systematically and the photon-number-dependent routing capability is investigated. Finally, prospects for applications of this system in quantum information science are discussed.

Kurzfassung

Licht wird im Normalfall als transversale Welle beschrieben, bei der das elektrische Feld senkrecht zur Ausbreitungsrichtung schwingt. Werden Photonen jedoch in dielektrischen Strukturen wie optischen Wellenleitern oder Flüstergaleriemoden-Resonatoren geführt, können starke longitudinale Polarisationskomponenten auftreten, welche die Licht–Materie Wechselwirkung grundlegend verändern. In der vorliegenden Arbeit wird dieses Phänomen im Rahmen der Resonator Quantenelektrodynamik experimentell und theoretisch untersucht. Grundlage der Versuche ist ein Flüstergaleriemoden-Resonator an den einzelne Rubidium 85 Atome gekoppelt werden.

Bisher wurde diese Art von Resonator ausschließlich als konventioneller Ringresonator mit zwei linear polarisierten, gegenläufigen Moden beschrieben. Im Gegensatz dazu zeigen die Studien dieser Arbeit, dass durch die longitudinale Polarisationskomponente des evaneszenten Feldes um den Resonator, die Ausbreitungsrichtung des Lichts mit seiner Polarisation verknüpft ist. Folglich müssen Flüstergaleriemoden-Resonatoren als völlig neue Klasse von Resonatoren angesehen werden, für welche die Licht–Materie Wechselwirkung bisher nicht ausreichend verstanden ist. Daher wird in der Arbeit ein neues theoretisches Modell für diese Resonatoren entwickelt und mit experimentellen Beobachtungen verglichen. Die experimentellen Ergebnisse stimmen sehr gut mit den theoretischen Vorhersagen überein und zeigen, dass durch die longitudinale Polarisationskomponente des geführten Lichts die Wechselwirkung zwischen Licht und Materie entscheidend beeinflusst wird.

Aufbauend auf diesen grundlegenden Erkenntnissen befasst sich diese Arbeit mit der Realisierung eines hoch effizienten Schalters für Licht, dessen Verhalten von einem einzelnen Atom gesteuert wird. Das Herzstück dieses Experiments ist ein Flüstergaleriemoden-Resonator an den zwei optische Fasern gekoppelt werden. Diese Anordnung ermöglicht es, abhängig von der Präsenz eines einzelnen Atoms im evaneszenten Feld des Resonators, Licht zwischen den beiden Fasern hin und her zu schalten. In der vorliegenden Arbeit wird das Verhalten dieses optischen Ein-Atom-Schalters charakterisiert und seine nicht-klassische Natur anhand der Photonenstatistik des geschalteten Lichts untersucht. Abschließend werden Anwendungsmöglichkeiten dieses Systems in der Quanteninformationsverarbeitung diskutiert.

List of Publications

Parts of this thesis have been published in the following journal articles:

- C. Junge, D. O'Shea, J. Volz, and A. Rauschenbeutel. Strong coupling between single atoms and nontransversal photons. *Phys. Rev. Lett.*, 110:213604, 2013.
- D. O'Shea, C. Junge, J. Volz, and A. Rauschenbeutel. Fiber-optical switch controlled by a single atom. *Phys. Rev. Lett.*, 111:193601, 2013.
- C. Junge, S. Nickel, D. O'Shea, and A. Rauschenbeutel. Bottle microresonator with actively stabilized evanescent coupling. *Opt. Lett.*, 36(17):3488–3490, 2011.
- D. O'Shea, C. Junge, S. Nickel, M. Pöllinger, and A. Rauschenbeutel. Ultra-high Q whispering-gallery-mode bottle microresonators: properties and applications. *Proc. SPIE 7913*, 79130N, 2011.
- D. O'Shea, C. Junge, M. Pöllinger, A. Vogler, and A. Rauschenbeutel. All-optical switching and strong coupling using tunable whispering-gallery-mode microresonators. *Appl. Phys. B*, 105:129–148, 2011.

Contents

1 Introduction **1**

2 Basic Properties of Bottle Microresonators **5**
- 2.1 General parameters of optical resonators 6
- 2.2 Whispering-gallery-mode microresonators 8
- 2.3 The bottle microresonator 11
- 2.4 Evanescent coupling to WGM microresonators with ultra-thin fibers 24

3 Active Stabilization of Evanescent Coupling **37**
- 3.1 Basic principal of the evanescent coupling stabilization 38
- 3.2 Technical implementation of the active evanescent coupling stabilization 46
- 3.3 Outlook: Stabilizing the evanescent coupling of two fibers to a WGM microresonator 52
- 3.4 Conclusion 56

4 Theory of Light–Matter Interaction with Non-Transversal Photons **57**
- 4.1 Modeling the atom–light interaction with a single cavity mode 58
- 4.2 Coupling of an atom to a ring resonator 63
- 4.3 Polarization of whispering-gallery-modes 66
- 4.4 Modeling the atom–resonator coupling with arbitrary mode polarization 75
- 4.5 Conclusion 79

5 Single Atoms Strongly Coupled to Non-Transversal Modes **81**
- 5.1 Experimental setup 82
- 5.2 Spectral properties of the bottle resonator and expected strength of the light–matter interaction 100
- 5.3 Detection and probing of single atoms coupled to the bottle resonator 103
- 5.4 Strong coupling of single atoms to non-transversally polarized bottle modes . . 113
- 5.5 Atomic state preparation via optical pumping 125
- 5.6 Summary of the experimental results 128

6 Switching Light with a Single Atom **131**
- 6.1 Overview of optical switching with WGM micro resonators 132
- 6.2 Concept of an optical switch controlled by a single atom 133

6.3 Experimental realization and characterization of the switch 134
6.4 Non-classical light from the switch 140
6.5 Outlook on deterministic generation of atom–light entanglement and optical Schrödinger cat states 146
6.6 Conclusion 151

7 Summary 153

Bibliography 157

CHAPTER 1

Introduction

The description of light as an electromagnetic plane wave is a common picture in optics. The polarization of a plane wave is perfectly transversal, meaning that the electromagnetic field oscillates exclusively perpendicular to the direction of propagation. However, realistic light fields deviate from this idealization by having a transversal intensity distribution like, e.g., a Gaussian beam. Lax et al. [1] pointed out that in this case the transversal gradient of the electric field gives rise to longitudinal field components which oscillate along the propagation direction of the light. In most situations, only weak transversal gradients occur and, as a consequence, the longitudinal components do not contribute in a decisive manner to the electromagnetic field. However, if light is tightly focused, steep transversal field gradients, for which the intensity varies significantly on a scale on the order of the wavelength, will appear, leading to strong longitudinal fields [2–6]. Moreover, in recent years, the capabilities to control and manipulate light on progressively shrinking length-scales have been enormously extended using dielectric or plasmonic structures. Possible realizations comprise, e.g., optical nano-fibers [7,8], microcavities and photonic crystals [9], metal nanoparticles [10] and many more. All these devices have in common that they confine the electromagnetic field to small dimensions which are defined by the size of the structure. The latter ranges typically from a few down to less than one wavelength. As a consequence, strong transversal field gradients occur which induce longitudinal polarization components of the light.

The longitudinal component of light has some remarkable properties. For instance, from Maxwell's equations one finds a phase shift of $\pi/2$ between the longitudinal and the transversal field. This leads locally to an elliptical polarization rotating in the plane of propagation [11,12]. Moreover, it has been shown that the longitudinal field can be focused below the diffraction limit for light [6, 13, 14], enabling improved resolution in near-field microscopy [15]. In addition, it was proposed to use the oscillation of the longitudinal field in the propagation direction of the light to accelerate charged particles [2, 3].

In the context of light–matter interaction, the properties of non-transversal light fields are crucial: In order to enhance the relatively weak coupling of light and matter in free space, alternative approaches rely on the confinement of light to small volumes and thereby enter into a regime where longitudinal fields occur. For instance, light–matter interaction can be enormously enhanced by strongly focusing light with high-numerical-aperture objectives onto atoms, molecules and ions [16–18] or by the use of optical resonators [9]. The latter case has been studied extensively in the framework of cavity quantum electrodynamics (CQED), which describes the interaction of a single mode of the electromagnetic field with a dipole emitter like, e.g., an atom [19]. Research in CQED has led to numerous cutting-edge experiments comprising studies of the quantization of the electromagnetic field and atom–photon entanglement [20–22], non-destructive photon detection [23, 24], deterministic single photon sources [25], quantum networks [26, 27] as well as single photon transistors [28] and sorters [29, 30]. The importance of CQED was underlined most recently, when Serge Haroche was awarded, together with David J. Wineland, the Nobel Prize in physics for his fundamental work on measurement and manipulation of individual quantum system with superconducting microwave cavities and Rydberg atoms [31]. The success of CQED is closely connected to the progressive enhancement of the coupling between light and matter. Over the last two decades, this research led to the development of optical microresonators [9]. These resonators allow one to establish strong light–matter coupling by confining the light to very small volumes in combination with long photon lifetimes in the resonator. In this way, a large enhancement of light–matter interaction strength compared to free space can be realized. Various types of optical microresonators have been established comprising Fabry-Pérot resonators based on high-reflective mirrors [32] or fiber facets [33], Bragg grating approaches with semiconductor micropillars [34, 35] and nano-fibers [36], photonic crystal cavities [37, 38] and whispering-gallery-mode (WGM) microresonators [39]. Among this variety, WGM resonators have attracted considerable interest. Their working principle is based on total internal reflection in a dielectric, monolithic structure which confines light to traveling wave modes with circular orbits. Since WGM microresonsators are compatible with standard chip-fabrication techniques [40] and enable extremely efficient in- and out-coupling of light, they promise to be easily scalable and integrable into existing technologies. This makes them promising candidates for the implementation of new and efficient quantum and photonic applications [41]. However, the ongoing miniaturization of resonators pushes CQED into a completely novel regime of light–matter interaction. Due to the small structure size of most new resonator types, light will possess transversal field gradients on the order of the wavelength, thereby inducing strong longitudinal polarization components. The presence of the non-transversally polarized field has the potential to fundamentally modify the coupling of light and matter and, therefore, calls for a detailed investigation of the underlying effects.

This work presents the first systematic study of strong light–matter interaction in an optical microresonator with non-transversal fields. For this purpose, strong coupling between single laser-cooled ^{85}Rb atoms and a WGM bottle resonator is realized in a CQED experiment. The bottle resonator is surrounded by an evanescent field that originates from the total internal reflection of light at the inner surface. This evanescent field decays exponentially with distance from the resonator on the scale of the wavelength of the light field. Due to this spatial field gradient, the evanescent field can have a large longitudinal component. Since the evanescent field is the interface that realizes light–matter coupling with WGM microresonators, the non-transversal polarizations should be essential for a correct description of the coupled system. However, so far, the non-transversal polarization of the evanescent field has not been taken into account for the modeling of light–matter interactions. Instead, WGM microresonators were being described as conventional ring resonators which sustain a pair of counter-propagating, degenerated modes with identical polarization.

Within this thesis, the properties of the non-transversally polarized WGMs are analyzed theoretically, leading to a more adequat model for the description of light–matter coupling. In order to verify the predictions of this model, the spectral response of the coupled atom–resonator system is experimentally investigated. The obtained vacuum-Rabi spectra are quantitatively analyzed with the model and give clear evidence of the decisive influence of the non-transversal polarization on the light–matter interaction.

The beneficial properties of this novel atom–resonator system with non-transversal light fields, are then made use of in order to realize a highly efficient optical switch controlled by a single atom. In this switch the presence of an atom in the evanescent resonator field, controls the flow of light between two ultra-thin fibers which interface the resonator. The switch is characterized to have high transfer efficiencies for light and shows photon-number-dependent routing capabilities.

The individual steps towards the above mentioned achievements are described as follows:

In chapter 2, the basic properties of WGM resonators are discussed exemplarily for the case of a bottle microresonator. Following the deviation of the resonator fields, it is explained how light can be coupled efficiently to the bottle resonator via the evanescent field using ultra-thin optical fibers. The evanescent coupling is in general sensitive to the distance between the WGM resonator and the ultra-thin fiber. Therefore, in chapter 3, an active stabilization of the evanescent coupling between the bottle resonator and an ultra-thin fiber is presented which relies on a phase modulation technique. In chapter 4, a theoretical model for the description of light–matter interaction with non-transversal polarization is developed. Starting from the Jaynes-Cummings model, the description of light–matter interaction in a ring resonator is introduced. Based on a discussion of the non-traversal field properties of WGMs, it is then explained how the standard model has to be extended in order to include arbitrary polarizations and multi-level effects of the atom.

In chapter 5, the experiments on strong coupling between a single ^{85}Rb atom and the bottle resonator are presented. First, the CQED setup is explained in detail, followed by a presentation of the measurements of the coupled atom–resonator system. The vacuum-Rabi spectra are quantitatively analyzed with the developed model and the influence of the non-transversal polarization is discussed. Based on the theoretical and experimental findings, chapter 6 presents, as first application of the CQED setup, an optical switch controlled by a single atom. The switch is characterized and the optimal working parameters are determined. Moreover, measurements of the intensity auto-correlation are preformed to investigate non-classical states of light. Finally, the potential of the optical switch for the generation of atom–light entanglement and optical Schrödinger cat states is analyzed.

CHAPTER 2

Basic Properties of Bottle Microresonators

Optical resonators serve to provide both spatial and temporal confinement of light. These requirements are fulfilled by a large variety of different physical systems where the most popular realization is the Fabry-Pérot resonator consisting of two highly reflective mirrors. When the frequency of the light matches the resonance condition of the resonator a strong intra-cavity field can build up. For this reason, resonators play an important role in the context of light–matter interaction which can be considerably enhanced by the temporal and spatial confinement of light inside the resonator. The confinement of light can be quantified by the quality factor Q and the mode volume V which describe the temporal storage of the light field in the resonator and its spatial extension, respectively. For a large interaction strength of light and matter, the storage time has to be maximized while the mode volume should remain minimal which is equivalent to optimizing the ratio Q/V. This requirement has led to the development of numerous optical microresonators [9] which combine high quality factors and small dimensions on the micrometer scale approaching the fundamental limit set by the wavelength of the light. Within this variety, whispering-gallery-mode (WGM) microresonators are of particular interest. These resonators are based on monolithic, dielectric structures and confine light by total internal reflection. They can reach ultra-high-Q factors, very small mode volumes and offer the unique property of coupling light in and out of the resonator with near-unity efficiency via ultra-thin fibers.

The basic properties of WGM microresonators are presented in this chapter. First, the most fundamental concepts of optical microresonators are discussed in the context of Fabry-Pérot resonators. Next, WGM microresonator are introduced and their basic properties are presented. The discussion will then focus on a novel type of WGM microresonator used in this work, the so-called bottle microresonator, including an explicit derivation of its electromagnetic mode structure. Finally, the process of coupling light in and out of a WGM microresonator with ultra-thin fibers is discussed.

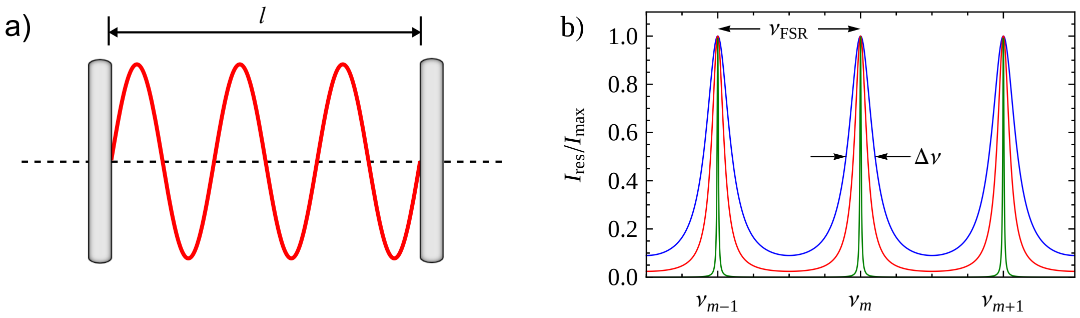

Figure 2.1: a) Working principle of the Fabry-Pérot interferometer which confines light between two parallel mirrors. When the separation l of the mirrors is an integer multiple of a half-wavelength $\lambda/2$ a standing wave can build up in the resonator. b) Intra-cavity intensity of a Fabry-Pérot resonator as function of the light frequency ν. The spectrum is calculated from Eq. (2.3) for three different values of finesse: $F = 5$ (blue), $F = 10$ (red) and $F = 100$ (green).

2.1 General parameters of optical resonators

To illustrate the basic working principle of an optical resonator, it is useful to consider the textbook example of the Fabry-Pérot interferometer (FPI). Here, only a short overview is given following the calculations in [42]. In the most simple case, this resonator type is constructed from two planar, parallel mirrors as shown in Fig. 2.1 a). When a light wave travels along the resonator axis interference of the initial wave with its reflections at the two mirrors will occur. When the separation between the mirrors l is an integer multiple of the half wavelength of the light, the electric fields in the resonator interfere constructively and a standing wave builds up. The resonance condition for such a resonator mode with the frequency ν is

$$\nu_m = \frac{c}{\lambda} = m\frac{c}{2l}\,, \tag{2.1}$$

where $m = 1, 2, ...$ is the mode number, λ and c are the wavelength and the speed of light, respectively. As a consequence, consecutive modes are separated by a frequency spacing of

$$\nu_{\rm FSR} = \frac{c}{2l}\,, \tag{2.2}$$

which is denoted as the resonators's free spectral range (FSR) of the resonator.

If the two mirrors are not perfectly reflecting, the amplitude of the wave will be reduced during the reflection at each mirror by its reflectivity coefficient r. The total field inside the resonator can be obtained by summation over the initial wave and all its multiple reflections leading to the intensity [42]

$$I_{\rm res} = \frac{I_{\rm max}}{1 + (2F/\pi)^2 \sin^2(\pi\nu/\nu_{\rm FSR})}\,, \tag{2.3}$$

where we have defined the maximum intra-cavity intensity $I_{\rm max} = I_{\rm in}/(1-r)^2$, with the intensity of the initial wave $I_{\rm in}$ and the finesse $F = \pi r/(1 - r^2)$. From Eq. (2.3) it follows that the intra-cavity intensity is maximal, whenever the resonance condition Eq. (2.1) is fulfilled. The intensity peaks in the spectrum of the FPI are separated by ν_{FSR} as shown in Fig. 2.1 b).

The finesse F characterizes the losses of the resonator. While in the case of the idealized FPI these losses originate exclusively from the imperfect reflectivity of the mirrors, light in real resonators is also lost due to other processes like, e.g., absorption or scattering. The losses limit the lifetime of light in the resonator and lead to a broadening of the discrete resonance peaks in the spectrum (compare the traces in Fig. 2.1 b)). From Eq. (2.3) we get the full width at half maximum (FWHM) of a resonance peak which for $F \gg 1$ reads

$$\Delta\nu = \frac{\nu_{\text{FSR}}}{F} \,. \tag{2.4}$$

Expressed in this way, the finesse quantifies the separation of the resonance peaks in units of their resonance width. The linewidth of the resonator is connected to the lifetime τ_0 of photons in the resonator via

$$\Delta\nu = \frac{1}{2\pi\tau_0} \,. \tag{2.5}$$

Therefore, the finesse is alternatively given by the number of round trips (times 2π) which a photon travels inside the cavity until it is lost via transmission through one of the mirrors.

The finesse is a very intuitive quantity to describe the losses of a FPI resonator since it is directly connected to the mirror reflectivity. However, for other types of optical resonators, where the dissipation of light has different physical origins, it is more convenient to measure the losses in terms of the quality factor Q. The quality factor can be used to characterize any kind of damped oscillator and is defined as [42]

$$Q = \frac{2\pi \cdot (\text{stored energy})}{\text{energy loss per cycle}} = 2\pi\nu_m\tau_0 = \frac{\nu_m}{\Delta\nu} \,. \tag{2.6}$$

Thus, using Eq. (2.4), it is easy to see that the quality factor is connected to the finesse via the relation $Q = \nu_m/\nu_{\text{FSR}} \cdot F$.

Besides the quality factor, the spatial confinement of the light in a resonator is an important quantity because the tighter the light is confined, the greater will be the intensity in the mode. One can characterize the spatial confinement by the mode volume V for which several definitions exist throughout the literature [39]. Here, we will use a definition which is related to the energy density of the mode [43], where V is defined as the spatial integral over the intensity distribution $I(\vec{r})$ of the mode normalized to unity [44]:

$$V = \int_{\mathbb{R}^3} n^2(\vec{r}) \frac{I(\vec{r})}{I_{\text{max}}} \, dr^3 \,, \tag{2.7}$$

with $n(\vec{r})$ being the refractive index, depending on the position vector $\vec{r}$, and I_{max} the peak intensity of the mode.

Following the above discussion, it becomes clear why optical resonators are powerful tools for enhancing the coupling between light and matter: Consider, for example, the case where a photon interacts with a single atom. In free space, the photon would pass the atom only once resulting in a relatively weak interaction. In contrast, when the photon is stored in an optical resonator with high Q, the photon will pass the atom multiple times thereby increasing the probability of interaction. A similar picture is true for the mode volume V: Inside the resonator, a photon can be confined to very small volumes comparable to a strong focus in free space. Thus, even with a single photon, very high intensities are achievable leading to strong enhancement of light–matter coupling.

In conclusion, the ratio Q/V is a crucial parameter for the description of light-matter interaction in optical resonators [9]. For very large ratios Q/V, it is even possible to reach the regime of "strong coupling", where the atom–photon interaction dominates over all dissipative processes in the system. This then results in an coherent exchange of energy between the light field and the atomic excitation. In chapter 5, this regime of strong coupling will be studied in detail for the case of single atoms interacting with a whispering-gallery-mode microresonator.

2.2 Whispering-gallery-mode microresonators

The example of the Fabry-Pérot resonator can be extended to consider other configurations. One such configuration would be to increase the number of mirrors thereby creating a ring cavity in which running waves can be resonantly enhanced. In this case, very different concepts for the confinement of light have been developed: For example, instead of discrete reflections at a mirror surface, light can be guided by continuous total internal reflection at the boundary of a monolithic structure. This is the underlying working principle of so-called whispering-gallery-mode (WGM) microresonators, where light is confined in dielectric cavity with cylindrical symmetry.

2.2.1 The discovery of whispering-gallery-waves

Whispering-gallery-waves were discussed for the first time at the end of the nineteenth century as an acoustical phenomenon. The discussion was based on the observation that inside buildings with a circular or spherical shape, sound traveled efficiently along the encircling walls. The most popular example for such a place is probably the gallery in St Paul's Cathedral in London. There, Lord Rayleigh observed the phenomenon [45] which led him later to the first theoretical description of acoustic whispering-gallery-waves [46]. Moreover, he could also show that a whispering gallery can support traveling sound vibration patterns with very great persistence [47], i.e., whispering-gallery-modes.

2.2.2 Total internal reflection in optical WGM microresonators

In analogy to WGMs in the acoustic domain, a similar effect can be observed for light waves propagating inside a dielectric structure with cylindrical symmetry when the light is guided by total internal reflection.

When a plane light wave propagating in a medium with refractive index n_1 encounters an interface to another medium with n_2 Snell's law gives the relation

$$n_1 \sin\Theta_1 = n_2 \sin\Theta_2 \,, \tag{2.8}$$

where Θ_1 is the angle of incidence and Θ_2 is the angle of the outgoing transmitted wave. As shown in Fig. 2.2 a), Snell's law determines the outgoing propagation vector $\vec{k}_\mathrm{t}$ of the transmitted

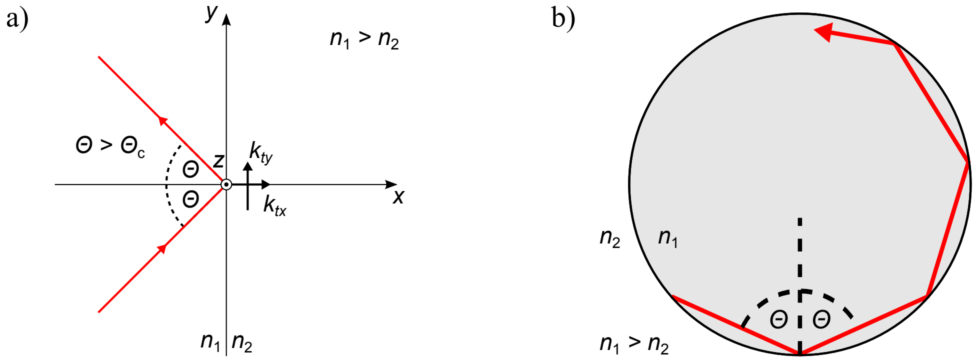

Figure 2.2: a) Total reflection at an interface of an incoming wave with an angle of incidence $\Theta \geq \Theta_\mathrm{c}$. In the optical thinner medium with n_2 the electric field decays exponentially with the wave vector components k_tx and k_ty. Figure adapted from Ref. [48]. b) Total reflection of a light ray in a circular, dielectric cavity.

wave, which for the component k_tx perpendicular to the interface is given by [48]

$$k_\mathrm{tx} \quad = \quad n_2 k_0 \sqrt{1 - (n_1/n_2 \sin\Theta_1)^2}\,, \tag{2.9}$$

with k_0 being the absolute value of the wave vector in vacuum. If the wave initially traveled in the optical thicker medium ($n_1 > n_2$) it is easy to see from Eq. (2.9) that there exists a critical angle

$$\Theta_\mathrm{c} = \arcsin(n_2/n_1)\,, \tag{2.10}$$

from which on k_tx becomes imaginary, and can be expressed as $k_\mathrm{tx} = i\tilde{k}_\mathrm{tx}$ with $\tilde{k}_\mathrm{tx}$ real. Thus, for incident angles greater than Θ_c the phase of the light wave transmitted into the second medium has the form [48]:

$$\mathrm{e}^{-i(\omega t - k_\mathrm{ty} y) - \tilde{k}_\mathrm{tx} x}\,, \tag{2.11}$$

where ω is the angular frequency of the light and k_ty is the component of the transmitted wave vector parallel to the interface. As a consequence, the transmitted wave propagates along the interface and decays exponentially into the second medium.

In order to describe the operating principle of an optical WGM resonator, let us consider a simplified picture in which a ray of light propagates inside a cylindrical dielectric structure as shown in Fig. 2.2 b). If the dielectric material is optically thicker than the surrounding material, a ray of light is totally reflected whenever it hits the inner surface under an angle larger than Θ_c. As it is evident from Fig. 2.2 b), in a cavity with cylindrical boundaries, the character of the ray path depends on the initial angle of incidence Θ, which defines the angle of all subsequent reflections. If Θ is close to Θ_c, the ray will transverse the cavity on relatively long trajectories in between two reflections events. The opposite is true for an initial angle of incidence close to $\Theta \approx \pi/2$, meaning that the ray is almost parallel to the interface at its reflection point. The distance between two reflections will be small and the ray propagates in this case close to the resonator surface. In the limit of $\Theta = \pi/2$, the path between two reflections becomes infinitesimal and the ray is continuously reflected. Thus, light is guided along the cylindrical boundary of the structure and forms the optical equivalent of an acoustic whispering-gallery wave.

Based on this effect, an optical WGM resonator can be realized in the following way: During one round trip in the cavity, a light wave accumulates a phase delay which can lead to constructive interference, similar to the situation in a FPI. When the optical path length in the circular structure is equal to an integer multiple of the wavelength of the light, a large field can build up since the total internal reflection leads, at least in this simple picture, to perfect confinement of the light. In contrast to FPIs, the reflection process at the boundary of the structure does not invert the propagation direction of the light and therefore no standing wave builds-up. Instead, the eigenmodes of the cavity resemble those of a ring resonator corresponding to so-called running waves. To grasp the complete properties of the electromagnetic field in WGMs resonators, we have to solve Maxwell's equations for the specific resonator geometry. This is done in section 2.3 for the case of the bottle microresonator.

A very important property of WGM resonators is the exponentially decaying light intensity at the outside of the around the resonator which occurs due to the total internal reflection at the boundaries. This so-called evanescent field plays a key role in the coupling of light into and out of the resonator. When a second interface to an optical thick medium is brought close to the WGM resonator, light is no longer totally reflected at the inner surface. If the gap size between the two interfaces becomes comparable to the decay length of the evanescent field, the incoming wave will enter into the second optically thick medium where it can propagate again. This process is denoted as frustrated total internal reflection (FTIR) and allows one to access the light field of a WGM resonator. The coupling technique is described in detail in section 2.4.

2.2.3 Types of WGM microresonators

Signatures of optical WGMs have been studied in a large variety of physical systems ranging from liquid droplets, to various glass and crystalline resonators [39]. For instance, in liquid droplets of aerosols high-Q WGMs were observed and exploited for cavity-enhanced spectroscopy [49]. However, for the realization of photonic devices, solid state systems are more practicable. As a consequence, major progress in the development of high-Q WGM microresonators was made with fused silica used as the primary material which has very low optical attenuation in the visible to near infrared spectral region.

The first high-Q WGMs in silica were observed in microspheres [50] with quality factors of about $Q \approx 10^8$ which were later further improved up to $Q = 8 \times 10^9$ [51]. These values were achieved only in conjunction with relatively large resonator structures and correspondigly large mode volumes: typical diameters of the spheres ranged up to several hundred micrometers. Therefore, aiming at optimizing the ratio Q/V, the possibility of using alternative resonator geometries with smaller mode volume has been investigated. A side effect of shrinking resonator dimensions is the increased sensitivity to surface induced losses (i.e., surface scattering losses) due to the higher mode intensity at the surface. Therefore, a trade-off between high Q and small V exists. For instance, in silica microdisk WGM resonators where the light is confined in a disk with a thickness of typically several micrometers, the lateral extension of the mode along

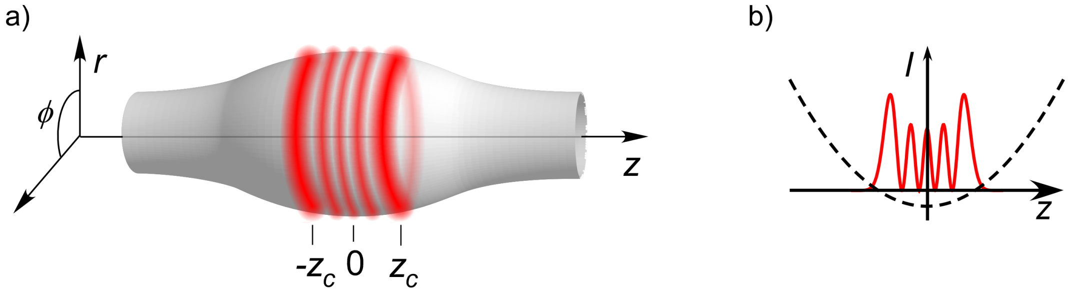

Figure 2.3: a) Schematic view of the bottle microresonator and its mode geometry. b) Harmonic potential defining the intensity distribution along the resonator axis. Figures taken from Ref. [53].

the resonator axis is reduced considerably. At the same time, the achievable quality factors also decrease to values in the range of $Q \approx 10^6$ for disk diameters of about $100\,\mu\mathrm{m}$ [52].

Further improvements in the Q/V ratio have been achieved with WGM microtoroids. These resonators are fabricated by a combination of lithography, dry-etching and a re-flow process with a CO_2-laser [43]. This way, a silica ring structure, a so-called toroid, is created, which confines the light to very small mode volumes. In addition, the processing with the CO_2-laser improves the surface quality of the toroid such that ultra-high quality factors ranging from 10^8 to 10^9 become achievable enabling Q/V-values of more than $10^6\,(\lambda/n)^{-3}$ [40].

More recently, a novel type of WGM microresonator has been developed, the so-called bottle microresonator, which will be the subject of the following section.

2.3 The bottle microresonator

Many applications of resonators require the resonance frequency to coincide with an external reference, like, e.g., an atomic transition frequency. Therefore, a WGM microresonator should be tunable over a full FSR to assure that it can be made resonant with any desired frequency. Most WGM microresonator geometries, like spheres, disks, and toroids typically confine light to a ring in the equatorial plane along the circumference of the resonator. On one hand, such a mode structure is beneficial because it yields a small mode volume and thus enables large light–matter coupling. On the other hand, the very small resonator diameter on the micrometer-scale results in very large FSR on the order of several THz. Tuning the resonance frequency over such a large frequency range is in general not possible for state-of-the-art WGM microresonators and only partial tuneability that spans up to $50\,\%$ of the FSR has been reported [54, 55].

This limitation can be overcome with a conceptually new WGM geometry provided by the bottle resonator. [44, 56]. The main idea of this novel WGM resonator type is to extend the mode structure into the third dimension along the resonator axis in a controlled way, thereby improving the tuning properties of the resonator spectrum. In Fig. 2.3 a) a schematic of the bottle resonator is shown. The resonator has a prolate shape along the resonator axis and can be fabricated by micro-structuring a standard optical glass fiber with a CO_2-laser [57]. As in all WGM microresonators, the light is radially confined by total internal reflection. However, the mode geometry is not restricted to the equatorial plane but instead extends along the resonator axis between two turning points, the so-called caustics (see Fig. 2.3 a)). The confinement along the resonator axis is realized by an angular momentum barrier which is defined by the resonator curvature. As we will see in section 2.3.4, the axial wave equation, which describes the axial intensity distribution, is formally equivalent to the one dimensional Schrödinger equation with a harmonic potential, as illustrated in Fig. 2.3 b). Accordingly, the intensity distribution of axial modes follows as a standing wave pattern where the number of axial intensity nodes is defined by the quantum number q [53, 58]. Axial modes with successive q are separated in frequency by an axial FSR which can be designed via the curvature of the resonator. In particular, it can be made considerably smaller than the azimuthal FSR. In section 2.3.6, it will will be discuss, how this property can be exploited to tune the resonator to arbitrary frequency by the use of several axial low-q modes.

In most types of WGM microresonators, the tuning of the resonance frequency is usually performed via variation of the temperature. As a consequence, the achievable tuning speed is rather low. In contrast, the fabrication of the bottle resonator from a standard optical glass fiber allows one to perform strain tuning of the frequency by pulling at the ends of the fiber. This can be easily realized with piezo actuator and facilitates an active frequency stabilization of the resonator frequency with high bandwidth of several kHz [59].

Besides full frequency tuneability, the bottle resonator features all beneficial attributes common to WGM resonators like ultra-high quality factors of 3×10^8 and small mode volume [58].

2.3.1 Fabrication of the bottle microresonator

The bottle microresonator is manufactured from a standard optical glass fiber in a heat-and-pull process. For this purpose, a fiber pulling rig is used which was developed to produce tapered optical fibers with predetermined waist diameters and taper transition profiles [57]. A schematic of the fiber pulling rig is shown in Fig. 2.4 a). The fiber is clamped onto two translation stages and is heated locally by an oxygen-hydrogen flame with a width of about 1 mm. While the lower translation stage controls which part of the fiber is heated, the upper translation stage moves outwards and elongates the hot part of the fiber. Note that the fiber is not heated to its melting point but only to temperatures which are high enough to reduce the viscosity of the glass such that it becomes meltable. The fiber pulling rig allows one to produce fibers with diameters down to several hundred nanometers while maintaining the transmission through the fiber very close to unity (more than 98 % is possible for fibers with diameters of 500 nm [36]). Moreover, within the travel range of the translation stages, arbitrary taper profiles can be created reproducibly.

As an alternative to the oxygen-hydrogen flame, a CO_2-laser, with an focal spot size of 100–120 μm, can be used as well to heat the fiber. The reduced heating-spot size allows to create more localized diameter-variations along the fiber than with the flame. Further details on the fiber pulling rig and the fabrication of ultra-thin fibers can be found in Ref. [57].

The fabrication of the bottle microresonator involves several processing steps and is entirely performed with the CO_2-laser. These steps allow the fiber to be microstructured and create a pre-calculated curvature profile of the resonator. In Figs. 2.4 b)-d) the pulling process is illustrated starting with a standard optical glass fiber with an initial diameter of 125 $\mu\mathrm{m}$. During a first pulling step the diameter of the fiber is reduced to about 35–40 μm depending on the desired final

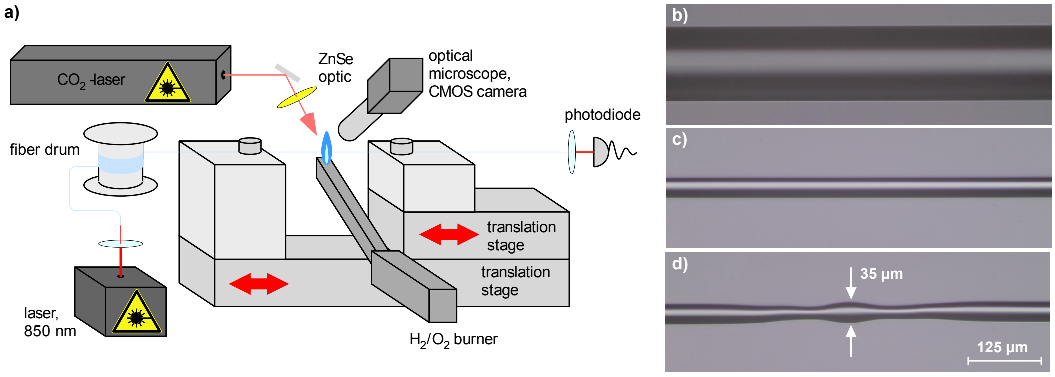

Figure 2.4: a) Schematic of the fiber pulling rig used for the fabrication of bottle microresonators and ultra-thin fibers. In order to heat the fiber, either an oxygen-hydrogen flame or a focused beam of a CO_2-laser is used. The fiber is clamped onto two translation stages, which allow one to translate and stretch the fiber. The fiber pulling process is monitored in real-time with an optical microscope and via the transmission of a laser with a wavelength of 850 nm through the fiber. b)-d) Microscope images of the bottle microresonator fiber in the pulling rig at different processing steps. b) Unprocessed fiber with a diameter of $125\,\mu\text{m}$. c) Central part of the tapered fiber with a diameter of $35\,\mu\text{m}$. d) Tapered fiber after micro-structuring with the CO_2-laser. The central bulge is the bottle microresoantor. Figures adapted from Ref. [53].

resonator diameter as shown in Fig. 2.4 c). Afterwards, the fiber is heated at two positions within a distance of $150\,\mu$m and slightly elongated to produce the two micro-tapers shown in Fig. 2.4 d). This micro-structuring step creates the bottle microresonator which is located in the central bulge of the fiber. The curvature of the bottle microresonator is determined by the positions, lengths and diameters of the two micro-tapers and defines the axial confinement of the light. In a final processing step the curvature can be further increased via the surface tension of the hot fiber. Therefore, the microresonator is heated again with the CO_2-laser without further pulling at the ends of the fiber. The final curvature of the bottle microresonator can be characterized with help of the optical microscope in the fiber pulling rig and is typically $\Delta k = 0.01$–$0.02\,\mu\text{m}^{-1}$. A detailed description of this characterization method can be found in Refs. [53, 57, 60].

Typical parameters of the bottle microresonator

The very low attenuation of light in silica glass fibers of around 5–7 dB/km in combination with the extraordinary smooth surface quality which can be achieved during the fabrication with the CO_2-laser allows to produce bottle microresonator with ultra-high quality factors. The dependency of the quality factor on the bottle resonator diameter was studied in Ref. [53]. While for resonator diameters between 30–105 μm ultra-high quality factors of about 3×10^8 could be achieved, it was observed, that Q dropped rapidly for smaller diameters. This fact is attributed to the more pronounced intensity at the surface of small resonators which makes them more sensitive to surface related losses. In terms of high Q/V-ratios the optimal diameters of bottle microresonators range between 35 – 45 μm.

2.3.2 Wave equation of the bottle microresonator

In what follows, the wave equation which describes the light fields in the bottle microresonator is solved. The procedure was introduced in Ref. [44] and is performed in detail in Ref. [53, 57]. Here, a summary is given following these references.

In the stationary case, the electric field $\vec{E}$ and magnetic field $\vec{H}$ of modes in the bottle microresonator have to respect the Helmholtz equation

$$(\vec{\nabla}^2 + k^2)\vec{\Psi} = 0\,, \tag{2.12}$$

with $\vec{\Psi} = \vec{E}, \vec{H}$ and $k = n{\cdot}k_0 = n{\cdot}\omega/c = 2\pi{\cdot}n/\lambda_0$ being the wave number of the mode with the vacuum wavenumber k_0, the angular frequency ω and the vacuum wave length λ_0. Here, c is the speed of light and n the refractive index of the medium in which the light is propagating. The azimuthal symmetry of the bottle microresonator suggests to describe the fields in cylindrical coordinates as it is shown in Fig. 2.3 a). The squared Nabla operator then reads

$$\vec{\nabla}^2 = \frac{1}{r}\partial_r + \partial_r^2 + \frac{1}{r^2}\partial_\phi^2 + \partial_z^2\,, \tag{2.13}$$

where r is the radial, z the axial and ϕ the azimuthal coordinate. Now, the procedure for solving the Helmholtz equation of the bottle microresonator is to separate the problem into wave equations for each coordinate. First of all, from the azimuthal symmetry of the bottle microresonator it is easy to see that the solutions of Eq. (2.12) will be proportional to $\exp{(im\phi)}$ with the azimuthal quantum number m. Thus, the solution will be of the form

$$\vec{\Psi}(r, \phi, z) = \vec{\Gamma}(r, z) \cdot \exp{(im\phi)}\,. \tag{2.14}$$

The part $\vec{\Gamma}(r, z)$ only depends on the radial and azimuthal coordinates and can be separated further with the method of adiabatic invariants [44]. For this purpose, the axial profile of the bottle microresonator is taken into account, which is approximated to be parabolic [57]:

$$R(z) = \frac{R_0}{\sqrt{1 + (\Delta k z)^2}} \approx R_0\left(1 - \frac{(\Delta k z)^2}{2}\right). \tag{2.15}$$

The profile is characterized by two parameters: the maximal radius R_0 at the central part of the resonator and the curvature Δk along the resonator axis. The curvature Δk is assumed to be small so that the radius of the resonator R varies only slightly along z and the condition $dR/dz \ll 1$ is fulfilled. For modes with maximal angular momentum the radial component of the wave number k_r then becomes negligible [44, 53] and the total wavenumber is

$$k \approx \sqrt{k_\phi^2 + k_z^2}\,. \tag{2.16}$$

The components k_ϕ and k_z of the wave vector can be obtained by considering once again the rotational-symmetry of the resonator around the z-axis. As a consequence, the projection of the angular momentum onto the z-axis is conserved and it follows $\partial_z(k_\phi(z)R(z)) = 0$. At the caustics positions $\pm z_\mathrm{c}$ the axial component of the wave vector vanishes and the wave number is therefore $k = k_\phi(\pm z_\mathrm{c})$. From these properties and Eq. (2.16) the expressions of the wave vector components for $|z| \leqslant z_\mathrm{c}$ are deduced as [44]:

$$k_\phi(z) = k\frac{R_\mathrm{c}}{R(z)}\,, \tag{2.17}$$

$$k_z(z) = \pm k\sqrt{1 - \frac{R_\mathrm{c}}{R(z)}}\,, \tag{2.18}$$

where $R_\mathrm{c} = R(\pm z_\mathrm{c})$ is the radius of the bottle microresonator at the caustics. Based on the adiabatic approximation along the z-axis, we make the assumption that the unknown part of the wave fuction $\vec{\Gamma}(r, z)$ in Eq. (2.14) is the product of an axial function $Z(z)$ and a radial function $\vec{\Phi}(r, R(z))$. For the latter we assume that due to the adiabatic variation of the resonator profile along the axis the z dependency is "weak" and only enters implicitly via the resonator radius $R(z)$. The complete solution of the Helmholtz equation then reads $\vec{\Psi}(r, \phi, z) = \vec{\Phi}(r, R(z)) \cdot Z(z) \cdot \exp{(im\phi)}$. Using this ansatz together with Eq. (2.17) and the assumption $\partial_z^2\vec{\Phi} \approx 0$ the Helmholtz equation can be separated into [44, 53]

$$\left(\partial_r^2 + \frac{1}{r}\partial_r + k_\phi(R(z))^2 - \frac{m^2}{r^2}\right)\vec{\Phi} = 0\,, \tag{2.19}$$

$$\left(\partial_z^2 \; + k^2 - k_\phi^2\right) Z = 0\,. \tag{2.20}$$

With the applied approximations the problem simplifies to a radial and axial wave equation which can be solved independently. Moreover, the solutions of these two equations are already known. While Eq. (2.19) has the form of the Bessel differential equation which is the same as for a dielectric cylinder [57], we will see later on that Eq. (2.20) corresponds to the differential equation of the harmonic oscillator [44].

Effective radial potential for light

The last two terms of the radial wave equation Eq. (2.19) can be interpreted as an effective potential $V_\mathrm{eff}(r)$ for the light in the resonator with [53]

$$V_\mathrm{eff}(r) = \frac{m^2}{r^2} - k_\phi^2\,. \tag{2.21}$$

The potential is plotted in Fig. 2.5 for $m = 206$. In the regime $V_\mathrm{eff}(r) > 0$ the potential defines a barrier for the light where it becomes an evanescent field. Inside the resonator the mode is guided in a region close to the surface where $V_\mathrm{eff}(r) \leq 0$. However, from a specific radius on the potential becomes also negative outside the resonator so that the light field can freely propagate. So there is a non-vanishing probability that light tunnels through the potential barrier which can be interpreted as an radiative loss channel of the resonator. The origin of the losses can be found in the physics of total internal reflection at a curved interface. In order to maintain planes of constant phase for light rotating around the resonator axis, the phase velocity has to increase with the distance from the resonator. Thus, at some point outside the resonator the

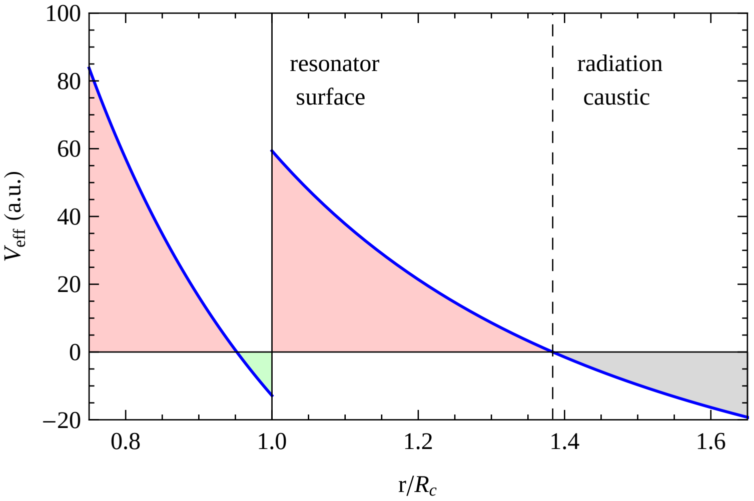

Figure 2.5: Plot of the effective radial potential $V_{\text{eff}}(r) = m^2/r^2 - k_\phi^2$ (blue) of the bottle microresonator which appears in the radial wave equation Eq. (2.19). The discontinuity is caused by the step in the refractive index at the resonator surface. The light field is confined in a region close to the resonator surface with $V_{\text{eff}}(r) \leq 0$ (green shaded area), while it decays exponentially for $V_{\text{eff}}(r) > 0$ (red shaded area). Guided light can also tunnel through the potential barrier in the region outside the resonator with $V_{\text{eff}}(r) \leq 0$ (gray shaded area) where it can freely propagate. The radius where the transition to free propagation occurs is denoted as radiation caustic (dashed line). For the plot typical parameters of our bottle resonators with $R_c = 18.48$, $\lambda = 780\,\text{nm}$, $m = 206$ and $n = 1.454$ were assumed.

vacuum light speed c is reached and for larger radii the light can not follow the rotation anymore. The radius where the phase velocity reaches c is denominated as "radiation caustic" and can be approximated for modes having only very weak tunneling losses by [61]

$$r_{\text{rad}} \approx \frac{n_{\text{resonator}}}{n_{\text{surrounding}}} \cdot R_c \,. \tag{2.22}$$

In the following section, all calculations including spatial integrals over the radial field distribution are performed only for the bound part of the mode ranging from zero to r_{rad}.

2.3.3 Solution of the radial wave equation

The solution of the radial wave function has been reduced to the calculation of the electromagnetic fields in a dielectric cylinder. In this geometry the solutions can be distinguished between two classes of polarization: Modes, where the electric field oscillates along resonator axis in z-direction, and thus is parallel to the resonator surface are denominated as transverse-electric (TE). Accordingly, one denotes modes having their magnetic field along the resonator axis which is parallel to the resonator surface as transverse-magnetic (TM)[1]. To calculate the radial field distribution it is sufficient to solve Eq. (2.19) for the axial components E_z and H_z. Then, the other field components can be simply deduced by use of the Maxwell's equations which can be written in the form

$$E_r = \frac{-i}{\epsilon\omega}\frac{1}{r}\partial_\phi H_z\,, \tag{2.23}$$

$$E_\phi = \frac{i}{\epsilon\omega}\partial_r H_z\,, \tag{2.24}$$

$$H_r = \frac{i}{\mu\omega}\frac{1}{r}\partial_\phi E_z\,, \tag{2.25}$$

$$H_\phi = \frac{-i}{\mu\omega}\partial_r E_z\,, \tag{2.26}$$

where $\epsilon = \epsilon_\mathrm{r}\cdot\epsilon_0$ and $\mu = \mu_\mathrm{r}\cdot\mu_0$ are the electric and magnetic permeability of the media with the vacuum permeabilities ϵ_0 and μ_0 and the relative permeabilities ϵ_r and μ_r. Since silica is nonmagnetic one finds $\mu_\mathrm{r} = 1$ and $\epsilon_\mathrm{r} = n^2$. When we consider again the two possible eigenpolarizations the choice of nomenclature becomes clearer since TE modes are solely described by the fields E_z, H_r and H_ϕ and therefore have a purely transversal electric field compared to the propagation direction along the ϕ coordinate. In analogy, for TM modes the only non-vanishing field components are H_z, E_r and E_ϕ. Thus, the electric field of TM modes is non-transversal meaning that a longitudinal component exists which oscillates in the direction of the light propagation. This property will give rise to very different light–matter interaction compared to transversal fields and is subject of chapter 4.

The radial wave equation Eq. (2.19) has the form of the Bessel differential equation. Therefore, the solutions of the radial wave equation $\Phi_i(r, R(z))$ are linear combinations of the Bessel functions of first and second kind J_m and Y_m. From the asymptotic behavior of the Bessel functions and the restriction to modes localized close to the resonator surface one can conclude that the solutions of the radial wave equation will have the form [53, 57]:

$$\Phi_i(r, R(z)) = \begin{cases} A_p \cdot J_m\left(\frac{k_0 n R_\mathrm{c}}{R(z)}\cdot r\right), & \text{for } r \le R(z)\,, \\ \\ B_p \cdot Y_m\left(\frac{k_0 R_\mathrm{c}}{R(z)}\cdot r\right), & \text{for } r > R(z)\,, \end{cases} \tag{2.27}$$

where i indicates the vectorial component and it is assumed that the resonator is surrounded by vacuum with $n_\mathrm{vac} = 1$. The constants A_p and B_p have to be determined by the boundary conditions of the fields at the resonator surface for the corresponding polarization p. Since the axial components E_z and H_z and the azimuthal components E_ϕ and H_ϕ are parallel to the resonator surface they have to be continuous at the interface at $r = R(z)$ yielding for TM polarization the conditions [53]

$$H_z: \quad A_\mathrm{TM}\cdot J_m(k_0 n R_\mathrm{c}) = B_\mathrm{TM}\cdot Y_m(k_0 R_\mathrm{c})\,, \tag{2.28}$$

---

[1] Note that sometimes in literature the nomenclature of TE and TM is defined inversely (especially in Refs. [53, 57]).

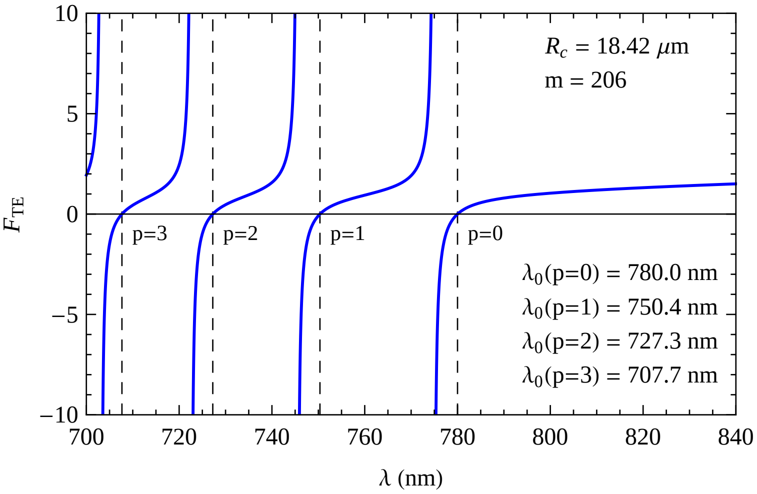

Figure 2.6: Graphical solution of Eq. (2.32) to determine the resonance wavelengths of TE modes with a caustic radius of $R_{\mathrm{c}} = 18.42\,\mu\mathrm{m}$ and an angular momentum of $m = 206$. The fundamental mode with the largest possible wavelength has the radial quantum number $p = 0$ whereas smaller wavelengths represent higher-order radial modes with $p \geq 1$.

$$E_\phi : \quad A_{\mathrm{TM}} \cdot J'_m(k_0 n R_{\mathrm{c}}) = n B_{\mathrm{TM}} \cdot Y'_m(k_0 R_{\mathrm{c}}) \, , \tag{2.29}$$

and for TE polarization

$$E_z : \quad C_{\mathrm{TE}} \cdot J_m(k_0 n R_{\mathrm{c}}) = D_{\mathrm{TE}} \cdot Y_m(k_0 R_{\mathrm{c}}) \, , \tag{2.30}$$

$$H_\phi : \quad n C_{\mathrm{TE}} \cdot J'_m(k_0 n R_{\mathrm{c}}) = D_{\mathrm{TE}} \cdot Y'_m(k_0 R_{\mathrm{c}}) \, , \tag{2.31}$$

where for the derivation of the expressions for E_ϕ and H_ϕ the Maxwell equations Eq. (2.24) and Eq. (2.26) have been applied and the prime stands for the derivative with respect to the argument of the Bessel functions.

To be resonant a mode with a given azimuthal quantum number m has to fulfill at the same time the boundary conditions for E_z and H_ϕ in the case of TE polarization and for H_z and E_ϕ in the case of TM polarization. Thus, to obtain a resonance condition for modes with TE and TM polarization, Eq. (2.31) and Eq. (2.29) are divided by Eq. (2.30), respectively, which then read [53]:

$$F_{\mathrm{TE}}(\lambda_0, R_{\mathrm{c}}) = n \frac{J'_m(k_0 n R_{\mathrm{c}})}{J_m(k_0 n R_{\mathrm{c}})} - \frac{Y'_m(k_0 R_{\mathrm{c}})}{Y_m(k_0 R_{\mathrm{c}})} = 0 \, , \tag{2.32}$$

$$F_{\mathrm{TM}}(\lambda_0, R_{\mathrm{c}}) = \frac{J'_m(k_0 n R_{\mathrm{c}})}{J_m(k_0 n R_{\mathrm{c}})} - n \frac{Y'_m(k_0 R_{\mathrm{c}})}{Y_m(k_0 R_{\mathrm{c}})} = 0 \, . \tag{2.33}$$

The relations F_{TE} and F_{TM} can be solved graphically which is done exemplarily for the case of TE polarization in Fig. 2.6. Here, we assume an angular momentum of $m = 206$ chosen such that the first mode which fulfills the resonance condition has a caustic radius close to the resonator radius in the CQED experiment ($R_0 \approx 18.5\,\mu\mathrm{m}$) and a wavelength of $\lambda_0 = 780\,\mathrm{nm}$.

In Fig. 2.6 each root of F_{TE} indicates a resonance wavelength for which a mode with $m = 206$ and caustic radius $R_{\mathrm{c}} = 18.42\,\mu\mathrm{m}$ is resonant. One can assign the radial quantum number p to the roots of F_{TE}, starting from 0 for the fundamental mode with the largest possible wavelength. With the parameters for m, R_{c} and λ_0 the boundary condition in Eq. (2.30) can be solved which allows to calculate the radial intensity distribution.

Figs. 2.7 a)-c) show the normalized radial intensity $I_{\mathrm{norm}} = |E_{\mathrm{z}}(r)|^2 / \int_0^{r_{\mathrm{rad}}} n(r)^2 |E_{\mathrm{z}}(r)|^2 r dr$ of the first three resonances in Fig. 2.6. Now, the meaning of the angular quantum number p becomes clearer: as we see it counts the number of nodes of the radial intensity distribution. Compared to the higher order radial modes the fundamental mode with $p = 0$ has only a single intensity maximum and is located closest to the resonator surface having the smallest mode volume. In contrast, the intensity of higher order radial modes has a larger radial extension and oscillates along r.

For TM polarization the resonance condition F_{TM} can be solved equivalently following the above discussion. The resulting electric field then has the components E_r and E_ϕ and is therefore non-transversal. The normalized radial intensity of the fundamental mode with $R_{\mathrm{c}} = 18.42\,\mu\mathrm{m}$, $m = 206$ andh $\lambda_0 = 780\,\mathrm{nm}$ is shown in Fig. 2.8 for both field components. The intensity of the radial field component $|E_r|^2$ is discontinuous at the resonator surface respecting the boundary conditions of electric fields perpendicular to an interface and features a single maximum inside the resonator corresponding to its radial order $p = 0$. In contrast, the azimuthal field intensity $|E_\phi|^2$ is minimal at the peak of $|E_r|^2$ and becomes maximal at the surface of the resonator. At the first glance the azimuthal component seems to be relatively small compared to the field in the radial direction. However, in chapter 4 we will see that this observation is not valid for the evanescent field where the field polarization can become highly non-transversal.

2.3.4 Solution of the axial wave equation

In section 2.3.2 the Helmholtz equation for the bottle resonator was separated and the axial part of the wave equation was deduced as

$$\left(\partial_z^2 + k^2 - k_\phi^2\right) Z = 0\,. \tag{2.34}$$

To solve this equation, first, the azimuthal wavenumber $k_\phi(z)$ has to be determined. For this purpose, one uses the relation between the axial component of the angular momentum L_z and the azimuthal wave number k_ϕ which is $L_z = m \cdot \hbar = R_{\mathrm{eff}} k_\phi(z) \cdot \hbar$. Here, we have introduced the effective radius of the mode $R_{\mathrm{eff}} = c_r \cdot R(z)$ reflecting the fact that the mode has no clearly defined radius but follows a radial intensity distribution. The correction factor c_r can be obtained by the calculation of the azimuthal wavenumber which is done by weighting $1/r$ with $n(r)^2|E(r)|^2$ [53,57]:

$$k_\phi = \frac{m}{c_r R(z)} = m \cdot \frac{\int n(r)^2 |E(r)|^2 \cdot (1/r) dr}{\int n(r)^2 |E(r)|^2 dr}\,. \tag{2.35}$$

For the intensity distributions at the caustics of the fundamental mode with $\lambda_0 = 780\,\mathrm{nm}$ and $m = 206$ (compare Fig. 2.7 a) and Fig. 2.8) one obtains $c_r = 0.972$ for TE and $c_r = 0.969$ for TM polarization.

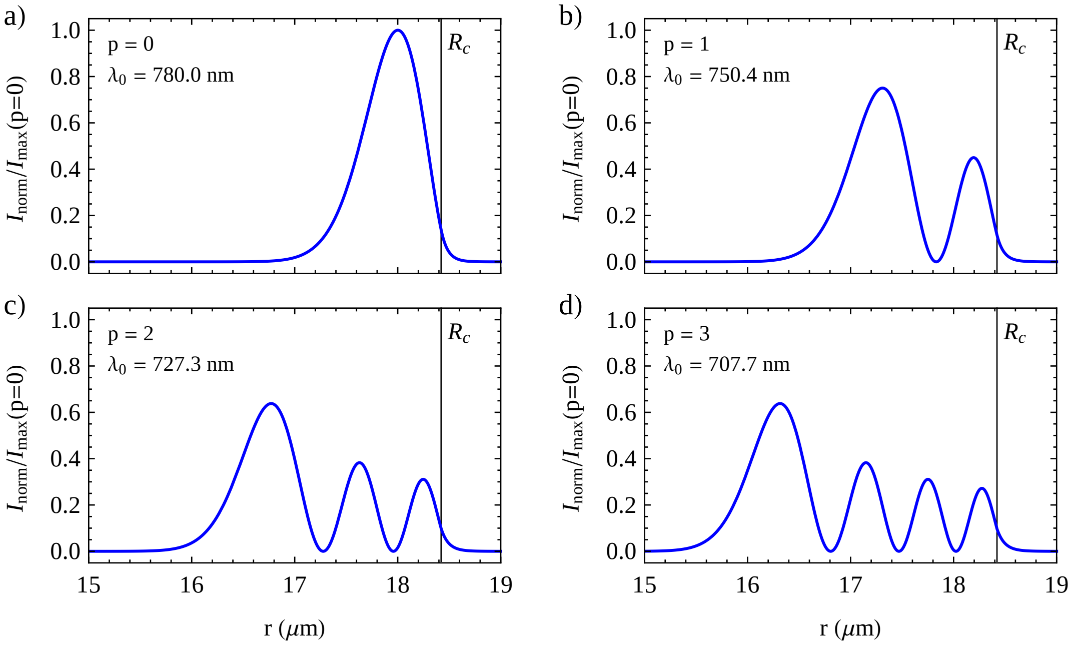

Figure 2.7: Normalized intensity distribution along r of the first four radial TE modes for $R_\text{c} = 18.42\,\mu\text{m}$ and $m = 206$ from the graphical solution of the radial wave equation in Fig. 2.6 where the quantum number p gives the number of radial intensity nodes. The intensity is weighted with the radial power density following the expression $I_\text{norm} = |E_\text{z}(r)|^2 / \int_0^{r_\text{rad}} n(r)^2 |E_\text{z}(r)|^2 r dr$ and is plotted relative to the maximum of the fundamental radial mode. The vertical line illustrates the resonator surface.

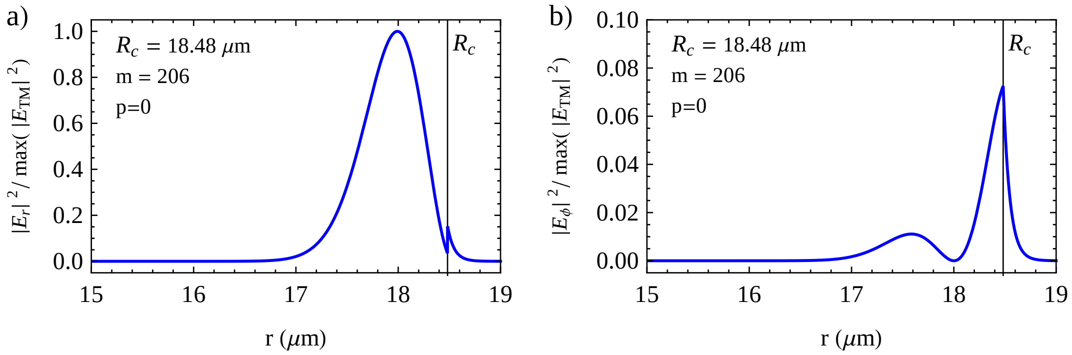

Figure 2.8: Normalized intensity distribution along r of the a) radial and b) azimuthal field component belonging to the fundamental radial TM mode at $\lambda = 780\,\text{nm}$ with $m = 206$. The intensity is normalized to the maximal value of the total field $|E_\text{TM}|^2 = |E_r|^2 + |E_\phi|^2$.

Now, $k_\phi(z)$ can be eliminated in the axial wave equation. As a consequence, the resonator profile $R(z)$ enters into the expression which is given by Eq. (2.15) so that the axial wave equation finally reads [53]

$$\left(\partial_z^2 + k^2 - \left(\frac{m}{c_r R_0}\right)^2 - \left(\frac{m\Delta k}{c_r R_0}\right)^2 \cdot z^2\right) Z = 0\,. \tag{2.36}$$

This expression is identical to the well known differential equation of the harmonic oscillator $\left(\partial_z^2 + E_{\text{kin}} - V(z)\right) Z = 0$, where the kinetic energy is identified with $E_{\text{kin}} = k^2 - m^2/(c_r R_0)^2$ and the harmonic potential has the form $V(z) = (\Delta E_m \cdot z/2)^2$ with $\Delta E_m = 2m\Delta k/(c_r R_0)$.

As a consequence, the solution of the axial wave equation has a discrete energy spectrum $E_{m,q} = (q + 1/2)\Delta E_m$ with the quantum number $q \in \mathbb{N}_0$ which counts the nodes of the axial intensity distribution. The latter is given by the expression [53,57]

$$Z_{m,q}(z) = C_{mq} \cdot H_q\left(\sqrt{\frac{\Delta E_m}{2}} \cdot z\right) \exp\left(-\frac{\Delta E_m}{4} z^2\right), \tag{2.37}$$

where $C_{mq} = \sqrt[4]{\Delta E_m/(\pi 2^{2q+1}(q!)^2)}$ and H_q is a Hermite polynomial.

To combine now the solutions of the radial wave equation with fixed parameters m and R_{c} and the axial wave equations with fixed parameters q and Δk the central radius of the bottle resonator R_0 has to be determined. To this end, we first consider the axial harmonic potential $V(z)$ which is zero at the center of the resonator ($z = 0$). As a consequence, at that point the eigenenergy will be purely "kinetic" so that we can set $E_{m,q} = E_{\text{kin}}$ from which we can deduce an expression for the eigenvalue of the wavenumber

$$k_{m,q} = \sqrt{\frac{m^2}{(c_r R_0)^2} + \left(q + \frac{1}{2}\right)\frac{2m\Delta k}{c_r R_0}}\,. \tag{2.38}$$

Setting this expression equal to $k = m/(c_r R_c)$ from Eq. (2.35) one finally optains [53]

$$\frac{m^2}{(c_r R_{\text{c}})^2} = \frac{m^2}{(c_r R_0)^2} + \left(q + \frac{1}{2}\right)\frac{2m\Delta k}{c_r R_0}\,, \tag{2.39}$$

which allows to solve for R_0. In Fig. 2.9 a-d) the intensity distribution $I(z) = |Z_{mq}(z)|^2$ is plotted for the four lowest axial modes with $q = 0$–3. While the fundamental axial mode with $q = 0$ has a single intensity maximum which is located in the center of the resonator, the intensity of higher-order radial modes oscillates along z. The peak-intensity is reached in the maxima close to the caustics at $\pm z_{\text{c}}$ while for $|z| > z_{\text{c}}$ the resonator field decays exponentially. For comparison, also an axial mode with much higher order of $q = 25$ is shown in In Fig. 2.9 e). It is apparent that for such a mode the peak intensity reduces considerably. Moreover, its spatial extension along the resonator axis spans approximately $40\,\mu\text{m}$ while the intensity node separation becomes smallest in the middle of the bottle microresonator where the minimal intensity occurs.

The caustics of higher-order radial modes are located more distant from the resonator center leading to smaller caustic radii. When the central resonator radius R_0 and the caustic radius R_{c}

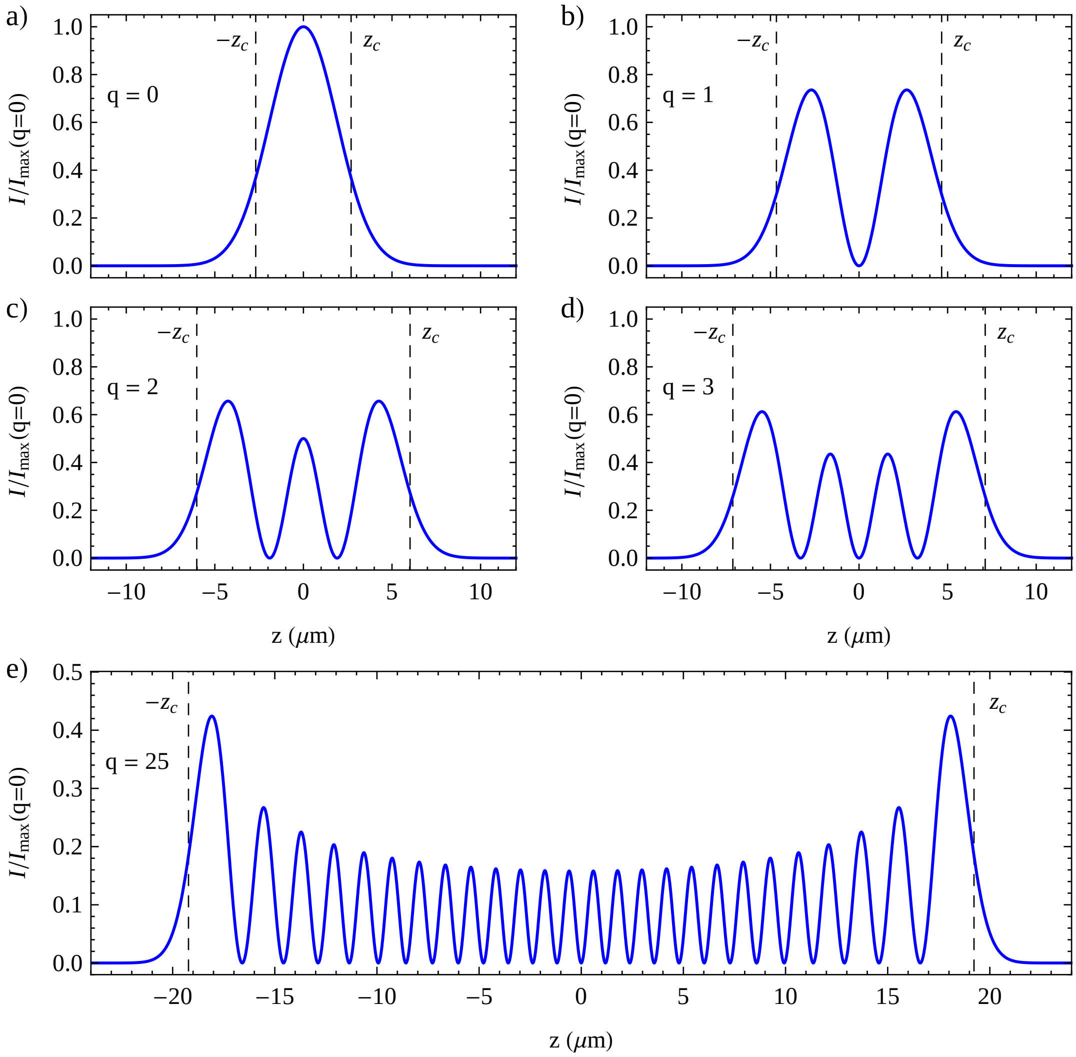

q	R_{c} (μm)	z_{c} (μm)	λ_0 (nm)	V (μm^3)
0	18.482	2.49	780.00	827
1	18.460	4.32	779.06	1121
2	18.437	5.57	778.13	1254
3	18.415	6.59	777.20	1341
25	17.945	17.94	757.53	1853

Figure 2.9: Intensity distribution $I(z) = |Z_{mq}(z)|^2$ of the four lowest axial TM modes (a-d) and a high axial q mode (e) with azimuthal quantum number $m = 206$ normalized to the maximum intensity of the fundamental axial mode. The caustic radius R_{c} of the fundamental axial mode with $q = 0$ was chosen to coincide with the radial mode in Fig. 2.8 having a resonance wavelength of $\lambda_0 = 780\,\mathrm{nm}$. With a resonator curvature of $\Delta k = 0.014\,\mu\mathrm{m}^{-1}$ the central resonator radius follows as $R_0 = 18.499\,\mu\mathrm{m}$. The table lists the caustic radii, the caustic positions, the resonance wavelengths and the mode volumes of the illustrated axial modes which can be calculated with Eqs. (2.39), (2.15), (2.33) and (2.40).

for a specific axial mode are known the caustic radii of other axial modes can be calculated by using Eq. (2.39) assuming that c_r remains approximately constant [53]. With the determined caustic radii the positions of the caustics $\pm z_\mathrm{c}$ can simply be deduced with help of the resonator profile given in Eq. (2.15).

Since the caustic radii R_c of higher-order axial modes are reduced compared to the fundamental mode while their angular momentum m is conserved their corresponding resonance wavelengths will shift to smaller values. The axial mode spectrum can be determined with the resonance conditions in Eqs. (2.32) and (2.33) from the caustic radii. This is performed exemplarily for the axial modes of Fig. 2.9 in the corresponding table.

2.3.5 Mode volume of bottle modes

The volume which is occupied by a mode can be calculated with the help of equation Eq. (2.7). Following the separation of the wave equation in section 2.3.2 the spatial integral can be solved in good approximation independently in each coordinate so that the mode volume is then defined as [53]

$$V_{m,q} \approx 2\pi \cdot \int_{-\infty}^{\infty} \left(\frac{Z_{m,q}(z)}{\max(Z_{m,q}(z))} \right)^2 dz \cdot \int_0^{r_\mathrm{rad}} n(r)^2 \left(\frac{|E(r)|^2}{\max(|E(r)|^2)} \right)^2 r dr \,. \tag{2.40}$$

In this expression the factor 2π originates from integration over the azimuthal coordinate and the electric field intensity is $|E(r)|^2 = |E_z(r)|^2$ for the case of TE polarization and $|E(r)|^2 = |E_r(r)|^2 + |E_\phi(r)|^2$ for TM polarized modes.

The mode volume of the four lowest axial modes shown in Fig. 2.9 is calculated with the above equation and given in the corresponding table. The volumes range from $827\,\mu\mathrm{m}^3$ to $1341\,\mu\mathrm{m}^3$ and are comparable with mode volumes of other WGM microresonator types [9]. From examination of the axial modes it is apparent that the fundamental mode with $q = 0$ has the smallest mode volume while for increasing q the differences in mode volume become less significant. For comparison also the mode volume of a higher axial mode with $q = 25$ is given which is only larger by a factor of ≈ 2 compared to the fundamental mode.

2.3.6 Frequency tuning properties of the bottle microresonator

One important advantage of the bottle microresonator compared to other types of WGM microresonators is the ability to tune the resonance frequency to arbitrary references by applying stress to the fiber. The superior tuneability arises from the fact that due to the axial quantum number q the bottle resonator not only has an azimuthal but also an axial FSR. The latter is customizable by the curvature Δk of the resonator and therefore allows to influence the mode spectrum. With help of the wave number eigenvalues in Eq. (2.38) the following expression for the azimuthal and axial FSR can be approximated [53]

$$\Delta\nu_m = \frac{c}{2\pi n} \cdot (k_{m+1,q} - k_{m,q}) \approx \frac{c}{2\pi n c_r R_0} \,, \tag{2.41}$$

$$\Delta\nu_q = \frac{c}{2\pi n} \cdot (k_{m,q+1} - k_{m,q}) \approx \frac{c\Delta k}{2\pi n} \,. \tag{2.42}$$

For the bottle microresonator used in all experiments within this thesis with a curvature of $\Delta k = 0.014$ and a central radius of $R_0 \approx 18.5\,\mu\mathrm{m}$ at a wavelength of $\lambda_0 = 780\,\mathrm{nm}$ the azimuthal FSR is $\Delta\nu_m = 1.834\,\mathrm{THz}$ corresponding to 3.718 nm while the axial FSR is only $\Delta\nu_q = 393\,\mathrm{GHz}$ or 0.798 nm, where a refractive index of $n = 1.454$ is assumed. To tune the frequency of a bottle mode the optical path has to be changed. This is possible either by a variation of the resonator radius or by a change of the refractive index of the resonator material which could be realized for instance with the thermo-optic effect. However, in the case of the bottle microresonator it is much more convenient to make use of the elasto-optic effect by applying strain. Since the bottle microresonator is fabricated from a standard optical glass fiber this can be simply achieved by pulling at the ends of the fiber. The strain results in an elastic deformation of the resonator which changes the resonator radius. Moreover, the refractive index is as well sensitive to strain in the material [53].

In Ref. [58] strain tuning of bottle modes was demonstrated over a range of 700 GHz which was only limited by the travel range of the piezo actuators. The applied strain was estimated to be 35 % of the typical damage threshold of silica. Comparing theses numbers with the azimuthal and axial FSR of the bottle microresonator it becomes clear that the tuning range is more than sufficient to span one axial FSR. Therefore, the azimuthal FSR can be bridged by use of several axial modes: when a specific frequency is not within the tuning range of a mode one can simply switch to another axial mode which is closer to the aimed frequency by a multiple of the axial FSR. In order to keep the mode volume small it is desirable to perform this tuning scheme with only a small number of modes with a low axial q. Comparing the azimuthal FSR of $\Delta\nu_m = 1.834\,\mathrm{THz}$ with the axial FSR of $\Delta\nu_q = 393\,\mathrm{GHz}$ therefore suggests that full tuneability of the bottle microresonator can be achieved by use of the four lowest axial modes with $q = 0$–3 (compare table in Fig. 2.9). As a consequence, the mode volume can be kept at low values of $V \lesssim 1300\,\mu\mathrm{m}^3$.

2.4 Evanescent coupling to WGM microresonators with ultra-thin fibers

In the preceding sections it was shown that WGM microresonators have extraordinary properties like ultra-high Q, very small mode volumes. The breakthrough of WGM resonators was mainly influenced by the development of reliable coupling techniques. In the beginning, the main mechanism for coupling light into WGM resonators was free-beam coupling which turned out to be very inefficient [39].

A much more promising way for coupling light to a WGM resonator was found by accessing its near field via frustrated total internal reflection (FTIR). This process was initially performed with prisms [50, 62] and side-polished optical fibers [63–65] such that the evanescent field of the coupler overlapped with the evanescent field of the resonator. The field overlap allows light to tunnel from the coupling device into the resonator and vice versa. The coupling efficiency between resonator and coupler modes is determined by the spatial overlap of the fields, by the resonance condition of the resonator and by the wave vectors of the mode in the resonator and the coupler. The latter corresponds to a phase-matching condition which has to be fulfilled to allow constructive interference between the fields of the coupler and the resonator at the

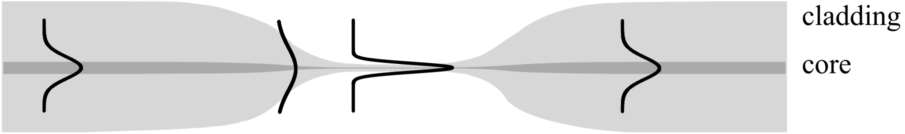

Figure 2.10: Schematic of the taper transition between a standard optical fiber and an ultra-thin fiber section. During the propagation through the taper the mode profile is compressed as illustrated by the black lines. Figure adapted from Ref. [57].

coupling junctions [66]. However, there is a considerable mismatch between the wave vector of light in side polished fibers and the one of small WGM microresonators which sets an limit to the coupling efficiency. Similarly, the coupling efficiency to prisms is limited due to their continuous mode structure [39]. For this reason, ultra-thin tapered optical fibers turn out to be ideal coupling devices for silica WGM microresonator: First, below a certain diameter these fibers support only the propagation of a single mode thereby suppressing the coupling of the WGM resonator to higher order fiber modes. Second, by control of the fiber diameter it is possible to customize the wave vector of light in the fiber for optimal phase-matching to the resonator [67].

2.4.1 Ultra-thin optical fibers

Typically, fibers with ultra-thin diameters are fabricated from standard optical glass fibers which are locally heated and tapered down as described in section 2.3.1 and illustrated in Fig. 2.10. In standard optical fibers, light is guided in the fiber core by total internal reflection at the interface to the surrounding fiber cladding. However, when the fiber is tapered down to typical diameters on the scale of the light wavelength, the fiber core no longer exists and the light is guided instead at the interface between the cladding and the surrounding medium. From the discussion of total internal reflection in section 2.2.2 it follows that the ultra-thin part of the fiber will be surrounded by an evanescent field which allows to access the guided light in the fiber. In the taper section the fiber mode undergoes a strong spatial compression of the mode (see Fig. 2.10). If this compression is performed adiabatically [57] the taper transmission from the standard fiber to the ultra-thin part can become extremely efficient, enabling transfer efficiencies larger than 98 % [36]. Thus, the coupling to ultra-thin optical fibers allows an efficient integration of WGM microresonators into existing standard optical fiber technologies.

At this point, we will only give a short summary of the electromagnetic mode structure in optical fibers, which are described in more detail in textbooks like, e.g., in Ref. [68]. Considering a dielectric cylinder with radius R and refractive index n_1 surrounded by another medium with smaller refractive index n_2 the electromagnetic fields in the fiber can be deduced. In cylindrical coordinates the solution of the wave equations for the field pointing along the fiber axis[2] (E_z

---

[2] In contrast to a freely propagating plane wave, waveguides modes can have longitudinal components pointing in the direction of propagation.

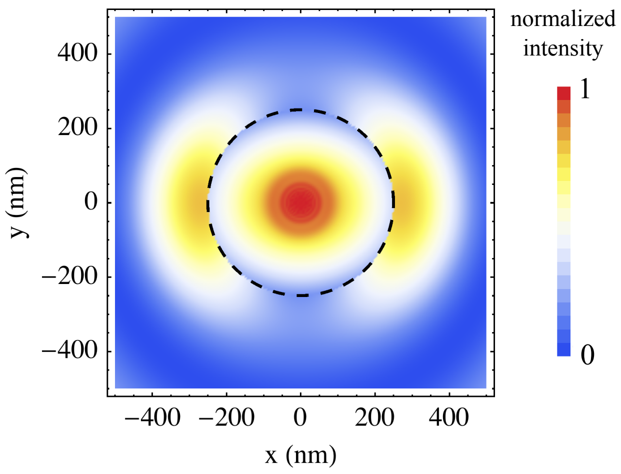

Figure 2.11: Normalized intensity distribution of the HE_{11} mode in an ultra-thin fiber with quasi-linear polarization along the x-direction (z defines the fiber axis, x and y the transversal directions). The intensity is normalized to its maximal value in the center of the fiber. For the plot a light wavelength of $\lambda_0 = 780\,\mathrm{nm}$ is assumed and the radius of the ultra-thin fiber is set to $R = 250\,\mathrm{nm}$ as indicated by the dashed line. The equation for the plot can be found in Ref. [69].

and H_z) take the form [57,68]

$$\Phi \propto \begin{cases} J_l\,(hr)\exp[(i(\omega t - \beta z \pm l\phi), & \text{for } r \leq R\,, \\ \\ K_l\,(qr)\exp[(i(\omega t - \beta z \pm l\phi), & \text{for } r > R\,, \end{cases} \tag{2.43}$$

where $l \in \mathbb{N}_0$ and J_l is the Bessel function of first kind while K_l is the modified Bessel function of second kind. The propagation constant of the fiber mode β also appears in the arguments of the Bessel functions as $h^2 = k_1^2 - \beta^2 > 0$ and $q^2 = \beta^2 - k_2^2 > 0$ with $k_i = n_i k_0$ being the wave number in the medium, respectively. From Eq. (2.43) all other field components can be deduced with help of the Maxwell's equations.

At the boundaries of the dielectric cylinder the tangential field components have to be continuous. From this condition a transcendent equation for β is obtained [70]

$$(\eta_1 + \eta_2)(k_1^2\eta_1 + k_2^2\eta_2) = l^2\beta^2\left(\frac{1}{(hR)^2} + \frac{1}{(qR)^2}\right)^2\,, \tag{2.44}$$

with $\eta_1 = J_l'(hR)/(hR \cdot J_l(hR))$ and $\eta_2 = K_l'(qR)/(qR \cdot K_l(qR))$. This equation gives for each l a set of β_m with $m = \mathbb{N}$ being the number of radial intensity anti-nodes [57]. The solutions of Eq. (2.44) can be divided into two sets of hybrid modes EH_{lm} and HE_{lm} which are defined by all six components of the electromagnetic field (E_z, E_r, E_ϕ and H_z, H_r, H_ϕ). The nomenclature is chosen such that the set HE contains the fundamental HE_{11} mode of the fiber. All other modes are restricted by a cutoff condition which sets a certain minimal fiber radius for each mode. Below this radius the corresponding mode is not guided in the fiber anymore [70]. Thus, for a fixed wavelength a decrease in the fiber radius reduces the number of guided modes as well. When the fiber radius R fulfills the cutoff condition [68]

$$k_0 R\sqrt{n_1^2 - n_2^2} < 2.405\,, \tag{2.45}$$

no other mode than the fundamental HE_{11}mode can exist in the fiber. Therefore, by reduction of the fiber radius it is possible to fabricate so-called "single mode fibers". For instance, for a light wavelength of $\lambda_0 = 780\,\mathrm{nm}$ an ultra-thin fiber made from silica ($n_1 = 1.454$) which is surrounded by vacuum ($n_2 = 1$) would become single mode for a fiber radius of $R < 283\,\mathrm{nm}$. Moreover, since the propagation constant of light in the fiber depends on the fiber radius it can be customized. As a consequence, it becomes possible to match the propagation constants in the ultra-thin fiber and a WGM microresonator [67] such that an optimal coupling between the light fields is achieved approaching unity efficiency [71].

The HE_{11} mode can have rotating polarization as well as quasi-linear polarization.[3] With the help of Eq. (2.43) and Eq. (2.44) one can find the solution of the wave equation for the HE_{11} mode and calculate the corresponding intensity distribution in and around an ultra-thin fiber (see Ref. [69] for details). In Fig. 2.11 the normalized intensity distribution of the HE_{11} mode with quasi-linear polarization along the x-direction is illustrated for an ultra-thin fiber with a radius of $R = 250\,\mathrm{nm}$. Compared to the intensity inside the fiber the evanescent field shows a strong azimuthal dependency which originates from the boundary conditions at the interface between silica and vacuum. Along the main polarization axis (x-direction) the field is predominantly perpendicular to the fiber surface and is therefore discontinuous. As a consequence, the evanescent field is much stronger on the main polarization axis compared to the positions where no intensity jump occurs since at this point the field is approximately parallel to the fiber surface ($x = 0$). From Fig. 2.11 it is evident that a considerably amount of the light in an ultra-thin fiber actually is guided in the evanescent field. This is a very beneficial property since it facilitates the coupling of light into WGM resonators via FTIR.

2.4.2 Modeling the evanescent coupling to a WGM

In the following the coupling between a WGM in a microresonator to the modes of an evanescent coupling device like, e.g., an ultra-thin fiber, is discussed in terms of a simple model introduced by Haus [72].

A schematic overview of the involved physical quantities of the model is given in Fig. 2.12. The temporal evolution of the amplitude a of a mode in the WGM microresonator excited from an evanescent coupling device which we will denote from now on simply as a waveguide can be

---

[3] Since the HE_{11} is hybrid it can be only quasi-linear polarized meaning that in a plane perpendicular to the fiber axis the transverse electric field points predominantly along one direction. However, there is also a longitudinal field component which is in general non-zero leading to an elliptical polarization of the total electric field. For details see Ref. [69].

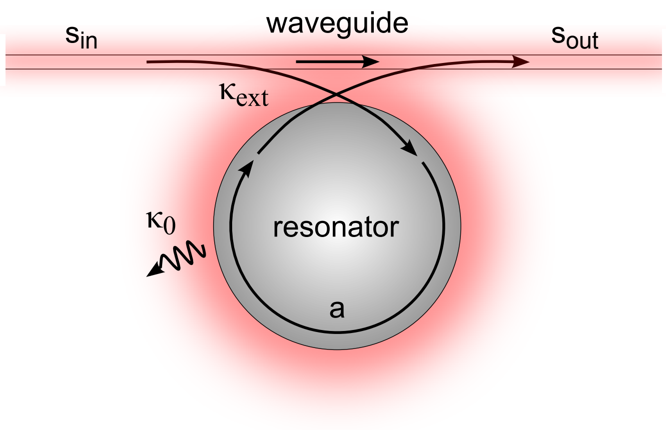

Figure 2.12: Schematic of the evanescent resonator–waveguide coupling. The resonator mode a is driven by the incoming waveguide field s_{in}. The evanescent coupling between the resonator and the waveguide is characterized with the coupling rate κ_{ext} while the internal dissipation of the resonator is given by the loss rate κ_0. The outgoing light field s_{out} in the waveguide is a superposition of the incoming light s_{in} and the out-coupled light from the resonator mode a (see main text for more details). Figure follows Ref. [71].

described by the first-order differential equation [72][4]

$$\frac{da}{dt} = -i(\omega_0 - \omega)a - (\kappa_0 + \kappa_{\text{ext}})a - \sqrt{2\kappa_{\text{ext}}}s_{\text{in}}\,. \tag{2.46}$$

Here, it is assumed that the resonator mode with angular frequency ω_0 either decays due to some internal resonator losses with the rate κ_0 or into the external waveguide with the coupling rate κ_{ext}. Moreover, the waveguide itself carries a wave with amplitude s_{in} and angular frequency ω which couples to the resonator with the same coupling rate κ_{ext} due to time reversibility. Note that according to this definition $W = |a|^2$ is the energy of the resonator mode and $|s_{\text{in}}|^2$ is the power of the incident wave. When the resonator is not driven from the waveguide ($s_{\text{in}} = 0$) the mode energy decays exponentially according to

$$\frac{dW}{dt} = a^*\frac{da}{dt} + a\frac{da^*}{dt} = -2(\kappa_0 + \kappa_{\text{ext}})W\,. \tag{2.47}$$

Thus, the lifetime of photons in the loaded resonator can be identified with $\tau = 1/2\,(\kappa_0 + \kappa_{\text{ext}})^{-1}$ which gives the full width at half maximum (FWHM) linewidth of the resonator as

$$\Delta\nu = \frac{1}{2\pi\tau} = \frac{1}{\pi}(\kappa_0 + \kappa_{\text{ext}})\,. \tag{2.48}$$

As a consequence, the resonator can be assumed to have an intrinsic linewidth $\Delta\nu_0 = \kappa_0/\pi$ which is broadened by the coupling to the waveguide by $\Delta\nu_{\text{ext}} = \kappa_{\text{ext}}/\pi$. With the help of

---

[4] In contrast to Ref. [72] we consider here the negative frequency component of the mode amplitude a and chose the relative phase of the input field to be -1.

Eq. (2.6) a similar consideration can be made for the loaded quality factor Q of the resonator which leads to the relation

$$Q_{\text{load}}^{-1} = Q_0^{-1} + Q_{\text{ext}}^{-1} = \frac{2}{\omega}(\kappa_0 + \kappa_{\text{ext}})\,, \tag{2.49}$$

where the intrinsic quality factor Q_0 and the "external" quality factor Q_{ext} have been introduced.

The wave in the waveguide after the interaction with the resonator can be simply described by

$$s_{\text{out}} = c_s s_{\text{in}} + c_a a\,, \tag{2.50}$$

where the coefficients c_s and c_a remain to be determined. For this purpose, one first considers the power which is escaping from the resonator into the waveguide. It can be found by assuming that no intrinsic resonator losses are present ($\kappa_0 = 0$) and that the resonator is not driven ($s_{\text{in}} = 0$). Then Eq. (2.47) can be set into relation with the outgoing power in the waveguide $-|s_{\text{out}}|^2$ by

$$\frac{d|a|^2}{dt} = -2\kappa_{\text{ext}}|a|^2 = -|s_{\text{out}}|^2\,. \tag{2.51}$$

Combining Eq. (2.50) and Eq. (2.51) we can identified the coefficient c_a with

$$c_a = \sqrt{2\kappa_{\text{ext}}}\,, \tag{2.52}$$

For the determination of c_s, the net power flow into the resonator is compared with the buildup and dissipation of the energy in the resonator which yields [72]

$$|s_{\text{in}}|^2 - |s_{\text{out}}|^2 = \frac{d}{dt}|a|^2 + 2\kappa_0|a|^2\,. \tag{2.53}$$

Moreover, from Eq. (2.46) we deduces

$$\frac{d}{dt}|a|^2 = -2(\kappa_0 + \kappa_{\text{ext}})|a|^2 - \sqrt{2\kappa_{\text{ext}}}(a^* s_{\text{in}} + a s_{\text{in}}^*)\,. \tag{2.54}$$

Combining Eqs. (2.52) to (2.54) and Eq. (2.50) then allows to determine c_s to be

$$c_s = 1\,. \tag{2.55}$$

Now, the steady-state transmission coefficient through the waveguide coupled to the resonator can be obtained from Eq. (2.50) by

$$t = \frac{s_{\text{out}}}{s_{\text{in}}} = 1 + \frac{a}{s_{\text{in}}}\sqrt{2\kappa_{\text{ext}}}\,. \tag{2.56}$$

In order to replace the mode amplitude a in this expression, one considers Eq. (2.46) in the steady-state ($da/dt = 0$) which gives

$$a = \frac{-s_{\text{in}}\sqrt{2\kappa_{\text{ext}}}}{i(\omega - \omega_0) + \kappa_0 + \kappa_{\text{ext}}}\,. \tag{2.57}$$

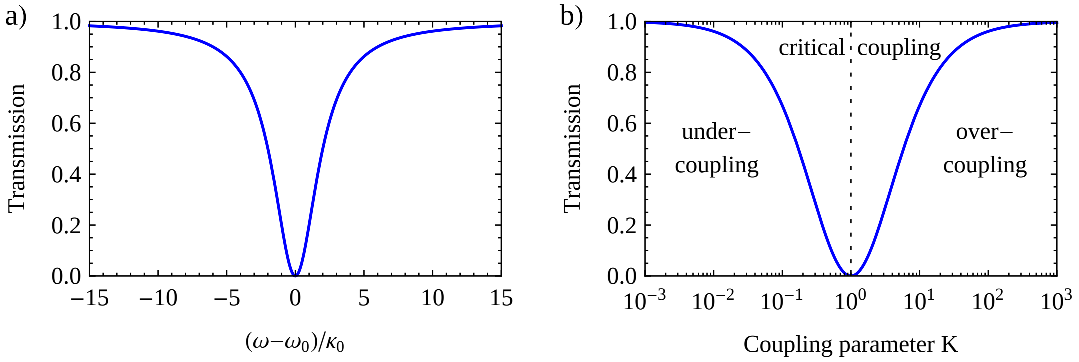

Figure 2.13: Transmission $T = |t|^2$ of the light intensity trough a waveguide coupled to a resonator. a) The transmission is plotted as a function of the resonator–light detuning, where the waveguide coupling rate κ_{ext} is chosen to be equal to the resonator losses κ_0. b) On-resonant transmission ($\omega = \omega_0$) as function of the coupling parameter K.

Comparing this expression with Eq. (2.50) we observe a π phase shift in the waveguide between the incoming light and the light coupling back from the resonator. As a consequence, in the waveguide destructive interference between the two fields will occur leading to the transmission coefficient

$$t = \frac{\kappa_0 - \kappa_{\text{ext}} + i(\omega - \omega_0)}{\kappa_0 + \kappa_{\text{ext}} + i(\omega - \omega_0)} . \tag{2.58}$$

The transmission $T = |t|^2$ is a function of the light frequency $\nu = \omega/(2\pi)$ which has a Lorentzian shape centered around the resonator frequency $\nu_0 = \omega_0/(2\pi)$ and a FWHM of $\Delta\nu = (\kappa_0 + \kappa_{\text{ext}})/\pi$, as shown in Fig. 2.13 a). The exact properties of the waveguide transmission coupled to the resonator depend on the ratio between the two coupling rates κ_0 and κ_{e} and will be investigated in the following.

2.4.3 Regimes of evanescent coupling

In the preceding section the evanescent coupling between the resonator and the waveguide has been described by the coupling rate κ_{ext} which can be interpreted as a loss channel of the resonator and at the same time also appears in the driving term in Eq. (2.46). From the discussion of ultra-thin fibers in section 2.4.1 it is clear that the magnitude of κ_{ext} is determined by several factors like the overlap between the fields and the phase matching between modes of the resonator and the waveguide. In order to evaluate the response of the combined resonator–waveguide system to incoming light, κ_{ext} has to be set in relation to the internal losses κ_0. For this purpose, it is useful to consider the intensity transmission of the coupled system on resonance ($\omega = \omega_0$) which follows from Eq.(2.58) as

$$T = \left(\frac{\kappa_0 - \kappa_{\text{ext}}}{\kappa_0 + \kappa_{\text{ext}}}\right)^2 = \left(\frac{1-K}{1+K}\right)^2 . \tag{2.59}$$

The on-resonant transmission depends purely on the two loss channels of the resonator κ_0 and κ_{ext} and is here expressed as function of their ratio $K = \kappa_{\text{ext}}/\kappa_0$, the so-called coupling parameter. In Fig. 2.13 b) the dependency of the on-resonant transmission on K is plotted. Accordingly, the evanescent coupling between the resonator and the waveguide can be divided into three cases:

- **Under-coupling** ($\kappa_{\text{ext}} < \kappa_0$, $K < 1$): When the intrinsic resonator loss dominates over the coupling to the waveguide, more light is dissipated in the resonator than out-coupled to the waveguide. As a consequence, light which re-enters from the resonator into the waveguide only partially interferes descrutively with the incoming light and the transmission is always non-zero.

- **Critical coupling** ($\kappa_{\text{ext}} = \kappa_0$, $K = 1$): At the point of critical coupling the losses induced by the waveguide to the resonator equal exactly the internal resonator losses. Then, the amplitudes of the light which is initially in the waveguide and the light coupling back from the resonator into the waveguide have the same magnitude and thus cancel each other completely on resonance. Therefore, the transmission becomes zero and all incoming light is transferred from the waveguide into the resonator.

- **Over-coupling** ($\kappa_{\text{ext}} > \kappa_0$, $K > 1$): When the coupling to the waveguide overcomes the internal resonator loss, the field coupling back from the resonator is larger than the initial field in the waveguide which is therefore canceled completely. The residual out-coupled light leads to a non-zero transmission which has a phase shift of π compared to the incoming light.

The point of critical coupling is of special interest since there it is possible to transfer the complete light power from the waveguide into the resonator where it is dissipated. As $\kappa_{\text{ext}} = \kappa_0$ it follows from Eq. (2.49) that the loaded quality factor at critical coupling is simply

$$Q_{\text{crit}} = \frac{Q_0}{2} \,. \tag{2.60}$$

Moreover, the maximal on-resonant energy in the resonator is reached when the resonator–waveguide system is critically coupled. This can be seen from Eq. (2.57) which gives

$$W_{\text{max}} = \frac{|s_{\text{in}}|^2}{2\kappa_0} = \frac{P_{\text{in}} Q_0}{2\omega_0} \,, \tag{2.61}$$

at critical coupling where $P_{\text{in}} = |s_{\text{in}}|^2$ is the power of the incoming field in the waveguide. The corresponding intra-cavity intensity is maximized under the same condition [53]

$$I_{\text{crit}} = P_{\text{in}} \frac{n^2 \lambda_0}{2\pi} \frac{Q_0}{V} \,. \tag{2.62}$$

As discussed in section 2.1 the ratio Q/V appears in the intra-cavity intensity as important parameter. To reach a maximal intensity in the resonator it is therefore necessary to optimize Q/V and to operate the combined resonator–waveguide system at critical coupling.

2.4.4 Ideality of the resonator–waveguide coupling

It was already mentioned before that the resonator–waveguide coupling is a tunable quantity for WGM resonator. Practically, the tuneability is realized by a variation of the separation between resonator and waveguide, changing thereby the overlap of the electric fields. Starting in the under-coupled regime the coupling rate $\kappa_{\text{ext}}(x)$ increases for a decreasing resonator–waveguide gap x until critical coupling is reached eventually. Whether critical coupling and even over-coupling can be established depends on the efficiency of the resonator–waveguide coupling. Obviously, $\kappa_{\text{ext}}(x)$ has to become equal to or larger than κ_0 before the waveguide touches the resonator. However, $\kappa_{\text{ext}}(x)$ also has to dominate over other parasitic coupling losses which are discussed in the following in the context of the ideality [71].

So far, it was assumed that light in the resonator is either dissipated by not further specified internal resonator losses or out-coupled into a single waveguide mode. However, in general a waveguide can support several propagating modes which eventually couple to the resonator, thereby introducing further loss channels. In addition, other dissipation processes can occur, e.g., via scattering of light at the waveguide–resonator coupling junction. All these losses are considered to be “parasitic” since they reduce the ability to transfer light from the resonator into the desired waveguide mode. The parasitic losses can be represented in the differential equation of the system in Eq. (2.46) as an additional loss term with the rate $\kappa_{\text{par}}(x)$ which in general also depends on the resonator–waveguide gap. The coupling parameter then is given by [71]

$$K(x) = \frac{\kappa_{\text{ext}}(x)}{\kappa_{\text{par}}(x) + \kappa_0} \,. \tag{2.63}$$

The coupling parameter can be divided into an intrinsic contribution $K_0 = \kappa_{\text{ext}}(x)/\kappa_0$ and a parasitic contribution $K_{\text{par}} = \kappa_{\text{ext}}(x)/\kappa_{\text{par}}(x)$ connected by $K^{-1} = K_0^{-1} + K_{\text{par}}^{-1}$. Then, the ideality can be defined which compares the power coupled into the desired mode with the power coupled to all modes [71] and reads

$$I = \frac{\kappa_{\text{ext}}(x)}{\kappa_{\text{ext}}(x) + \kappa_{\text{par}}(x)} = \frac{1}{1 + K_{\text{par}}^{-1}} \,. \tag{2.64}$$

The ideality is unity when the system is free of any parasitic losses and light in the resonator couples solely into the desired waveguide mode. To evaluate the ideality one first has to consider the spatial dependence of the coupling rates $\kappa_{\text{ext}}(x)$ and $\kappa_{\text{par}}(x)$. The coupling between the resonator and the desired waveguide mode is determined by the overlap of the corresponding fields which decay exponentially outside the dielectric structures. Therefore, $\kappa_{\text{ext}}(x)$ follows a exponential-like dependency as function of the resonator–waveguide separation [61]. The same is true for $\kappa_{\text{par}}(x)$ if one assumes that the parasitic losses are dominated by the coupling to a single higher waveguide mode which is reasonable according to Ref. [71]. Thus, the coupling rates $\kappa_{\text{ext}}(x)$ and $\kappa_{\text{par}}(x)$ can be approximated with exponential functions of the resonator–waveguide gap x having the form [71]

$$\kappa_i(x) = \bar{\kappa}_i \exp(-x/\gamma_i) \,, \tag{2.65}$$

here $\bar{\kappa}_i$ and γ_i are constants corresponding to the coupling rate at $x = 0$ and the spatial decay length of the coupling, respectively. When the coupling gap is varied the coupling parameter K

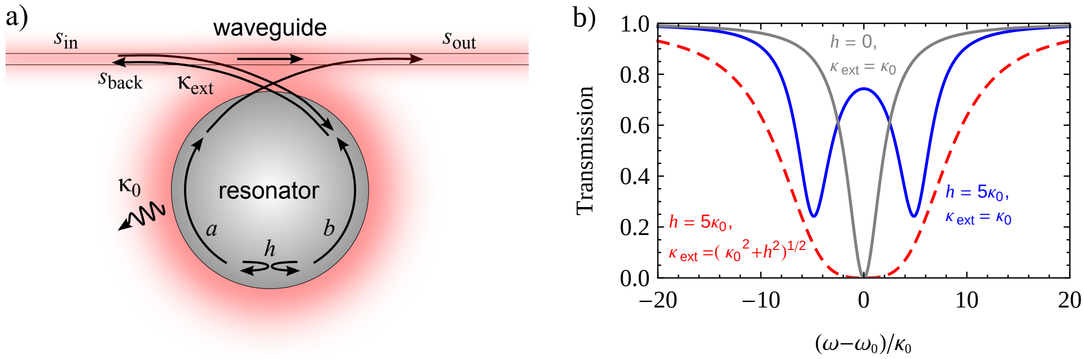

Figure 2.14: a) Schematic of mode coupling in a WGM resonator between the counter-propagating modes a and b. The light field s_{in} in the waveguide couples to the resonator with the coupling rate κ_{bus} and excites mode a. Due to mode coupling, light from mode a is redirected into mode b with rate h. Since b couples also to the waveguide with the rate κ_{ext} a counter-propagating waveguide field s_{back} arises. Figure follows Ref. [71]. b) Waveguide transmission for a WGM resonator with (blue line) and without (gray line) mode coupling. To fulfill the critical coupling condition in the presence of mode coupling κ_{ext} has to be increased leading to a broader linewidth which deviates from a Lorentzian (red, dashed line).

can be extracted from the transmission via inversion of Eq. (2.59). Since in general $\kappa_{\mathrm{ext}}(x)$ and $\kappa_{\mathrm{par}}(x)$ have different spatial dependencies one observes according to Eq. (2.63) two different exponential slopes of K as function of x when parasitic losses are present. Then, following the procedure in Ref. [71] one can determine K_{par}^{-1} which finally gives the ideality.

With this method it was shown that a high-Q WGM microsphere resonator coupled to a 2 μm diameter tapered ultra-thin fiber could reach ideality values of up to 99.97 % in contact [71]. For the case of the bottle micro resonator coupled to a 500 nm ultra-thin fiber comparable results are readily achieved with idealities larger than 99 % [53].

2.4.5 Mode coupling in WGM microresonators

In the preceding discussion we have considered only a single mode in a WGM microresonator. However, due to the circular geometry light can propagate clockwise or counter-clockwise in the resonator. Therefore, WGM microresonators support pairs of degenerated modes, which counter-propagate inside the resonator. Whether the clockwise or counter-clockwise rotating mode is excited from a waveguide depends on the direction of propagation of the light inside the waveguide as shown in Fig. 2.14 a). In an ideal resonator the two modes are uncoupled and do not interact with each other. However, Rayleigh scattering at imperfections of the surface or in the bulk material of the resonator can inverse the propagation direction of light in one mode and redirect it to the other [73]. Thus, there exists a coupling between the two running modes of a WGM resonator which can be modeled by extending the theory of section 2.4.2 to a second mode. For this purpose, a pair of coupled differential equations is introduced which describes the temporal evolution of the clockwise rotating mode amplitude a and the counter-clockwise rotating mode amplitude b [73]:

$$\frac{da}{dt} = -i(\omega_0 - \omega)a - (\kappa_0 + \kappa_{\text{ext}})a - ihb - \sqrt{2\kappa_{\text{ext}}}s_{\text{in}}\,, \tag{2.66}$$

$$\frac{db}{dt} = -i(\omega_0 - \omega)b - (\kappa_0 + \kappa_{\text{ext}})b - iha\,. \tag{2.67}$$

Here, only mode a is driven from the waveguide. Both modes couple with the same rate κ_{ext} to the waveguide and are coupled to each other with the scattering rate h (compare Fig. 2.14 a)).

An important consequence of the mode coupling is the appearance of a reflection signal when light is coupled into the resonator. Light that is scattered from the driven mode into the counter-propagating mode changes its direction of propagation. Thus, the corresponding out-coupled field in the waveguide will also propagate into the opposite direction and one therefore also speaks of “back-scattering”. The amplitude of the reflected light, which we denote as s_{back}, depends on the internal mode coupling rate h and can become significant when the mode coupling is strong. In this case, one can transform the running wave modes into new decoupled eigenmodes $(a \pm b)/\sqrt{2}$. The coupling between the running waves lifts the degeneracy of the eigenmodes leading to new resonance frequencies $\omega_{\pm} = \omega_0 \pm h$. When the coupling is strong such that it dominates the loss rates ($h > \kappa_0, \kappa_{\text{ext}}$) one will observe as a consequence a frequency splitting in the spectrum of the resonator with a peak separation of $\Delta\nu_{\text{modesplitting}} = h/\pi$ as shown in Fig. 2.14 b) [73].

Moreover, the condition for critical coupling is modified by the mode coupling. Since light is scattered from the driven mode to the counter-propagating mode the total resonator losses are higher. Thus, the waveguide has to be brought closer to the resonator to maintain critical coupling such that the condition [73]

$$\kappa_{\text{ext}} = \sqrt{\kappa_0^2 + h^2} \tag{2.68}$$

is fulfilled. At critical coupling κ_{ext} is the dominant loss rate of the resonator and therefore no mode splitting is observable anymore. However, the line shape of the transmission signal will be significantly broadened compared to the Lorentzian profile of an resonator without mode coupling (compare Fig. 2.14 b)).

2.4.6 The add-drop configuration – two waveguides coupled to a WGM microresonator

So far, we have considered only the evanescent coupling of a single waveguide to a WGM microresonator. However, it is possible to approach a second waveguide to the resonator. In Fig. 2.15 this so-called “add-drop” configuration is shown. As before, the resonator is excited from one waveguide, the so-called bus waveguide, which carries the input field s_{in} and and has the coupling rate κ_{bus} to the resonator. Now, also a second waveguide couples to the resonator which can be simply treated as an additional loss channel. Since light from the resonator is “dropped” into the second waveguide, where it propagates as field e_{out}, it is also denominated as

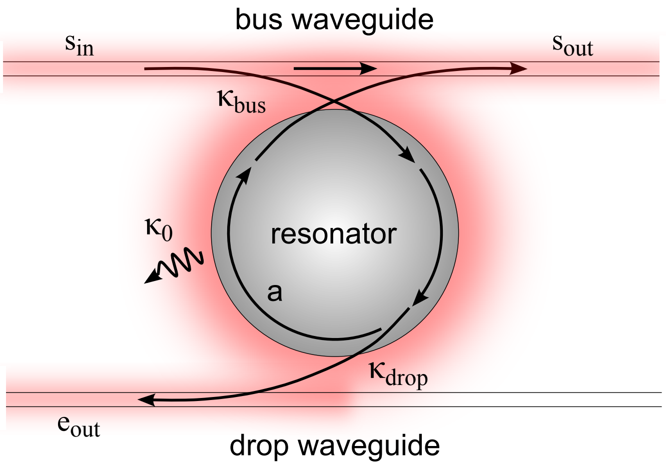

Figure 2.15: Schematic of the add-drop configuration. The light field s_{in} in the bus waveguide couples to the resonator with the coupling rate κ_{bus} and excites mode a. The drop waveguide acts as a loss channel to the resonator with the coupling rate κ_{drop} and extracts light from the resonator into the waveguide field e_{out}.

drop waveguide with the coupling rate κ_{drop}. The differential equation describing the temporal evolution of the resonator mode amplitude a then is

$$\frac{da}{dt} = -i(\omega_0 - \omega)a - (\kappa_0 + \kappa_{\text{bus}} + \kappa_{\text{drop}})a - \sqrt{2\kappa_{\text{bus}}} s_{\text{in}} \,. \tag{2.69}$$

From this expression the FWHM linewidth of the coupled system follows as $\Delta\nu = (\kappa_0 + \kappa_{\text{bus}} + \kappa_{\text{drop}})/\pi$.

To achieve critical coupling for the bus waveguide, κ_{bus} not only has to equalize the internal resonator losses but also the out-coupling to the drop waveguide such that the condition for critical coupling changes to

$$\kappa_{\text{bus}} = \kappa_0 + \kappa_{\text{drop}} \,. \tag{2.70}$$

Following the same procedure as in section 2.4.2 one can obtain an expression for the transmission coefficient of the bus fiber which reads

$$t_{\text{bus}} = \frac{s_{\text{out}}}{s_{\text{in}}} = \frac{\kappa_0 + \kappa_{\text{drop}} - \kappa_{\text{bus}} + i(\omega - \omega_0)}{\kappa_0 + \kappa_{\text{drop}} + \kappa_{\text{bus}} + i(\omega - \omega_0)} \,. \tag{2.71}$$

In a similar manner, it is also possible to determine the transmission coefficient to the drop waveguide yielding [53]

$$t_{\text{drop}} = \frac{e_{\text{out}}}{s_{\text{in}}} = \sqrt{2\kappa_{\text{drop}}}\frac{a}{s_{\text{in}}} = \frac{-2\sqrt{\kappa_{\text{bus}} \cdot \kappa_{\text{drop}}}}{\kappa_0 + \kappa_{\text{drop}} + \kappa_{\text{bus}} + i(\omega - \omega_0)} \,. \tag{2.72}$$

Again, the transmission of the bus waveguide is subject to the interference of the incoming driv-

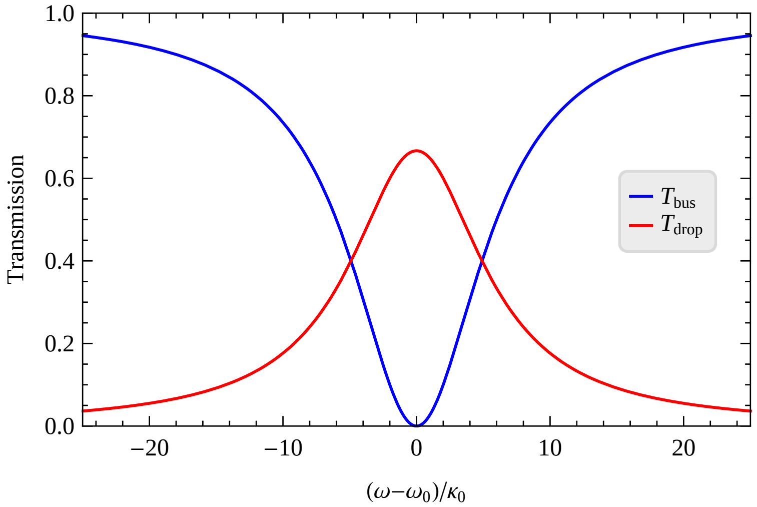

Figure 2.16: Transmission $T_{\text{bus}} = |t_{\text{bus}}|^2$ and $T_{\text{drop}} = |t_{\text{drop}}|^2$ of the bus and drop waveguide as function of the light frequency. The plot parameters are $\kappa_{\text{bus}} = 3\kappa_0$ and $\kappa_{\text{bus}} = 2\kappa_0$ and the bus waveguide is therefore critically coupled to the resonator. Note that on-resonance the transfer efficiency into the drop waveguide reaches its maximum of $T_{\text{drop,max}} = \kappa_{\text{drop}}/(\kappa_0 + \kappa_{\text{drop}}) \approx 0.67$.

ing field and the out-coupled resonator field. In contrast, the transmission to the drop waveguide is simply composed of the light which couples out from the resonator field and no interference occurs accordingly. Fig. 2.16 shows the calculated intensity transmissions of the bus and drop waveguide $T_{\text{bus}} = |t_{\text{bus}}|^2$ and $T_{\text{drop}} = |t_{\text{drop}}|^2$ as function of the light frequency. When light is transferred from the bus waveguide into the resonator it will be partially coupled out into the drop waveguide. The transferred power depends on the ratio of the coupling rate κ_{drop} compared to the internal resonator losses κ_0 and can be obtained for on-resonant excitation from the relation [74]

$$\left(1 + \frac{\kappa_0}{\kappa_{\text{drop}}}\right) T_{\text{drop}} = 1 - T_{\text{bus}} \,. \tag{2.73}$$

which follows from Eq. (2.71) and Eq. (2.72). For fix κ_0 and κ_{drop} and the amount of transferred light becomes maximal at critical coupling and reaches the value [74]

$$\max(T_{\text{drop}}) = 1 - \frac{2Q_{\text{load}}}{Q_0} = \frac{\kappa_{\text{drop}}}{\kappa_0 + \kappa_{\text{drop}}} \,. \tag{2.74}$$

Thus, to achieve a high transfer efficiency the dissipation inside the resonator has to be as small as possible which corresponds to a large intrinsic quality factor Q_0. In addition, the coupling to the drop waveguide can be increased as well by bringing the waveguide closer to the resonator. However, in general there is a trade-off between the achievable transfer efficiency and the loaded quality factor since the coupling to the drop waveguide introduces losses and thereby reduces Q which is a critical parameter for many applications.

CHAPTER 3

Active Stabilization of Evanescent Coupling

The evanescent coupling of light into WGM microresonators is one of their most attractive features since it allows the near lossless transfer of energy, and the coupling rate is fully tunable. In particular, when ultra-thin fibers are used for the coupling process light can be transferred into the WGM resonators with an ideality of up to 99.97 % [71] stating that parasitic losses to modes other than the resonator mode can be neglected.

The coupling strength between an ultra-thin fiber and a WGM resonator is determined by the spatial overlap of their electric fields and requires, in general, control over the distance between the two devices with nanometer precision. Therefore, the coupling process is extremely sensitive to fluctuations in the resonator–fiber gap and is influenced by mechanical and acoustical noise as well as thermal drifts. In practical, applications it is often necessary to operate the coupled resonator–fiber system in the regime of critical coupling in which the out-coupling to the fiber equals the intrinsic resonator dissipation. This balancing of losses leads to total destructive interference of the light fields in the fiber so that the light is transferred completely into the resonator (compare section 2.4.3). Therefore, it is highly desirable to achieve and sustain the regime of critical coupling as long and stable as possible. Besides the evanescent coupling strength, the resonance frequency of a resonator mode is another crucial parameter for the in-coupling of light. Only when the frequency of the mode matches the one of incoming light in the ultra-thin fiber can efficient power transfer into the resonator be achieved.

In the following sections a technique is presented which allows to actively stabilize the evanescent coupling to a WGM bottle resonator and its resonance frequency simultaneously. This method relies on the Pound–Drever–Hall (PDH) technique which is based on laser phase modulation. While the PDH technique is standard for the stabilization of resonator frequencies, we will show here that it can also be applied for the control of the evanescent coupling to a WGM microresonator. In particular, this method enables us to operate the resonator–fiber system in the regime of critical coupling over long time scales, on the order of hours. The basic working principal of the stabilization scheme is introduced in the first part of the chapter. Then, its successful operation is verified, and from an analysis of the transmission noise the tapered fiber, the stability of the coupling gap is estimated. Finally, we give a brief outlook on how this technique could be extended to simultaneously stabilize the coupling of two ultra-thin fibers to a resonator. Parts of the results presented here were published in Ref. [75].

3.1 Basic principal of the evanescent coupling stabilization

In order to actively stabilize the evanescent coupling of light from an ultra-thin fiber into a WGM microresonator, two main requirements have to be fulfilled. First of all, the resonance frequency of the resonator mode which we want to excite has to match the frequency of the incoming light. Thus, we need to infer the frequency deviation between the resonator resonance and the light. Second, a measure of the evanescent coupling strength is required which reveals deviations of the resonator–fiber gap from its intended position. The most natural way to measure these properties would be to make use of the light in the fiber itself thereby avoiding any additional readout. Therefore, it is worth to investigate if useful information can be gained from the light transmitted trough the fiber.

In section 2.4.2 the transmission properties of an ultra-thin fiber coupled to a WGM micro resonator were already derived resulting in Eq. (2.58) which reads

$$t(x,\omega) = \frac{\kappa_0 - \kappa_{\text{ext}}(x) + i(\omega - \omega_0)}{\kappa_0 + \kappa_{\text{ext}}(x) + i(\omega - \omega_0)}\,, \tag{3.1}$$

where we have added now explicitly the dependence of κ_{ext} on the coupling gap x between fiber and resonator (compare Eq. (2.65)). The quantities κ_0 and $\kappa_{\text{ext}}(x)$ can be interpreted as intrinsic resonator half linewidth and the linewidth broadening due to the losses induced by the ultra-thin fiber, respectively, which in therms of angular frequency add up to the resonator HWHM $\kappa(x) = \kappa_0 + \kappa_{\text{ext}}(x)$.

The transmission coefficient $t(x,\omega)$ clearly depends on the frequency deviation between light and resonator $\omega - \omega_0$ as well as on the κ_{ext} which quantifies the strength of the evanescent coupling. Thus, $t(x,\nu)$ holds some informations which would be useful for the stabilization of the resonators frequency and the evanescent coupling. However, it is not possible to measure the transmission coefficient directly since one only detects the intensity of the light in the fiber, yielding $T(x) = |t(x,\omega)|^2$. Unfortunately, in this signal the phase information of the light is lost which, as we will see, is essential for the quantities we want to infer. This becomes clearer when we reconsider Fig. 2.13 a) and b) where the intensity transmission was plotted as a function of the resonator frequency and in dependence of the coupling parameter K, respectively. Although one observes a variation of T with respect to $\omega - \omega_0$ and K, which in principle would give us information about the frequency deviation and the evanescent coupling strength, we note that the signal has in both plots a symmetric shape and is therefore not unique. Moreover, the symmetry points are exactly the one to which we want to stabilize the system, to be specific, at perfect resonance with $\omega - \omega_0 = 0$ in case of Fig. 2.13 a) and at critical coupling with $K = 1$ or $\kappa_0 - \kappa_{\text{ext}}(x) = 0$ in case of Fig. 2.13 b). Thus, for small deviation from these points the intensity transmission gives no unique information about the sign of the deviation and is therefore not suitable as an error-signal for an active stabilization.

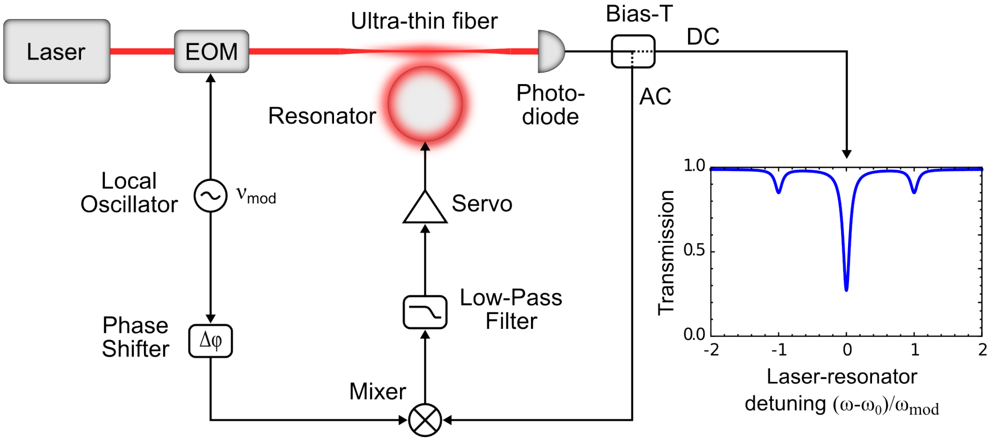

Figure 3.1: Setup for the Pound–Drever–Hall frequency stabilization scheme. The inset shows the DC-part of the photodiode transmission signal as a function of laser–resonator detuning, where the central carrier and the two first-order sidebands are visible.

As we will see in the following sections, exactly this information about the sign of a deviation is contained in the phase of the transmission coefficient $t(x, \omega)$ which one can recover by means of the PDH laser phase modulation technique [76]. First, we will apply this method to actively stabilize the frequency of a bottle resonator. Based on the frequency stabilization we then implement an off-resonant variant of the PDH-technique which allows to actively stabilize the evanescent coupling between the bottle resonator and an ultra-thin fiber.

3.1.1 The Pound–Drever–Hall stabilization technique

The PDH technique is typically applied to stabilize the frequency of a laser to the resonance of a reference resonator, or vice versa. This is achieved by sensing the reference resonator with phase modulated laser light. After the interaction the light contains information about the deviation between laser and resonator frequency which can be used to deduce an error signal by electrical demodulation.

A schematic of a PDH setup is shown in Fig. 3.1. The laser light is sent through an electro-optical-modulator (EOM) which performs a phase modulation and creates frequency sidebands with the modulation frequency ω_{mod}. Thereafter, the light is coupled into a fiber with an ultra-thin section which couples to the resonator. The light coming from the resonator is detected with a fast photodiode. When the laser frequency is scanned over a resonance of a resonator mode the resulting DC-transmission signal reveals the central resonance dip of the carrier and typically the first two lowest-order sidebands as shown in the inset of Fig. 3.1. Here we assume the linewidth of the laser light to be negligible compared to the resonator linewidth so that the transmission spectra purely reflects the lifetime of the resonator mode. As discussed before, the

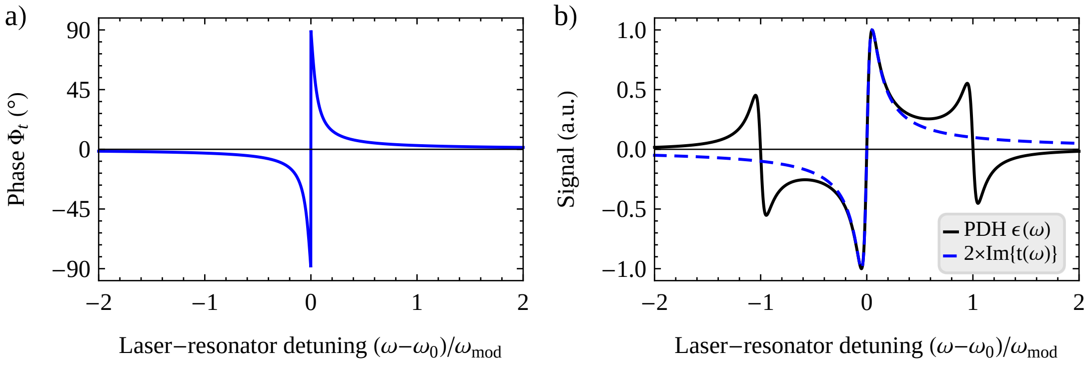

Figure 3.2: a) Phase of the resonator transmission coefficient $\Phi_t(\omega)$, b) Pound–Drever–Hall error signal $\epsilon(\omega)$ and imaginary part $\mathrm{Im}\{t(\omega)\}$ as function of the laser–resonator detuning. Parameters for the plots are $\omega_{\mathrm{mod}} = 40\kappa_0$ and $\kappa_{\mathrm{ext}}(x) = \kappa_0$.

DC-transmission signal is symmetric around zero detuning and is therefore not suitable as error signal for the frequency stabilization since it gives no information about the sign of a frequency deviation from resonance.

In contrast, the AC-part of the photodiode signal contains more useful information about the system. Since the carrier and the sidebands of the laser light have a fix phase relation one can observe a beating signal in the AC part of the photodiode oscillating with ω_{mod}. Assume now, the carrier frequency is near resonant with a resonator mode and the modulation frequency of the sidebands is much larger than the mode linewidth. In this situation, the carrier part of the incident light couples to the resonator and eventually experience a phase shift while the light at the sideband frequencies is transmitted through the fiber without interacting with the resonator. As a consequence, the phase of the beating signal at the photodiode will change according to the phase shift accumulated by the light during the interaction with the resonator mode. The phase of the amplitude transmission coefficient $\Phi_t(\omega) = \arg(t(\omega))$ is shown in Fig. 3.2 a) as a function of the laser–resonator detuning. When the detuning is scanned over resonance the phase features a sudden jump of π which reveals the sign of a frequency deviation and thus can be used for stabilizing the resonance frequency.

To demodulate the phase information of the transmitted light, the photodiode signal is electrically mixed with the local oscillator which also drives the EOM (see Fig. 3.1). If the delays of the two mixed signals are chosen correctly and all high frequencies components $\omega \geq \omega_{\mathrm{mod}}$ are filtered out the resulting error signal can be described by the expression [77]

$$\epsilon(\omega) \propto \mathrm{Im}\{t(\omega)t^*(\omega + \omega_{\mathrm{mod}}) - t^*(\omega)t(\omega - \omega_{\mathrm{mod}})\}\,, \tag{3.2}$$

where $t(\omega)$ is the amplitude transmission coefficient of the resonator mode given in Eq. (3.1). The error signal $\epsilon(\omega)$ is shown in Fig. 3.2 b) and shows around resonance a very similar behavior compared to the plot of the phase in Fig. 3.2 a). This relationship becomes clearer when one considers the regime $\omega_{\mathrm{mod}} \gg 2\kappa$, in which for a resonant carrier, the sidebands are completely transmitted since $t(\omega \pm \omega_{\mathrm{mod}}) \approx 1$. Then Eq. (3.2) simplifies to

$$\epsilon(\omega) \propto 2\,\mathrm{Im}\{t(\omega)\} = 2|t(\omega)|\sin(\Phi_t(\omega))\,, \tag{3.3}$$

indicating that the error signal is directly proportional to the sine of the phase of the transmitted light as illustrated in Fig. 3.2 b). Thus, the PDH signal reflects the phase jump at resonance and shows a steep slope with a zero-crossing which is ideally suited as error signal for a frequency stabilization.

Experimental verification of PDH frequency stabilization with a bottle microresonator

The experimental demonstration of an actively frequency-stabilized bottle resonator is described in Refs. [59, 60, 78]. Only a brief summary of these results is presented here to describe the performance of the system which is crucial for the evanescent coupling stabilization.

The PDH technique is applied to stabilize the resonance frequency of a bottle resonator to the laser frequency according to the setup described in Fig. 3.1. For this purpose, the EOM is driven by a RF-signal with frequency $\omega_{\text{mod}}/2\pi = 42.8\,\text{MHz}$ and the light from the resonator is monitored with a high-bandwidth avalanche photodiode. A bias-T allows to separate the photodiode signal into a DC part which corresponds to the fiber intensity transmission and into a AC part which carries the phase information of the light. The AC signal is demodulated by mixing it with ω_{mod} to create the PDH error signal which serves as input to a PID servo circuit. Then, the latter applies a feedback voltage to a piezo actuator that pulls at the ends of the bottle resonator fiber thereby tuning its resonance frequency. The measurements presented here were performed with a bottle resonator with ultra-high intrinsic quality factor of $Q = 2 \times 10^8$ corresponding to a $\kappa/2\pi = 2\,\text{MHz}$ at critical coupling. Thus, the condition $\omega_{\text{mod}} \gg 2\kappa$ is readily fulfilled.

To investigate the performance of the system, first, the frequency of the bottle resonator is scanned in open-loop mode. Fig. 3.3 a) and b) show the DC and the demodulated AC signal of the photodiode corresponding to the intensity transmission and the PDH error signal, respectively. The transmission spectrum clearly reveals the carrier frequency of the light and the two sidebands which are created by the phase modulation in the EOM. The PDH error signal follows the theoretical predicted shape in Fig. 3.2 b). In particular, around resonance one finds a steep slope with a zero crossing on resonance.

In the next step, the system is characterized in closed-loop mode, by measuring the fiber transmission while the resonator frequency is actively stabilized. Ideally, one would perform this measurement with the resonator perfectly locked to the frequency of the incoming laser light ($\omega = \omega_0$). However, at this point the fiber transmission is, to first order, insensitive to frequency fluctuations. Therefore, an offset is introduced to the lock point of the servo circuit to stabilize the resonator frequency slightly off-resonant to the laser light as indicated by the dashed horizontal line in Fig. 3.3 b). As a consequence, there is a monotonic transformation from frequency fluctuations to changes of the fiber transmission and we can use the slope of the signal in Fig. 3.3 a) to deduce the frequency noise. Figure 3.3 c) shows the results from such a measurement in which the stabilization is operated in closed-loop mode over a duration of 5 ms. This time interval is 20 times longer than the response time which is set by the control loop bandwidth of 4 kHz. The stabilization locks the resonator frequency close to the desired value. In order to evaluate the performance of the lock, the residual frequency fluctuations are analyzed, which have a rms value of 206 kHz corresponding to 5 % of the resonator linewidth in the considered time interval. Several sources for the observed residual frequency noise are

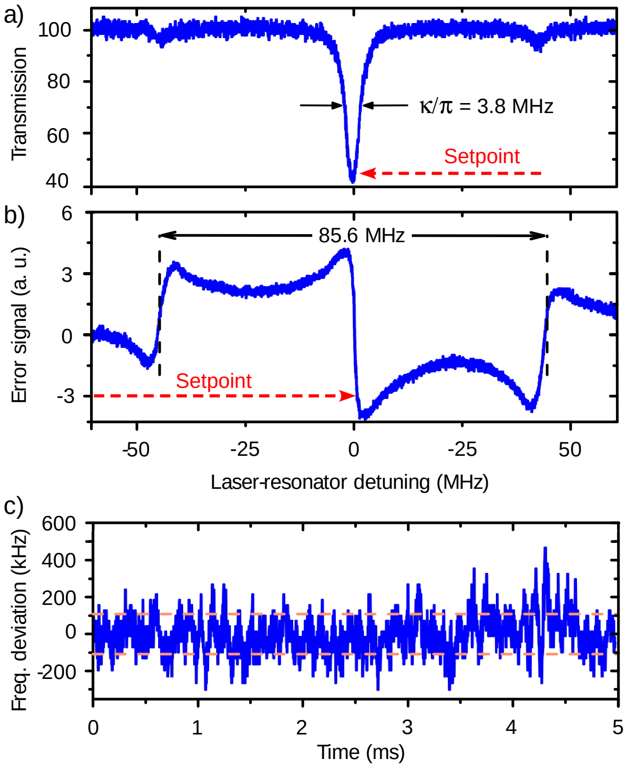

Figure 3.3: Characterization of the PDH frequency stabilization of an ultra-high Q bottle mode. Open-loop mode: a) Fiber transmission showing the carrier and sidebands of a bottle mode with a FWHM of $\Delta\nu = \kappa/\pi = 3.8\,\mathrm{MHz}$; b) Corresponding PDH error signal where the dashed red line indicates the setpoint for the stabilization during the measurement in c). Note that due to an additional phase delay in the experimental setup the error signal is inverted compared to the theory plots. Closed-loop mode: c) Residual frequency deviation from the setpoint over time of the active stabilization with a rms value of 206 kHz (dashed orange lines). Figures adapted from Ref. [59].

discussed in Ref. [59]: Electrical noise of the high-gain voltage amplifier which is connected to the resonator piezo and the laser linewidth of 100 kHz could be possible origins. Moreover, a strong 9 kHz component was identified in the frequency spectrum of the measured transmission which is beyond the bandwidth of the stabilization. On longer timescales the PDH-lock of the bottle resonator was able to compensate for much larger frequency drifts ranging over more than 200 MHz in 50 s [59].

These results clearly demonstrate that it is possible to stabilize the resonance frequency of a ultra-high Q bottle mode to a fraction of its linewidth and to compensate for long-term frequency drifts. Thus, one of the two major requirements for the evanescent coupling stabilization is readily fulfilled. In the next section we will discuss how the PDH technique can be employed to derive a coupling strength-depended error signal.

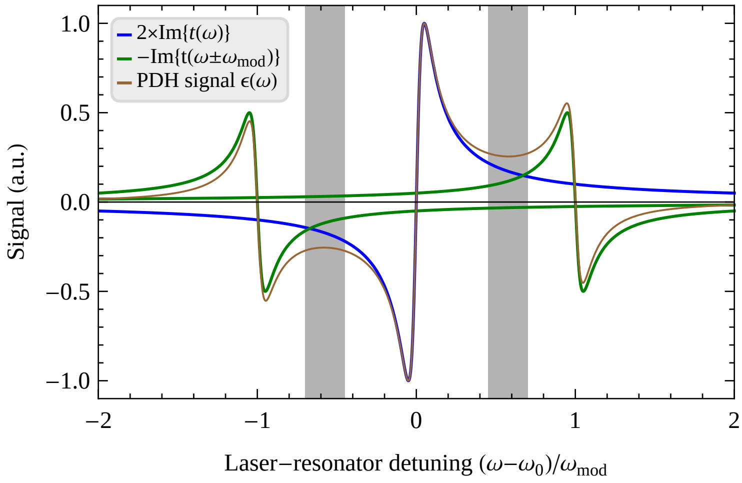

Figure 3.4: Plot of the different components constituting the PDH signal under the condition $\omega_{\mathrm{mod}} \gg 2\kappa$. The gray areas indicate the overlap region between the phase components of carrier and sidebands where the signal magnitude is used as indicator for the coupling strength. The plot parameters are the same as in Fig. 3.2 were used.

3.1.2 Creating a coupling strength-dependent error signal

As we have seen in Fig. 3.2 b), the PDH error signal has a zero crossing at resonance with a steep slope which is ideally suited for a stabilization of the resonator frequency to an external reference. However, for detunings in the range between the carrier and the sidebands, this it not the only interesting feature of the PDH-signal. The off-resonant part of the signal shows a plateau-like, almost constant region indicated with gray bars in Fig. 3.4. In the following we will show that the magnitude of the signal in this region depends on the coupling strength between the resonator and the ultra-thin fiber, and that it offers the possibility to stabilize the evanescent coupling.

According to Fig. 3.4, the complete shape of the PDH signal corresponds in good approximation to the overlap of the imaginary parts of the carrier and sideband transmission as long as the condition $\omega_{\mathrm{mod}} \gg 2\kappa$ is fulfilled. To get a more quantitative understanding of the signal behavior in between the carrier and the sidebands, it is useful to evaluate $\epsilon(x,\omega)$ at the point $\omega-\omega_0=\omega_{\mathrm{mod}}/2$, which can be written with help of Eq. (3.1) and Eq. (3.2) as

$$\epsilon(x,\omega_{\mathrm{mod}}/2) = 4\cdot\mathrm{Im}\left\{\frac{\kappa_{\mathrm{ext}}(x)\omega_{\mathrm{mod}}^2(i\omega_{\mathrm{mod}}/2-\kappa_0)}{(\omega_{\mathrm{mod}}/2+i\kappa)^2(\omega_{\mathrm{mod}}/2-i\kappa)(3\omega_{\mathrm{mod}}/2+i\kappa)}\right\}, \tag{3.4}$$

where the resonance frequency ω_0 is chosen to be zero. When the modulation frequency is much larger than the cavity decay rate ($\omega_{\mathrm{mod}} \gg 2\kappa$), we can simplify the above expression to

$$\epsilon(x,\omega_{\mathrm{mod}}/2) \approx \frac{32}{3}\frac{\kappa_{\mathrm{ext}}(x)}{\omega_{\mathrm{mod}}}. \tag{3.5}$$

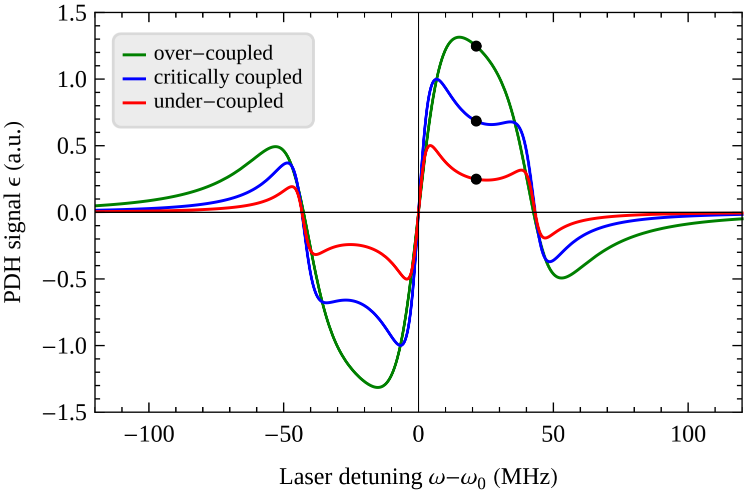

Figure 3.5: PDH error signal as a function of the laser-resonator detuning calculated for three different coupling regimes. The black circles mark the signal amplitude in between the carrier and the sidebands which changes when the coupling conditions are varied. Parameters for the plot follow the experimental conditions with $\omega_{\mathrm{mod}}/2\pi = 42.8\,\mathrm{MHz}$ and intrinsic resonator linewidth $\kappa_0/2\pi = 3.2\,\mathrm{MHz}$.

Thus, in this regime the off-resonant PDH signal is directly proportional to the evanescent coupling strength $\kappa_{\mathrm{ext}}(x)$ between the resonator and the ultra-thin fiber. A qualitative interpretation of this dependence can be obtained from Fig. 3.4. An ultra-thin fiber coupled to a WGM microresonator will induce losses to the resonator and thereby broaden the resonance linewidth. As a consequence, also the width of the phase signal in Fig. 3.2 will become broader leading to a larger overlap of the carrier and sideband $\mathrm{Im}\{t(\omega)\}$-signals, thereby increasing the off-resonant amplitude of the PDH signal. Hence, the behavior can be interpreted as an indirect sensing of the resonator linewidth broadening which originates from the evanescent coupling the ultra-thin fiber.

In Fig. 3.5 the PDH signal is calculated according to Eq. 3.2 as a function of the laser–resonator detuning for three different coupling regimes. In the under-coupled system the coupling to the ultra-thin fiber is marginal and the off-resonant amplitude of the PDH signal (indicated by black circles) is small. In contrast, in the regime of over-coupling the resonator losses are dominated by the evanescent coupling to the fiber and the resonance linewidth broadens considerably. As expected, this linewidth broadening effect can be observed as increase of the off-resonant PDH signal.

Now, one can study the dependence of the off-resonant PDH signal $\epsilon(x_{\mathrm{rel}}, \omega_{\mathrm{mod}}/2)$ on the resonator–fiber gap x_{rel}. In Eq. (2.65) we found an approximately exponential relation between the evanescent coupling strength and the resonator–fiber gap which reads $\kappa_{\mathrm{ext}}(x_{\mathrm{rel}}) = \kappa_0 \exp(-x_{\mathrm{rel}}/\gamma_{\mathrm{ext}})$. Here, x_{rel} is the coordinate of the resonator–fiber gap which we define such that $x_{\mathrm{rel}} = 0$ occurs at critical coupling. The decay length of the evanescent coupling is defined by γ_{ext}. Combining this expression with Eq. (3.2) we can plot the off-resonant PDH signal in

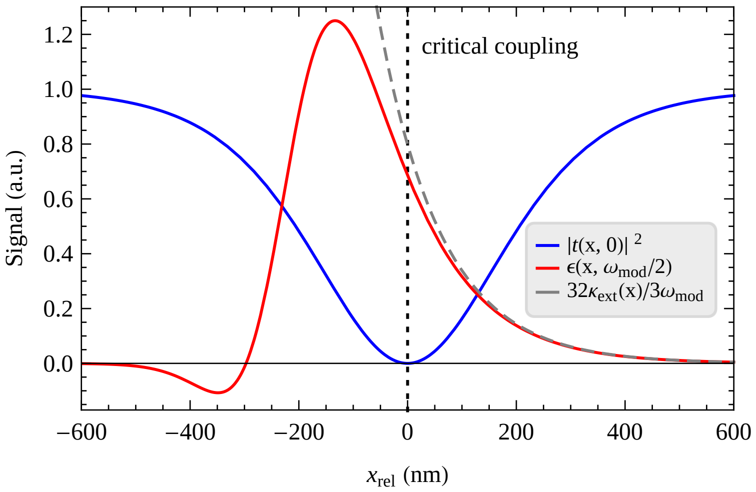

Figure 3.6: On-resonant fiber transmission $|t(x_{\mathrm{rel}}, 0)|^2$ (blue line) and amplitude of the off-resonant PDH signal $\epsilon(x_{\mathrm{rel}}, \omega_{\mathrm{mod}}/2)$ (red line) calculated as a function of the resonator–fiber gap x_{rel}, where the critical coupling point is at $x_{\mathrm{rel}} = 0$ and $x_{\mathrm{rel}} > 0$ ($x_{\mathrm{rel}} < 0$) indicates under-coupling (over-coupling). The gray dashed line illustrates an approximation of $\epsilon(x_{\mathrm{rel}}, \omega_{\mathrm{mod}}/2)$ for $\omega_{\mathrm{mod}} \gg 2\kappa$. Parameters used for the plot correspond to typical experimental values with $\gamma_{\mathrm{ext}} = 116.7\,\mathrm{nm}$ and all other as in Fig. 3.5.

dependence of the resonator–fiber gap as it is shown in Fig. 3.6. For a decreasing gap in the deeply under-coupled regime the resonator linewidth increases due to the losses introduced by the ultra-thin fiber. As a consequence, the off-resonant PDH signal initially follows the exponential increase of $\kappa_{\mathrm{ext}}(x_{\mathrm{rel}})$. Then, as soon as the resonator linewidth starts to be comparable to the modulation frequency, our approximation $\epsilon(x_{\mathrm{rel}}, \omega_{\mathrm{mod}}/2) \propto \kappa_{\mathrm{ext}}(x_{\mathrm{rel}})$ is no longer valid and the exponential growth of the signal comes to a halt (compare red and gray dashed line in Fig. 3.6). In this regime the signal has an almost linear slope which finally transforms into a roll-off when $\kappa_{\mathrm{ext}}(x_{\mathrm{rel}}) \approx 2\omega_{\mathrm{mod}}$ with a zero crossing at $\kappa_{\mathrm{ext}}(x_{\mathrm{rel}}) \approx 4\omega_{\mathrm{mod}}$.

In conclusion, we find that the position of the linear slope and the roll-off of the PDH signal can be controlled by an adequate choice of the modulation frequency ω_{mod} compared to the resonance decay rate κ. This is a very favorable situation since it allows to create an error signal for the stabilization of the evanescent coupling having a quasi-linear and monotone response which can be easily set to any coupling regime of interest, especially to the important point of critical coupling. Moreover, the off-resonant part of the PDH-signal is almost constant for small frequency deviations (compare Fig. 3.4) and, therefore, is robust against laser and resonator frequency noise. The use of an off-resonant signal has the additional advantage that only a very weak part of the light actually couples into the resonator with the consequences that undesired side effects like, e.g., thermal resonance shifts, can be avoid.

3.2 Technical implementation of the active evanescent coupling stabilization

To actually realize an active stabilization of the evanescent coupling between a WGM microresonator and an ultra-thin fiber with the aid of an off-resonant PDH signal, which we call coupling stabilization (CS) signal from now on, several technical challenges have to be addressed. In order to create the CS signal a PDH setup, similar to the scheme shown in Fig. 3.1, can be used. The only important difference to the usual PDH frequency lock is that now we are interested in the off-resonant amplitude of the error signal. Therefore, one has to introduce a detuning of the laser carrier frequency compared to the resonator resonance which we set to $\omega - \omega_0 \approx \pm\omega_{\text{mod}}/2$. As pointed out already, the magnitude of the modulation frequency ω_{mod} depends on the desired coupling regime. For stabilization to critical coupling, the condition $\omega_{\text{mod}} \approx 6\kappa_{\text{crit}}$ should be fulfilled in order to be in the linear-response region of the CS error signal.

The frequency detuning of the CS error signal requires a fixed frequency relation between the resonator resonance and the incident light. Thus, as discussed before, in order to implement the CS lock, the frequency stabilization of the resonator is required. For this purpose, a second on-resonant PDH lock operates in parallel to the CS signal in order to stabilize the resonator frequency. The two PDH locks are generated with two different modulation frequencies $\omega_{\text{mod,c}}$ for the CS and $\omega_{\text{mod,f}}$ for the frequency stabilization allowing one to separate the signals by demodulation with the corresponding modulation frequencies.

A detailed overview of the experimental setup used for the implementation of the CS is shown in Fig. 3.7. A laser beam tuned close to resonance with the resonator frequency, is split up into two parts. While the first beam is modulated with $\omega_{\text{mod,f}}$ for the frequency lock, the second beam is frequency-shifted with an acousto-optical modulator (AOM) to create the frequency offset of the CS lock and is then modulated with $\omega_{\text{mod,c}}$. Both beams are combined again on a fiber-based beam splitter and sent via the ultra-thin fiber to the bottle microresonator. Finally, a high-bandwidth avalanche photodiode (APD) detects the light transmitted past the resonator. This allows one to perform the CS stabilization with very low powers of the nanowatts level, thereby minimizing thermal frequency shifts. The electrical APD signal is split up, where one part is demodulated with $\omega_{\text{mod,c}}$ and the other with $\omega_{\text{mod,f}}$ to create the CS and frequency stabilization error signal, respectively. Using the error signal of the frequency lock, a servo circuit creates the feedback which is then applied to the piezo stack that tunes the resonance frequency of the bottle microresonator. We limit the bandwidth of the frequency lock to about 20 Hz in order to correct only for slow frequency drifts and to avoid any excitation of mechanical vibrations of the resonator fiber. The CS signal acts as input for a computer based servo loop which is connected to the positioning stage of the ultra-thin fiber and thereby controls the evanescent coupling to the bottle microresonator. A low-pass filter sets the bandwidth of the CS loop to frequencies below 1 Hz such that it corrects only for slow drifts of the coupling strength while avoiding the excitation of mechanical resonances.

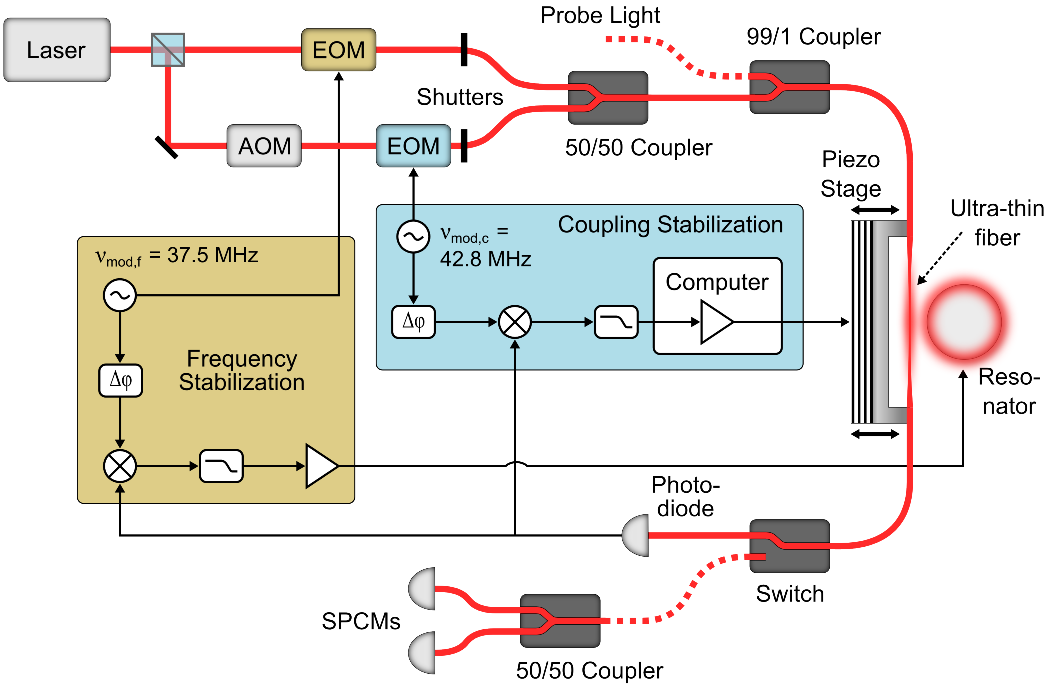
Laser
EOM
AOM
EOM
Probe Light
99/1 Coupler
Shutters
50/50 Coupler
Piezo Stage
Ultra-thin fiber
$\nu_{\mathrm{mod,c}}$ = 42.8 MHz
Coupling Stabilization
Computer
Δφ
$\nu_{\mathrm{mod,f}}$ = 37.5 MHz
Frequency Stabilization
Δφ
Reso-nator
Photo-diode
Switch
SPCMs
50/50 Coupler

Figure 3.7: Setup for the coupling stabilization scheme. Light from a single laser is split and prepared – one for the frequency and one for the coupling stabilization. After the recombination of the two beams, they both couple to the resonator and are thereafter detected with a photodiode. The electrical signals are separated by demodulation and used as inputs for two servo circuits, respectively. The feedback of the frequency stabilization controls the resonator frequency while the coupling stabilization feedback connects to a piezo stage regulating the position of the ultra-thin fiber. The additional probe light and the two single photon counting modules (SPCM) allow one to measure the resonator transmission independently from the stabilization light.

3.2.1 Experimental verification

The experimental setup in Fig. 3.7 is realized with an external cavity diode laser[1] that operates at a wavelength of 780 nm and that has a short-term linewidth of 100 kHz. The EOM modulation frequencies for the two PDH-locks are $\omega_{\mathrm{mod,f}}/2\pi = 37.5\,\mathrm{MHz}$ and $\omega_{\mathrm{mod,c}}/2\pi = 42.8\,\mathrm{MHz}$, respectively, and the frequency offset of the CS signal is set with the AOM in the plateau region of the PDH signal at a detuning of about 20–25 MHz.

The measurements are performed with the bottle microresonator in the CQED setup which is described in more detail in chapter 5. Due to the requirements of the CQED experiment, the resonator is in ultra-high vacuum and has excellent passive isolation from mechanical and acoustic noise in the lab. The resonator has a diameter of 38 μm and the modes considered here

---

[1] Toptica, DL pro

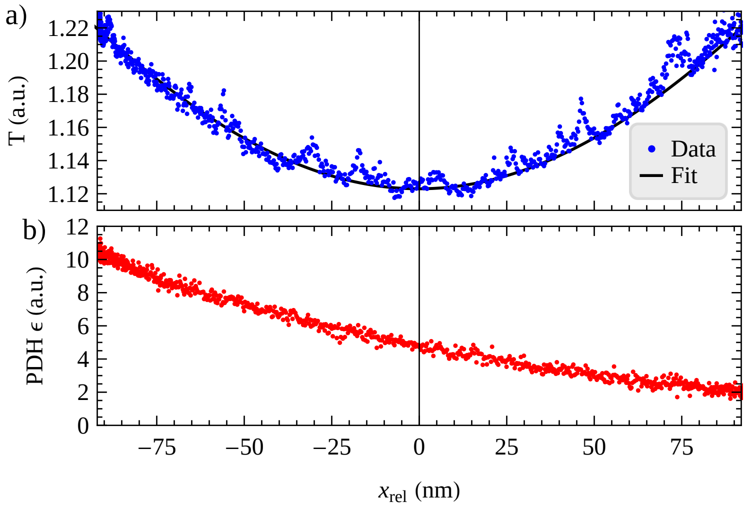

Figure 3.8: a) Measured intensity transmission T and b) off-resonant PDH signal ϵ as a function of the coupling gap change $x_{\rm rel}$, where $x_{\rm rel} = 0$ corresponds to critical coupling. The black line in a) is a fit to the data with $|t(x, \nu_0)|^2$ according to Eq. 3.1. The transmission is not zero at critical coupling since the off-resonant sidebands of the probing light do not couple into the resonator.

have typical HWHM linewidths of $\kappa/2\pi = 4$–$8\,\mathrm{MHz}$. The power of the incident light at the resonator is limited to the range of about 20 nW in order to avoid thermally induced frequency drifts of the modes.

First, the open-loop properties of the CS are investigated while, simultaneously, the frequency stabilization of the resonator is in closed-loop mode. For this purpose, the transmitted intensity at the APD and the CS signal are recorded while the resonator-fiber gap is varied as shown in Fig. 3.8. From the symmetric behavior of the transmission it apparent that the system undergoes a transition from the under-coupled to over-coupled regime. At the same time, the CS signal shows the desired monotone slope which is almost linear around the critical coupling point. These experimental results are in good agreement with the theoretical predictions from Fig. 3.6.

In order to verify the functionality of the CS in the closed-loop mode, the system is examined with a lock-probe method. For this scheme, the resonator–fiber system is locked to critical coupling and the stabilization is interrupted cyclically for short times to probe the residual transmission through the coupling fiber. During this probing phase with a weak additional laser beam (see Fig. 3.7), the light fields of the frequency lock and the CS lock are switched off to enable a background-free transmission measurement. For a better signal-to-noise ratio of the small transmitted powers, the transmission is recorded with two single photon counting modules (SPCMs). For this purpose, a fiber-based switch allows one to change the light path after the resonator from the APD to the SPCMs. The probing cycle is repeated every second with an probe duration of 5 ms.

In Fig. 3.9, a longterm measurement of the transmission is shown. For the first 97 min

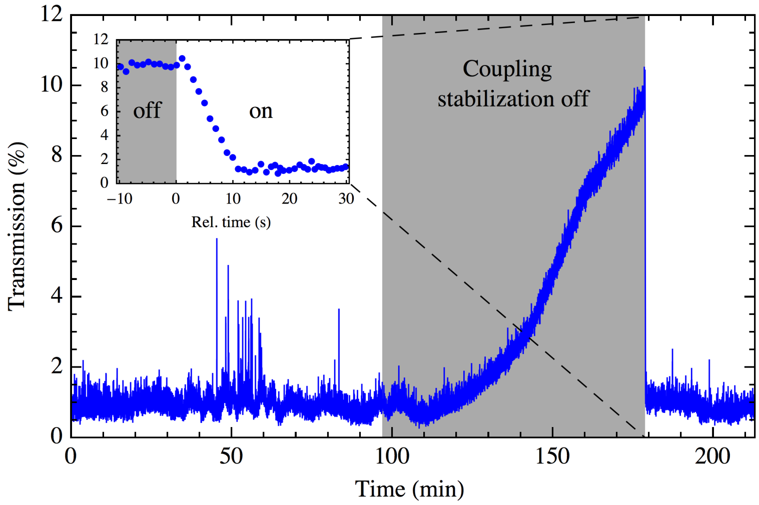

Figure 3.9: Long-term transmission through the coupling fiber with the coupling stabilization in closed-loop mode and set to critical coupling. The transmission was periodically probed for 5 ms every second. In the gray section from 97 min to 179 min, the coupling stabilization was deactivated. The inset shows a zoom on the temporal behavior of the transmission when the coupling stabilization is turned on again.

the CS is operating in closed-loop mode at critical coupling. Then, the CS is switched off for about 80 min indicated by the gray shaded area. Afterwards, the CS is switched back to closed-loop mode operation. While the CS is operating the average residual transmission in the fiber remains as low as $0.9 \pm 0.3\,\%$. In contrast, one observes a clear increase in the transmission to up to $10\,\%$ in a 80 min period when the CS is switched off, indicating that the resonator-fiber is no longer critically coupled. When the CS stabilization is switched to closed-loop mode again, it re-establishes the condition of critical coupling within $10\,\mathrm{s}$, as can be seen from the inset of Fig. 3.9. From this dynamics a bandwidth of 0.1–$0.2\,\mathrm{Hz}$ is estimated for the CS, limited by the low-pass filter in the servo loop. Apart from the very low average transmission during the closed-loop mode, one observes several noise peaks around $t = 50\,\mathrm{min}$ which probably arise due to mechanical vibrations in the setup. The time scale of these pertubations is on the order of 1–7 s so that the CS does not correct for them due to the limited loop bandwidth.

In conclusion, the experiments show that the off-resonant PDH signal indeed has the desired, almost linear, monotone slope around critical coupling. Based on this technique, we demonstrated that it is possible to simultaneously actively stabilize the frequency and the evanescent coupling of a bottle resonator, thereby enabling a reliable operation at the critical coupling point over extended periods of time.

3.2.2 Estimation of position noise

In addition to the direct measurement of the transmission fluctuations in the last section, it would be of great interest for the characterization of the CS to quantify the stability of the resonator–

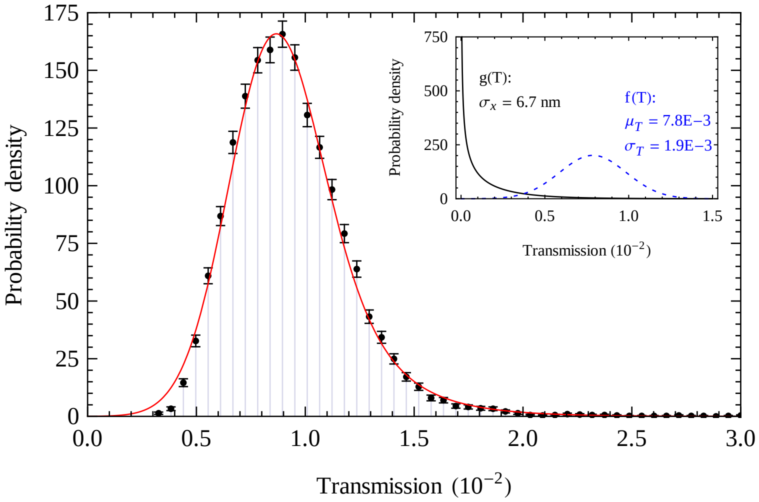

Figure 3.10: Noise distribution of the transmission (black data points) through the coupling fiber stabilized to critical coupling for the data from Fig. 3.9 with active CS ($t < 80\,\mathrm{min}$). The red line is a fit with the convolution of the two probability distributions $g_{\sigma_x}(T)$ (black line) and $f_{\mu_T,\sigma_T}(T)$ (blue dashed line), as shown in the inset. $g_{\sigma_x}(T)$ represents transmission fluctuations induced by changes of the resonator–fiber gap while $f_{\mu_T,\sigma_T}(T)$ is a normal distribution, describing other present noise sources like, e.g., detection noise.

fiber gap. As we will see, we can obtain information about the latter by analyzing the fluctuations of the transmitted light. For the data of Fig. 3.9 with active CS, the distribution of the fluctuating transmission is given in Fig. 3.10 in a normalized histogram, thereby representing the corresponding probability density. Interestingly, the distribution shows a clear asymmetry. In the following, this asymmetry is used to estimate an upper bound for the fluctuations of the resonator–fiber gap x_{rel}.

When the resonator–fiber system is very close to critical coupling, a variation of x_{rel} cannot reduce the transmission below the minimal value at critical coupling, which is ideally zero (see Fig. 3.6). Therefore, the transmission will be limited to values equal to or higher than that at critical coupling, no matter if the variation of x_{rel} is positive or negative. The resulting distribution of transmission values due to fluctuations in x_{rel} around critical coupling is therefore asymmetric and offers the possibility to distinguish this specific origin of noise from other sources with a symmetric distribution. For instance, the detector noise of the SPCMs would give a symmetric distribution to the noise of the transmission also if the count rates are high enough. It should be emphasized that some other noise sources will contribute to an asymmetric distribution of transmission values. For instance, frequency fluctuations of the laser–resonator detuning around resonance will also always result in an increased transmission compared to the resonant value. For this reason, we can only estimate an upper bound for the resonator–fiber gap fluctuations assuming that it is the dominant noise source with an asymmetric distribution.

In order to model the observed distribution from Fig. 3.10, we assume that the on-resonance transmission $T = |t(\omega_0)|^2$ through the ultra-thin fiber has the following dependence on the resonator–fiber gap x_{rel}

$$T(x_{rel}) = \left(\frac{1 - \exp(-x_{rel}/\gamma_{\text{ext}})}{1 + \exp(-x_{rel}/\gamma_{\text{ext}})}\right)^2 , \tag{3.6}$$

where the exponential dependence of the coupling rate $\kappa_{\text{ext}}(x_{\text{rel}}) = \kappa_0 \exp(-x_{\text{rel}}/\gamma_{\text{ext}})$ from Eq. (2.65) has been inserted into Eq. (3.1). This equation can be inverted to obtain an expression for the resonator–fiber gap as function of T, yielding

$$x_{\pm}(T) = \gamma_0 \ln \left\{ \frac{1 \pm \sqrt{T}}{1 \mp \sqrt{T}} \right\} , \tag{3.7}$$

where $x_{rel} = 0$ at critical coupling and x_+ (x_-) denote positive (negative) values of x in the under (over) coupled regime. We assume here that fluctuations of the resonator–fiber gap follow a normal distribution f_{μ_x,σ_x} with the mean position μ_x, corresponding to the deviation from critical coupling, and the standard deviation σ_x, which we want to determine. Since we are only interested in an upper bound for the gap fluctuations, it is assumed that the fiber moves exactly around critical coupling, which results in the strongest asymmetry of the transmission distribution. As a consequence, we set $\mu_x = 0$ and can express f_{μ_x,σ_x} on its definition interval as a function of x_+, yielding

$$\int_{-\infty}^{\infty} f_{0,\sigma_x}(x_{rel}) dx_{rel} = 2 \cdot \int_0^{\infty} f_{0,\sigma_x}(x_+) dx_+ . \tag{3.8}$$

Next, a variable substitution from x_+ to T is performed with the help of Eq. 3.7. The resulting distribution $g_{\sigma_x}(T)$ quantifies the fluctuation of the transmission due to the noise of the resonator–fiber gap σ_x and reads

$$= 2 \cdot \int_{T(0)}^{T(\infty)} f_{0,\sigma_x}(T) \frac{dx_+}{dT} dT = \int_0^1 g_{\sigma_x}(T) dT . \tag{3.9}$$

This distribution is highly asymmetric, as can be seen from the inset of Fig. 3.10, and reaches its maximum value at $T = 0$. In order to describe the experimentally observed transmission distribution, one also has to take into account other noise sources which lead to a symmetric distribution of the transmission, like, e.g., detector noise. For simplicity, we represent this symmetric noise term by a single normal distribution $f_{\mu_T,\sigma_T}(T)$ with the mean μ_T, specifying a residual transmission offset and the standard deviation σ_T. By fitting the convolution of $g_{\sigma_x}(T)$ and $f_{\mu_T,\sigma_T}(T)$ which is given by

$$(g_{\mu_x,\sigma_x} * f_{\mu_T,\sigma_T})(T) = \int_0^1 g_{\mu_x,\sigma_x}(\tau) f_{\mu_T,\sigma_T}(T - \tau) d\tau , \tag{3.10}$$

to the experimental data in Fig. 3.10 we determine the parameters σ_x, σ_T and μ_T.

The best fitting convoluted distribution has a residual transmission value of $\mu_T = 0.78\,\%$ with a standard deviation of $\sigma_T = 0.19\,\%$. For the normal distribution of the fiber gap a standard deviation of $\sigma_x = 6.7\,\mathrm{nm}$ is obtained. Hence, taking into account the time interval of 5 ms for which the transmission is averaged during the measurement, we estimate an upper bound for the fluctuation of the resonator–fiber gap of about 7 nm for frequencies up to 200 Hz. The deviation of the fitted convolution from the experimental distribution for small values of T in Fig. 3.10 is most likely explained by a small residual misalignement of the fiber from critical coupling.

3.3 Outlook: Stabilizing the evanescent coupling of two fibers to a WGM microresonator

As already described in chapter 2, WGM microresonators offer the possibility to couple two ultra-thin fibers to the resonator. Figure 3.11 a) shows such an add-drop configuration that enables extremely efficient switching of light between two fibers [74]. WGM bottle microresonators are especially suited for these applications since their three-dimensional mode structure permits one to align two fibers in a simple way at the resonator such that they both couple to the same mode. Based on the Kerr nonlinearity of silica, efficient and extremely fast switching at record-low light levels was demonstrated for a WGM bottle microresonator [79]. However, for optimal performance of these devices, simultaneous evanescent coupling of two tapered fibers to the resonator is required. Moreover, the main properties of the switch, like its bandwidth and transfer efficiency, are extremely sensitive to variations of the separation between the resonator and the two fibers. Thus, for the reliable operation of such an add-drop filter, an active stabilization of the evanescent coupling of the two fibers to the resonator would be highly desirable.

3.3.1 Modeling two fibers evanescently coupled to a WGM resonator

A simple model that describes the evanescent coupling of two tapered fibers to a WGM microresonator was presented in section 2.4.6. In summary, from the perspective of the bus fiber which initially carries the light, the drop fiber is treated as an additional loss channel to the resonator mode. The implementation of a coupling stabilization in this system is complicated by the fact that changes in the coupling of one fiber to the resonator also modify the coupling condition of the other fiber. Consider for example the situation illustrated in Figure 3.11 a), where the bus fiber is critically coupled to the combined resonator–drop fiber system. When the drop fiber moves towards the resonator, its coupling increases and thereby results in a corresponding change in coupling condition of the bus fiber from critically to under-coupled. A suitable coupling stabilization scheme therefore has to be able to differentiate between the position fluctuations and drifts of the two fibers. Based on the analysis in section 2.4.6 and 3.1, the following part will give an outlook on how such a coupling stabilization could be realized with the help of the PDH-technique.

It is instructive to investigate in more detail the above situation in which the bus fiber is critically coupled to the resonator–drop fiber system. In this case, the condition $\kappa_{\text{bus}} = \kappa_0 + \kappa_{\text{drop}}$ is fulfilled while the total resonator HWHM is $\kappa = \kappa_0 + \kappa_{\text{drop}} + \kappa_{\text{bus}}$. From this relation, it is evident that a change of the gap between resonator and bus or drop fiber in both cases has the same effect on the resonator linewidth. A similar observation is true for the intensity transmission past the resonator: No matter which of the two fibers changes its position – the condition for critical

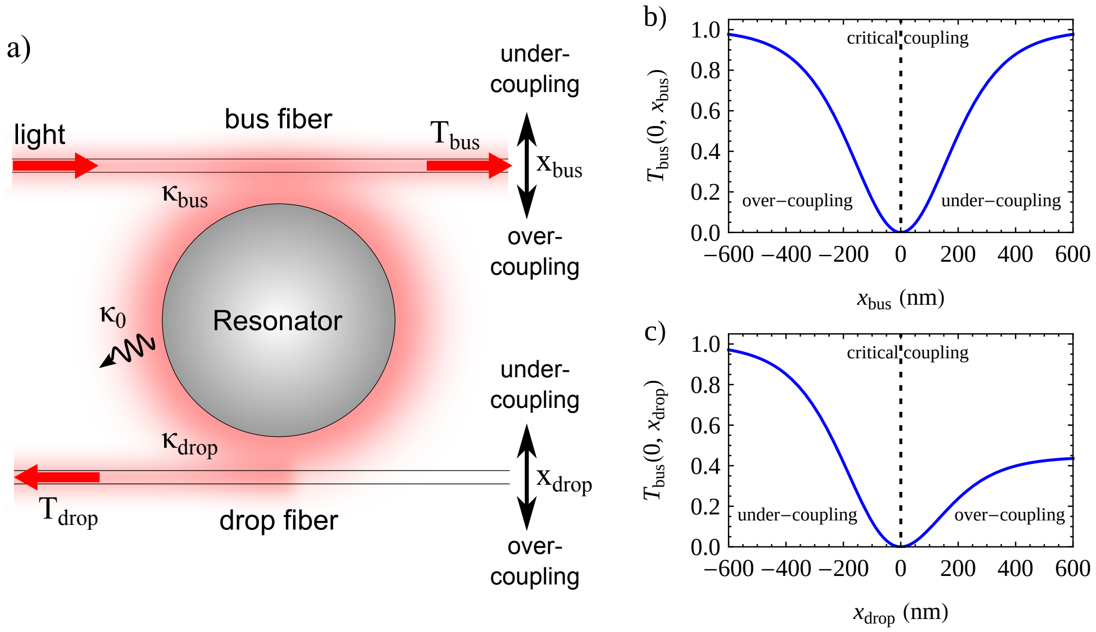

Figure 3.11: a) Schematic of two ultra-thin fibers coupled to a WGM resonator in the add-drop configuration. b) On-resonant bus fiber transmission $T(0, x_{\text{bus}})$ as function of x_{bus} for a fixed x_{drop}: When the bus fiber is critically coupled to the combined resonator–drop fiber system, a reduction of the bus fiber–resonator gap x_{bus} brings the system into over-coupling while an increase of x_{bus} under-couples the system. c) In contrast, a change of the drop fiber–resonator gap x_{drop} has the inverse effect on the bus fiber transmission. Parameters of the plots are $\kappa_0/2\pi = 5\,\text{MHz}$, a) $\kappa_{\text{drop}}/2\pi = 20\,\text{MHz}$, $\kappa_{0,\text{bus}} = /2\pi = 25\,\text{MHz}$, and b) $\kappa_{\text{bus}}/2\pi = 25\,\text{MHz}$, $\kappa_{0,\text{drop}} = /2\pi = 20\,\text{MHz}$.

coupling will be no longer valid and, as a consequence, the bus fiber transmission increases as it is shown in Figure 3.11 b) and c). Thus, neither the linewidth nor the transmission are good indicators for the individual coupling strengths of the two fibers to the resonator.

Even though the effect of position changes of the bus and drop fiber have an identical effect on the resonator linewidth and transmission, it should be pointed out that the underlying physical situation for the two cases is different. If one intends to over-couple the system by shifting of the bus fiber, the fiber has to approach the resonator resulting in an increased resonator linewidth (see Figure 3.11 b)). By contrast, if the regime of over-coupling should be reached by a movement of the drop fiber, the fiber has to be pulled back (see Fig. 3.11 c)). Therefore, we now have a somewhat counterintuitive situation in which reaching an over-coupled system with the drop fiber results in a reduction of the resonator linewidth. Note that, in this case, the bus fiber transmission saturates at a non-unity value since the influence of the drop fiber becomes negligible while the coupling to the bus fiber dominates the resonator losses, as shown in Fig. 3.11 c).

The substantially different behavior of bus and drop fiber in the evanescent coupling process can be revealed with the off-resonant PDH-signal. First, let us consider the expression of the transmission coefficient for the bus fiber in the add-drop configuration, which according to

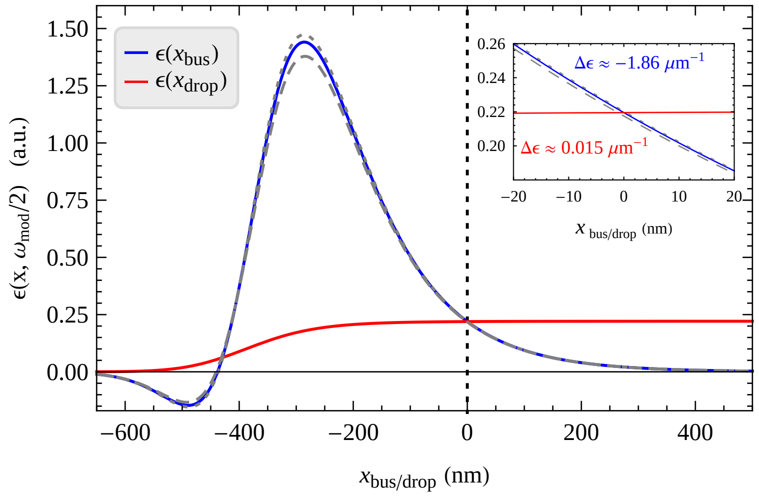

Figure 3.12: Calculated variation of the CS signal in the bus fiber as function of the gap between bus fiber x_{bus} (blue) and drop fiber x_{drop} (red), respectively, where $x_{\text{bus/drop}} = 0$ denotes critical coupling. The inset shows a magnification of the signal around critical coupling with the corresponding approximated linear slopes. Parameters for the plot are $\kappa_0/2\pi = 5\,\text{MHz}$, $\omega_{\text{mod}} = 1.2\,\text{GHz}$ and $\gamma_{\text{ext}} = 116.7\,\text{nm}$. For the blue (red) signal, the drop (bus) fiber coupling is fixed to $\kappa_{\text{drop}}/2\pi = 20\,\text{MHz}$ ($\kappa_{\text{bus}}/2\pi = 25\,\text{MHz}$) and the coupling of the bus (drop) fiber follows the dependence $\kappa_{\text{i}}(x_{\text{i}}) = \kappa_{0,\text{i}} \cdot \exp\left(-x_{\text{i}}/\gamma_{\text{ext}}\right)$ with $i =$ bus (drop) and $\kappa_{0,\text{bus}} = 50\,\text{MHz}$ ($\kappa_{0,\text{drop}} = 40\,\text{MHz}$). In order to further illustrate the insensitivity of the CS signal to the coupling of the drop fiber, $\epsilon(x_{\text{bus}})$ is also plotted for the cases $\kappa_{0,\text{drop}} = 40\,\text{MHz}$ (grey dashed line) and $\kappa_{0,\text{drop}} = 10\,\text{MHz}$ (gray dotted line).

Eq. (2.71), can be expressed as

$$t_{\text{bus}}(\omega, x_{\text{bus}}, x_{\text{drop}}) = \frac{\kappa_0 + \kappa_{\text{drop}}(x_{\text{drop}}) - \kappa_{\text{bus}}(x_{\text{bus}}) + i(\omega - \omega_0)}{\kappa_0 + \kappa_{\text{drop}}(x_{\text{drop}}) + \kappa_{\text{bus}}(x_{\text{bus}}) + i(\omega - \omega_0)}\,. \tag{3.11}$$

It is clear that, from the perspective of the bus fiber, there is no difference between intrinsic resonator losses κ_0 and the coupling to the drop fiber κ_{drop}. No matter through which of the two channels light is lost, it will reduce the amount of light which couples back into the bus fiber. Thus, we could introduce the quantity $\kappa_0' = \kappa_0 + \kappa_{\text{drop}}$ which would transform Eq. (3.11) into an equivalent form of the transmission coefficient from the single fiber case in Eq. (3.1). Following this line of argumentation, our approximation for the CS signal (under the condition that the modulation frequency is much bigger than the resonator linewidth $(\omega_{\text{mod}} \gg 2\kappa)$) remains valid, and now reads

$$\epsilon(x_{\text{bus}}, \omega_{\text{mod}}/2) \approx \frac{32}{3}\frac{\kappa_{\text{bus}}(x_{\text{bus}})}{\omega_{\text{mod}}}\,. \tag{3.12}$$

From this expression, it is clear that in this regime the CS signal is proportional to changes of the bus fiber coupling wheras it remains insensitive to fluctuations of the drop fiber coupling.

In Fig. 3.12 the off-resonant PDH signal, derived from the light transmitted through the bus fiber, is plotted for the case of two fibers coupling to the resonator, where the gap x_{bus} and x_{drop} between resonator and bus or drop fiber is scanned, respectively, while keeping the other constant. Depending on which fiber position is changed, the CS signal shows a fundamentally different behavior. While the variation of x_{bus} closely reproduces the monotone slope of the CS signal around critical coupling already know from Fig. 3.6, a change in x_{drop} has a much smaller effect and only for very strong resonator-fiber coupling a roll-off of the signal can be observed. Thus, as expected from the approximation, the CS signal is much more sensitive to variations of the bus fiber than the drop fiber gap and therefore opens up the opportunity to stabilize simultaneously the coupling of two fibers to a WGM microresonator.

3.3.2 Proposal for a technical implementation of the coupling stabilization with two fibers

Our study shows that the CS signal is, to a good approximation, only sensitive to coupling changes of the bus fiber as long as the condition $\omega_{\text{mod}} \gg 2\kappa$ is fulfilled. In this situation, variations of the coupling between the drop fiber and the resonator have only negligible influence on the CS signal. If one considers the parameter regime of Fig. 3.12 for instance, the slopes of the CS signal for variations of x_{bus} and x_{drop} around critical coupling differ by more than factor 100 (compare inset in Fig. 3.12). As a consequence, the CS signal derived from the light in transmitted through the bus fiber can be used to exclusively stabilize the bus fiber position to the critical coupling point, as long as the drop fiber position does not deviates excessively from its initial value. In order to stabilize the evanescent coupling of the two fibers to the resonator, a technical solution could be to create a CS error signal for each fiber using two stabilization laser beams, one sent along the bus fiber and one along the drop fiber.

In order to realize such a stabilization scheme, several technical challenges have to be addressed. Firstly, it is important to sufficiently differentiate the two CS signals from each other. Since the light fields from which the two signals are derived propagate in two different fibers and the carrier and sidebands are off-resonant to the resonator, this condition is already fulfilled to a certain degree. Nevertheless, a small part of the light fields in the fibers will couple via the resonator into the other fiber, respectively. Therefore, two different modulation frequencies have to be applied and their difference should be large enough to efficiently separate the two CS signals.

An even more important aspect to consider is the required magnitude of the modulation frequencies. To suppress the influence of the drop-fiber on the CS signal of the bus fiber and vice versa, the system has to operate with modulation frequencies exceeding the loaded resonator linewidth by a factor of approximately 10. If the add-drop configuration is realized with high switching efficiency, the two fibers have to couple strongly to the resonator, thereby broadening its linewidth considerably. For instance, an intrinsic resonator half linewidth of $\kappa_0 = 5\,\text{MHz}$ would have to be increased to $\kappa = 50\,\text{MHz}$ to enable transfer efficiencies of $T_{\text{drop}} = 80\,\%$. Accordingly, the modulation frequencies of the CS signals have to be adapted to maintain the condition $\omega_{\text{mod}} \gg 2\kappa$. Therefore ω_{mod} will be on the order of $1\,\text{GHz}$ and the optical and electrical components of the CS described in Fig. 3.7 have to support this high frequency range.

However, state of the art fiber-based micro-integrated EOMs and silicon photodetectors can be operated beyond frequencies of several GHz and should allow one to straight-forwardly realize the CS stabilization with two ultra-thin fibers.

The typical application scenario of the described stabilization scheme would be the case of two fibers coupled to the resonator with comparable coupling strength, as is for example required for efficient transfer of light between the fibers. In addition, further theoretical analysis of the system shows that the CS should operate just as well when the coupling strength of the two fibers to the resonator is more asymmetric. As long as the main condition $\omega_{\text{mod}} \gg 2\kappa$ remains valid, the only effect of an asymmetric coupling strength is the reduction of the CS signal amplitude for the fiber which couples less to the resonator. This effect could be easily compensated by a corresponding adjustment of the power of the incident light field.

3.4 Conclusion

In summary, this chapter presented an experimental technique which enabled, for the first time, the full active stabilization of a whispering-gallery-mode microresonator, comprising the resonance frequency and the evanescent coupling to an ultra-thin fiber. The method is based on the well-established Pound–Drever–Hall phase modulation technique and can be applied to stabilize the resonator–fiber coupling over a wide range of coupling strengths including the important point of critical coupling. The coupling stabilization allows one to compensate for long-term drifts of the resonator–fiber separation and demonstrated the ability to maintain the critical coupling condition over extended periods of time. Moreover, the scheme operates with off-resonant light and therefore minimizes distortion effects like, e.g., thermally induced shifts of the resonator frequency. Thus, the presented technique holds great potential for the field of evanescently coupled whispering-gallery-mode microresonators, whenever a high long-term stability is required, especially in applications where long-term stability is required. Possible areas of application range from CQED with WGM resonators [29, 80], single molecule detection and sizing [81, 82], to nonlinear optical process and mirco-lasers which require maximal intracavity intensity [83–86]. In addition, the described method is of interest for optical impedance matching of other types of resonators. For instance, in interferometer-based gravitational wave detectors variable reflectivity compound mirrors can be used in order to impedance-match coupled resonator system [87]. In this scenario the coupling stabilization technique could be well applied.

Finally, in was shown how the coupling stabilization technique could be extended to two fibers simultaneously coupled to the resonator in add-drop configuration. The theoretical analysis showed that the system parameters can be chosen such that the coupling stabilization signal is only sensitive to variations of the fiber which carries the light signal. By using two coupling stabilization signals, this fact would allow one to control the coupling of both fibers to the resonator simultaneously. Such a system would be especially beneficial for the realization of long-term stable, highly efficient add-drop filters [79].

CHAPTER 4

Theory of Light–Matter Interaction with Non-Transversal Photons

The coupling of light and matter in high-finesse cavities has been investigated in numerous outstanding experiments. The subjects of study include fundamental research like atom–photon entanglement [20], the creation and control of photon Fock states [22], applications like non-destructive photon detection [23, 24], deterministic single photon sources [25], basic quantum network elements and tools in quantum information science [26, 27], and single photon transistors [28]. This very broad and multifaceted field of research is in generally referred to as "cavity quantum electrodynamics" (CQED). The theoretical fundament of CQED has been established already in the sixties of the 20th century by Jaynes and Cummings [88] and since then CQED has become extremely successful.

The continuing success of CQED originates from several important technological advancements in quantum optics. Firstly, the precise control of matter has been improved considerably from thermal atomic beams in early works to optically cooled and trapped clouds of atoms. Nowadays, it is possible to control the position and motion of individual atoms by light, thereby enabling a precise and stable coupling to the resonator field. The second important technological ingredient for the breakthrough of CQED was the development of high-finesse cavities with small mode volume. This development started initially with superconducting microwave cavities with long photon lifetimes, followed by progress in the fabrication of dielectric coatings which enabled the construction of optical Fabry-Pérot-type resonators with ultra-high Finesse. Since then, Fabry-Pérot cavities have improved even further resulting in a considerable reduction of mode volume, e.g., through the implementation of fiber and nano-fiber based cavities [33, 36].

The research for high-Q cavities with even smaller mode volume has also paved the way for alternative resonator concepts, like photonic crystal cavities and WGM microresonators [9]. The latter has been discussed in detail in chapter 2 where we have seen that these resonators can reach ultra-high Q and very small mode volumes. Beside these extraordinary properties WGM microresonators offer the ability to couple light in and out with near unity efficiency, which is extremely attractive for many CQED applications [29, 89]. However, the ongoing effort to miniaturize the mode volume of resonators results in a situation in which the properties of the guided light fields deviate drastically from what is know from light propagating in free space. As a consequence, the light field can no longer be described as a transversally polarized wave but also has longitudinal field components. These new properties of the cavity light field modify the light–matter interaction considerably and give rise to new and surprising and beneficial effects.

In this chapter we introduce the theoretical background necessary to describe the interaction of matter with non-transversally polarized light. We start with a short introduction to the Jaynes–Cummings model which describes the coupling between a two-level atom and a single cavity mode. Then we will show how interactions with the environment like dissipation and driving can be incorporated into the model. Then we discuss the extension of the formalism to treat ring cavities which support two counter-propagating modes. This model has been used so far to describe light–matter interaction in WGM microresonators. However, as we will see, the approach is in general not appropriate as the non-transversal polarization of the light in the resonator is neglected. Therefore, we next discuss in detail the polarization of WGMs, in particular of the evanescent field, which is the interface to couple atoms to the resonator field. Based on these polarization properties of the WGMs, we investigate the consequences for light–matter interactions and shown how the Jaynes–Cummings model can be modified to include the non-transversal polarization leading to a quantitative description of light–matter coupling in WGM resonators.

Parts of this chapter were published in Ref. [90].

4.1 Modeling the atom–light interaction with a single cavity mode

An atom in free space can interact with an infinite number of radiation modes. As a consequence, the process of spontaneous emission of a photon is irreversible. However, the density of modes the atom is interacting with is modified by the presence of an optical cavity. In this case, it is possible to realize a situation in which the coupling of the atom to a specific cavity mode is much stronger than to all other modes. Then the spontaneous emission of a photon is no longer irreversible and re-absorption and emission cycles can be observed, which are often referred to as Rabi oscillations.

4.1.1 The Jaynes–Cummings model

The formalism introduced by Jaynes and Cummings [88] describes the interaction of a two-level atom with ground state $|\mathrm{g}\rangle$ and excited state $|\mathrm{e}\rangle$ with a single quantized mode of the electromagnetic field (e.g. a cavity mode) which is described by the photon annihilation and creation operators $\hat{a}$ and $\hat{a}^\dagger$. In the dipole and rotating wave approximation (RWA) the Hamiltonian of the coupled atom–light system can be written as

$$H_{\mathrm{JC}}/\hbar = \underbrace{\omega_{\mathrm{g}} |g\rangle \langle g| + (\omega_{\mathrm{g}} + \omega_{\mathrm{a}}) |e\rangle \langle e|}_{=H_{\mathrm{a}}} + \underbrace{\omega_{\mathrm{c}} \hat{a}^\dagger \hat{a}}_{=H_{\mathrm{c}}} + \underbrace{(g \hat{a} \hat{d}^\dagger + g^* \hat{a}^\dagger \hat{d})}_{=H_{\mathrm{int}}}, \tag{4.1}$$

H_{a} represents the atomic part of the Hamiltonian with the energies of the ground state $\hbar\omega_{\mathrm{g}}$ and excited state $\hbar(\omega_{\mathrm{g}} + \omega_{\mathrm{a}})$, where ω_{a} is the frequency of the atomic transition. For now, zero energy is chosen without loss of generality to lie exactly in between the two atomic levels such that $\omega_\mathrm{g} = -\omega_\mathrm{a}/2$. The cavity field is represented by H_c which contains the photon number operator $\hat{a}^\dagger\hat{a}$ and the resonance frequency ω_c of the mode. The last term of the Hamiltonian H_int describes the interaction between the light field and the atom where we use the atomic operators $\hat{d} = |g\rangle\langle e|$ and $\hat{d}^\dagger = |e\rangle\langle g|$. The strength of the interaction is characterized by the coupling parameter g which is in general position dependent and given by [19]

$$g(\vec{r}) = \sqrt{\frac{\mu^2\omega_\mathrm{c}}{2\hbar\epsilon_0 V}}\Psi(\vec{r})\,, \tag{4.2}$$

where the resonator-mode function $\Psi(\vec{r})$ is normalized such that the mode volume of the resonator is $V = \int dr^3|\Psi(\vec{r})|^2$, while $\mu = \langle e|\,\hat{\mu}\,|g\rangle$ is the off-diagonal element of the dipole operator $\hat{\mu}$ [91].

The interaction term introduces a coupling between the states $|\mathrm{e}, n\rangle$ and $|\mathrm{g}, n+1\rangle$ where n is the photon number in the cavity mode. These states are also denoted as "bare" states and represent the eigenstates of the uncoupled system ($g = 0$). The interaction between the atom and the cavity mode results in new eigenstates which can be obtained by diagonalizing the Hamiltonian yielding [91]

$$\begin{aligned} |n,+\rangle &= \quad\cos(\Phi_n/2)\,|\mathrm{e},n\rangle + \sin(\Phi_n/2)\,|\mathrm{g},n+1\rangle\ , \\ |n,-\rangle &= -\sin(\Phi_n/2)\,|\mathrm{e},n\rangle + \cos(\Phi_n/2)\,|\mathrm{g},n+1\rangle\ , \end{aligned} \tag{4.3}$$

where the angle for the base transformation is $\Phi_n = \tan^{-1}(2g\sqrt{n+1}/\Delta_\mathrm{ac})$, which is $\pi/2$ if the atom-cavity detuning $\Delta_\mathrm{ac} = \omega_\mathrm{a} - \omega_\mathrm{c}$ is zero. Thus, the new eigenstates of the coupled system are a mixture of the bare states and are also referred to as "dressed" states with the corresponding eigenenergies

$$E_{\mathrm{d}\pm} = \left(n + \frac{1}{2}\right)\hbar\omega_0 \pm \frac{1}{2}\hbar\Omega_n(\Delta_\mathrm{ac})\,, \tag{4.4}$$

where we have used the definition of the Rabi frequency

$$\Omega_n(\Delta_\mathrm{ac}) = \sqrt{\Delta_\mathrm{ac}^2 + 4g^2(n+1)}\,. \tag{4.5}$$

The energies of the lowest lying dressed states $|0, \pm\rangle$ are plotted in Fig. 4.1 as a function of the atom-cavity detuning Δ_ac. For large detuning, the dressed states converge to the bare states. However, on resonance (Δ_ac = 0) the dressed states show an avoided crossing in contrast to the bare states which are degenerate at this point. The splitting on resonance is caused by the coupling between the atom and the cavity and is proportional to $2g\sqrt{n+1}$. Thus, even the interaction with an empty cavity will lift the degeneracy of the eigenstates and one therefore speaks of the "vacuum Rabi splitting" [92].

If we assume the initial state of the coupled system to be $|\mathrm{e}, 0\rangle$, then the dynamics of the system consist of a sequence of spontaneous emission and re-absorption cycles of a photon where the rate of the energy exchange is the Rabi frequency given by Eq. 4.5. Since even for an empty cavity the Rabi frequency is non-zero, the system evolves coherently such that the spontaneous emission becomes, in this sense, a reversible process [91].

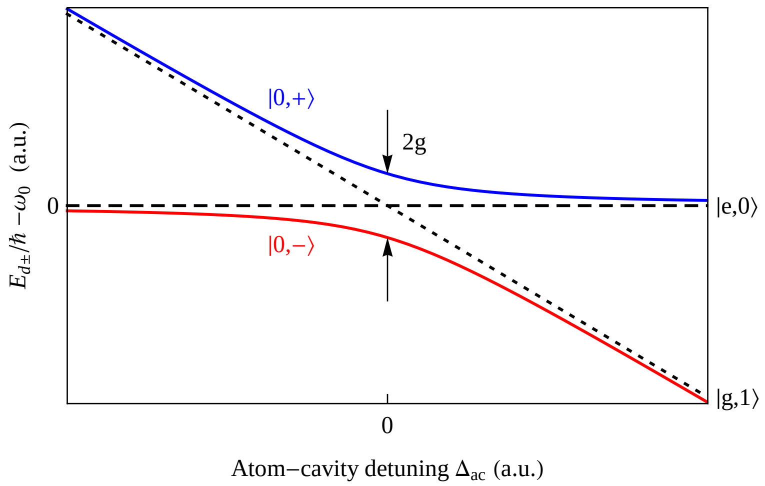

Figure 4.1: Frequencies of the lowest lying dressed states $|0,\pm\rangle$ as function of the atom–cavity detuning Δ_{ac}. For $\Delta_{\text{ac}} = 0$ the states show an avoided crossing with a splitting frequency of $2g$. For large detuning the dressed states approach the bare states of the uncoupled system $|\text{g},1\rangle$ and $|\text{e},0\rangle$ (dotted and dashed lines) .

4.1.2 Introducing driving and dissipation to the model

So far, we have considered a closed atom–cavity system without coupling to the environment. This is, however, a very idealized picture. In reality, it is very difficult to realize a situation in which the atom dominantly couples to a single cavity mode. Thus, there will also be a residual coupling to other free space modes. Moreover, the cavity itself couples to the environment and photons from the resonator field can be absorbed or scattered away. These dissipative processes will remove energy from the coupled atom–cavity system which is therefore considered to be open. However, the coupling to the environment allows also to excite the system externally and to compensate for the losses. This can be achieved by coupling the resonator to the field of an external waveguide as shown in Fig. 4.2. Before we discuss the dissipation processes in more detail we first examine how the external excitation of the resonator can be added to the model.

We can introduce the external driving formally as an additional pumping term in the Jaynes–Cummings Hamiltonian which treats the in-coupled light from the waveguide as a classical field with frequency ω_{p} and field strength η and reads [93]

$$H_{\text{p}}/\hbar = (\hat{a} + \hat{a}^\dagger)(i\eta e^{i\omega_{\text{p}}t} - i\eta e^{-i\omega_{\text{p}}t}) \approx i\eta(\hat{a}e^{i\omega_{\text{p}}t} - \hat{a}^\dagger e^{-i\omega_{\text{p}}t})\,, \tag{4.6}$$

where in the last step of the expression the RWA was performed to neglect fast oscillating terms with $\omega_{\text{c}} + \omega_{\text{p}}$. To remove the remaining time dependency of the Hamiltonian it is convenient to transform the system into a reference frame rotating with ω_{p}. The extended Jaynes–Cummings Hamiltonian then becomes [93]

$$H_{\text{JC}}/\hbar = \Delta_{\text{ap}}\,|e\rangle\,\langle e| + \Delta_{\text{cp}}\hat{a}^\dagger\hat{a} + (g\hat{a}\hat{d}^\dagger + g^*\hat{a}^\dagger\hat{d}) + i\eta(\hat{a} - \hat{a}^\dagger)\,, \tag{4.7}$$

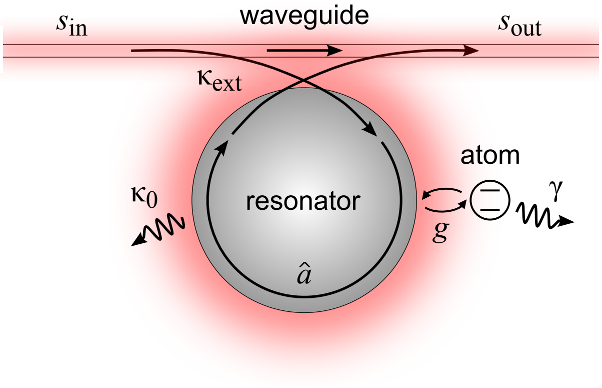

Figure 4.2: Schematic of a two-level atom coupled to a resonator mode $\hat{a}$ with coupling strength g. The atomic excitation decays with rate γ into free space, while the resonator mode is damped by intrinsic losses κ_0 and the coupling to the waveguide κ_{ext}. The resonator mode is driven via the waveguide field s_{in}.

where we have introduced the atom–pump detuning $\Delta_{\text{ap}} = \omega_{\text{a}} - \omega_{\text{p}}$ and cavity–pump detuning $\Delta_{\text{cp}} = \omega_{\text{c}} - \omega_{\text{p}}$.

Above, we already started to discuss the physical origin of dissipation in a CQED-system which are summarized in Fig. 4.2. On the one hand, the atom is not only coupled to the cavity mode but can also emit photons into free space which are then irreversibly lost from the system. On the other hand, photons can also be absorbed or scattered away by imperfection in the cavity or can couple out into defined modes of, e.g., a waveguide. In order to account for theses losses in an open quantum system, the master equation formalism has been developed. In brief, the basic idea of this approach is to treat the dissipation as the coupling of the system under study S to a large reservoir R where the state of the composite system $S \bigotimes R$ is described by the density operator ρ_{SR}. Starting from the Schrödinger equation $d\rho_{SR}/dt = -i/\hbar[H, \rho_{SR}]$ one can obtain an expression for the temporal evolution of the reduced density operator of the system $\rho(t) = \text{tr}_R(\rho_{SR}(t))$ by tracing over the states of the reservoir. In the final expression the properties of R then enter only as parameters [94]. This is the so-called master equation which for our system can be written in the Born–Markov approximation as [95]

$$\frac{d\rho}{dt} = \mathcal{L}\rho = -\frac{i}{\hbar}[H_{\text{JC}}, \rho] + \kappa\mathcal{D}[\hat{a}]\rho + \gamma\mathcal{D}[\hat{d}]\rho\,, \tag{4.8}$$

with the Liouvillian superoperator $\mathcal{L}$. Here, κ and γ are the decay constants of the cavity field and the atomic excited state, respectively. $\mathcal{D}[\hat{c}]$ is the decay superoperator acting on an arbitrary operator $\hat{c}$ and is defined for a reservoir at zero temperature by

$$D[\hat{c}]\rho = 2\hat{c}\rho\hat{c}^\dagger - \hat{c}^\dagger\hat{c}\rho - \rho\hat{c}^\dagger\hat{c}\,. \tag{4.9}$$

The assumption of a reservoir at zero temperature is, in general, a good approximation for optical cavities as optical frequencies are much higher than the frequency spectrum of the black body radiation emitted by the environment at room temperature.

The master equation now allows us to calculate the temporal evolution of the coupled system as well as important steady state quantities like the transmission spectrum of the cavity. To this end, we first determine the temporal evolution of the expectation value $\langle \hat{a} \rangle = \mathrm{tr}(\hat{a}\rho)$ of the annihilation operator for a cavity without an atom ($g = 0$) yielding [94]

$$\frac{d \langle \hat{a} \rangle}{dt} = -i\Delta_{\mathrm{cp}} \langle \hat{a} \rangle - \kappa \langle \hat{a} \rangle - \eta \,, \tag{4.10}$$

where we have used the cyclic permutation property of the trace and the commutator relation $[\hat{a}, \hat{a}^\dagger] = 1$. The expression is identical to the first order differential equation of the mode amplitude in Eq. (2.46) which we have introduced in chapter 2 to describe the dynamics of the resonator. Comparing the two expressions we can obtain the relation $\eta = \sqrt{2\kappa_{\mathrm{ext}}} \cdot s_{\mathrm{in}}$ between the pump field with strength η and the incoming field in the waveguide s_{in} which couples with the rate κ_{ext} to the resonator. As before, the total decay constant $\kappa = \kappa_0 + \kappa_{\mathrm{ext}}$ comprises the intrinsic resonator losses κ_0 and the coupling to the waveguide κ_{ext}. Following the derivation in chapter 2, we can also make use of the definition of the transmission coefficient t in Eq. (2.56) which becomes

$$t = 1 + \frac{\langle \hat{a} \rangle}{s_{\mathrm{in}}} \sqrt{2\kappa_{\mathrm{ext}}} \,. \tag{4.11}$$

In order to obtain an analytic expression of the transmission coefficient for the coupled atom–resonator system, one can consider the case of weak driving where the intra-cavity photon number is $n = \left\langle \hat{a}\hat{a}^\dagger \right\rangle \ll 1$. In this situation, it is sufficient to take only cavity states with one photon into account which allows one to solve the master equation in the steady state ($\mathcal{L}\rho = 0$). For small driving strength the transmission coefficient then yields according to Eq. (4.11) in first approximation

$$t = \frac{g^2 + (\gamma + i\Delta_{\mathrm{ap}})(\kappa_0 - \kappa_{\mathrm{ext}} + i\Delta_{\mathrm{cp}})}{g^2 + (\gamma + i\Delta_{\mathrm{ap}})(\kappa_0 + \kappa_{\mathrm{ext}} + i\Delta_{\mathrm{cp}})} \,. \tag{4.12}$$

Strong coupling

The dynamics of the system will depend on its loss rates, which have to be compared to the coupling strength between the atom and the cavity field. If dissipation dominates, photons will be lost from the system rapidly and no coherent atom–field interaction can be observed. However, if the atom–cavity interaction is strong compared to the dissipative processes, the system can undergo Rabi oscillations before the excitation is lost eventually. This regime is denoted as “strong coupling” and requires the coupling strength g to dominate over the dissipation constants κ and γ, thus $g \gg \kappa, \gamma$. A signature of strong coupling is the appearance of the vacuum Rabi splitting of the dressed states, e.g., in the transmission spectrum. In Fig. 4.3, the intensity transmission is plotted for a waveguide coupled to a cavity as a function of the cavity–pump detuning. If no atom is coupled to the cavity, the transmission spectrum shows a single Lorentzian dip of the cavity resonance with a FWHM of 2κ. In contrast, in the strong coupling regime and in the limit of weak driving the transmission spectrum splits into two resonances, which correspond to the two lowest dressed states $|0, \pm\rangle$.

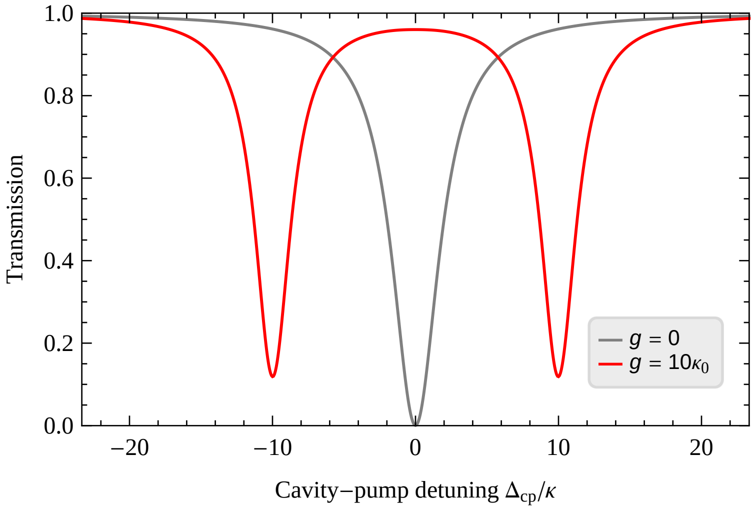

Figure 4.3: Calculated transmission spectrum $T = |t|^2$ as function of the cavity–pump detuning for a waveguide coupled to a single cavity mode which is not coupled (grey) and strongly coupled (red) to a two-level atom, respectively. Parameters for the plot are $\gamma = \kappa_{\text{ext}} = \kappa_0$, $\omega_{\text{a}} = \omega_{\text{c}}$ and g is as indicated in the legend. The cavity is driven weakly with an on-resonant intra-cavity photon number of 0.01 when no atom is present.

Another way of quantifying the coupling between the atom and the resonator mode is the cooperativity parameter, which is given by [19]

$$C = \frac{g^2}{2\gamma\kappa}, \tag{4.13}$$

where $C > 1$ if the system is strongly coupled. The cooperativity can also be interpreted as the inverse of the critical atom number $N_0 = 1/C$ which specifies the number of atoms which are necessary to significantly alter the on-resonant transmission of the resonator.

4.2 Coupling of an atom to a ring resonator

So far, we have considered only a single cavity mode interacting with the atom. However, a WGM resonator supports pairs of counter propagating modes. Therefore, it seems self-evident to treat the WGM resonator conceptually identical to a ring cavity. So far, this has been the standard procedure in literature [80, 89, 96–101] which we will introduce briefly at this point.

For instance, such a ring resonator can be realized using a three-mirror geometry as it is shown in Fig. 4.4 a). Light can propagate in a ring resonator in pairs of degenerate modes with one running clockwise and the other counter-clockwise. Thus, we have to extend our model such that it contains two counter-propagating modes $\hat{a}$ and $\hat{b}$. The Hamiltonian then takes the

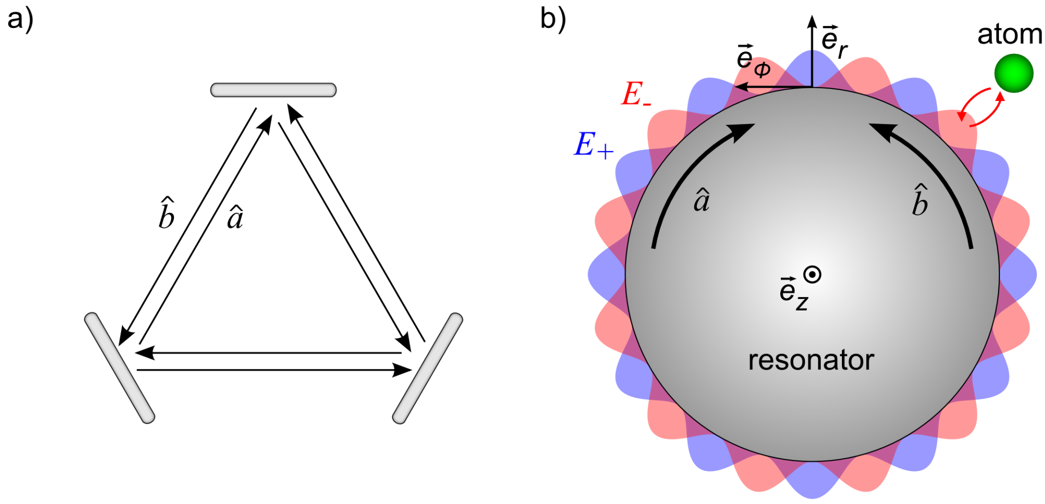

Figure 4.4: a) Simple model of a three-mirror ring cavity with two degenerate, scalar light waves $\hat{a}$ and $\hat{b}$, propagating clockwise and counter-clockwise, respectively. b) Equivalent description of a WGM resonator as ring cavity. The superposition of the two scalar running waves $\hat{a}$ and $\hat{b}$ creates two standing waves $\hat{u}_+$ and $\hat{u}_-$, which are spatially shifted against each other by $\pi/2$. The phase of the standing wave pattern can always be chosen such that the atom couples only to one of the standing waves.

typical form of a ring cavity [96, 102] reading

$$\begin{aligned} H_{\text{ring}}/\hbar = \quad & \Delta_{\text{ap}} \left|e\right\rangle \left\langle e\right| + \Delta_{\text{cp}}(\hat{a}^\dagger\hat{a} + \hat{b}^\dagger\hat{b}) + h\hat{a}^\dagger\hat{b} + h^*\hat{b}^\dagger\hat{a} \\ & + (g_a\hat{a}\hat{d}^\dagger + g_a^*\hat{a}^\dagger\hat{d}) + (g_b\hat{b}\hat{d}^\dagger + g_b^*\hat{b}^\dagger\hat{d}) \\ & + i\eta_a(\hat{a} - \hat{a}^\dagger) + i\eta_b(\hat{b} - \hat{b}^\dagger)\,, \end{aligned} \tag{4.14}$$

where the interaction between the atom and the two cavity modes is characterized by the coupling constants g_a and g_b, respectively. Note that we have also introduced a mode coupling term which represents the coherent scattering of light between the two cavity modes with the rate h. As discussed in section 2.4.5, the mode coupling results in a splitting of the resonator resonance in the transmission spectrum when $h > \kappa$, which is due to the formation of the normal modes $(\hat{a} \pm \hat{b})/\sqrt{2}$. However, for the bottle microresonator this is in general not the case and typically only in the very under-coupled regime ($\kappa_0 \gg \kappa_{\text{ext}}$) a splitting is observed for some modes.

The presence of the second resonator mode has important consequences for the light–matter interaction in the resonator. This becomes clear when one considers the spatial intensity distribution of the normal modes for the case of a circular ring cavity as shown in Fig. 4.4 b). Under the assumption that the two counter-propagating modes $\hat{a}$ and $\hat{b}$ have the same amplitude and identical polarization one can describe the corresponding electric fields with the scalar running waves $E_a \propto \mathrm{e}^{-ik\phi}$ and $E_b \propto \mathrm{e}^{+ik\phi}$, where k is the wave number along the azimuthal propagation direction. As a consequence, the electric field of the normal modes $E_\pm = E_a \pm E_b$ has the

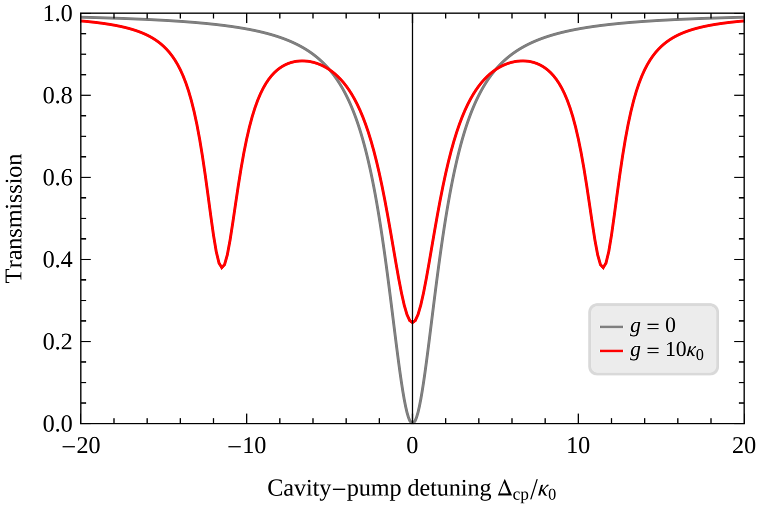

Figure 4.5: Calculated transmission spectrum $T = |t|^2$ as function of the cavity–pump detuning for a waveguide coupled to a ring cavity which supports two counter-propagating modes. The red curve shows the situation for a two-level atom strongly coupled to both cavity modes with $g_a = g_b = 10\kappa_0$. For comparison also the case where no atom is present is shown (grey). Parameters for the plot are $\gamma = \kappa_{\mathrm{ext}} = \kappa_0$, $h = 0$ and $\omega_{\mathrm{a}} = \omega_{\mathrm{c}}$. Only one of the modes is driven from the waveguide with an on-resonant intra-cavity photon number of 0.01 when no atom is present.

azimuthal dependency

$$\begin{aligned} E_+ &\propto \cos(k\phi)\,, \\ E_- &\propto \sin(k\phi)\,, \end{aligned} \tag{4.15}$$

meaning that the normal modes form a pair of standing waves which are shifted against each other such that the antinodes of one mode coincide with the nodes of the other mode as sketched in Fig. 4.4 b).

The equivalent description of the running waves as a superposition of standing waves reveals a fundamental problem of ring resonators which has far reaching consequences for light–matter interaction. The phase of the two standing waves is arbitrary and can always be chosen such that at a specific point around the resonator one standing wave has a node. Thus, it is always possible to arrange a situation in which an emitter placed at any point in the resonator field will interact only with one of the standing waves while the other one remains uncoupled as shown in Fig. 4.4 b). A signature of this effect can be found in the transmission spectrum calculated for the Hamiltonian of the ring resonator from Eq. (4.14). As we see in Fig. 4.5, in the case of a two-level atom strongly coupled to a ring cavity the transmission shows a three-peak spectrum. The two off-resonant dips correspond to the standing wave mode which has an anti-node at the position of the atom and shows therefore a Rabi splitting. In comparison with the Rabi-splitting of the single mode cavity from Fig. 4.3 we observe for the ring cavity a larger splitting of the coupled normal mode with a peak separation of $\sqrt{2} \cdot 2g$. This can be attributed to the fact, that the intensity is now spatially modulated along the circumference of the resonator resulting in a smaller mode volumes. As a consequence, the atom sees a stronger electric field in the anti-node of the standing wave. However, this larger coupling is obtained in exchange for a completely uncoupled second standing wave which has no intensity at the position of the atom. The signature of this uncoupled mode is the central peak in the spectrum in Fig. 4.5 which limits the on-resonant transmission change an atom can induce to 25%. Thus, in contrast to a Fabry-Pérot resonator, only 50 % of the light in the cavity interacts with the atom. This is of course a severe limitation for many practical applications of CQED systems that often rely precisely on a large modification of the on-resonant transmission by an atom like, e.g., in optical switching [28, 103–111]. As a consequence, ring cavities turn out to be not well suited for most of these applications. This restriction seems to hold as well for WGM microresonators since in most theoretical descriptions the field of WGM has been approximated as scalar such that the model of conventional ring resonators applies. In the next section we will see that this assumption is in general not correct since the light–matter interaction can be modified drastically when the full vectorial description of WGM field polarization is taken into account.

4.3 Polarization of whispering-gallery-modes

In the discussion of total internal reflection in chapter 2, the evanescent field was introduced. This exponentially decaying part of the WGM field surrounds the microresonator and plays a key role for accessing the confined light. As discussed in section 2.4, light can be coupled into and out of WGM resonators via the evanescent field by frustrated total internal reflection with the help of an ultra-thin fiber. Moreover, since the light is guided in a monolithic structure, any realization of light–matter coupling in WGM resonators which does not refer directly to the resonator material itself is necessarily performed via the evanescent field. As a consequence, any emitter that should couple to a WGM has to be brought extremely close to the resonator surface in order to interact with the evanescent field. A comprehensive understanding of the interaction between WGM and matter therefore requires precise knowledge of the properties of the evanescent field.

In contrast to paraxial light propagating in free space, which is well described by a transverse wave, the evanescent field has also longitudinal polarization. Interestingly, these polarization properties have so far not received attention in the context of light–matter coupling in WGM resonators.

In this section, the polarization of the evanescent field is first presented in the very general context of total internal reflection at an interface. The obtained results then help to refine the basic understanding of the polarization of WGMs which we already started to discuss in the context of the electric field solutions of the bottle resonator in section 2.3.3. Finally, the consequence of the evanescent field polarization for the interaction of light and matter are analyzed for the case of the ring resonator.

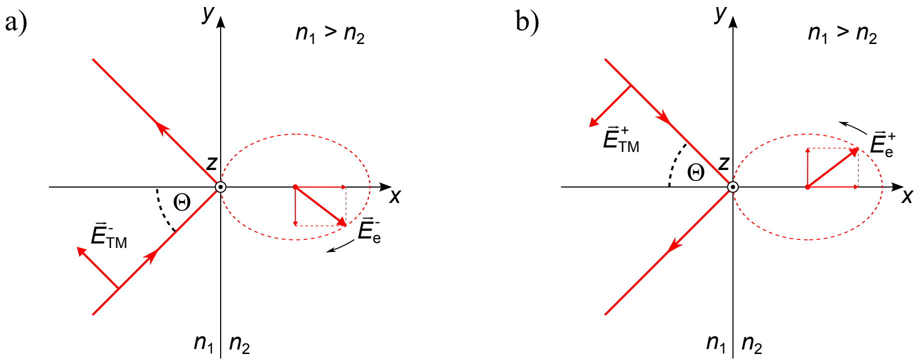
a)
y
$n_1 > n_2$
z
Θ
x
$\vec{E}_{\mathrm{TM}}^{-}$
$\vec{E}_{\mathrm{e}}^{-}$
n_1
n_2
b)
y
$n_1 > n_2$
$\vec{E}_{\mathrm{TM}}^{+}$
Θ
z
$\vec{E}_{\mathrm{e}}^{+}$
x
n_1
n_2

Figure 4.6: Total internal reflection of a TM polarized wave $\vec{E}_{\mathrm{TM}}^{\pm}$ at the interface to an optical thinner medium. The propagation of the evanescent wave along the interface is in the a) positive and b) negative y-direction. In the second medium ($x > 0$) the polarization state of the evanescent field $\vec{E}_{\mathrm{e}}^{\pm} = E_{\mathrm{trans}}\vec{e}_x \pm iE_{\mathrm{long}}\vec{e}_y$ is illustrated, where the rotation sense of the elliptical polarization depends on the propagation direction of the incoming wave. Figures follow Refs. [48, 112].

4.3.1 Polarization of the evanescent field

The properties of the evanescent field have been studied extensively in the context of the Goos-Hänchen effect [113, 114] and in various experiments, e.g, with fluorescence [11] and opto-galvanic spectroscopy [48]. A short summary of these findings will be presented here. In the discussion of the electric field equations of the bottle microresonator in section 2.3.3, it was shown that the solutions of the wave equation can be divided into two orthogonal polarizations: transverse electric (TE) and transverse magnetic (TM). In terms of the more general description of total internal reflection, these polarizations are defined with respect to the plane of incidence spanned by the propagation vector of the light and the surface normal of the interface where the reflection occurs (xy-plane in Fig. 4.6). In this definition, light with a linearly polarized electric field $\vec{E}_{\mathrm{TE}} = E_z \cdot \vec{e}_z$ perpendicular to the plane of incidence, along the basis vector $\vec{e}_z$ in z-direction, is denoted as TE. Light which has a linear magnetic field component perpendicular to the plane of incidence is denoted as TM, having the electric $\vec{E}_{\mathrm{TM}} = E_x\vec{e}_x + E_y\vec{e}_y$ with the basis vectors $\vec{e}_x$ and $\vec{e}_y$ pointing along x and y, as shown in Fig. 4.6.

For the case of an incoming TM or TE polarized light wave, which is totally reflected at a plane interface between two dielectric media, the components of the evanescent field $\vec{E}_{\mathrm{e}}$ relative to the initial amplitude at the interface can be deduced from the Fresnel equations, yielding

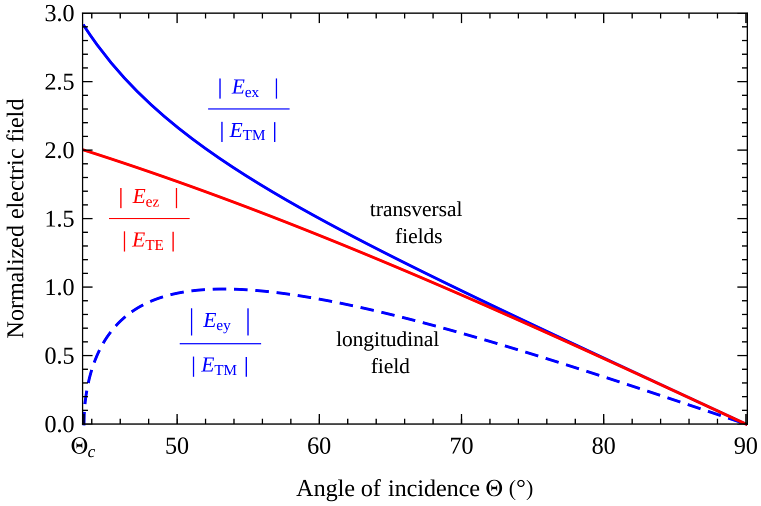

Figure 4.7: Normalized evanescent field components of a TM (blue) and a TE (red) wave at the interface as a function of the angle of incidence Θ following Eqs. (4.16) to (4.18). Solid lines represent transversal field components while the dashed line indicates a longitudinal field. The interface is considered between silica ($n_1 = 1.454$) and vacuum ($n_2 = 1$) yielding a critical angle for total internal reflection of $\Theta_c = 43.45\,°$.

[11,48]:

$$E_{\text{ex}} = \frac{2\cos\Theta\sin\Theta}{\sqrt{n_{21}^4\cos^2\Theta + \sin^2\Theta - n_{21}^2}} E_{\text{TM}} \cdot \mathrm{e}^{-i\delta_{\text{TM}}/2} = E_{\text{trans}}\,, \tag{4.16}$$

$$E_{\text{ey}} = \frac{2\cos\Theta\sqrt{\sin^2\Theta - n_{21}^2}}{\sqrt{n_{21}^4\cos^2\Theta + \sin^2\Theta - n_{21}^2}} E_{\text{TM}} \cdot \mathrm{e}^{-i(\delta_{\text{TM}}+\pi)/2} = -iE_{\text{long}}\,, \tag{4.17}$$

$$E_{\text{ez}} = \frac{2\cos\Theta}{\sqrt{1-n_{21}^2}} E_{\text{TE}} \cdot \mathrm{e}^{-i\delta_{\text{TE}}/2}\,. \tag{4.18}$$

Here, the ratio of the refractive indices is $n_{21} = n_2/n_1$, Θ is the angle of incidence and E_{TM} and E_{TE} are the electric field amplitudes of the incoming waves, respectively. Note that, the evanescent fields for TM and TE polarizations both have a phase shift, δ_{TM} and δ_{TE}, compared to the incoming wave which is further discussed in Ref. [11].

It is important to note that the real part of the wave vector in the evanescent field points along the interface in y-direction (compare section 2.2.2). This means that an incoming TE wave creates a purely transversally polarized evanescent field which is exclusively defined by the component E_{ez}. In contrast, for an incoming wave with TM polarization one obtains an

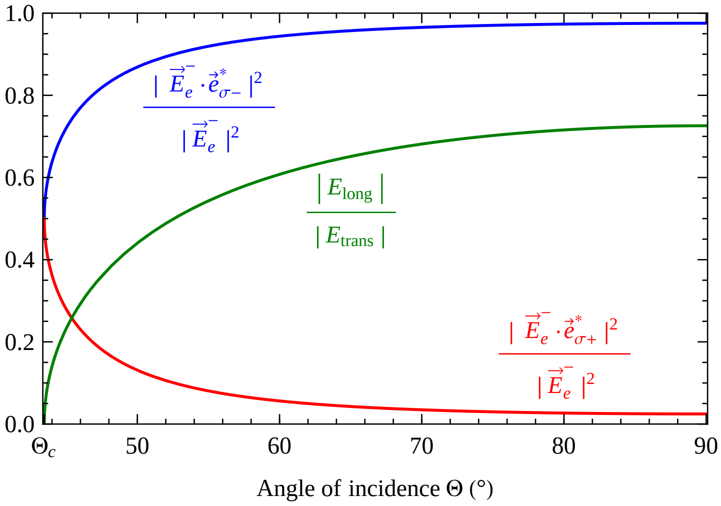

Figure 4.8: Ratio $|E_{\text{long}}/E_{\text{trans}}|$ of the electric field components of the evanescent wave (green) and its overlap $|\vec{E}_{\text{e}}^- \cdot \vec{\epsilon}^*_{\sigma\pm}|^2/|\vec{E}_{\text{e}}^-|^2$ with circularly polarized light $\vec{\epsilon}_{\sigma\pm} = (\vec{e}_x \pm i\vec{e}_y)/\sqrt{2}$ (red, blue) as functions of the angle of incidence Θ for the case of an incoming TM wave totally reflected at at an interface between silica ($n_1 = 1.454$) and vacuum.

evanescent field with a transversal electric field component $E_{\text{ex}} = E_{\text{trans}}$ as well as a longitudinal field component $E_{\text{ey}} = -iE_{\text{long}}$. The latter oscillates parallel to the real part of the wave vector and is $-\pi/2$ out of phase with respect to the transversal component. Figure 4.7 shows the components of the evanescent field as function of the angle of incidence Θ. The magnitude of the evanescent field decreases towards zero when Θ approaches the case of grazing incidence. The longitudinal component E_{long} in y-direction is initially zero for the critical angle of total reflection Θ_{c}, but can reach a significant magnitude for larger angles. In particular, it can become comparable to the transversal component E_{trans}, as it is illustrated in Fig. 4.8. In the limit of $\Theta = \pi/2$ their ratio becomes

$$\left|\frac{E_{\text{long}}}{E_{\text{trans}}}\right| = \sqrt{1 - n_{21}^2}\,, \tag{4.19}$$

which is approximately ≈ 0.73 for the case of an interface between fused silica with $n_1 = 1.454$ and vacuum.

So far, we have not commented on the fact that the longitudinal component is out of phase by $-\pi/2$ with respect to the transverse electric field. Due to this phase difference, the field vector of the evanescent field of TM modes rotates in the plane of propagation. One can calculate the overlap with circular polarized light according to

$$S(E_{\text{e}}, \sigma_\pm) = \frac{|\vec{E}_{\text{e}}^\pm \cdot \vec{\epsilon}^*_{\sigma\pm}|^2}{|\vec{E}_{\text{e}}^\pm|^2}\,, \tag{4.20}$$

with the unit vector of circularly polarized light $\vec{\epsilon}_{\sigma\pm} = (\vec{e}_x \pm i\vec{e}_y)/\sqrt{2}$. According to Fig. 4.6 a), the field vector of the evanescent field propagating along y is $\vec{E}_{\text{e}}^- = E_{\text{trans}}\vec{e}_x - iE_{\text{long}}\vec{e}_y$. The overlap of this field with σ_+ and σ_- polarized light is plotted in Fig. 4.8 as function of Θ for the case of silica. When the incoming wave is nearly parallel to the interface, the overlap can reach values greater than 0.97. Thus, in this case, the evanescent field is almost fully circularly polarized. It is important to note that the electric field does not rotate in a plane transverse to the propagation direction as known from the classical description of circular polarization. Instead, it circulates in the plane of propagation as is indicated by the dashed ellipse in Fig. 4.6.

Finally, let us now consider a TM wave which propagates in the inverse direction, as shown in Fig. 4.6 b). In this case, the evanescent field will have the form $\vec{E}_\mathrm{e}^+ = E_\mathrm{trans}\vec{e}_x + iE_\mathrm{long}\vec{e}_y$ which has a large overlap with σ_+ polarized light. Thus, we note that the inversion of the propagation direction also inverts the rotation sense of the polarization. In the following sections, we will see how this effect modifies the interaction of light and matter.

4.3.2 Longitudinal polarization in whispering-gallery-mode resonators

In WGM resonators, light is confined by continuous total internal reflection. Thus, one also expects a longitudinal polarization component for TM modes, which we actually already encountered in the discussion of the radial wave equation of the bottle resonator in section 2.3.3. We found that TM-polarized WGM modes have two electric field components — A transverse one that points in the radial direction, reading $E_r = -i\partial_\phi H_z / r\omega\epsilon$, and a longitudinal one in the azimuthal direction defined by $E_\phi = i\partial_r H_z/\omega\epsilon$. In analogy to the Fresnels equation, we also find a phase difference between the transversal and the longitudinal components of $\pi/2$ which stems from the differentiation of $H_z \propto \exp(im\phi)$ with respect to ϕ in the expression of E_r. It follows that the field of TM modes is in general elliptically polarized where the exact polarization state is defined by the ratio between the transversal and longitudinal components. In order to study the polarization of TM modes in the bottle resonator, we plot the electric field components E_r and E_ϕ as well as their ratio E_r/E_ϕ as a function of the radial coordinate in Fig. 4.9. Along r, we initially observe a drop of $|E_r|/|E_\phi|$ due to the increasing radial electric field. Accordingly, the mode polarization is transformed from elliptical to perfectly linear at the maximum of E_r where the azimuthal field E_ϕ is zero. Then, however, the azimuthal field increases again and even dominates the radial field close to the resonator surface. Thus, in this region the polarization changes to almost circular. At the interface, E_r undergoes a discontinuity jump and is slightly larger than E_ϕ. Finally, outside the resonator in the evanescent field the ratio between the field components remains almost constant within the considered region.

Figure 4.10 shows a magnification of Fig. 4.9 comprising the region of the evanescent field which is of special interest for the coupling of atoms to the resonator. The exponential decay of the radial and azimuthal components has approximately the same decay length so that their ratio remains almost constant. Furthermore, at the resonator surface, one finds $|E_r|/|E_\phi| = 0.69$. This is close to the value of 0.73 which was obtained in section 4.3.1 for the evanescent field of a TM wave totally reflected under grazing incidence. As a consequence, the overlap of the evanescent field polarization with circular polarized light reaches $S_{E_\mathrm{TM}\sigma_-} = 0.967$, corresponding well to our predictions for the general case of total internal reflection. In particular, one finds that the evanescent field of TM modes is almost perfectly circularly polarized and oscillates in the plane of propagation.

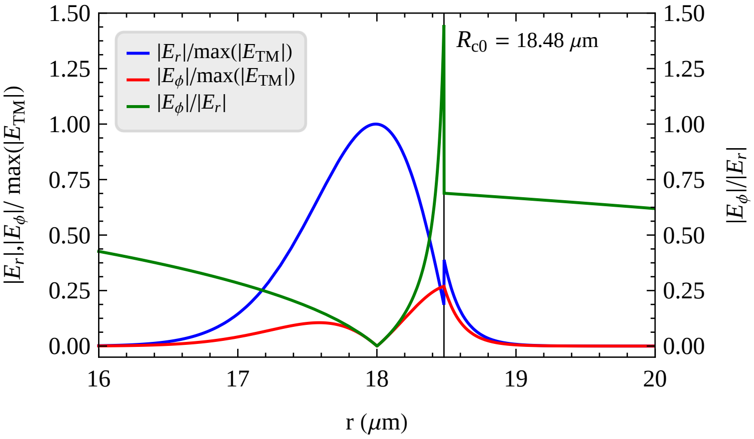

Figure 4.9: Radial (blue) and azimuthal (red) electric field component of the fundamental radial TM mode at $\lambda = 780\,\mathrm{nm}$ with $m = 206$ for a bottle microresonator with $R_0 \approx 18.5\,\mu\mathrm{m}$. The electric field is normalized to its maximum value $\max(|E_{\mathrm{TM}}|)$. The green line represents the ratio $|E_\phi|/|E_r|$ of the two field components. E_r and E_ϕ are defined according to section 2.3.3.

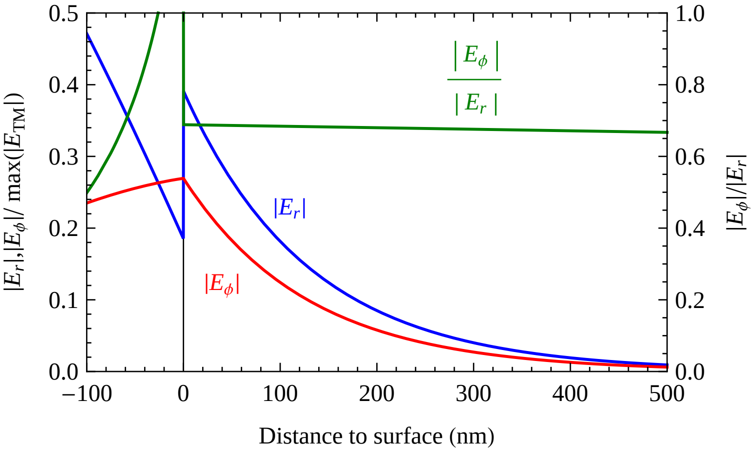

Figure 4.10: Evanescent field relevant for the coupling of atoms to the resonator: Radial (blue) and azimuthal (red) field components of the fundamental radial TM mode as function of the distance to the resonator surface with the same parameters as in Fig. 4.9. The ratio $|E_\phi|/|E_r|$ (green) remains almost constant over the considered region of the evanescent field.

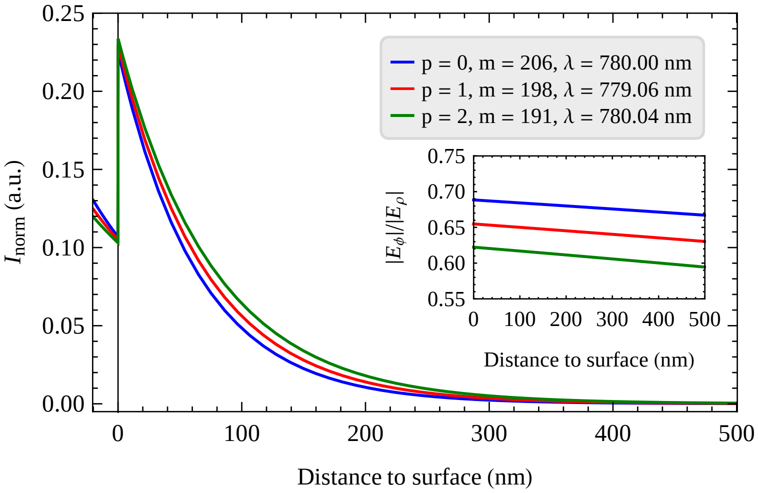

Figure 4.11: Total intensity of the evanescent field for TM modes with increasing radial order p as function of the distance to the resonator surface. The caustic radius of $R_\mathrm{c} = 18.48\,\mu\mathrm{m}$ is kept constant for all modes. Higher order radial modes have smaller m and in general a different resonance wavelength λ_0. The intensity is normalized to the radial power density in analogy to Fig. 2.7. The inset shows the corresponding ratio $|E_\phi|/|E_r|$ of the evanescent field components for the three radial modes.

So far, only the fundamental radial mode was investigated. From an practical point of view it is, however, also interesting to study the properties of the evanescent field for higher order radial modes, because it is difficult to determine their exact angular momentum experimentally. In Fig. 4.11, the intensity of the evanescent field of the fundamental mode is compared with the next two higher order radial modes having all the same caustic radius of $R_\mathrm{c} = 18.48\,\mu\mathrm{m}$. This corresponds to the typical experimental situation where the diameter of the resonator is fixed and higher radial order modes with similar wavelength λ_0 then have smaller angular momentum m.

Interestingly, the evanescent field intensity of radial modes increases with their radial quantum number p. This is surprising at the first sight, since the intensity distribution of higher order radial modes extends deeper inside the resonator and the peak intensity is smaller (compare also Fig. 2.7). This can be explained by the confinement of the higher radial modes which is not as tight as for the fundamental mode so that they are located deeper inside the resonator. In the simplified ray-picture of a WGM resonator, which was discussed in section 2.2.2, this would correspond to smaller angles of incidence. Figure 4.7 shows that in this case the evanescent field is more pronounced than for angles which are very close to the case of grazing incidence. In contrast to the total evanescent field intensity, the ratio $|E_r|/|E_\phi|$ becomes smaller with increasing radial order p. This can similarly be attributed to the fact that higher order radial modes correspond to smaller angles of incidence and therefore have a smaller longitudinal evanescent field component (see Fig. 4.8) Thus, for higher order radial modes, one expects a smaller overlap with circular polarization than for the fundamental radial mode.

4.3.3 Effect of the longitudinal polarization component

The above discussed polarization properties of the evanescent field have major implications for the physical description of WGM microresonators. In what follows, we will see that for TE modes, the common scalar description of the light field is often well justified since they are predominantly transversally polarized.[1] In contrast, for TM modes, the assumption of scalar fields neglects the longitudinal component of the light and leads to a wrong description of the actual field properties. Thus, a vectorial treatment of the electric field is required which can be obtained by an extension of the model of a ring resonator in section 4.2. For this purpose, we introduce two counter-propagating, running waves modes $\hat{a}$ and $\hat{b}$ which we describe now in a vectorial form to account for the transversal and longitudinal components of the TM mode. According to the discussion in section 4.3.1 the sign of the longitudinal component flips when the propagation direction is inverted such that the electric fields of the two modes read

$$\begin{aligned} \vec{E}_a = &\ \left(E_\text{trans}\vec{e}_r + iE_\text{long}\vec{e}_\phi\right) \mathrm{e}^{-i(\omega t - m\phi)} \,, \\ \vec{E}_b = &\ \left(E_\text{trans}\vec{e}_r - iE_\text{long}\vec{e}_\phi\right) \mathrm{e}^{-i(\omega t + m\phi)} \,, \end{aligned} \tag{4.21}$$

where $E_\text{trans} = |E_r|$ and $E_\text{long} = |E_\phi|$ are the transversal and longitudinal components of the electric field in the radial and azimuthal direction with the basis vectors $\vec{e}_r$ and $\vec{e}_\phi$. This vectorial description has immediate consequences for the properties of the mode fields: For a non-vanishing longitudinal, component the polarization states of the evanescent field are elliptical and rotate in opposite sense for counter-propagating modes as shown in Fig. 4.12 a) and b). In particular, for a fixed point in time, the direction of the electric field vector in the evanescent field describes a so-called cycloid in the resonator plane which is illustrated in Fig. 4.12 c).

The effect of the longitudinal field component can be discussed as well in terms of the normal modes. The corresponding superpositions of the electric fields $\vec{E}_\pm = \vec{E}_a \pm \vec{E}_b$ yield

$$\begin{aligned} \vec{E}_+ = &\ \sqrt{2}\left[E_\text{trans}\cos(m\phi)\vec{e}_r + iE_\text{long}\sin(m\phi)\vec{e}_\phi\right] \mathrm{e}^{-i\omega t} \,, \\ \vec{E}_- = &\ \sqrt{2}\left[E_\text{trans}\sin(m\phi)\vec{e}_r + iE_\text{long}\cos(m\phi)\vec{e}_\phi\right] \mathrm{e}^{-i\omega t} \,. \end{aligned} \tag{4.22}$$

A closer look on these fields shows that each vectorial component E_trans and E_long is spatially modulated along the circumference of the resonator. However, the modulation of both components is in quadrature and, as a consequence, the total field vector never vanishes. The exact form of the electric field depends on the ratio between E_trans and E_long. In the case of $|E_\text{long}/E_\text{trans}| = 0$, one simply recovers the situation of the scalar model where the running modes interfere to form two fully intensity modulated standing waves. However, for an increasing longitudinal component E_long, the contrast of the standing wave is diminished. For $|E_\text{long}/E_\text{trans}| = 1$ one finally encounters a situation where the running waves are perfectly circularly polarized with counter-rotating senses of polarization [compare the signs between the vectorial components in Eqs. (4.21)]. In this case, the two counter-propagating modes have orthogonal polarization states ($|\vec{E}_a \cdot \vec{E}_b| = 0$) and, therefore, their superposition is free from any spatial intensity modulation.

---

[1] In special resonator geometries like microdisks and toroids TE modes can also have significant longitudinal field components due to the strong lateral confinement along the resonator axis.

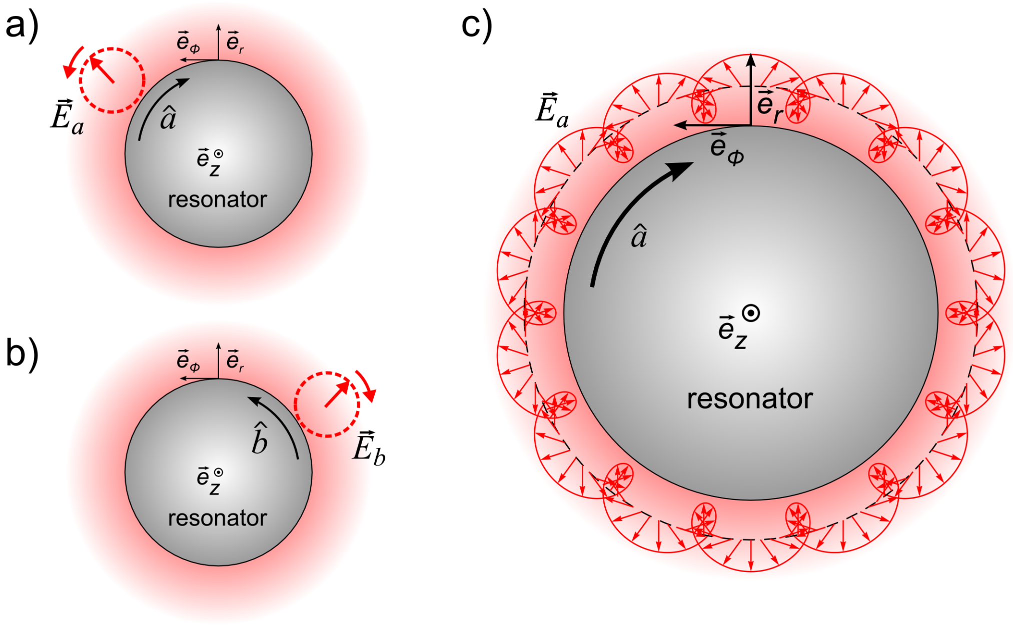

Figure 4.12: a) TM polarized mode propagating clockwise in the WGM microresonator. The red arrows illustrate the rotation sense of the nearly circular polarization of the evanescent field. b) Same as a) but for a counter-clockwise propagating TM mode. c) The polarization vector of the evanescent field describes a cycloid along the circumference of the resonator in the case of perfect circular polarization ($|E_{\text{long}}/E_{\text{trans}}| = 1$).

We find that the evanescent field at a silica–vacuum interface can reach a ratio between the longitudinal and transversal field component of $|E_{\text{long}}/E_{\text{trans}}| = 0.73$ when a TM wave is reflected close to grazing incidence. In this case, the overlap with circular polarization is larger than 0.96, meaning that in WGM microresonators, counter-propagating TM modes of low radial order are nearly orthogonally polarized. Thus, the formation of standing waves in the evanescent field will be decisively suppressed. This becomes apparent in the expression of the visibility of the azimuthal intensity modulation

$$V = \frac{|E_{\text{trans}}|^2 - |E_{\text{long}}|^2}{|E_{\text{trans}}|^2 + |E_{\text{long}}|^2} \approx 0.31\,, \tag{4.23}$$

which would be unity for fully intensity modulated standing waves. Although there is a weak remaining spatial variation of the evanescent field intensity, it is not possible anymore to represent running TM modes in the resonator as a superposition of two fully intensity modulated standing waves.

Thus, we conclude that the longitudinal polarization component renders counter-propagating TM modes distinguishable and therefore prevents their full destructive interference. In this sense, WGM microresonators define a novel type of optical resonator in which the polarization state is intrinsically linked to the propagation direction of the light. In addition, the two almost orthogonal polarization states of counter-propagating TM modes are complemented by the polarization of TE modes. As a consequence, in the evanescent field of WGM resonators, three almost perfectly orthogonal polarization states can exist simultaneously. This leads to a unique situation that is fundamental different from the case of Fabry-Pérot resonators which only support two orthogonal eigen-polarizations.

4.4 Modeling the atom–resonator coupling with arbitrary mode polarization

As we have seen in the preceding section, the assumption that WGM microresonators are conventional ring resonators and that WGM can be described in a standing wave basis is only valid for TE modes. For TM polarization, no intensity modulated standing waves exist and we therefore have to develop a more general model to describe the light–matter interaction in WGM resonators. The non-transversal polarization of TM modes must be incorporated into the formalism of the ring cavity from section 4.2 such that arbitrary mode polarization can be described. However, this generalization also has consequences for the modeling of the atom. If modes with different polarizations are present in the cavity, the assumption of a two-level atom is no longer valid: Depending on the polarization, different transitions in the magnetic sub-structure of the atomic levels are driven which thus has to be included into the modeling.

4.4.1 Derivation of the Hamiltonian

In the discussion of the preceding sections, we found that the evanescent field of TE-polarized WGMs is approximately linearly polarized. TM modes, however, have a large overlap with circular polarization, which oscillates in a plane orthogonal to the TE polarization. Therefore, depending on the excited mode, light with different polarization components is present in the cavity. If we consider a cavity resonant to the $F \to F'$ hyperfine transition of a coupled atom, the polarization of the light will determine which transitions between the Zeeman states with quantum numbers m_F and $m_{F'}$ are driven. Light that is π-polarized relative to the quantization axis will drive transitions with $\Delta m_F = m_F - m_{F'} = 0$ while $\sigma_\pm$-polarized light drives transitions with $\Delta m_F = \pm 1$ as shown in Fig. 4.13 a). Therefore, it is necessary to include the full Zeeman-structure of the atomic levels into the modeling of the system. In a reference frame rotating at the pump light frequency ω_p, the uncoupled part of the Hamiltonian $H_0 = H_\mathrm{a} + H_\mathrm{c}$ then reads

$$\begin{aligned} H_0/\hbar \quad = \quad & \sum_{m_F=-F}^{F} \mu_B g_F m_F B \left|F, m_F\right\rangle \left\langle F, m_F\right| \\ & + \sum_{m_{F'}=-F'}^{F'} (\mu_B g_{F'} m_{F'} B + \Delta_{ap}) \left|F', m_{F'}\right\rangle \left\langle F', m_{F'}\right| \\ & + \Delta_{cp}(\hat{a}^\dagger \hat{a} + \hat{b}^\dagger b) \, , \end{aligned} \tag{4.24}$$

where $|F, m_F\rangle$ and $|F', m_{F'}\rangle$ are the atomic ground and excited states, respectively. Here, we also assume the presence of a magnetic field B that defines the quantization axis and lifts the degeneracy of the Zeeman states. The induced Zeeman shift for each level is $\Delta E_Z/\hbar = \mu_B g_F m_F B$ where μ_B is the Bohr magneton and g_F is the Landé g-factor of the corresponding energy level.

Before deriving the interaction Hamiltonian, we introduce the atomic lowering operator $\hat{d}$ of a multi-level atom for a transition with $\Delta m_F \in \{+1, 0, -1\}$ which can be written as [95]

$$\hat{d}_{\Delta m_F} = \sum_{m_F=-F}^{F} |F, m_F\rangle \langle F, m_F| \, \hat{\mu}_{\text{norm}} \, |F', m_F + \Delta m_F\rangle \langle F', m_F + \Delta m_F| \ , \tag{4.25}$$

where the dipole operator $\hat{\mu}_{\text{norm}}$ is normalized such that for a cycling transition the dipole transition matrix element[2] fulfills $\langle F, m_F| \, \hat{\mu}_{\text{norm}} \, |F', m_F + \Delta m_F\rangle = 1$. From Eq. (4.14), we know the interaction part of the Hamiltonian of a ring resonator coupled to a two-level atom which is

$$H_{\text{int}}/\hbar = g_a \hat{a} \hat{d}_a^\dagger + g_a^* \hat{a}^\dagger \hat{d}_a + g_b \hat{b} \hat{d}_b^\dagger + g_b^* \hat{b}^\dagger \hat{d}_b \, . \tag{4.26}$$

In order to generalize this expression to the case of a WGM resonator interacting with a multi-level atom, we have to assume arbitrary polarization of the cavity modes $\hat{a}$ and $\hat{b}$ leading to atomic operators $\hat{d}_a$ and $\hat{d}_b$ which in general, are not identical anymore. If the modes are polarized in a superposition of π and $\sigma_\pm$ light, atomic transitions with different Δm_F are driven simultaneously. We therefore express the atomic lowering operators $\hat{d}_a$ and $\hat{d}_b$ as a linear combinations of the corresponding polarization-dependent operators from Eq. (4.25)

$$\begin{aligned} \hat{d}_a = & \ \alpha_{\sigma_+} \hat{d}_{+1} + \alpha_\pi \hat{d}_0 + \alpha_{\sigma_-} \hat{d}_{-1} \, , \\ \hat{d}_b = & \ \beta_{\sigma_+} \hat{d}_{+1} + \beta_\pi \hat{d}_0 + \beta_{\sigma_-} \hat{d}_{-1} \, . \end{aligned} \tag{4.27}$$

The complex coefficients α_i and β_i reflect the polarization states of modes $\hat{a}$ and $\hat{b}$. They can be obtained by the projection of the complex unit polarization vectors $\vec{\epsilon}_a$ and $\vec{\epsilon}_b$ of the cavity modes on those of the polarization states π and $\sigma_\pm$ yielding, e.g., for α_{σ_+}

$$\alpha_{\sigma_+} = \vec{\epsilon}_a \cdot \vec{\epsilon}^{\,*}_{\sigma_+} \, . \tag{4.28}$$

Let us now suppose that the magnetic field B which defines the quantization axis points along the resonator axis. Given that the latter is identical to the z-direction, the unit polarization vectors of the atomic eigen-polarizations have the form $\vec{\epsilon}_\pi = \vec{e}_z$ and $\vec{\epsilon}_{\sigma_\pm} = \vec{e}_r \pm i\vec{e}_\phi$. We can now express the interaction Hamiltonian in the basis of the atomic lowering operators from Eq. (4.25). This yields after lengthy but straightforward calculation

$$\begin{aligned} H_{\text{int}}/\hbar = & \ (g_a \alpha^*_{\sigma_+} \hat{a} + g_b \beta^*_{\sigma_+} \hat{b}) \hat{d}^\dagger_{+1} + (g^*_a \alpha_{\sigma_+} \hat{a}^\dagger + g^*_b \beta_{\sigma_+} \hat{b}^\dagger) \hat{d}_{+1} \\ & + (g_a \alpha^*_\pi \hat{a} + g_b \beta^*_\pi \hat{b}) \hat{d}^\dagger_0 + (g^*_a \alpha_\pi \hat{a}^\dagger + g^*_b \beta_\pi \hat{b}^\dagger) \hat{d}_0 \\ & + (g_a \alpha^*_{\sigma_-} \hat{a} + g_b \beta^*_{\sigma_-} \hat{b}) \hat{d}^\dagger_{-1} + (g^*_a \alpha_{\sigma_-} \hat{a}^\dagger + g^*_b \beta_{\sigma_-} \hat{b}^\dagger) \hat{d}_{-1} \, . \end{aligned} \tag{4.29}$$

---

[2] In Ref. [115], the dipole transition matrix elements for the D_2-line of ^{85}Rb can be found which are, however, normalized to $\langle F = 3, m_F = \pm 3| \, \hat{\mu}_{\text{norm}} \, |F' = 4, m_F = \pm 4\rangle = 1/\sqrt{2}$ for $\sigma_\pm$.

Combining Eqs. (4.24) and (4.29) and introducing mode coupling and driving of the mode, the full Hamiltonian of the coupled atom–cavity system finally reads

$$H/\hbar = (H_0 + H_{\text{int}})/\hbar + h\hat{a}^\dagger\hat{b} + h^*\hat{b}^\dagger\hat{a} + i\eta_a(\hat{a} - \hat{a}^\dagger) + i\eta_b(\hat{b} - \hat{b}^\dagger)\,. \tag{4.30}$$

As described in section 4.1.2, the temporal evolution of the system can be determined by the master equation which, including all loss channels, now is

$$\frac{d\rho}{dt} = -\frac{i}{\hbar}[H,\rho] + \kappa\mathcal{D}[\hat{a}]\rho + \kappa\mathcal{D}[\hat{b}]\rho + \gamma\sum_{\Delta m_F=-1}^{1}\mathcal{D}[\hat{d}_{\Delta m_F}]\rho\,. \tag{4.31}$$

4.4.2 Simulations of Rabi spectra with non-transversal polarized light

With the explicit expression of the master equation at hand, it is now possible to investigate the effect of the longitudinal polarization component of TM modes in WGM microresonators and to compare it to the case of TE polarization. For this purpose, we study the spectral behavior of a waveguide coupled WGM resonator which is interacting with a four-level atom. The atomic level scheme shown in Fig. 4.13 a) is the most simple one that supports all three types of possible Δm_F-transitions. The two counter-propagating modes of the resonator are assumed to couple with the same strength to the atom. In order to investigate the influence of the longitudinal polarization component on the transmission spectrum of the system, we initially start with two perfectly transversally polarized TM modes with the unit polarization vector pointing along the radial direction such that $|E_{\text{long}}/E_{\text{trans}}| = 0$. Then, the longitudinal electric field E_{long} is increased successively until it is as large as the transversal field component E_{trans}. In Figs. 4.13 b)-f) the simulated steady state spectra are shown as a function of the polarization of the resonator field using Eq. (4.31). With increasing longitudinal field, one observes a dramatic change of the spectral properties. While for purely transversally polarized modes, the spectrum shows the three characteristic resonance dips of a ring resonator, we recover for the case of equal longitudinal and transversal field amplitudes a two-dip Rabi splitting similar to a single mode cavity. For intermediate longitudinal fields the spectrum shows a transition between the two extreme cases, where the central resonance starts to split as well, while simultaneously the separation of the two outer Rabi peaks is reduced.

The interpretation of the observed behavior is straightforward when the system is described in terms of the normal modes which we introduced in section 4.3.3. According to Eqs. (4.22) one can determine the intensity distribution of the two normal modes which are the symmetric and anti-symmetric superpositions of the running waves in the cavity. For each spectra in Fig. 4.13 the corresponding intensity distribution of the normal modes are illustrated. In the case of zero longitudinal field, two identically polarized, counter-propagating modes occur, which can interfere destructively. As a consequence, the normal modes form a pattern of two standing waves with full intensity modulation, where the nodes of one wave coincide with the anti-nodes of the other wave. The central resonance of the three-dip spectrum in Fig. 4.13 b) provides the evidence of the normal mode that has an intensity node at the position of the atom. When the longitudinal field increases, the running wave modes become distinguishable since the arising elliptical polarization has different sense of rotation for counter-propagating waves. Therefore, the contrast

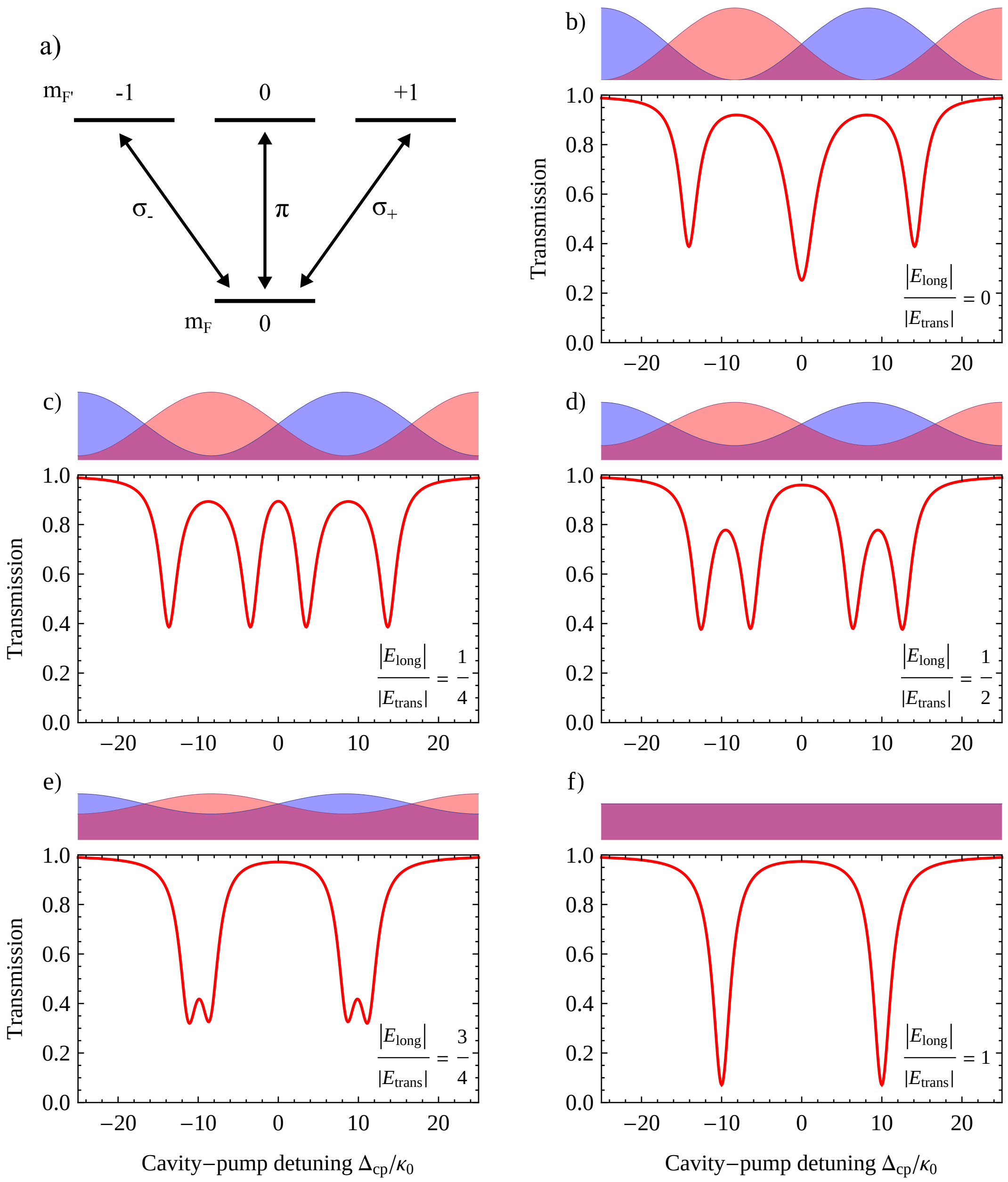

Figure 4.13: Simulated transmission spectra of a ring resonator coupled to a multi-level atom for different ratios of $|E_{\mathrm{long}}/E_{\mathrm{trans}}|$. a) Atomic level scheme indicating the possible transitions between ground and excited states. b-f) Spectra for TM polarization with an increasing longitudinal component. Above each spectrum, the intensity modulation of the two normal modes in the resonator is illustrated according to Eqs. (4.22). Parameters for the plot are $\gamma = \kappa_{\mathrm{ext}} = \kappa_0$, $h = 0$, $\omega_{\mathrm{a}} = \omega_{\mathrm{c}}$ and $g_a = g_b = 10\kappa_0$. Only one of the modes is driven from the waveguide with an on-resonance intra-cavity photon number of 0.01 if no atom is present.

of the standing wave pattern of the normal modes diminishes as illustrated in Fig. 4.13. In this case, even when the atom is located in the node of one of the standing waves, it couples still to the residual field of the corresponding mode. A soon as this field is strong enough to induce a coupling larger than the cavity decay rate, a splitting of the central peak becomes observable. Moreover, the intensity in the anti-nodes decreases when the contrast of the normal modes diminishes. As a consequence, the coupling to the atom is reduced at these points, leading to a smaller separation of the outer Rabi peaks in the spectrum. When the longitudinal field finally reaches the same magnitude as the transversal component, the counter-propagating modes are orthogonally polarized and cannot interfere destructively anymore. Then the normal modes no longer form a pair of intensity modulated standing waves but instead have equal intensity along the resonator circumference. Accordingly, both normal modes couple everywhere equally to the atom and therefore have the same Rabi splitting, as shown in Fig. 4.13 f).

Up to this point, only TM modes haven been considered. However, for TE polarization the simulated spectrum is identical to Fig. 4.13 b) since TE modes are to good approximation transversally polarized such that they obey the predictions for conventional ring resonators.

It should be pointed out as well that the interpretation of the spectral behavior given here did not consider any internal dynamics of the atom. This is valid in the considered case, since the assumed four-level atom has only one ground state. As a consequence, optical pumping effects cannot occur and the spectral behavior can be attributed solely to the intensity distribution of the normal modes. However, in a realistic model of a multi-level atom, optical pumping between multiple ground states is likely due to large overlap with $\sigma_{\pm}$-polarization of the non-transversal resonator modes. Therefore, one expects an even richer spectral behavior when it comes to more realistic multi-level atoms. This situaion will be discussed in detail in the context of the experiments with ^{85}Rb atoms in the next chapter.

The above findings have major implications for the description of WGM resonators. As we see from Fig. 4.13 c), already a weak longitudinal component is able to prevent occurence of the full destructive interference of counter-propagating WGMs. Moreover, in WGM microresonators like the bottle resonator, the longitudinal polarization of the evanescent field is realtively strong, corresponding approximately to the situation shown in Fig. 4.13 e). As a consequence, the drawback of conventional ring resonators that the atom only induces a weak modification of the on-resonant transmission and is only interacting with half of the light in the cavity is avoided for TM-polarized WGMs. On the contrary, when an atom couples to a pair of TM-polarized WGMs, a spectrum similar to the one of a Fabry-Pérot resonator arises. Moreover, since TE-polarized modes show the spectral behavior of a conventional ring resonator identical to Fig. 4.13 b), one can operate a CQED system based on a WGM resonator in both regimes depending on the desired properties.

4.5 Conclusion

In summary, we have seen how the coherent interaction between a single atom and resonator mode can be described by the Jaynes–Cummings model. It is straightforward to extend this formalism to the case of a ring resonator, which supports two counter-propagating running wave modes. This model provided the standard description of light–matter interaction in WGM microresonators so far. However, here, it was demonstrated that this formalism is not sufficient to grasp the full underlying physics of WGMs since it does not account for the non-transversal polarization. Within this chapter, we showed that the longitudinal field is a direct consequence of the guiding of light by total internal reflection in WGM microresonators and that it has important consequence for light–matter coupling. The longitudinal polarization component of TM-polarized WGMs prevents the full destructive interference of counter-propagating modes and thereby avoids the formation of intensity modulated standing wave modes along the circumference of the resonator. This effect is especially pronounced in the evanescent field, which is the interface for coupling atoms to the resonator field.

In order to describe light–matter interaction in this new CQED regime, the Jaynes–Cummings model was extended to allow for arbitrary polarization of the WGMs and to take into account the multi-level structure of atoms. The obtained formalism allows one to predict qualitatively very different and beneficial spectral properties for the coupled atom–resonator system compared to the so far employed model of conventional ring resonators. This becomes evident when considering the on-resonant transmission change that a single atom can induce to the system: It is considerably larger when the non-transversal polarization is included into the description of the system.

Within this thesis, light–matter interaction with WGM has been discussed so far only theoretically. In the following chapters, we test the predictions of our model experimentally with single ^{85}Rb atoms coupled to a bottle microresonator.

CHAPTER 5

Single Atoms Strongly Coupled to Non-Transversal Modes

The coupling of single emitters to WGM microresonators has been studied in numerous cutting-edge experiments comprising sensor applications like molecule detection [81] and particle sizing [82], the demonstration of strong coupling with atoms [80] and quantum dots [101] and the realization of quantum information devices like a photon turnstile [29, 89]. In parallel, important work on the theoretical description of light–matter interaction with WGMs has been published [96–98, 100, 116] opening up a great perspectives for possible future applications. All of this work has in common that the analysis is based on the modeling of WGM microresonators as classical ring resonators where the modes are either described as transversal, linearly polarized fields or simply assumed to be scalar. The discussion typically concentrates exclusively on the case of TE polarized modes for which these assumptions generally correct, depending on resonator geometry, and either omits the case of TM polarization or even assumes that the findings of TE should hold as well for TM modes, making no difference between the two polarizations. However, as we have seen in the theoretical studies in the preceding chapter, the evanescent field of TM modes possess a significant longitudinal polarization component. Since in WGM microresonators the light–matter coupling is established via the evanescent field it should be essential to take the longitudinal field into account for the modeling.

This chapter presents the first systematic experimental studies of the effects arising from the strong coupling between single atoms and non-transversally polarized photons in a WGM microresonator. The chapter begins with an overview of the experimental apparatus which allows us to couple single ^{85}Rb atoms to the modes of a bottle microresonator. In the following, the capabilities to detect single atoms in the resonator mode in real-time are explained and we investigate the lifetime of the atoms in the resonator field. Afterwards, the discussion of the spectral response of the coupled atom–resonator system gives detailed insight into the effect of the non-transversal fields compared to transversally polarized modes. Finally, the results are summarized and their impact for future applications is discussed.

Parts of this chapter have been published in Ref. [90].

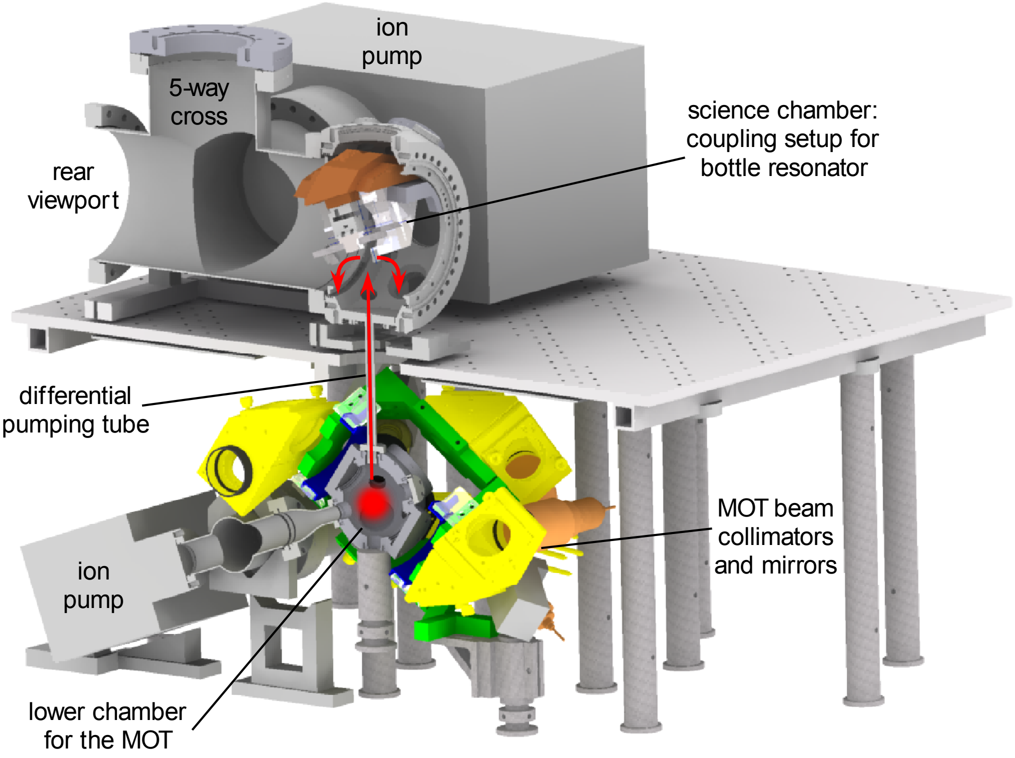
ion pump
5-way cross
rear viewport
science chamber: coupling setup for bottle resonator
differential pumping tube
MOT beam collimators and mirrors
ion pump
lower chamber for the MOT

Figure 5.1: The bottle resonator CQED experiment: Cut through the two-chamber setup. In the lower vacuum chamber a cloud of 10^7 ^{85}Rb atoms with a temperature of 7 μK is prepared in a magneto optical trap and subsequently accelerated upwards. The atomic fountain delivers the cold atomic cloud through a differential pumping tube into the upper science vacuum chamber where the coupling setup for the bottle resonator is situated. The turning point of the cloud trajectory is chosen to be in close proximity of the bottle resonator. The coupling setup allows to access the resonator light field with two ultra-thin fiber couplers which can be controlled with two independent positioning units. Picture following Ref. [117].

5.1 Experimental setup

5.1.1 Overview

In order to realize strong coupling between single atoms and WGMs of a high-Q bottle microresonator, considerable experimental efforts have to be made: To optimize the interaction time between the atoms and the resonator field, the atoms should be as slow as possible, corresponding to very low temperatures. To achieve these low temperatures, laser-cooling techniques are applied which require the experiment to operate under ultra-high vacuum conditions.

Figure 5.1 shows an overview of the main vacuum setup of the CQED apparatus. The system can be divided into two parts: In the lower vacuum chamber a magneto-optical trap (MOT) [118] for ^{85}Rb atoms is created. Then, by a detuning of the cooling light frequency the atomic cloud is accelerated upwards through a differential pumping tube into a second vacuum chamber in which the bottle microresonator is situated. The cloud's trajectory is determined by the initial velocity acting against gravity and can be chosen such that its turning point lies in close proximity of the bottle resonator. Because of this control, the interaction time of the cloud with the resonator light field is maximized. The bottle resonator is placed exactly in the center of the upper vacuum chamber and is interfaced with two ultra-thin coupling fibers which can be moved by piezoelectric translation stages having nanometer resolution.

In addition to the setup shown in Fig. 5.1, the experiment comprises a laser setup and a fiber network which allow to prepare light fields with various detunings and powers for probing the coupled atom–resonator system. High bandwidth intensity modulators are integrated into the fiber network and enable ultra-fast switching of these probing beams. Furthermore, the laser setup provides the beams for the atomic fountain and for the Pound–Drever–Hall lock of the resonator frequency. After the interaction with the bottle resonator, the light guided in the fiber network is detected with single photon counters (SPCMs), which depending on the intended measurement, can be placed at all outputs of the fiber network. Finally, the signals from the SPCMs are time-tagged and evaluated with the aid of field programmable gate arrays (FPGAs) which allow to react in real-time on the coupling of single atoms to the resonator.

In the following section the mentioned components of the CQED setup will be described in more detail.

5.1.2 Vacuum chamber

The vacuum setup is composed of two separate chambers which are connected via a small differential pumping tube as shown in Fig. 5.1. In the chamber on the lower level the MOT is created which serves as source of cold atoms for the atomic fountain. The upper level of the setup carries the so-called "science chamber" with the bottle resonator coupling setup. The differential pumping tube has a diameter of 7 mm and a length of 200 mm and allows to realize different pressures in the two chambers by limiting the particle flow of the residual gas between them.

There are several important reasons for the separation of the vacuum system into these two "zones": First of all, atoms are trapped and cooled in the MOT from the background gas which requires a constant supply of thermal atoms. In our setup these atoms are emitted by rubidium dispensers when a current of several ampere is applied to them. However, this source of hot atoms can be detrimental for WGM microresonators when atoms start to stick to the surface of the resonator, eventually leading to a reduction of the quality factor [89]. It is therefore desirable to isolate the resonator from this source of contamination as good as possible.

In addition, to attain reasonable background gas pressures for the MOT, the vacuum setup has to be baked-out. However, the resonator–fiber coupling setup is rather complex and comprises many technical components like, e.g., positioning stages with adhesive joins, cables and fiber feed-throughs that limit the possible bake-out temperature. The two-chamber setups allows us to bake-out the lower chamber at high temperatures while at the same time keeping the upper chamber at moderate temperatures. In doing so, we can reach pressures low enough to operate a MOT in the lower chamber and maintain the functionality of the resonator–fiber coupling setup in the science chamber.

The lower chamber has six major anti-reflection coated (780 nm) viewports (CF40) through which the MOT beams (with a diameter of 27 mm) enter. In addition, the chamber also has eight smaller openings (CF16) which are used for the connection to the pumps and to the upper chamber, for the electrical connection of the Rb dispensers, for the supply of repumping light of the MOT and for viewports that allow to monitor the MOT with cameras. As shown in Fig. 5.1, the lower chamber is surrounded by a cage-system holding six beam collimators and additional alignment mirrors which create the MOT beams with predefined polarization from two fiber clusters.[1] Moreover, the cage-system also holds the main magnetic field coils of the MOT, while six smaller coils for the compensation of residual magnetic fields are mounted directly around the viewports of the fountain beams at the chamber. The functionality of the atomic fountain is explained in more detail in section 5.1.3.

The upper science chamber is placed on a breadboard above the MOT chamber which is held by metal post that supports the weight of the chamber and pumps. The science chamber itself has two main openings (CF160), where the one at the front is an anti-reflection coated (780 nm) viewport giving optical access to the resonator–fiber coupling setup. The latter is designed such that the bottle resonator is situated exactly in the center of the science chamber and approximately 30 cm above the MOT in the lower chamber. To the rear-opening of the chamber a five-way cross is mounted that is connected to an ion-getter and a turbo pump as well as to another CF160 viewport which allows optical access to the coupling setup from the backside. Furthermore, the science chamber possess two side and one top viewport (CF40) and various small opening (CF16) which serve as cable and fiber feedthroughs. The latter are realized by so-called "swagelok"-tubes with teflon-adapters containing small holes for the fibers. When the swagelok is tightened the teflon adapter is compressed such that the fiber feedthrough is sealed.

Both chambers are connected to a turbomolecular pump, respectively, which allow to evacuate the chambers until the working pressure of two ion-getter pumps[2] is reached. At this point the turbo pumps can be disconnected from the chambers with valves so that the vacuum is maintained solely by the ion-getter pumps, which is desirable to avoid mechanical vibrations of the setup. After several bake-out steps of the vacuum system, a final pressure of approximately 1×10^{-8} mbar is reached in the lower chamber while in the upper chamber the pressure is close to 5×10^{-10} mbar. Further details on the vacuum apparatus of the CQED experiment can be found in Refs. [60, 117].

5.1.3 Atomic fountain

In order to facilitate strong light–matter interactions, single atoms should remain as long as possible in close vincitiy of a bottle mode. Therefore, the ideal solution would be to locate atoms within the mode volume of the resonator in optical traps similar to the case of Fabry-Pérot resonators [119, 120]. Unfortunately, this is a major technical challenge since for the case of WGM resonators, atoms would have to be trapped as close as 100 nm from the resonator surface to enable reasonable coupling rates (see Fig. 5.13). This requirement rules out almost all

---

[1] 3 port cluster, Schäfter+Kirchhoff

[2] VacION Plus Starcell 40 and 300, Varian

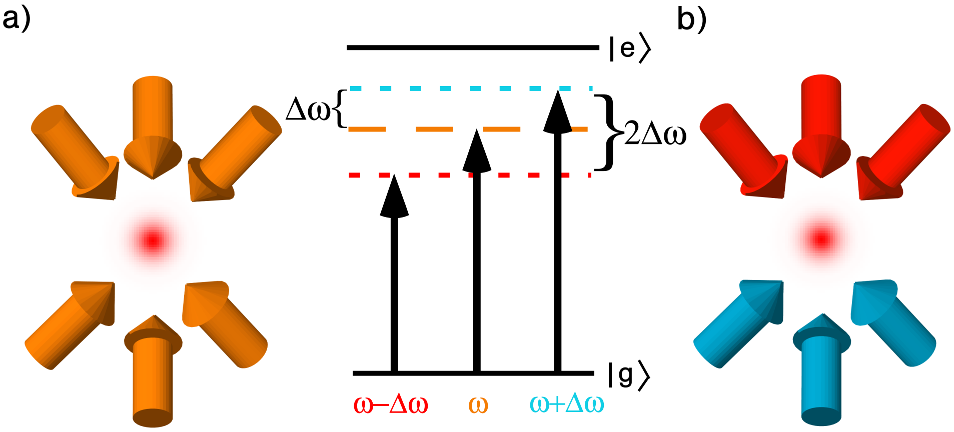

Figure 5.2: Principle of the moving molasses: a) A cloud of ^{85}Rb-atoms is cooled in a MOT formed by six pairwise counter-propagating light beams and an inhomogeneous magnetic field (not shown). All six light beams are red-detuned by the same frequency compared to the optical cooling transitions $|e\rangle \rightarrow |g\rangle$ of the ^{85}Rb-atoms and have the frequency ω. b) When the frequency of the beams from below and above is blue- and red-detuned relative to ω, respectively, the cloud moves upwards. This can be interpreted as a transfer into a moving reference frame in which the cloud is static since the Doppler shift of the light fields exactly cancels the detuning of the two counter-propagating beams. Picture taken from Ref. [117].

state-of-the-art approaches for trapping like, e.g., optical dipole traps for which the ultimate limit of attainable spatial resolution is on the order of the light wavelength allowing only trapping distances of hundreds of nanometers from the resonator surface [38]. Although it has been proposed to circumvent this problem with near field optical dipole traps [8,121], to date trapping of atoms in the mode volume of WGM microresonators has not been achieved. Therefore, the most common procedure for coupling atoms to a WGM resonator has been to release cold atoms from a magneto-optical trap (MOT) or a dipole trap above the resonator [29,80,89,99]. During their passage trough the evanescent field the coupling of individual atoms to the resonator is typically limited to a few microseconds. Here, a similar approach is pursued using an atomic fountain [122,123] well known from atomic clocks [124], which accelerates from below a cloud of cold atoms towards the bottle resonator. The cloud is decelerated by gravity and the turning point of the trajectory is chosen such that it lies close to the resonator. Thereby, in contrast to dropping of a MOT from above, the center of mass of the cloud comes to a halt before it eventually begins its downward acceleration..

Basic concept of the atomic fountain

The working principal of the atomic fountain is illustrated in Fig. 5.2. First, a cloud of cold atoms is prepared in a MOT [118]: With the help of six pairwise counter-propagating light beams an optical molasses of cold decelerated atoms is produced. The beams are aligned in a 1-1-1 configuration, as shown in Fig. 5.2 a), in which all beams have a angle of $\Theta = \cos^{-1}(1/\sqrt{3}) = 54.7\,^\circ$ to the vertical axis. The polarization of the beams is chosen such that counter-propagating beams are always σ_+–σ_- polarized. When the crossing point of the beams is overlapped with the zero point of a magnetic field in the anti-Helmholtz configuration the atoms also feel a spatial dependent force towards the zero-point of the magnetic field. As shown in Fig. 5.2 a) for the atomic fountain the MOT light beams are oriented such that the atoms are pushed towards the center of the trap by three beams from below and three beams from above, respectively. In addition, the MOT requires all beams to be slightly red-detuned from the cooling transition (see level scheme of Fig. 5.2).

After the preparation of a cold atomic cloud in the MOT the magnetic field is switched off and a moving molasses is created, which accelerates the atoms vertically upwards, thereby realizing the atomic fountain. For this purpose, the upper and lower MOT beams are detuned with respect to each other by $2\Delta\omega$. The cloud can be described in a moving reference frame in which the frequency detuning of the beams is cancelled by the Doppler shift which arises from the movement. The initial center-of-mass velocity v_0 of the cloud moving in the vertical direction (here assumed along the coordinate z') can be deduced from the Doppler shift, yielding

$$\Delta\omega t - \vec{k}\vec{r}' = 0 \quad \Rightarrow \quad v_0 = \frac{z'}{t} = \sqrt{3}\frac{\Delta\omega}{k}\,, \tag{5.1}$$

where the factor of $\sqrt{3}$ stems from the 1-1-1 configuration of the MOT beams [117]. On its way upwards gravity will decelerate the atoms until the center-of-mass of the cloud reaches the turning point of its trajectory which is given by

$$h_{\max} = \frac{3}{2}\frac{\Delta\omega^2}{g \cdot k^2}\,, \tag{5.2}$$

with the gravitational acceleration g. Therefore, by choosing the frequency detuning between counter-propagating MOT beams it is possible to precisely control the turning point of the atomic cloud such that it is located at the bottle resonator.

Experimental realization of the atomic fountain

Here, we will limit the discussion of the atomic fountain to the most important parts and parameters of the setup. A detailed description of the setup can be found in Ref. [117]. For the CQED experiment the element ^{85}Rb was chosen for the realization of strong coupling between single atoms and WGMs. This choice has several benefits: First of all, as shown in Fig. 5.3, the D_2 transition of the alkali ^{85}Rb has an excitation wavelength of 780 nm for which is convenient for the operation of semiconductor diode lasers. In addition, single photon counter modules (SPCMs) with high detector efficiency are available at this wavelength. Furthermore, compared to other alkalis the $5^2\mathrm{S}_{1/2}$ ground state of ^{85}Rb has a relatively small hyperfine splitting of

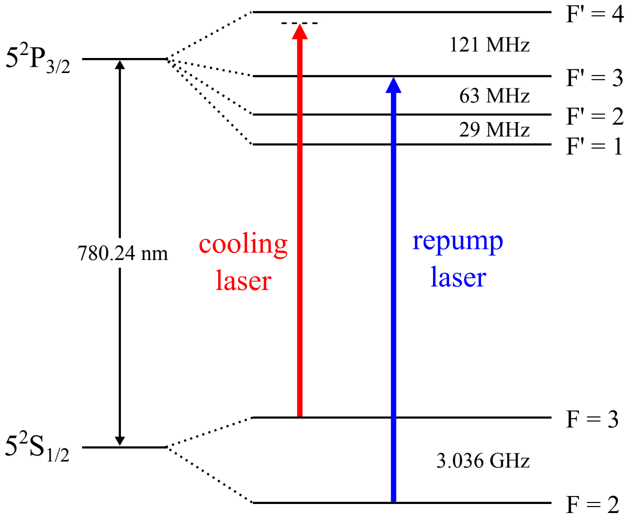

Figure 5.3: Hyperfine structure of the ^{85}Rb D_2-line: The frequencies on the right indicate the energy splitting of the hyperfine levels. The red (blue) arrow illustrates the cooling (repump) transition which is addressed with the laser system to create the magneto optical trap. Note that the cooling laser operates slightly red-detuned from the $|F = 3\rangle \rightarrow |F' = 4\rangle$ transition. Level scheme following Ref. [115].

3 GHz. This is advantageous for light based state manipulation as required, e.g., for optical switching application which are discussed in chapter 6.

The MOT for the atomic fountain operates slightly red-detuned from the $|F = 3\rangle \rightarrow |F' = 4\rangle$ cooling transition of the ^{85}Rb D_2 line (see level scheme in Fig. 5.3). The laser light for the cooling transition is generated with the setup shown in Fig. 5.4. A tapered amplifier[3] (TA) operating at 780 nm provides an output power of 1 W. In order to control the frequency of the upper and lower fountain beams independently, the light is split into two beams that pass through acousto-optic modulators[4] (AOMs) in a double pass configuration, respectively. Thus, the frequency of the laser is shifted by twice the AOM modulation frequency. Due to the double-passage trough a quarter wave plate ($\lambda/4$), which is placed in each beam branch, the polarization is turned by 90 ° such that on its way back the light is reflected at a polarizing beam splitter cube and is subsequently coupled into a polarization maintaining (PM) fiber. The two PM fibers transport the light to the experiment table where the light from each fiber is divided into three beams with a fiber port cluster[5], respectively. The three outputs of each cluster are connected to the MOT beam collimators with PM fibers. Each collimator widens the beam diameter to 27 mm and transforms the light to circular polarization with a quarter wave plate. The cage system shown in Fig. 5.1 holds all six collimators such that the beams enter into the lower vacuum chamber under the desired angle of $54.7\,°$. An internal photo diode in the fiber cluster monitors the input power and

---

[3] Serval Plus, Sacher Lasertechnik

[4] all AOMs in the experiment are of type AOMO 3200-124 with 200 MHz center frequency, Crystal Technology

[5] 3 port cluster, Schäfter+Kirchhoff

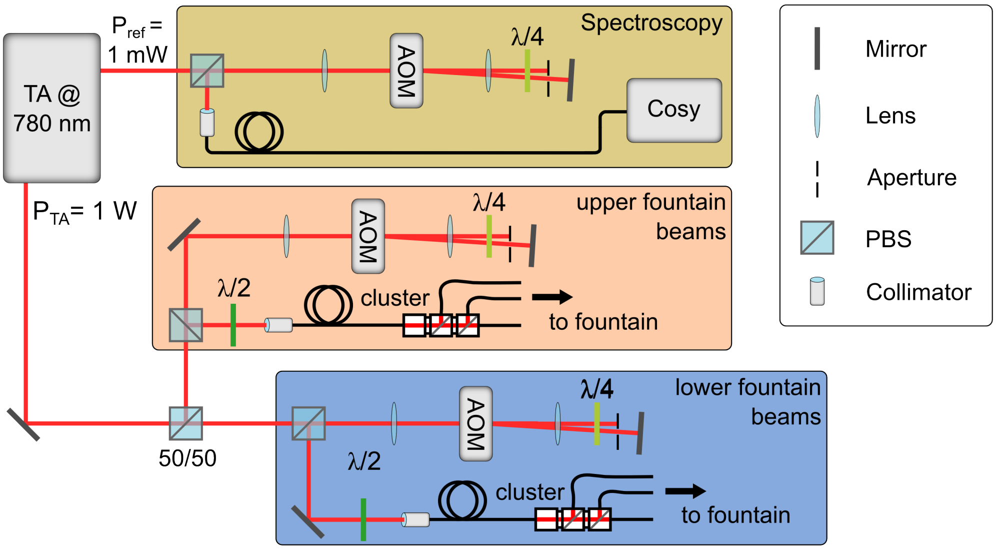

Figure 5.4: Simplified laser setup for the main beams of the atomic fountain: The light from a tapered amplifier (TA) is split up at a semi-transparent beam splitter cube (50/50) and passes in each branch through an acousto-optic modulator (AOM) in the double-pass configuration. Polarizing beam splitter (PBS) cubes branch off the light towards polarization-maintaining fibers which transfer it to the fiber clusters where the upper and lower fountain beams are created. A weak reference beam of the TA passes as well through an AOM and before it is send to a fiber-coupled Rb spectroscopy setup (Cosy) for laser frequency stabilization.

serves to provide the error signal for an intensity stabilization which controls the radio-frequency (RF) power sent to the AOMs in the upper and lower fountain beam branches, respectively. This allows us to control the power of the fountain beams with a bandwidth of 50 kHz up to a maximal power of about 20 mW. The RF signal for the AOMs are generated by two direct digital synthesizer (DDS) sources[6] that allow to drive arbitrary predetermined frequency ramps upon a trigger signal.

The TA is seeded from a master laser which is a grating stabilized external cavity diode laser (ECDL) in Littman/Metcalf configuration and has 13 mW output power. A small part of the master laser light is separated before the TA diode and serves as reference beam for the frequency stabilization of the laser. As shown in Fig. 5.4, the reference beam is shifted in frequency similar to the fountain beams with an AOM in double-pass configuration and is then directed to a fiber-coupled Doppler-free Rb saturation spectroscopy setup.[7] To lock the laser to the $|F=3\rangle \to |F'=4\rangle$ transition, the spectroscopy light is frequency modulated with $\nu_{\text{mod}} = 570\,\text{kHz}$ in the AOM. The obtained spectroscopy signal is then demodulated with ν_{mod}, creating thereby an error signal with a zero crossing at the $|F=3\rangle \to |F'=4\rangle$ transition. The

---

[6] AODS 20160 STD, Crystal Technology

[7] Cosy, TEM Messtechnik

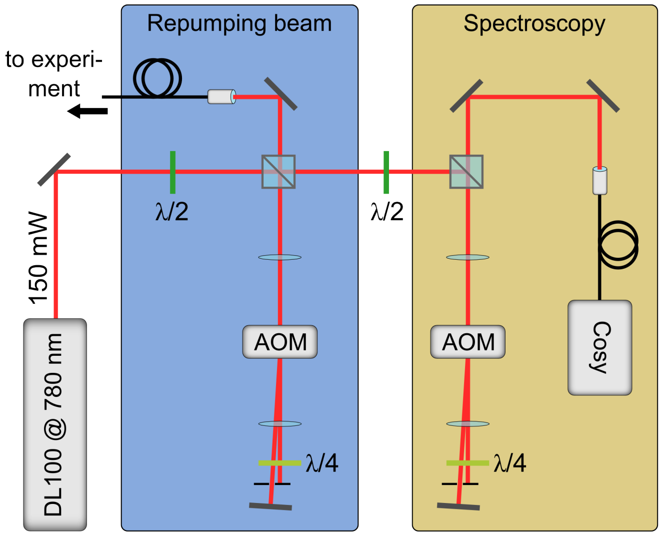

Figure 5.5: Laser setup for the MOT repumper: The light from an ECDL with 150 mW of output power is split up into the repumper branch and a branch for the Rb spectroscopy. Both beams are shifted in frequency with AOMs in double-pass configuration and are subsequently fiber-coupled. For symbol definition see Fig. 5.4.

error signal serves as input for a PID-servo which gives feedback to the grating of the master laser to lock the laser frequency. Due to the AOM in the spectroscopy branch, the frequency of the TA has an offset to the $|F = 3\rangle \rightarrow |F' = 4\rangle$ transition. However, this can be compensated with the AOMs in the branches for the upper and lower fountain beams and allows to set any desired offset frequency between the fountain light and the $|F = 3\rangle \rightarrow |F' = 4\rangle$ transition.

Although the $|F = 3\rangle \rightarrow |F' = 4\rangle$ cooling transition is closed, some atoms will be excited off-resonantly to the $|F' = 3\rangle$ level of the excited state from where they can decay into the $|F = 2\rangle$ ground state and are thus lost from the cooling cycle (see Fig 5.3). In order to bring the lost atoms back into the cooling cycle, additional repump light, resonant to the $|F = 2\rangle \rightarrow |F' = 3\rangle$ transition, is required. The setup of the repump laser is shown in Fig. 5.5. The laser source is a grating stabilized ECDL[8] running at 780 nm with 150 mW of output power. The laser beam is divided into two parts which both pass through AOMs in the double-pass configuration. One beam is coupled into a standard optical fiber and transferred to the experiment table. There, a collimator directs the repump light beam with a diameter of about 13.5 mm trough a viewport of the lower vacuum chamber onto the MOT region. The power of the beam is typically set to several mW. The second beam of the laser setup is coupled to a Rb spectroscopy unit. In contrast to the TA setup, the frequency lock of the repump laser simply uses the side of the $|F = 2\rangle \rightarrow |F' = 3\rangle$ spectroscopy resonance as error signal which is fed back to the grating of the ECDL with a PID circuit. Since the frequency precision of the repump light is less critical for the performance of the MOT this locking method is sufficient although the derived error signal is less stable than the RF spectroscopy.

---

[8] DL 100, Toptica Photonics

To create the MOT, a current of about 3 A is applied to the rubidium dispenser in the lower vacuum chamber while a current of 6 A runs through the anti-Helmholtz coils around the chamber. The resulting inhomogeneous magnetic field has a gradient of about 5 G/cm along the main axis and 2.5 G/cm along the perpendicular axes. The six fountain beams each have a power of 18 mW and are red-detuned by 14 MHz from the $|F=3\rangle \rightarrow |F'=4\rangle$ cooling transition. When the repump beam is turned on, a cloud of cold atoms with a diameter of about 1 mm forms at the center of the vacuum chamber with a loading rate of 1.88×10^8 atoms/s and typical maximal atom numbers of 5×10^7. The lifetime of the MOT is about 0.3 s where the limit is mainly set by collisions with the atoms from the background gas.

After the MOT has been loaded the atomic cloud is transferred to a moving molasses. For this task, the magnetic field is switched off and the frequencies of the lower and upper fountain beams are linearly ramped with a slope of $1\,\mathrm{MHz/ms}$ to a detuning of $\Delta\omega = \pm 2\pi \cdot 3.54\,\mathrm{MHz}$ compared to their initial MOT frequency. To reduce the temperature of the now moving atomic cloud further, a polarization gradient cooling (PGC) step is performed. The cooling effect of PGC arises from the σ_+–σ_- polarization configuration of the MOT beams which leads to a stronger scattering of counter-propagating photons by a multi-level atom compared to co-propagating photons [125]. To establish optimal PGC conditions the lower and upper fountain beams are red-detuned within 0.3 ms by 50 MHz from the $|F=3\rangle \rightarrow |F'=4\rangle$ transition while their relative detuning of $2\Delta\omega$ is kept constant. Simultaneously, also the power per beam is reduced to one third of the initial value. These settings are then maintained until the atomic cloud has left the fountain beams. The repump light is on during the whole procedure.

Characterization of the fountain

In order to characterize the atomic fountain, time-of-flight measurements (TOF) are performed on the upward moving atomic cloud in the science chamber. For this purpose, an elliptical light beam (light sheet) with beam diameters of 18 mm and 0.5 mm resonant with the $|F=3\rangle \rightarrow |F'=4\rangle$ transition transverses the science chamber slightly below the bottle resonator. The fluorescence emitted when the atomic cloud passes the light sheet is detected with a photomultiplier and a typical trace is shown in Fig. 5.6. When the initial velocity of the atoms is chosen high enough, the atomic cloud passes the light sheet two times, once while it is moving upwards, and once again while it is falling down. Thus, one observes two fluorescence peaks in Fig. 5.6 corresponding to the upward and downward moving atoms.

During its trajectory the atomic cloud expands from its initial diameter in the MOT of $D \approx 1\,\mathrm{mm}$ due to its residual temperature. Therefore, the temporal width of the fluorescence peaks is a measure of the temperature of the atomic cloud and the fluorescence signal can be fitted with the function [126]

$$f(h,t) = \frac{a_0}{\sqrt{2\pi}\sigma(t)} \left[1 - \exp\left(-\frac{\rho^2}{2\sigma^2(t)}\right)\right] \exp\left(-\frac{(h - v_0 t + \frac{1}{2}gt^2)^2}{2\sigma^2(t)}\right), \qquad (5.3)$$

where h is the distance between the MOT position and the light sheet. The amplitude a_0 is proportional to the atom number in the cloud and the normal distribution in the square brackets

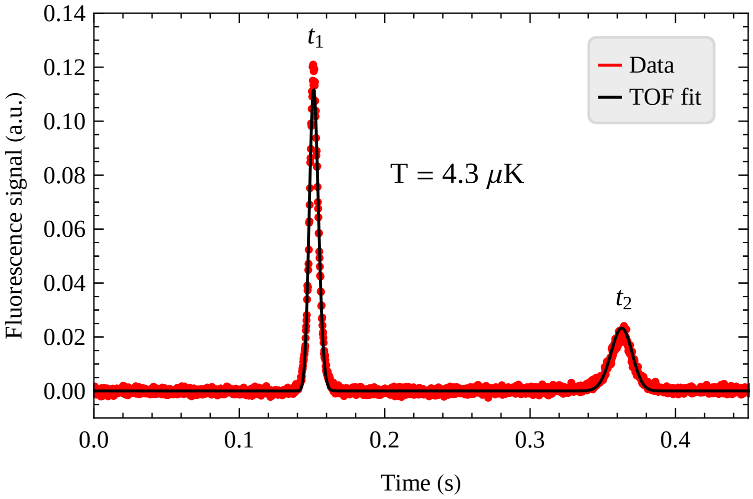

Figure 5.6: Time-of-flight measurement of the atomic fountain: Fluorescence signal of the upward (t_1) and downward (t_2) moving atomic cloud averaged over eight launches. The time trace is put together from two independent fountain cycles where for detection of the down falling cloud the light sheet is switched off for the first 0.2 s since otherwise the atoms would be heated away on their upward trajectory.

with ρ reflects the probability to loose atoms during the two detection phases, which occurs, e.g., when the cloud becomes broader than the diameter of the light sheet. The dependence on the cloud temperature T enters via the diameter of the cloud which is

$$\sigma(t) = \sqrt{D^2 + \frac{k_\mathrm{B}T}{m}t^2}\,, \tag{5.4}$$

with the Boltzmann constant k_B and the atomic mass m.

For the fountain parameters described in the preceding section, temperatures in the range 4 to 7 μK are extracted from TOF measurements [117]. The resonator is located $s = 30\,\mathrm{cm}$ above the MOT. Therefore, if the turning point of fountain trajectory is chosen to lie exactly at the resonator, the atomic cloud requires $t = \sqrt{2s/g} \approx 247\,\mathrm{ms}$ to cover the distance. In this time the cloud expands according to Eq. (5.4) to a diameter of 6.5 mm with a corresponding maximal mean density of $3 \times 10^8\,\mathrm{atoms/cm^3}$, if one assumes that all atoms from the MOT are transferred to the moving molasses.

5.1.4 Vacuum-compatible resonator–fiber coupling setup

In order to transfer light into and out of the bottle resonator via the evanescent field, ultra-thin fiber couplers are brought as close as several hundred nanometers to the resonator surface. Moreover, the resonator–fiber separation must be controlled on the nanometer scale to allow stable coupling conditions between the devices which, in addition, have to be operated under ultra-high vacuum conditions. To exploit the full potential of the bottle resonator as an add-drop

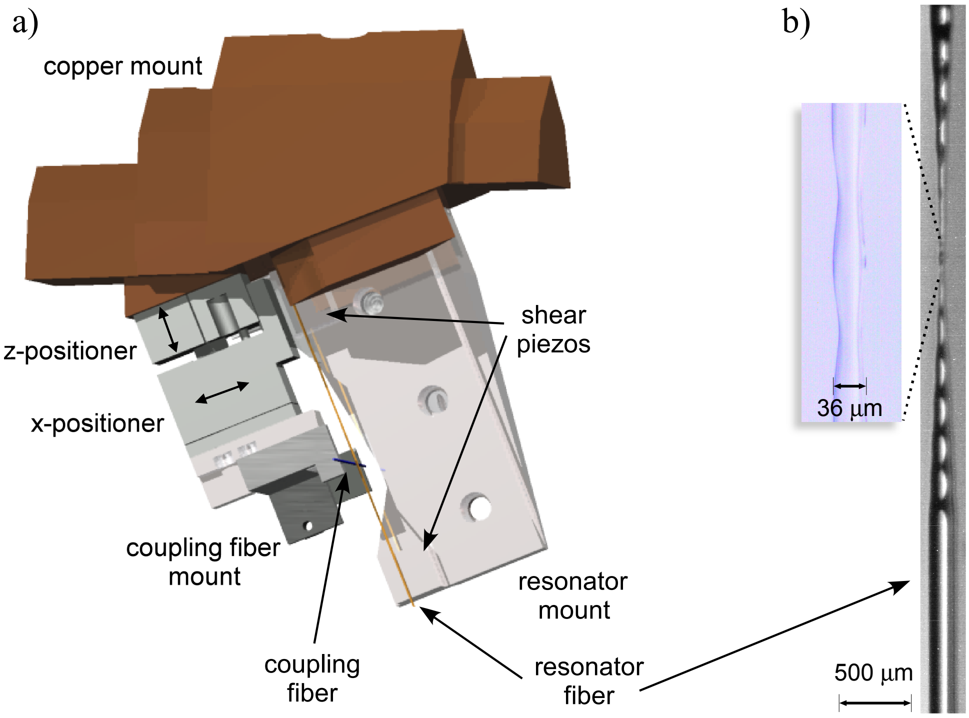

Figure 5.7: a) Overview of the resonator–fiber coupling setup: A massive copper mount serves as basis for the setup which is oriented top-side-down in the science chamber. The bottle resonator frequency can be tuned with two shear piezo actuators. The ultra-thin fiber is moved with two nano-positioning stages along (z-positioner) and perpendicular to (x-positioner) the resonator axis. The setup comprises a second ultra-thin fiber coupling unit with the same degrees of freedom which is left out here for clearer presentation. b) Micrograph of the bottle resonator fiber with the taper-transitions to the resonator region which is shown in a magnified view. Figures adapted from Refs. [127] and [60].

device, it should also be possible to couple two ultra-thin fibers simultaneously to the resonator. Thus, the resonator–fiber coupling setup has to fulfill several demanding requirements and is presented here briefly while more informations can be found in Refs. [60, 127].

Figure 5.7 a) illustrates the main parts of the coupling setup. The whole system is designed in a top-side-down configuration and is mounted in the upper part of the science chamber to allow free optical access to the upward moving cloud of the atomic fountain. The base of the setup is a massive gold-coated copper mount (2 kg) which rests on two metal beams in the chamber. Viton rings, placed in between the copper mount and the beams, provide an isolation against external mechanical vibrations of the setup.

The fiber of the bottle resonator is glued onto two shear piezo actuators on an aluminum mount. The piezo actuators have a travel range of $10\,\mu$m, respectively, and allow to tune the resonance frequency of the bottle resonator. The mount is aligned such that the resonator axis is tilted by an angle of 20° from the vertical axis. The dimensions of the whole setup are chosen such that the bottle resonator is located in the center of the science chamber, exactly above the atomic fountain.

The bottle resonator for the CQED experiment is fabricated with the fiber pulling rig according to the description in section 2.3.1. The initial resonator fiber[9] has a diameter of $200\,\mu\mathrm{m}$ and is tapered down to $36\,\mu\mathrm{m}$ over a length of 6 mm as shown in Fig. 5.7 b). After the microstructuring processing step with the CO_2-laser the curvature of the bottle resonator is measured to be $0.014\,\mu\mathrm{m}^{-1}$. The spectral characterization of the bottle resonator is presented in section 5.2.

The setup is designed to couple two ultra-thin fibers simultaneously to the bottle resonator. The two fibers are aligned skew to each other and cross the bottle resonator fiber under an angle of 90°. Each fiber is glued on a mount which has a bending piezo actuator with a travel range of 5 mm at one end to enable the tensioning of the fiber. The fiber mount is connected to two stacked nano-positioning units[10] which control the fiber position in two axes, i.e., along and towards the resonator. The positioning units can be operated in two different modes: In the so-called “slip-stick mode” the positioning unit is moved in discrete steps of given size and frequency. Thereby, the coupling fiber can travel over a distance of up to 5 mm which allows a coarse positioning at the resonator. However, each step excites mechanical vibrations of the coupling fiber such that the fiber could come in contact with the resonator if their separation is too small. To avoid this contact, the positioning units are operated in a scanning mode as soon as the resonator–fiber separation is small enough. In this mode an internal piezo actuator allows to scan the fiber position continuously over a range of $4\,\mu\mathrm{m}$, which is sufficient for the fine adjustment at the resonator.

Both ultra-thin fibers have a minimal diameter of 500 nm and are tapered down from standard optical single-mode glass fibers[11] with an initial diameter of $125\,\mu\mathrm{m}$. In order to adapt the propagation constant of light in the evanescent field of the fiber as close as possible to the one of the bottle resonator, the fiber is not aligned exactly with the ultra-thin part at the resonator but rather in the region where the transition to the tapered region occurs. In this way, it is possible to optimize the coupling by moving the fiber along the resonator axis. In doing so, one effectively changes the fiber diameter and the propagation constant of the light in the section which couples to the resonator. We determined the transmission of both ultra-thin fibers including the taper-transitions in the setup to be larger than 95 % (for more details see section 5.1.6).

5.1.5 Guiding magnetic field at position of the bottle resonator

At the position of the bottle resonator a guiding magnetic field can be applied via a single coil, which is placed on the top of the science chamber. The coil has six windings and an inner diameter of 18 cm. Figure 5.8 a) illustrates the positioning of the coil relative to the bottle resonator where the center of the axis of the coil is aligned with the resonator axis. The main purpose of the single coil is to create a well defined magnetic field at the resonator which overcomes other

---

[9] PWF 200 T, Ceramoptik

[10] ANPx101/NUM and ANPz101/NUM, attocube systems

[11] F-SF, Newport

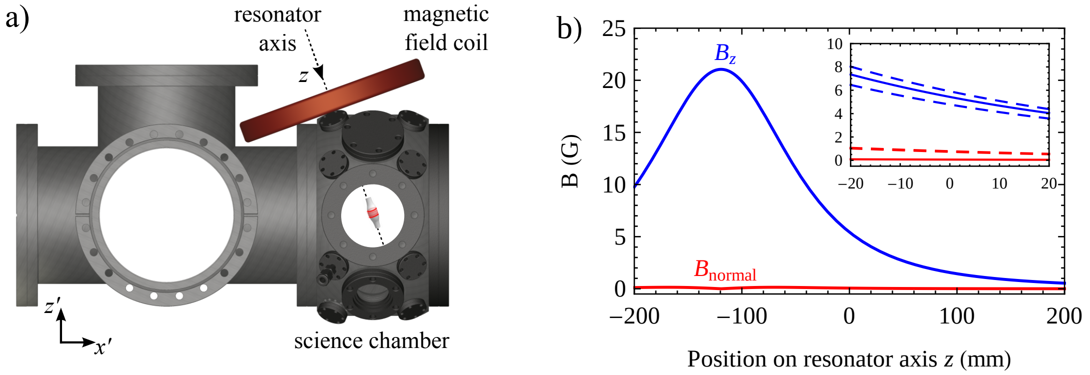

Figure 5.8: Guiding magnetic field: a) Position of the field coil at the science chamber. The axes of the coil and the resonator are parallel. b) Magnetic field parallel (B_z, blue) and normal (B_{normal}, red) to the resonator axis. The position of the resonator is approximately at $z = 0$. This region is magnified in the inset where the dashed lines assume a displacement of $\pm 20\,\text{mm}$ along x' between the resonator and the coil axis.

interfering magnetic fields originating, e.g., from the ion-getter pumps or the earth's magnetic field. The coil induces an in-homogeneous and rather weak B-field which is, however, designed and aligned parallel to the resonator axis such that over the length of the bottle resonator the field is approximately constant. In Fig. 5.8 b) the magnetic field strength parallel and normal to the resonator axis is calculated as a function of the position on the resonator axis. With an applied current of 55 A the parallel magnetic field at the resonator position ($z = 0$) reaches a value of $B_z \approx 5\,\text{G}$ whereas the normal field B_{normal} is negligible. However, the alignment of the coil relative to the resonator is not very accurate such that deviations from this ideal situation have to be expected. Therefore, in the inset of Fig. 5.8 b) the fields are shown also for a displacement between the resonator and the coil axis of $\pm 20\,\text{mm}$ along the horizontal direction (x'). The misalignment would result in a weak B-field normal to the resonator axis with $B_{\text{normal}} \approx 0.15 B_z$. An error in the angular alignment of the coil of $\pm 5\,^\circ$ would give a normal B-field of similar order. In addition, if one also assumes that the position of the resonator along the resonator axis is known only with the same precision the actual magnetic fields would range between $3 - 8\,\text{G}$. Measurements of the Zeeman level shift of atoms close to the resonator suggest that the axial B-field is rather at the lower edge of this range and has approximately a value of $B_z \approx 3\,\text{G}$ when a current of 55 A is applied to the coil (see section 5.4.2). In any case, we can conclude from the inset of Fig. 5.8 b) that the gradient of the axial B-field is small, having a value of $\partial_z B_z \approx 80\,\text{mG/mm}$. As a consequence, over the axial extension of typical bottle modes $\Delta z \lesssim 20\,\mu\text{m}$ the magnetic field can be assumed to be constant. The configuration has to be seen as an interim solution as the first design of the CQED setup did not include magnetic field coils for the science chamber. For future experiments much stronger magnetic fields will be required in the science chamber. Therefore, new field coils have been designed which will be implemented into the setup [128].

In order to estimate strength of interfering magnetic fields originating from other sources like, e.g., the ion pumps at the position of the resonator, we measured at different points around

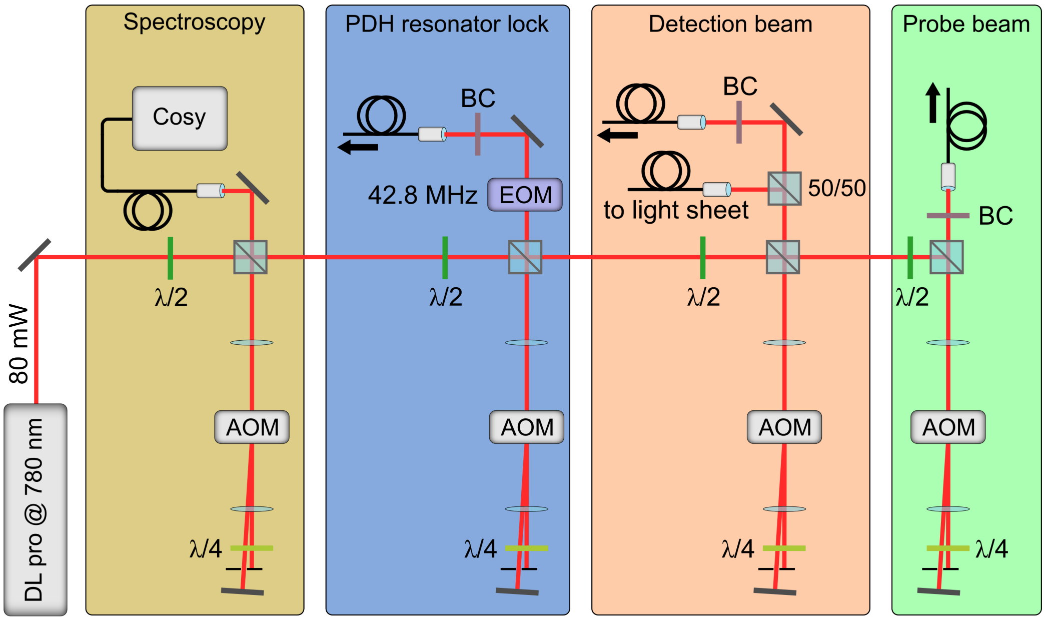

Figure 5.9: Simplified laser setup for the bottle resonator spectroscopy: The light from an ECDL with 80 mW output power is divided into multiple beams which can be controlled individually in amplitude and frequency with AOMs in double-pass configuration. For the Pound–Drever–Hall frequency lock of the bottle resonator, an electro-optical modulator (EOM) with 42.8 MHz is placed in the corresponding branch. The detection, probe and resonator lock beams are coupled into polarization-maintaining (PM) fibers where the polarization in front of the fibers is adjusted with help of Berek compensators (BC). Then, the PM fibers transfer the light into the fiber network of the bottle microresonator. For symbol definitions, see Fig. 5.4.

the science chamber with a Gauss meter.[12] Assuming linear gradients between the measurement points we infer a magnetic field of 1.27 G along and 1.16 G normal to the resonator axis from the measurement.

5.1.6 Resonator laser setup and fiber network

In order to probe the bottle resonator in the CQED setup, several light beams are required: First of all, the resonance frequency of the resonator has to be stabilized to the ^{85}Rb D$_2$-transition. As we will see later on, it is also necessary to detect atoms at the resonator with light of certain frequency and power while probing of the coupled atom–resonator system after the atom detection eventually is performed with other frequency and power settings. Therefore, separate detection and probing light fields are required.

---

[12] Model 6010, Sypris

Laser setup

In Fig. 5.9 the laser setup for the resonator is depicted which creates all required beams. The laser source is a grating stabilized ECDL[13] running at 780 nm with an output power of 80 mW. From the laser several beams are derived which all pass through AOMs in double-pass configuration to allow the individually control of amplitude and frequency for each beam. The first beam is coupled to a Rb spectroscopy cell to stabilize the ECDL to the $|F = 3\rangle \rightarrow |F' = 4\rangle$ transition of the D_2-line. For this purpose, the same frequency modulation technique as for the MOT laser is applied to create an error signal (see section 5.1.3) which is then fed back using a PID-servo to the piezo actuator of the laser grating.

The second beam is used to create a locking signal for the bottle resonator frequency, which should be stabilized to the laser frequency with the help of the PDH technique following the procedure described in chapter 3.1.1. For this purpose, the beam passes a resonant electro-optic modulator (EOM) where it is phase-modulated with a frequency of 42.8 MHz to create the frequency sidebands required for the PDH lock. Afterwards, the beam is coupled into a PM-fiber and transferred into the bottle resonator fiber network (see following section). A Berek compensator in front of the fiber allows to adjust the polarization precisely to the input polarization of the PM fiber.

The detection and probing beams are derived in a similar manner from the laser light and are transferred as well to the bottle resonator network in PM-fibers. Before the detection beam is fiber-coupled, half of the light is branched off with a beam splitter to supply the light sheet for the TOF measurement of the atomic fountain.

With the help of the double-pass configuration, an arbitrary detuning relative to the $|F = 3\rangle \rightarrow |F' = 4\rangle$ transition of ^{85}Rb can be set for each beam. Moreover, it allows to actively stabilize the power of the resonator lock, the detection and the probe beam.

Bottle resonator fiber network

The light from the laser setup is transferred into a fiber network which has two purposes: First of all, it allows to prepare and control the light fields which are sent to the bottle resonator, and secondly it efficiently directs the light which has interacted with the resonator to the detectors. Figure 5.10 gives an overview of the components in the fiber network. The central parts of the network are the two fibers with ultra-thin sections used to interface the bottle resonator evanescently which we denote from now on as coupling fiber 1 and 2. The two coupling fibers leave the vacuum chamber of the CQED experiment via teflon feed-throughs and are connected to a larger fiber network outside the chamber.

The light which is used to lock the resonator frequency first passes a fiber-based 50/50-beamsplitter where half of the light is redirected to a photodiode (PD). The PD signal serves as error signal for an intensity stabilization which acts on the corresponding AOM in the laser setup. The rest of the light passes through a fiber bench in which it is coupled out to a freely propagating beam over a small distance before it is fiber-coupled again. Inside the fiber bench a half- ($\lambda/2$) and a quarter-wave ($\lambda/4$) plate allow to manipulate the polarization of the light. Afterwards, the light path is combined with the detection and probe fields on a 99/1-beamsplitter before it

---

[13] DL pro, Toptica Photonics

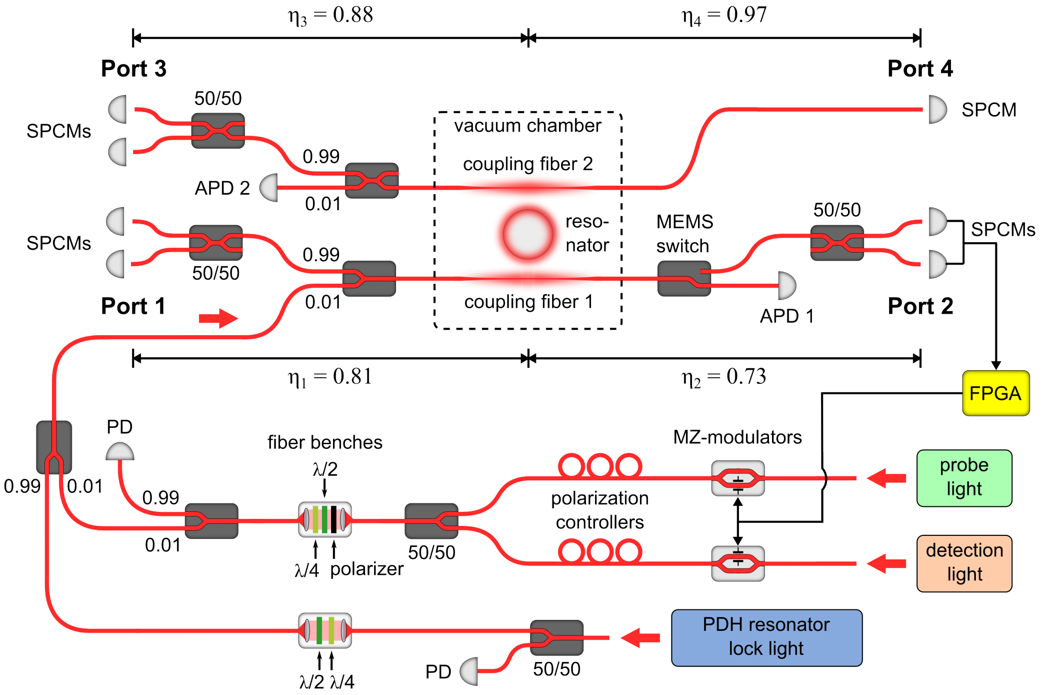
η3 = 0.88
η4 = 0.97
Port 3
Port 4
50/50
SPCMs
SPCM
vacuum chamber
0.99
coupling fiber 2
APD 2
0.01
reso-
nator
MEMS
switch
50/50
SPCMs
SPCMs
50/50
0.99
0.01
coupling fiber 1
APD 1
Port 1
Port 2
η1 = 0.81
η2 = 0.73
FPGA
PD
fiber benches
λ/2
MZ-modulators
0.99
0.01
0.99
polarization
controllers
probe
light
0.01
λ/4 polarizer
50/50
detection
light
PDH resonator
lock light
λ/2 λ/4
PD
50/50

Figure 5.10: Bottle resonator fiber network for light preparation and signal detection: The detection, probe and resonator-lock light from the laser setup in Fig. 5.9 are recombined and send to the bottle resonator via coupling fiber 1. The polarization of each beam can individually be controlled and is intensity stabilized by monitoring the power with photodiodes (PD). The probe and detection beams can be switched on and off with fast Mach–Zehnder (MZ) intensity modulators. Light can be detected with single photon counting modules (SPCMs) at four ports of the network where ports 1-3 are equipped with fiber-based 50/50-beamsplitters to allow for Hanbury–Brown–Twiss-type measurements (note, that the experiment is equipped with only four SPCMS in total). The transmission of the fiber paths from the bottle resonator to the detectors is indicated with the corresponding values η_i. In the branch of port 2 a MEMS fiber optic switch allows to redirect the light to an avalanche photodiode (APD 1) for detection of the PDH resonator-lock light. Similarly, a fiber-based 99/1 beam splitter extracts a weak signal (APD 2) from light in the branch towards port 3. The signals from the SPCMs are analyzed in real-time by a field programmable gate array (FPGA) which controls the MZ modulators. The light of the probe as well of the detection beam can be send into the network also via ports 2 to 4 (not shown).

enters through the 1%-input-port of another 99/1-beamsplitter into coupling fiber 1 which leads to the bottle resonator in the vacuum chamber. Light in coupling fiber 1 that has passed the resonator can be redirected with a fiber-integrated MEMS switch[14] between two output ports with a switching time of 1 ms. One of these ports connects to an avalanche photo diode (APD 1) which is used to detect the light of the bottle resonator PDH lock. Typical powers of the locking light at the APD range up to several nanowatt.

The light fields for atom detection and resonator probing arrive from the laser setup in PM fibers and first pass each through a fiber-integrated Mach–Zehnder (MZ) intensity-modulator.[15] The MZ modulators allow sub-nanosecond switching of the light fields and are controlled by a field programmable gate array (FPGA) which will be discussed later on. The detection and probe light then pass through polarization controllers, respectively, before the paths of the two light fields are combined with a 50/50-beamsplitter. Afterwards, the light is transmitted through a fiber bench where first the polarization is cleaned with a thin-film polarizer before a half-wave and a quarter-wave plate allow to adjust the polarization of detection and probe light simultaneously. The light path is then combined with the one of the resonator lock in a 99/1-beamsplitter where it enters through the 1%-input-port and is therefore attenuated by a factor of 100 compared to the locking light. As described before, another 99/1-beamsplitter then couples the light fields into coupling fiber 1 to transfer them to the bottle resonator. At the resonator the detection and probe light fields have powers on the order of picowatt.

Light that has interacted with the bottle resonator leaves the system via coupling fiber 1 and 2 through different output ports as indicated in Fig. 5.10. The ports 1 to 3 have 50/50-beamsplitters at their outputs to allow for Hanbury–Brown–Twiss type measurements with two detectors. In port 1 the 99/1-beamsplitter directs almost all light coming from the bottle resonator towards the detectors while at the same time it also allows to in-couple the locking, detection and probing light, respectively. In the path of port 2, the already mentioned MEMS switch is integrated and allows one to direct the light either to an APD for frequency locking or to the 50/50-beamsplitter, typically used for single photon detections. Thus at this port, at this port light fields with very different power levels can be measured. Similarly, in the path of port 3 a 99/1-beamsplitter is implemented which enables to either measure a small portion of “strong” light fields (several nanowatt) with an avalanche photo diode (APD 2) or to detected single photons at the 50/50-beamsplitter output.

The transmission efficiencies η_i to the ports 1 to 4 were characterized and are indicated in Fig. 5.10. The efficiencies range between 0.73 to 0.97 and are predominantly influenced by the numerous integrated components like the beamsplitters and the MEMS switch. The transmission efficiencies through the ultra-thin parts and the taper-transitions of coupling fiber 1 and 2 were measured separately before the fibers were connected to the fiber network and are larger than 0.95 which is consistent with the total efficiencies of ports 1 to 4.

The whole experiment is equipped with four single photon counting modules[16] (SPCMs) which are placed at the outputs of ports 1 to 4 depending on the requirements of the performed

---

[14] MEMS OSW12, Thorlabs

[15] NIR-MX800-LN-10, Photline

[16] SPCM-AQRH-13-FC, Perkin Elmer

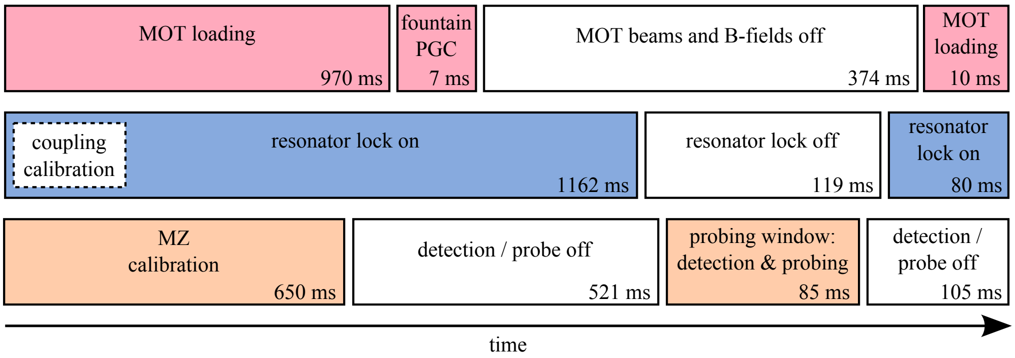
MOT loading
970 ms
fountain PGC
7 ms
MOT beams and B-fields off
374 ms
MOT loading
10 ms
coupling calibration
resonator lock on
1162 ms
resonator lock off
119 ms
resonator lock on
80 ms
MZ calibration
650 ms
detection / probe off
521 ms
probing window: detection & probing
85 ms
detection / probe off
105 ms
time

Figure 5.11: Timing scheme of the experimental sequence: The three rows indicate the atomic fountain (red), the frequency lock of the bottle resonator (blue) and the atom detection and probing system (orange). After 300-500 sequence repetitions a calibration of the evanescent coupling between resonator and the coupling fibers is performed (dashed box). Note that the the size of the boxes are not to scaled to the actual duration.

measurement. The signals of the SPCMs are processed with the help of FPGAs[17] which enable the recording of the photon detection times with sub-nanosecond resolution and which also allow a real-time analysis of the arriving photons.

So far, only the standard configuration of the fiber network has been discussed as it is shown in Fig. 5.10. Beyond this setup, it is also possible to send in the probe and detection light through all other ports of the fiber network. This flexibility comes at the cost of higher photon losses due to the additional fiber components which then have to be integrated into the network. It should be emphasized that probe and detection light can also be sent into the network through different ports. Throughout the thesis this capability will be used extensively for the study of the coupled atom–resonator system.

5.1.7 Temporal sequence of the CQED experiment

In order to synchronize all parts of the described experimental setup, a computer-based control system is implemented. A computer program defines the temporal sequence which controls all mayor components like, e.g., AOMs, switches and power sources for magnetic fields via numerous analog and digital outputs[18] with a temporal resolution of 10 μs.

Fig. 5.11 shows the overview of the experimental sequence which we use to deliver the cloud of cold atoms to the bottle resonator and to subsequently probe the system. In the first part, the MOT loading is performed. After 970 ms the atomic cloud is then accelerated upwards and simultaneously the polarization gradient cooling (PGC) step is applied. During the whole MOT loading phase, and for much of the duration of the cloud's trajectory, the resonance frequency of the bottle mode under study is locked with the PDH locking beam to the desired Rb-transition.

---

[17] XEM3005 and XEM3010-1500P, Opal Kelly

[18] (DAQ, models PCI-6259 and PCI-6733, National Instruments

However, 9 ms before the first atoms arrive at the resonator the frequency lock is interrupted with an sample-and-hold circuit and the locking light is switched off, which would be far too intense for the SPCMs. Then, the MEMS switch is triggered to redirect all light coming from the bottle resonator to the SPCMs. The atomic cloud spends approximately 85 ms in close vicinity of the bottle resonator. During this time, which we will denote as "probing window" from now on, the atom detection light is sent to the bottle resonator. A FPGA controls both the detection and probe beams and can switch in real-time between them while an atom is transiting through the resonator field. This real-time detection and probing system is described in more detail in section 5.3.2.

When the atomic cloud has passed the resonator the detection beam is switched off and the light is redirected again to APD1 to re-establish the frequency lock of the resonator. The frequency of the bottle resonator is stable enough to deviate during the probing window only very slightly from the set-point of the lock such that when the system is critically coupled, a minimal transmission of 1-2 % can be maintained over the full 85 ms.

As soon as the resonator is frequency-locked again, the sequence cycle is finished. In parallel to these processes, during each sequence run the working points of the MZ intensity modulators are calibrated to obtain optimal extinction of the detection and probe light in the off state (for more details see Ref. [129]).

The distance between the bottle resonator and the coupling fibers is not stabilized actively during the experimental sequence. While under ambient conditions the evanescent coupling between resonator and fiber is not longterm-stable, the very good isolation of the system in the vacuum chamber against mechanical, acoustic and especially thermal influences allows us to operate the system without any active stabilization. We attribute this extraordinary stability to the air conditioning of the laboratory, which controls the temperature of the table to fluctuations of less than $0.1\ ^\circ$C. To compensate for very slow drifts, we perform every 300–500 sequence runs ($\widehat{=}$ 5–8 min) a scan of the resonator-fiber separation and detect the fiber transmission. This way, the position of critical coupling can be inferred and set automatically from the point of minimal transmission. During the scan the sequence is stopped in the MOT loading phase. When the two coupling fibers are operated simultaneously at the resonator, both fibers are scanned in a similar procedure which is described in Ref. [60].

5.2 Spectral properties of the bottle resonator and expected strength of the light–matter interaction

The structural properties of the bottle resonator in the CQED setup were determined directly after the micro-structuring process in the fiber pulling rig. The central part of the resonator was measured to have a diameter of $36\,\mu\mathrm{m}$ while the curvature of the resonator was determined to be $0.014\,\mu\mathrm{m}^{-1}$. These parameters define the spectral attributes of the bottle resonator which we characterize with several laser sources. In order to obtain a spectrum that spans several free spectral ranges (FSR) of the resonator, an external cavity diode laser[19] is coupled into the fiber network via port 1. This laser allows to scan its output wavelength mode-hop-free over a range

---

[19] Velocity, New Focus

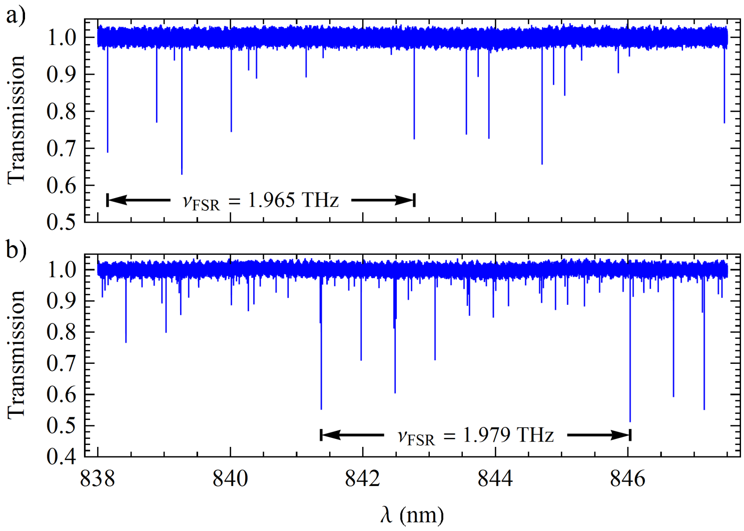

Figure 5.12: Spectrum of the bottle resonator in the CQED experiment: Coupling fiber transmission as function of the laser wavelength λ for a) TM and b) TE polarization. From the characteristic spectral mode patter, the free spectral range ν_{FSR} can be identified.

of 16 nm centered around 845 nm which covers several FSRs of a the bottle resonator. In order to measure the spectrum of the resonator, coupling fiber 1 is aligned approximately at the center of the mode structure of the bottle resonator and the laser frequency is scanned over 10 nm with a scanning speed of 0.02 nm/s. The transmission signal through the fiber is detected with APD 1 and recorded with a digital oscilloscope with a sampling rate of 4 GSa/s. In Fig. 5.12 the obtained transmission spectra for TM and TE polarization are shown. The coupling fiber is only weakly coupled to the resonator and we observe several modes in the under-coupled regime. From the repeating characteristic patterns formed by the excited modes we identify the FSR for the considered mode to be $\nu_{\mathrm{FSR}} = 1.965\,\mathrm{THz}$ for TM and $\nu_{\mathrm{FSR}} = 1.979\,\mathrm{THz}$ for TE polarization according to Eq. (2.41) indicates resonator radius of about $R_0 = 17.2\,\mu\mathrm{m}$. This result is in reasonable agreement with the value of $R_0 = 18\,\mu\mathrm{m}$ obtained from the microscope measurement in section 5.1.4.

The resonator supports ultra-high intrinsic quality factors ranging up to 8×10^7 for both polarizations. The majority of the investigated modes shows no or only very weak mode-splitting in the under-coupled regime which indicates only small mode coupling in the resonator.

Beside the spectral properties of the resonator, it is also of interest to identify the attributes of individual resonator modes. Some parameters like, e.g., the resonance frequency and the linewidth are easy to access and can be directly extracted from spectral measurements with the probe laser setup. In contrast, it is more complicated to determine the polarization of bottle modes. By rotation of the polarization state with help of the wave plates in the fiber bench (compare Fig. 5.10) one can easily separate all modes into two polarization entities. However, by probing through the fiber it is impossible to decide which of these two polarization states is TE and which is TM. Therefore, we monitor the bottle resonator from outside the science chamber

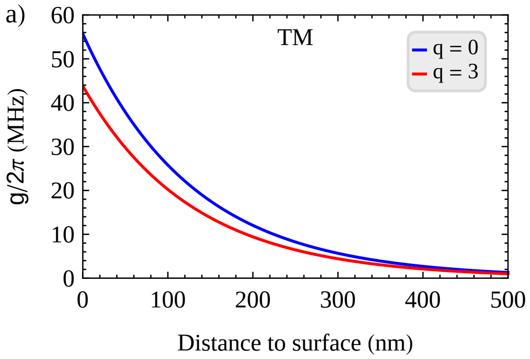

Figure 5.13: Coupling strength g of a ^{85}Rb atom to the bottle resonator excited on the cycling $|F = 3\rangle \rightarrow |F' = 4\rangle$ transition of the D$_2$-line as a function of the distance from the resonator surface. The coupling strength is calculated for different axial q modes for a) TM and b) TE polarization assuming fundamental radial mode order, a resonator diameter of $R_0 = 18.5\,\mu\mathrm{m}$ and an axial resonator curvature of $\Delta k = 0.014\,\mu\mathrm{m}^{-1}$.

through the front viewport with a microscope objective. The intrinsic resonator losses partially originate from scattering due to surface imperfections and other defects and result in light scattering into the environment. Under the assumption that the scattering process is polarization-maintaining, the scattered light can be used to determine the polarization of the bottle modes. We collect the scattered light with the microscope objective and analyze it with a polarization filter in front of it. When a mode is excited with up to several microwatt from the coupling fiber, depending on which of the two eigen-polarizations it belongs to, the scattered light is preferentially polarized along or perpendicular to the axis of the bottle resonator. In this way we assign modes with scattered light preferentially polarized along (perpendicular to) the resonator axis to TE (TM) polarization.

In order to fully characterize a bottle mode, it would be also necessary to determine the radial, azimuthal and axial quantum numbers p, m and q. This is, however, challenging since these parameters can not be obtained exclusively from the spectrum. The azimuthal quantum number m could in principal be estimated taking into account the resonator diameter and the resonance wavelength if the radial quantum number p is known. Unfortunately, it is practically impossible to determine the p of a mode experimentally since for this purpose one would have to count the number of radial intensity nodes which are all located inside the resonator where they are not accessible. However, the coupling of the resonator mode to an ultra-thin fiber can give some indication about the radial quantum number. All experiments are exclusively performed with the first bottle modes in the fiber spectrum which become visible when the fiber approaches the resonator. Calculations based on coupled mode theory [130] suggest that for our experimental parameters these modes should have the lowest radial order $p = 0$. This would yield for the azimuthal quantum number a values close to $m \simeq 200$.

In contrast to the radial and azimuthal quantum number, it is possible to experimentally determine the axial quantum number q of a bottle mode. For this purpose, one can scan a coupling fibers along the resonator axis and count the number of intensity minima which occur in the coupling to the resonator mode. However, in the CQED experiment this is a difficult challenge since the axial extension of the bottle modes exceeds the vertical scan range of the piezo actuator in the nano-positioning stages. For this reason, to count the intensity minima of a mode, one has to make use of the slip-stick mode of the positioning stages which, however, results in unpredictable jumps of the fiber position such that is is very difficult to perform a continuous scan. It is also possible to obtain a rough estimation of the axial extension of the bottle mode when the scattered light from the mode is observed with a camera behind the microscope objective. With this method, we assured that only bottle modes with relatively small axial quantum numbers of $q \lesssim 4$ are used to perform the experiments presented throughout this thesis. In order to quantify the expectable coupling strength g of a ^{85}Rb atom excited on the cycling transition of the D$_2$-line, we plot g as a function of the distance from the resonator surface in Fig. 5.13. As expected from the mode volume, the coupling strength is highest for the fundamental mode ranging up to $g/2\pi = 56\,\text{MHz}$ ($g/2\pi = 45\,\text{MHz}$) at the surface for TM (TE) polarization. However, also the axial mode with $q = 3$ reaches up to $g/2\pi = 44\,\text{MHz}$ ($g/2\pi = 36\,\text{MHz}$) for TM (TE) polarization which would be high enough to put the system into the strong coupling regime when typical experimental resonator decay rates of $\kappa/2\pi = 10\,\text{MHz}$ are assumed.

5.3 Detection and probing of single atoms coupled to the bottle resonator

The CQED apparatus presented in the preceding section allows to deliver a cloud of laser-cooled atoms to the bottle resonator. In this section, it is described how individual atoms can be detected and probed when they interact with the evanescent field of a bottle mode.

5.3.1 Observation of atom transits in a bottle mode

In order to observe transits of single atoms in the evanescent field of a bottle mode, we exploit the atom-induced change in fiber transmission when it couples strongly to the resonator. This procedure has already been proven in similar experiments to be a reliable method for the detection of single atoms [80]. As we have discussed in chapter 4 the strong coupling between an atom and a resonator mode will induce a vacuum Rabi splitting in the spectrum, which although it is expected to be very different for TE and TM modes, should in both cases result in a change of the resonant transmission (see Fig. 4.13).

In order to detect atom-induced transmission changes, it is beneficial to operate the coupling fiber in the critical coupling regime. In this case, all light is initially coupled from the fiber into the bottle resonator where it is dissipated and the fiber transmission is therefore approximately zero. When the atom–resonator coupling is sufficiently strong, the transmission will increase due to the vacuum-Rabi splitting. Therefore, one expects an optimal signal-to-noise ratio for the detection at critical coupling.

In order to characterize the detection method, we chose a TM-polarized bottle mode with an estimated, low axial quantum number of $q \approx 3$, an intrinsic loss rate of $\kappa_0/2\pi = 5\,\text{MHz}$, yielding a total loss rate of $\kappa/2\pi = 10\,\text{MHz}$ at critical coupling, and a negligible mode coupling rate of $h/2\pi < 2\,\text{MHz}$. The mode resonance is locked to the $|F = 3\rangle \rightarrow |F' = 4\rangle$ transition

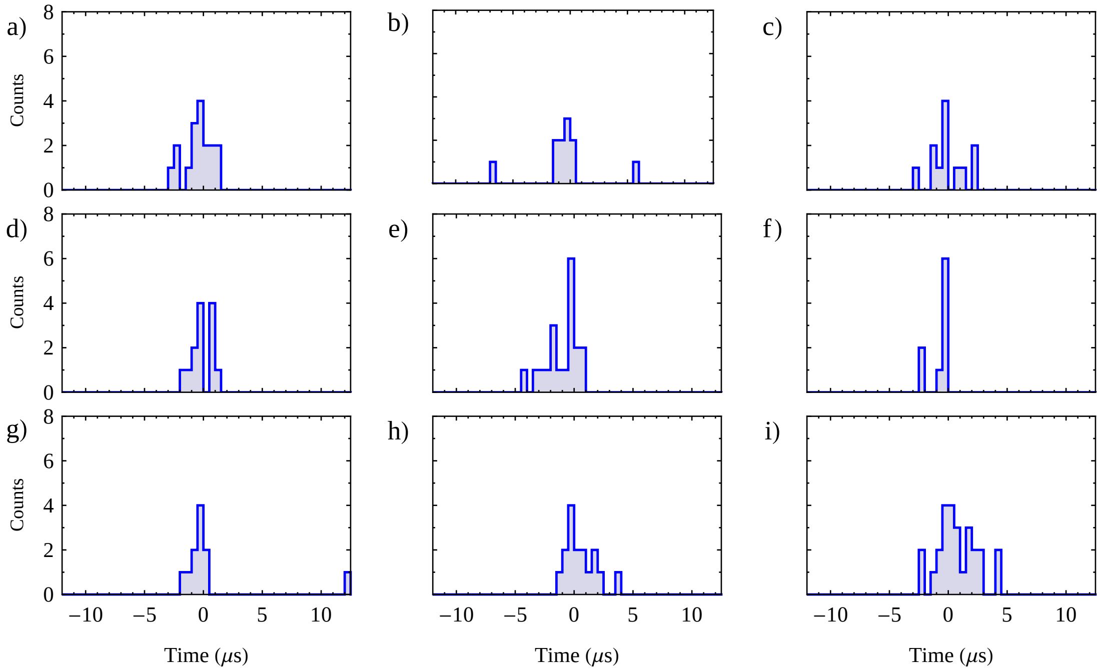

Figure 5.14: Observation of single atom transits: Typical temporal evolution of the coupling fiber transmission when a single ^{85}Rb atom couples to the evanescent field of a TM-bottle mode. The transits in a)-i) are randomly selected from a large collection of trigger events of the atom detection scheme where the zero of the time-axis is defined by the time-stamp of the trigger. Time bins are in steps of 500 ns and the trigger settings are $\Delta t_{\text{trig}} = 1.28\,\mu\text{s}$ and $N_{\text{tresh}} \geq 6$. Note that due to the trigger selection, the time interval $-1.28\,\mu\text{s} \leq t \leq 0$ necessarily contains six or more counts while the rest of the trace is unbiased.

of ^{85}Rb using the PDH frequency lock with a light power of several nW. The experimental sequence is then executed which launches the atomic fountain and switches off the resonator stabilization. At this point, detection light is sent through coupling fiber 1 for the duration of the probing window. This light field is also resonant to the $|F=3\rangle \rightarrow |F'=4\rangle$ transition and has a power of 4 pW leading to an intra-cavity photon number of 0.24 on critical coupling in the absence of an atom. The low power level assures that the coupled atom–resonator system is not saturated, while at the same time it is large enough to achieve a high incoming photon flux of 15 photons/μs through the coupling fiber. The SPCMs at port 2 detect light from the resonator and we record the SPCM signals with the help of a FPGA. The mean transmission through coupling fiber 1 is averaged over the full 85 ms of the probing window and remains as low as $(2 \pm 1)\,\%$ during this interval. However, when the recorded transmission is investigated on a much shorter timescale on the order of microseconds, deviations from this very low transmission value are found. Examples for such traces are shown in Fig. 5.14 where one observes an increase in transmission for durations in the range from one to several microseconds. Since the total power of the detection light that is coupled to the bottle resonator corresponds to a count rate of

6 to 7 cnts/μs at the SPCMs, we can conclude that we observe events with transmission increases ranging up to unity.

In order to verify that the observed events in transmission are signatures of single atoms which couple to the bottle resonator, a reasonable approach is to compare the number of such events in cases where an atomic cloud is launched to cases where the fountain is switched off. For this purpose, one however requires a quantitative criterion which signifies a transmission event. A simple method to decide whether a potential atom coupling event has occurred or not is to count the photon detection events from the SPCMs which arrive in a certain time window. When the photon number reaches a pre-defined threshold we then conclude that a single atom transit has been detected [89]. Using this method, the transmission traces of the experiment have been analyzed for various combinations of time window durations and count thresholds [129]. In order to evaluate the different trigger criteria, we compared the number of detected events for cases where the atomic cloud was launched to cases where the MOT was turned off. This way, a false-detection rate can be defined which is used to evaluate an optimum between a high atom-detection rate and an minimal false-detection rate. The best performance was achieved with a criterion having a time window of $\Delta t_{\text{trig}} = 1.28\,\mu\text{s}$ and a count threshold of larger than $N_{\text{tresh}} = 6$. With this trigger criterion we detect for the considered dataset an average number of atom transits of 4.1 ± 2.3 per sequence run while the false detection rate is determined to be $1.4\,\%$. According to this result, there is clear evidence that the transmission increases are atoms coupling to the resonator mode. Moreover, we observe a linear dependence between the number of atoms in the atomic cloud of the fountain and the number of detected transit events [60], which is a clear indicator that the transmission increase is indeed induced by single atoms and does not originate from multi-atom effects. This conclusion is further supported by the fact that a rough estimation of the atomic density in the mode volume of the evanescent field yields approximately 20 atoms around the bottle resonator, which is in reasonable agreement with the detected number of 4 transit events [60].

Figure 5.15 shows a distribution of the coupling fiber transmission averaged over 3420 atom coupling events. In this measurement, atoms are detected according to the trigger criterion $\Delta t_{\text{trig}} = 1.28\,\mu\text{s}$ and $N_{\text{tresh}} = 6$. In order to correctly align the time-axis of the individual traces, a relative time axis is defined for each event such that $t = 0$ corresponds to the center-of-mass of the corresponding photon distribution. Finally, all traces are averaged to give the transmission distribution in Fig. 5.15. The average trace of coupling events has an asymmetric shape and shows some discontinuity features which are biasing effects of the atom detection scheme [60, 99]. Moreover, the asymmetries suggest that the atoms approach the resonator field slower than they are leaving it, since the distribution has a steeper slope for positive times. The FWHM of the distribution is $1.43\,\mu\text{s}$ which corresponds to the average interaction time of a single atom that is detected with the above mentioned trigger criterion. This result fits well to the expected time scale for single atoms which pass the evanescent field of the bottle resonator.

In Fig. 5.13, the coupling strength of TE and TM modes was calculated as a function of the distance from the resonator surface. We have seen that reasonable coupling strength are expected only for atoms which come closer than 150 nm to the resonator surface. Moreover, very close to the resonator, for distances smaller than 50 nm, surface interactions start to modify the atomic level structure, thereby shifting the atom off-resonant to the mode [60, 100]. Thus,

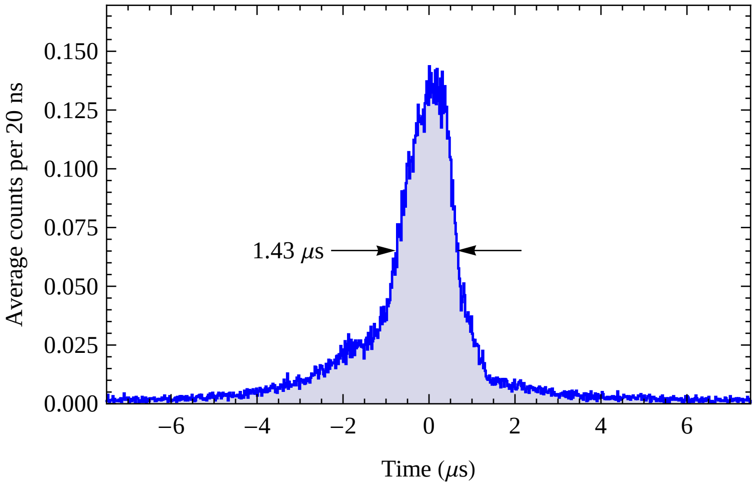

Figure 5.15: Averaged coupling fiber transmission of 3420 atomic transit events. The relative time axis of each individual event is aligned to the mean of the corresponding photon distribution, which is calculated from photons in a window of $\pm 1.5\,\mu$s around the trigger time stamp. Trigger settings are $\Delta t_{\text{trig}} = 1.28\,\mu$s and $N_{\text{tresh}} = 6$.

by assuming that the atoms move normal to the resonator surface and eventually crash into the resonator, we can obtain an rough estimation of the interaction length in the evanescent field of 100 nm. If one takes into account the temperature of the atomic ensemble of $7\,\mu$K, which corresponds to a mean thermal velocity of about $0.04\,\mathrm{m/s}$, we end up with typical observable interaction times on the order of $2.5\,\mu s$ what is in good agreement with the measured results. More detailed studies on the motion of atoms in the evanescent field of a microresonator have been performed in Refs. [60, 99, 100]. The results suggest that optical dipole forces due to a detunings between the atomic transition and the light field, as well as Casimir–Polder forces originating from the interaction with the resonator surface, influence the trajectory of an atom during its passage through the evanescent field.

5.3.2 Real-time atom detection and ultra-fast probing

We have seen that the interaction times of single atoms with the resonator are limited — due to their motion — to several microseconds. As a consequence, the whole experimental procedure has to be adapted to this timescale. In particular, one requires a system which is able to detect atom coupling events and to react on them in a fraction of the total duration of the interaction so that there is sufficient time to perform measurements of the atom–resonator system.

For this purpose, the above described trigger criterion is evaluated in real-time: A FPGA[20] continuously counts the photons detected by the SPCMs in the time window Δt_{trig} and checks whether the threshold N_{tresh} is exceeded (for more details on the technical implementation see Ref. [129]). The FPGA runs with an internal clock rate of 100 MHz and requires typically four clock cycles to decide if an atom coupling event occurred. Then, the time stamp of this event relative to the beginning of the probing window of 85 ms, is saved and transferred to a computer. In addition, a TTL pulse is sent out which is recorded and time-tagged together with the photon signals of the SPCMs by a second FPGA.[21] This recording-FPGA reaches a sub-nanosecond resolution by making use of internal hardware delays on the chip. The recorded time stamps of all detected photons are then transferred to a computer. In order to reduce the amount of recored data, a computer program saves only the photons in a time window of $\pm 25\ \mu$s relative to the time stamp of a trigger event.

---

[20] XEM3010, Opal Kelly

When a single atom has been detected at the bottle resonator, the trigger-FPGA allows to react on this event by changing the light field sent through the coupling fiber. For this purpose, the FPGA controls the MZ-intensity modulators already introduced in section 5.1.6. In a typical experiment, first the atom detection light is coupled into the resonator. When the FPGA detects an atom, it switches off the detection light with the MZ-modulator and simultaneously turns on the probe light which is pre-configured to a desired frequency and intensity. In this way, it is possible to detect atoms always under identical optimal conditions (with on-resonant light) and to investigate them with various settings of the probe light. At this point it should be mentioned that this method allows to measure only one setting of the probe light per atom such that parameter scans have to be performed over many coupling events.

Figure 5.16 shows the averaged transmission over 5966 detected atomic transits where the described switching process has been applied. In this measurement, the probe light had the same frequency and slightly smaller intensity than the detection light field. In the figure, the time stamps of the photons are aligned all relative to the corresponding atom detection event, which defines $t = 0$. As a consequence, the average transmission trace contains strong bias effects which originate from the trigger method. These are related to the fact that we only select events where at $t = 0$ a photon is detected (large peak). Exactly Δt_{trig} before the arrival of this photon, no photon can be present (dip to zero) because otherwise the trigger criterion would have been fulfilled earlier. However, these effects are restricted to the length of the trigger window and leave the rest of the transmission trace unbiased.

From Fig. 5.16, it is possible to infer the total reaction delay of the switching process. Besides a delay of approximately 40 ns, which the FPGA requires for the trigger decision, the electrical and optical signal paths and the rise time of the MZ-modulator finally add up to a delay of 180 ns until the probe light arrives at the resonator. Thus, taking also into account the trigger time window Δt_{trig}, about $1.5\ \mu$s are required to detect and react on an atom in the field of the bottle resonator. As this duration is comparable to the average interaction time it is likely that atoms are lost during the probing phase. This becomes apparent in the approximately exponential decrease of the transmission signal after the detection of an atom in Fig. 5.16. There are several possible reasons for the loss of atoms: The atoms could either simply leave the evanescent resonator field on their trajectory or eventually could also crash into the resonator surface, which would be accompanied with a large shift of the atomic transition due to surface interactions. These effects lead to a large variation of individual transmission traces, as it is apparent from Fig. 5.14.

---

[21] XEM3005, Opal Kelly

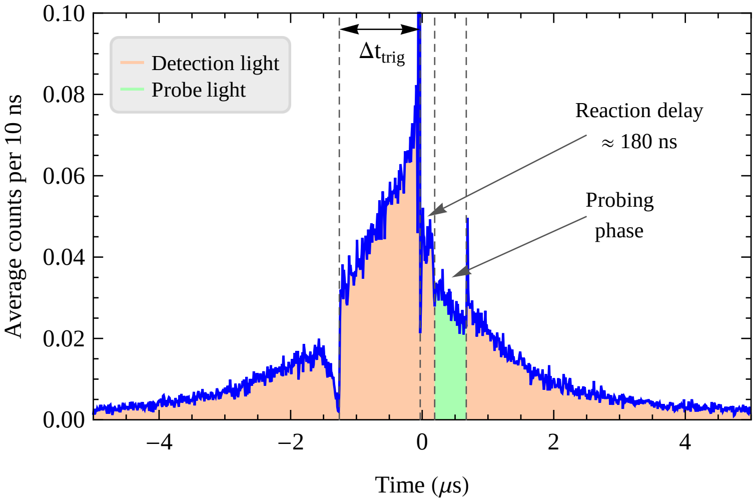

Figure 5.16: Averaged coupling fiber transmission of 5966 atom transit events where all photon time stamps are aligned relative to the atom detection at $t = 0$. After the registration of a trigger event, the detection light field is switched off and a probe light field with the same frequency and similar intensity is switched on for 500 ns before the light is switched back to the detection field. The transmission spike at $t = 0.7\,\mu$s is due to a small temporal overlap of the detection and probe light. Trigger setting are the same as in Fig. 5.15.

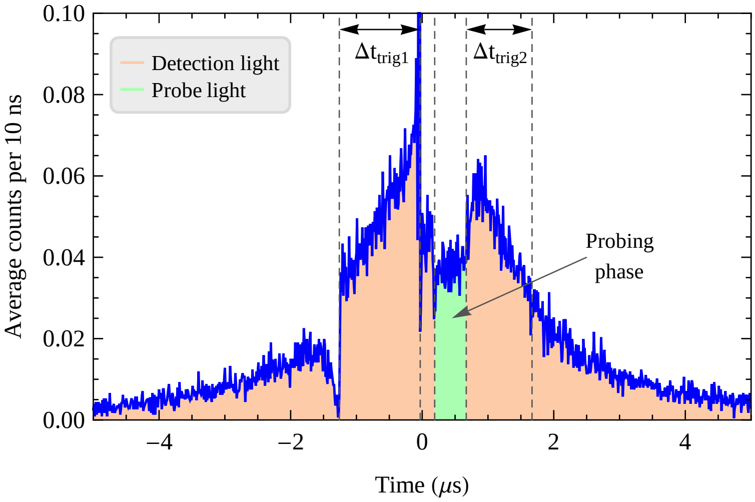

Figure 5.17: Atom re-detection with the second trigger criterion: Same data as in Fig. 5.16 where in the post-analysis only those events are taken into account which have in a second trigger window $\Delta t_{\mathrm{trig2}} = 1\,\mu$s more than $N_{\mathrm{tresh2}} = 1$ photons. Thereby, the total number of events is reduced to 2260.

It is important to select only those atoms from the data which remain coupled to the resonator over the complete duration of the probing phase. For this purpose, a second atom detection phase is performed in which the light in the fiber is switched back from the probe to the detection field. The basic idea is based on the same principal as the first atom trigger: When the atom is still present after the probe phase with a typical duration of 500 ns, the transmission of the detection beam remains high while it will drop to zero when the atom has left the evanescent resonator field. By selecting only those events were the transmission is still high after the probing interval, we can assure that the atom was well coupled to the resonator field during the measurement. Figure 5.17 shows the average coupling fiber transmission of the same dataset as in Fig. 5.16 but with the difference that now only transit events are taken into account which have in a second trigger window $\Delta t_{\text{trig2}} = 1\,\mu$s more than $N_{\text{tresh2}} = 1$ photon. This procedure can be performed in post-analysis and reduces the number of relevant transit events to 2260, a factor of three lower. The beneficial effect of the second trigger analysis is obvious. Now, we observe a fiber transmission which remains almost constant during the whole probing interval. Thus, we indeed select only those atoms which are stably coupled to the resonator mode over this period of time. Moreover, the additional application of the second trigger criterion also results in fewer false trigger events; for example, in this dataset, the false detection rate drops from 2 % to practically zero.

5.3.3 Lifetime of atoms in the evanescent field as a function of the applied magnetic field

In Fig. 5.16 we observed a high fiber transmission directly after the detection of an atom at $t = 0$ which then dropped approximately exponentially to zero. We attributed this transmission decrease to the loss of atoms from the evanescent field either by crashing into the resonator or simply by moving away from it. From the exponential decay of the transmission we can obtain a time constant τ_a which we will denote as the “lifetime” of atoms in the evanescent field after their detection. Obviously, this lifetime depends on the motion of the atoms and can give at least some qualitative understanding of the forces which influence the trajectories of the atoms. It was already mentioned before that a frequency detuning between the resonator light field and the atomic transition frequency will give rise to optical dipole forces. A red detuning of the resonator field compared to the atomic transition results in an attractive force towards regions of higher intensity, i.e. the resonator surface, while a blue detuning has the opposite effect [60, 99, 100]. Here we want to study the influence of the atom–light detuning on the lifetime of atoms in the evanescent field by applying a magnetic field B_z along the resonator axis. This field induces a Zeeman shift of the atomic m_F levels which scales according to $\Delta E/\hbar = \mu_B g_F m_F B_z$, as it was described in section 4.4.1. As a consequence, the applied magnetic field will shift the atomic transition frequencies relative to the light frequency.

At this point, it should be emphasized that the atomic motion is not only influenced by light-induced dipole forces but that also other forces comprising, e.g., velocity dependent forces and forces of van der Waals and Casimir-Polder type [100] occur. The latter two arise from the presence of the dielectric resonator surface which induces a modification of the spontaneous decay rate of the atom and a shift of the atomic levels. However, these effects become only dominant in

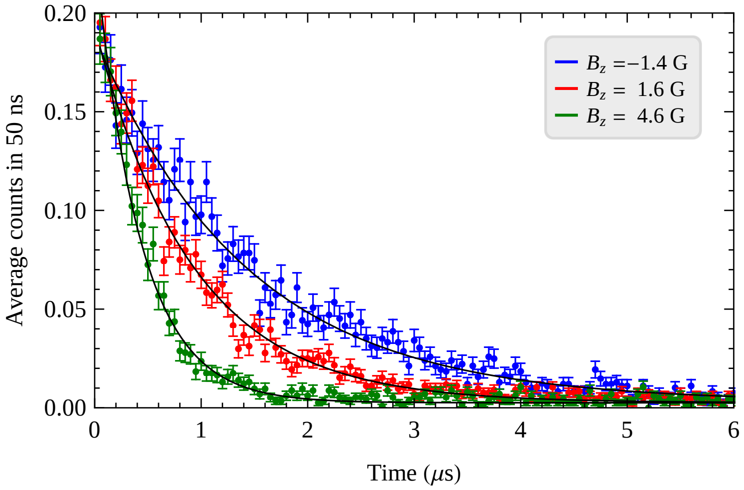

Figure 5.18: Average coupling fiber transmission of a TM mode coupled to a single atom as function of time for three different magnetic fields B_z; error bars correspond to 1σ-statistical error of the count rate; the black lines are fits of an exponential function with decay constant τ_a; $t = 0$ defines the moment the atom detection event occurred.

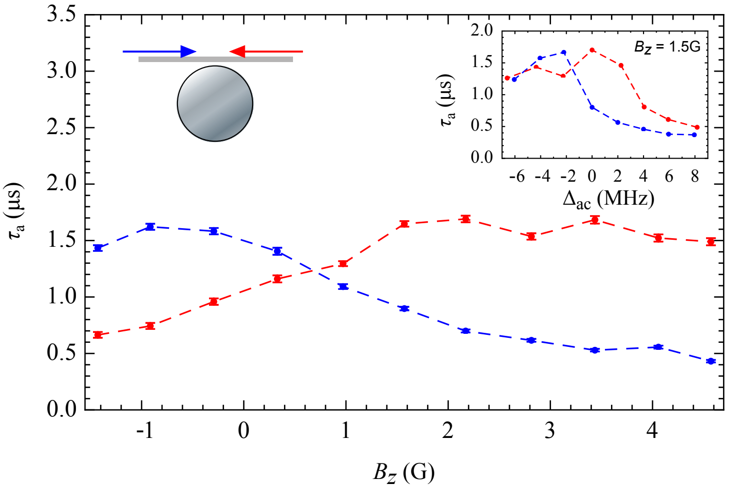

Figure 5.19: Time constant τ_a of the exponential decay of the coupling fiber transmission after an atom detection as a function of the axial magnetic field B_z. The light is sent in via port 1 (blue) or port 2 (red) of the fiber network (as shown by the right inset), dashed lines are guide to the eye, error bars correspond to the parameter uncertainty of the exponential fit. The left inset shows τ_a as a function of the atom–cavity detuning Δ_{ac} for both propagation directions of the light.

a region closer than 50 nm to the resonator surface where they start to shift the involved atomic transitions heavily off-resonant [60]. The detuning effectively reduces the atom–light coupling which suppresses the influence of the atom on the fiber transmission. Therefore, we assume that as long as the atom is visible in the transmission of the fiber, optical dipole forces will dominant influence the trajectory of the atom.

In order to study the effect of a magnetic field on the lifetime τ_a, we use the same TM mode as in the preceding experiment in section 5.3.1 and couple single ^{85}Rb atoms to the resonator. During the measurement, we do not use the probe light but simply leave on the detection light after an atom transit has been detected. Moreover, the second trigger criterion is not applied, since we are interested in the exponential decay of the transmission directly after the atom detection. The TM mode is set resonant to the $|F = 3, m_F = 0\rangle \rightarrow |F' = 4, m_{F'} = 0\rangle$ transition and coupling fiber 1 is critically coupled to the bottle resonator. We start the experiment by sending the resonant detection light field via port 1 into the fiber network such that the TM modes is populated with an intra cavity photon number of 0.18 when no atom is present. Then we scan the magnetic field along the resonator axis B_z and average the transmission after a trigger has occurred for each setting of B_z over several hundred atomic coupling events. Note, that due to the residual magnetic offset of approximately $1.5\,\mathrm{G}$ at the resonator, it is only possible to scan B_z in the interval from $-1.5\,\mathrm{G}$ to $4.6\,\mathrm{G}$. The applied field should allow to shift the frequencies of the cycling transitions $|F = 3, m_F = \pm 3\rangle \rightarrow |F' = 4, m_{F'} = \pm 4\rangle$, for which the Zeeman shift is $\pm 1.4\,\mathrm{MHz/G}$, between $\mp 2.1\,\mathrm{MHz}$ and $\pm 6.4\,\mathrm{MHz}$.

Figure 5.18 shows an example of three traces of the average coupling fiber transmission as a function of time for different magnetic fields. We clearly observe that for a magnetic field changing from negative to positive values the lifetime of the atoms in the resonator field reduces considerably. The measurement is repeated for several different magnetic field strengths. For the analysis the trace of the fiber transmission for each setting is fitted with an exponential decay with the time constant τ_a. In Fig. 5.19, the atomic lifetime as function of the magnetic field along the resonator axis is shown. When the TM mode is excited via port 1 of the fiber network (blue data) we observe an almost constant atomic lifetime of $\tau_\mathrm{a} = 1.5\,\mu\mathrm{s}$ for negative values of B_z while for positive values of B_z the atomic lifetime starts to drop and is finally reduced by a factor of 3.

This measurement alone gives no indication which sign of the magnetic field corresponds to red and which to blue detuning. Therefore, we perform a second experiment where we switch off the external magnetic field coil and instead detune the mode resonance with respect to $|F = 3, m_F = 0\rangle \rightarrow |F' = 4, m_{F'} = 0\rangle$ transition. In addition, the detection light is shifted simultaneously to stay in resonance with the mode such that an atom–cavity detuning is introduced. Note that due to the residual magnetic offset field in the resonator, the measurement is performed with approximately $B_z = 1.5\,\mathrm{G}$. The inset on the left in Fig. 5.19 shows the lifetime of atoms in the evanescent field, obtained from the transmission decay for different atom–cavity detunings Δ_ac. If we send light via port 1 to the resonator (blue data), we observe for blue detuning of the resonator light field ($\Delta_\mathrm{ac} < 0$), a relatively stable lifetime of $\tau_\mathrm{a} = 1.5\,\mu\mathrm{s}$ which reduces for red detuning ($\Delta_\mathrm{ac} > 0$) to $\tau_\mathrm{a} = 0.5\,\mu\mathrm{s}$. Thus, for light coming from port 1 in the fiber network we can attribute a negative magnetic field to blue detuning of the light field relative to the atomic transition and a positive magnetic field to red detuning.

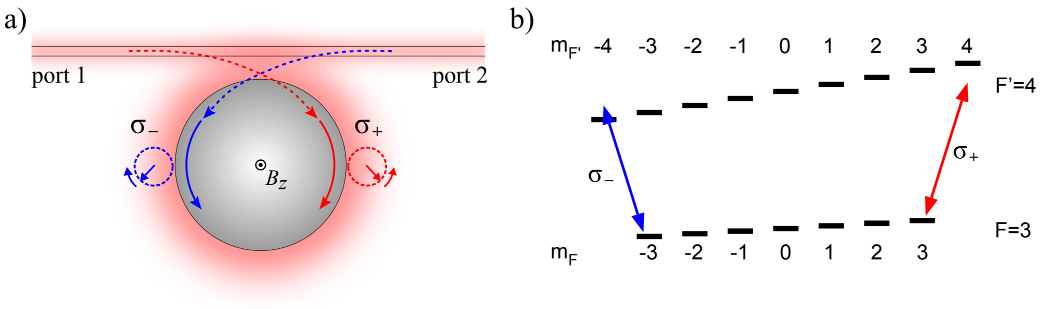

Figure 5.20: a) Illustration of the rotation sense of the polarization vector of counter-propagating TM modes in the bottle resonator. b) Level scheme of the $|F = 3, m_F = \pm 3\rangle \rightarrow |F' = 4, m_{F'} = \pm 4\rangle$ transition of the ^{85}Rb D_2 line when an magnetic field is applied. Light with σ_+ polarization drives $\Delta m_F = +1$ transitions while σ_- light drives $\Delta m_F = -1$ transitions.

Qualitatively, the dependence of the atom lifetime on the light detuning can be well explained by optical dipole forces. For blue-detuned light, the dipole force will decelerate an atom approaching the resonator since the intensity of the light field increases towards the surface (see, e.g., Fig. 4.10). As a consequence, the atom becomes slower and remains longer in the region. On the other hand, if the light field is red-detuned, an atom is attracted towards the resonator, and therefore, it is more likely that it crashes into the resonator resulting in a shorter lifetime in the evanescent field. This interpretation fits well to the results in Ref. [99, 100] where, due to optical dipole forces, longer lifetimes for blue detuning and shorter lifetimes for red detuning were reported.

An interesting behavior can be observed when the propagation direction of the detection light is reversed. We repeat exactly the same two experiments from before, where we either change the applied magnetic field or the atom–cavity detuning Δ_{ac} and measure the lifetime of atoms in the evanescent field. The only difference now is that the detection light is sent into the fiber network via port 2 such that, compared to the preceding experiments, we excite the counter-propagating TM mode. The results are shown in the Fig. 5.19 and its inset as red data points. As a main outcome of the measurements, we observe that the magnetic field dependence is inverted, yielding short lifetimes for negative and long lifetimes for positive B_z, while the dependence on the atom–cavity detuning remains similar and is only shifted to red detuning. The latter finding suggest that also for the counter-propagating mode, a blue detuning results in long lifetimes and red detuning in short lifetimes. Thus, the magnetic field seems to induce an opposite detuning between the resonator light field and the atomic transition when the counter-propagating mode is excited. This indicates that in this case, the light is interacting with an atom on a different transition having the opposite magnetic field dependence.

A possible explanation for the behavior would be to assume different polarizations of the two resonator modes. According to our developed model from chapter 4, counter-propagating TM modes have almost orthogonal circular polarization, as shown in Fig. 5.20 a). If the quantization axis of the atom lies along the resonator axis, these two polarization states overlap almost perfectly with σ_+ and σ_- polarized light. Thus, for a multilevel atom, as shown in Fig. 5.20 b) for the $|F=3\rangle \rightarrow |F'=4\rangle$ transition of the ^{85}Rb D$_2$-line, σ_+ light will drive $\Delta m_F = +1$ transitions while σ_- light will drive $\Delta m_F = -1$ transitions. As the coupling strength g of the atom to the resonator field is strongest on the cycling transitions $|F=3, m_F=\pm 3\rangle \rightarrow |F'=4, m_{F'}=\pm 4\rangle$ it is likely that our detection method preferentially triggers on atoms in the extremal $m_F = \pm 3$ states. Figure 5.20 b) clearly illustrates that in this case the Zeeman shifts of the transition frequencies will be inverse for the $|F=3, m_F=3\rangle \rightarrow |F'=4, m_{F'}=4\rangle$ and the $|F=3, m_F=-3\rangle \rightarrow |F'=4, m_{F'}=-4\rangle$ transition leading to different detunings relative to the light field. Thus, the assumption that counter-propagating modes have orthogonal circular polarization and therefore couple to atoms in different m_F states would perfectly explain our measurement results. Furthermore, this interpretation would also explain the shift of the lifetime dependence on Δ_{ac} between the counter-propagating modes in the inset of Fig. 5.19. Since during the measurement a residual magnetic field of $B_z = 1.5$ G was present, the absolute atomic transition frequency experiences a Zeeman shift. The sign of the shift will be different for the two transitions interacting with the two modes, leading to an initial detuning relative to the resonator light field.

We note as well that in Fig. 5.19 one would expect for the two data sets to have identical atomic lifetimes for zero magnetic field. However, we observe the crossing point of the two curves to be shifted slightly to a positive value of B_z. This behavior is most likely explained by the fact that when the magnetic guiding field along the resonator axis becomes small, other unwanted fields in the science chamber (see section 5.1.5) will start to dominate the atomic level shifts such that in this regime, we can no longer assume a well defined magnetic field.

In conclusion, by observing the lifetime of atoms in the evanescent field as a function of the magnetic field we found evidence that optical dipole forces influence the motion of the atoms in the resonator field. Moreover, the inverse magnetic field dependence of the lifetime for counter-propagating TM modes supports the central prediction of our theoretical model: Since the propagation direction in the resonator fixes the polarization of the two modes to be orthogonal, they interact with atoms in different extremal m_F-states. In order to strengthen the validity of our model further, a quantitative comparison between theory and experimental data is necessary. For this purpose, we will study in the next section the spectral properties of the coupled atom–resonator system.

5.4 Strong coupling of single atoms to non-transversally polarized bottle modes

The previous section described how single ^{85}Rb atoms can be detected and probed in real-time while they couple to the evanescent bottle resonator field. In the following section we will apply this measurement scheme to perform spectroscopy of the coupled atom–resonator system for TE and TM polarized modes, in order to study the influence of the non-transversal polarization on the light–matter interaction.

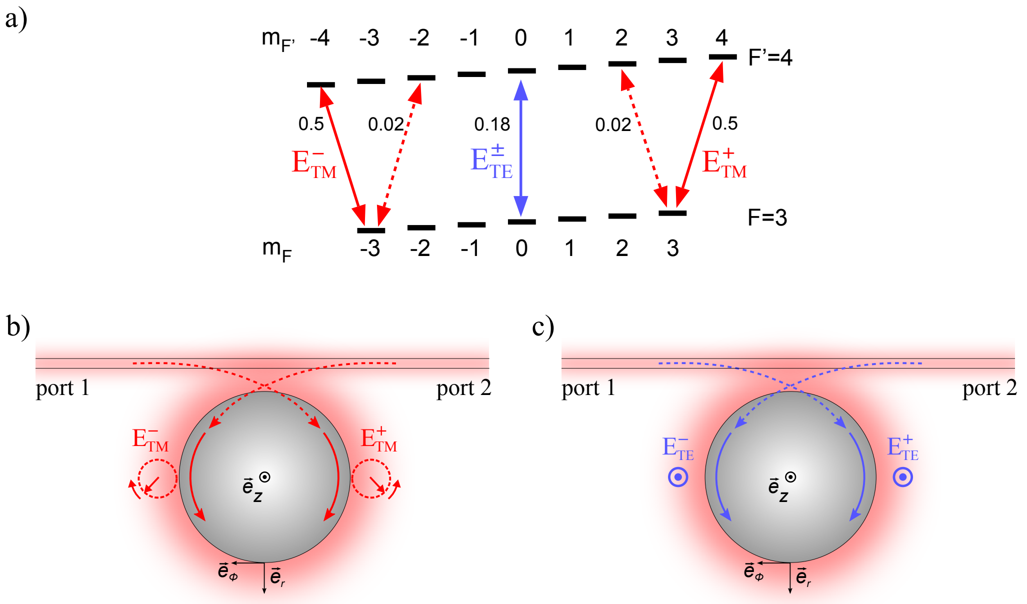

Figure 5.21: a) Atomic level scheme of ^{85}Rb for the $|F = 3\rangle \rightarrow |F' = 4\rangle$ transition of the D_2-line: We assume a magnetic field along the resonator axis $\vec{e}_z$ which induces a Zeeman-shift of the atomic levels. TE modes are π-polarized and drive transitions with $\Delta m_F = 0$ (blue). In contrast, TM modes overlap strongly with $\sigma_\pm$-polarization and drive transitions with $\Delta m_F = \pm 1$ (red) which results in optical pumping to the extremal ground states with $m_F = \pm 3$ where a closed cycling transition occurs. Moreover, in these extremal states, the large difference in transition strength (indicated by numbers beside arrows) effectively decouples the counter-propagating resonator mode (dashed arrows). b-c) Configuration of the evanescent field around the resonator for a counter-propagating mode pair with b) TM and c) TE polarization.

5.4.1 Vacuum-Rabi splitting of TM and TE polarized bottle modes

Theoretical predictions

In chapter 4 the effect of the non-transversal polarization on light–matter interaction was discussed from a theoretical point of view. We found that counter-propagating TM modes are orthogonally polarized such that they cannot interfere destructively, while counter-propagating TE modes have identical polarization and should form standing waves. With the newly developed theoretical model from section 4.4 at hand, which accounts for arbitrary mode polarization, we want to investigate this situation for our experimental conditions. First, we calculate the vacuum-Rabi spectrum for a strongly coupled atom–resonator system in the case of TM and TE polarization, respectively. For the calculation we include the full Zeeman sub-level structure of the $|F = 3\rangle \rightarrow |F' = 4\rangle$ transition from the D_2-line in ^{85}Rb, which is shown in Fig. 5.21 a), as well as the polarization properties of the evanescent fields. We denote the counter-propagating mode pairs in the resonator as $E_{\mathrm{TM}}^{\pm}$ and $E_{\mathrm{TE}}^{\pm}$ for TM and TE polarization, respectively, where

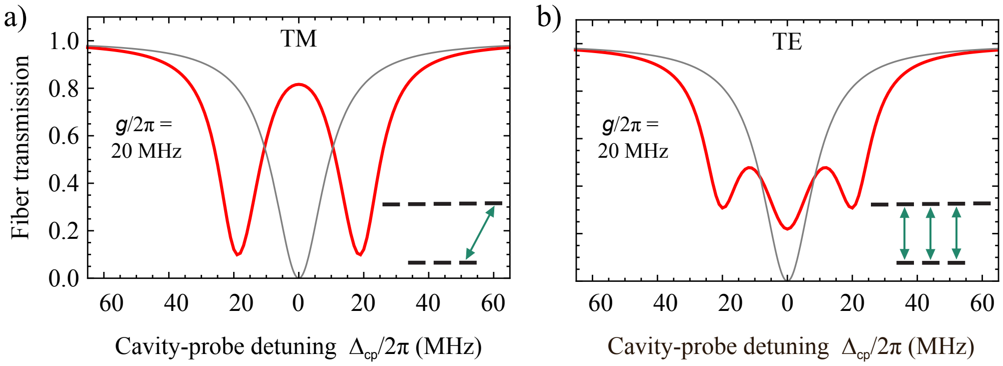

Figure 5.22: Simulated steady state transmission spectra of an ultra-thin fiber coupled to a) a TM and b) a TE mode of our bottle resonator system. Without light–matter coupling the spectra show a Lorentzian resonance (gray lines), while a vacuum-Rabi splitting occurs if the resonator mode is coupled to a ^{85}Rb atom with coupling strength $g/2\pi = 20\,\mathrm{MHz}$ (red lines). All other parameters are set to the experimental values (see text). For the TM mode an overlap of 96 % with σ_+ polarization is assumed which is obtained for our resonator parameters assuming a fundamental radial mode. The insets illustrate the dominant driven transitions in a simplified atomic level scheme.

the sign defines the propagation direction of the mode according to Fig. 5.21 b) and c). For the simulation, we assume that only one of the two counter-propagating modes is driven from the coupling fiber with a weak probing field (E^+_{TM} and E^+_{TE}, respectively). Moreover, the cavity is set resonant to the $|F = 3\rangle \rightarrow |F' = 4\rangle$ transition and we assume critical coupling between the coupling fiber and the resonator. Figure 5.22 shows the theoretical spectra expected for our system for a TM- and TE-polarized mode when the laser frequency is scanned. The spectra clearly show the qualitative difference between non-transversal TM modes and transversal TE modes: While for TE polarization we observe three resonances in the spectrum, where the central one is the signature of the uncoupled standing wave, the spectrum of the TM mode shows a two-resonance structure without any evidence for interference between counter-propagating light fields.

In the following, we define the quantization axis along the resonator axis such that the linear polarization of TE modes corresponds to π polarized light. As a consequence, TE modes will drive only $\Delta m_F = 0$ transition between the atomic Zeeman sub-levels, as shown in Fig. 5.21 a). In contrast, the situation is fundamentally different for TM polarized light: The two counter-propagating modes overlap with two almost fully orthogonal circular polarization states which can be identified with σ_+ and σ_- polarized light, as depicted in Fig. 5.21 b). In this situation, the propagation direction of the light defines whether optical $\Delta m_F = +1$ or $\Delta m_F = -1$ transitions are preferentially driven. In combination with the multilevel structure of the atom, this results in optical pumping which is dependent on the propagation direction of the mode. As a consequence, the atom will be transferred into one of the extremal ground states of the level scheme, as illustrated in Fig. 5.21 a). For instance, if mode E^+_{TM}, which has a large overlap with σ_+-

polarization, is excited from the fiber, the atom is pumped to the ground state $|F = 3, m_F = 3\rangle$ from where the mode can only drive the closed transition to the $|F' = 4, m_{F'} = 4\rangle$ excited state. This situation occurs naturally and is highly advantageous for two reasons: First, the closed cycling transition maximizes the coupling strength of the atom to the electromagnetic field. Second, the selection rules for dipole transitions lead to a much smaller coupling strength which prevents the atom from emitting light into the orthogonally polarized, counter-propagating mode with σ_- polarization, as shown in Fig. 5.21 a). Despite the simultaneous existence of two degenerate resonator modes, this effectively leads to the ideal case of a two-level atom that only interacts with a single traveling-wave mode. Thus, as depicted in Fig. 5.22 a), our theoretical model predicts a spectrum of the coupled atom–resonator system that exhibits the vacuum Rabi splitting of a single mode cavity by $2g$ [90].

Measurement of vacuum-Rabi spectra

In order to verify the prediction of our theoretical model we measure the spectra of the coupled atom–resonator system for TM and TE polarization, respectively. For this purpose, two bottle modes with the corresponding polarizations are selected. The TM mode is the same as the one used earlier to study single transit events in section 5.3. Thus, it has an axial quantum number $q \approx 3$ and an intrinsic dissipation rate of $\kappa_0/2\pi = 5\,\text{MHz}$. Similarly, the TE mode has a small axial extension which we estimate to be smaller $q \lesssim 4$ and an intrinsic loss rate of $\kappa_0/2\pi = 5\,\text{MHz}$. Both modes are chosen carefully to have only low intrinsic mode coupling, determined by measuring the bare resonator spectrum in the under-coupled regime. From these measurements (dashed lines in Fig. 5.23 a) and b)) we infer a mode coupling rate of $h/2\pi < 2\,\text{MHz}$ for the TM and $h/2\pi \approx 4\,\text{MHz}$ for the TE mode. These values are considerably smaller than the half-width-half-maximum (HWHM) linewidth of the cavity $\kappa/2\pi = \kappa_0/\pi$ at critical coupling and we therefore neglect for simplicity the effect of mode coupling in our theoretical description.

For the measurement a magnetic field of $B_z = 4.5\,\text{G}$ is applied along the resonator axis to lift the degeneracy of the atomic hyperfine levels and to overcome the influence of magnetic stray fields. The B-field defines the quantization axis such that light coming from port 1 of the fiber network will drive the mode E^+_{TM}, as shwon in Fig. 5.21 b). Taking into account the Zeeman-level-shift the resonator is then set resonant with the $|F = 3, m_F = 3\rangle \rightarrow |F' = 4, m_{F'} = 4\rangle$ transition which we expect to be preferentially populated due to strongest coupling with σ_+ polarized light. For the case of the TE polarization the mode E^+_{TE} is excited from port 1 (see Fig. 5.21 c)) and the resonator light field will be π-polarized such that no optical pumping effects are expected. Therefore, the TE mode is locked to the central $|F = 3, m_F = 0\rangle \rightarrow |F' = 4, m_{F'} = 0\rangle$ transition of the atomic level scheme.

In order to detect single atoms in the evanescent field of the bottle resonator, coupling fiber 1 is set to critical coupling and the resonant detection light field with correct polarization for either the TM or the TE mode is send in from port 1 and detected subsequently at port 2 of the fiber network. The detection light flux is $1.2 \times 10^7\,\text{photons/s}$ which corresponds to an intra-cavity photon number of 0.18 when no atom is present. In the case of the TM mode the criterion for the first trigger is set to a time window of $\Delta t_{\text{trig1}} = 1.28\,\mu\text{s}$ and a threshold of $N_{\text{trig1}} = 6$. However, we observe this criterion to be too strict for the detection of atoms with the TE mode since the

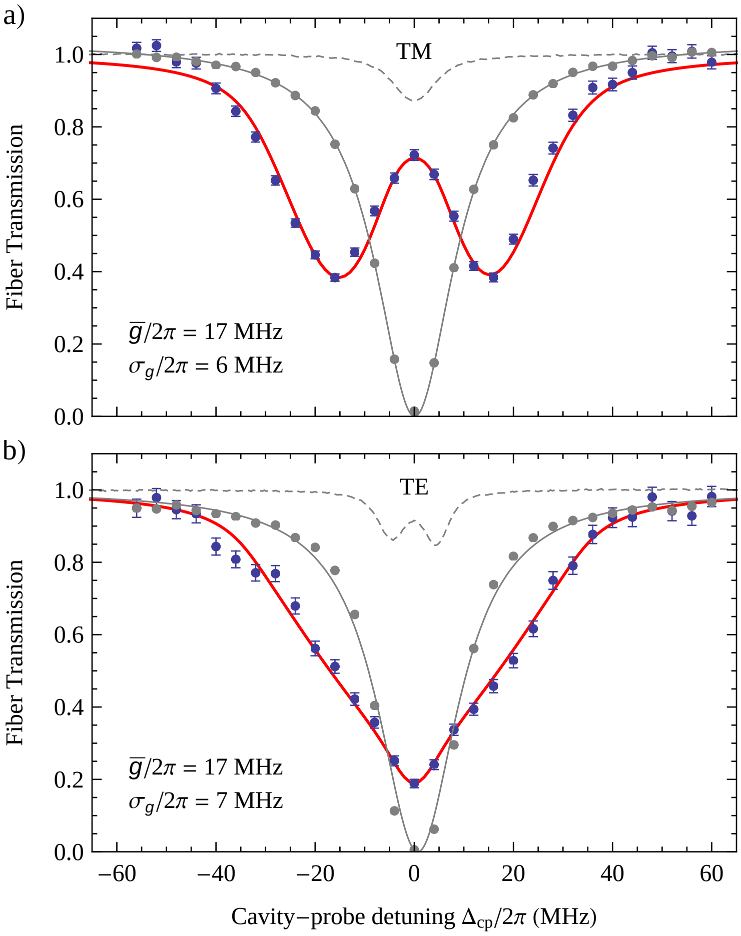

Figure 5.23: Experimental transmission spectra for a TM and a TE bottle mode: Coupling fiber transmission for the coupled atom–resonator system (blue points, error bars correspond to 1σ-statistical error) and the empty resonator (gray points). The gray line is a Lorentzian fit while the red lines corresponds to a simulated spectrum averaged over a g distribution with a mean value $\bar{g}$ and a standard deviation σ_g (see text). The parameters of the distribution are obtained from a fit of the simulated spectrum to the data in a) for TM and b) for TE polarization. The dashed lines in a)-b) correspond to the under-coupled empty cavity spectrum and show no (TM), or only weak (TE), splitting due to mode coupling.

predicted on-resonant transmission change is too small when an atom couples (see Fig. 5.22 b)). Therefore, we reduce the threshold in this case to $N_{\text{trig1}} = 4$ which is still high to avoid any false detection events in combination with the second trigger criterion.

When the FPGA-trigger signifies the presence of an atom, the light in coupling fiber 1 is switched for 500 ns to the probe light with same direction, polarization and power as the detection light. This field has a variable cavity–probe detuning $\Delta_{\text{cp}}/2\pi$ which is stepwise scanned over a range of $\pm 60\,\text{MHz}$, where per atomic transit event, only one frequency setting is measured. After the probing phase, the light is switched back to the detection field to allow for the evaluation of the second trigger criterion which is performed in post analysis in a time window of $\Delta t_{\text{trig2}} = 1\,\mu\text{s}$ and a threshold of $N_{\text{trig2}} = 2$. The transmission in the probing phase is averaged for each frequency detuning over typically 1000 detection events and normalized to the power of the incoming light field.

Figure 5.23 a) and b) show the transmission spectra which are obtained in this measurement for the TM and the TE mode, respectively. We observe a clear qualitative difference between the two cases: While for the TM mode the spectrum shows a two-peak vacuum Rabi-splitting with an on-resonant transmission change of $70\,\%$, the spectrum of the TE mode is dominated by a central peak which rises on resonance to only $20\,\%$. Thus, comparing the results with the simulations in Fig. 5.22, we observe clear evidence for the suppression of standing waves in the evanescent field of the TM mode while for the TE mode the small on-resonant transmission change indicates the presence of an uncoupled standing wave.

In order to analyze these results quantitatively with our theoretical model, we have to deal with the fact that the atoms are moving in the evanescent field and therefore no well defined coupling strength g exists. Therefore, we assume a normal distribution of coupling strength and calculate Rabi spectra for a range of g which are averaged according to the distribution. This averaged spectrum is fitted to the experimental data yielding a mean value $\bar{g}$ and a standard deviation σ_g which characterize the distribution of the coupling strength. At this point, we want to discuss the results of this analysis while the exact procedure will be described in more detail in the next section.

Excellent agreement is found between the measured data and the calculations of the theoretical model shown as red lines in Fig. 5.23 a)-b). In the case of the TM mode the simulations are able to reproduce the two-peak vacuum-Rabi splitting. This gives clear evidence that the situation indeed is very close to the case of a single mode cavity interacting with a two level atom. Moreover, also for TE polarization the spectral properties are very well described by our model. In particular, it becomes clear why the experimental TE spectrum rather resembles to a triangular shape than to the predicted three dips: When the spectrum is averaged over a larger set of coupling strengths g the three resonances start to merge together and form the characteristic triangular profile. From the fits to the data in Fig. 5.23 a)-b) we infer an average coupling strength of $\bar{g}/2\pi = 17\,\text{MHz}$ with a standard deviation of $\sigma_g/2\pi = 6\,\text{MHz}$ for the case of TM polarization whereas for TE polarization we also obtain $\bar{g}/2\pi = 17\,\text{MHz}$ with a standard deviation of $\sigma_g/2\pi = 7\,\text{MHz}$. Comparing these values to the resonator decay rate at critical coupling of $\kappa/2\pi = 10\,\text{MHz}$ and the natural linewidth of the ^{85}Rb D_2 line of $\gamma/2\pi = 3\,\text{MHz}$ we find a cooperativity of $C = g^2/2\kappa\gamma = 4.6$. Thus, the atom–resonator interaction evolves clearly in the strong coupling regime. Moreover, we note that for TM and TE polarization we observe almost identical distributions of the coupling strength. Therefore, it seems evident that although different trigger criteria where used in the two cases the measurement were performed on very similar ensembles of detected atoms.

Simulation of vacuum-Rabi spectra

We have already used our theoretical model to calculate single spectra for a well-defined value of the coupling strength g in Fig. 5.22. However, as mentioned before, in the experiment the

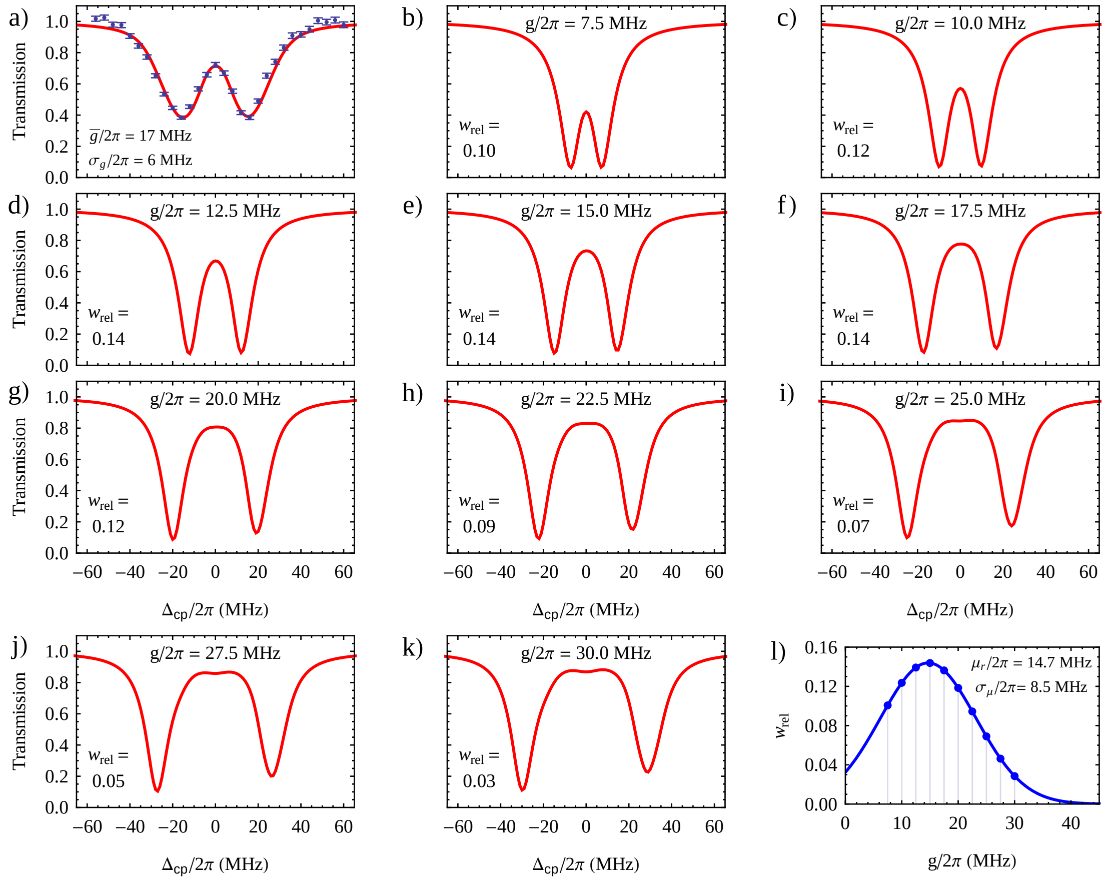

Figure 5.24: Procedure for the simulation of the experimental transmission spectra: a) Experimental spectra (blue points) from Fig. 5.23 a) for which the procedure is demonstrated exemplarily. b)-k) Simulated transmission spectra for a set of various coupling strengths g. Other parameter are $\kappa_0/2\pi = \kappa_{\text{ext}}/2\pi = 4.5\,\text{MHz}$, $\gamma/2\pi = 3\,\text{MHz}$, $h = 0$ and $B_t = 4.5\,\text{G}$. Taking Zeeman-shifts into account, the TM mode is set to resonance with the $|F = 3, m_F = 3\rangle \rightarrow |F' = 4, m_{F'} = 4\rangle$ D_2 transition of ^{85}Rb. The two resonator modes are TM-polarized with an overlap of 96 % with $\sigma_\pm$ polarization where only the E^+_{TM} mode is pumped from the coupling fiber. The intra-cavity photon number of the empty cavity then is 0.18. l) Normal distribution with the mean value μ_g and the standard deviation σ_μ describing the relative weighting w_{rel} of each simulated spectrum in the average spectrum which is fitted to the experimental data (red line in a)).

coupling strength will vary from shot to shot due to the motion of the atoms in the evanescent field. As a consequence, the variation of g has to be included in the simulation, in order to describe the experimental situation adequately.

For this purpose, we calculate for each experimental setting a set of theoretical spectra with varying g as demonstrated exemplary in Fig. 5.24 for the case of the TM mode. In this set $g/2\pi$ ranges from 7.5 MHz to 30 MHz where the lower value is the weakest coupling for which one still observes a reasonable on-resonant transmission modification and one thus expects the FPGA to trigger a measurement. The highest value corresponds to the coupling strength at a distance of approximately 50 nm from the resonator surface (compare Fig. 5.13). For closer distances g still increases but simultaneously due to the atom–surface interaction the frequency shift of the atomic transition becomes larger than g which effectively reduces the atom–resonator coupling [60, 100].

For simplicity, we assume g to vary according to a normal distribution. An average transmission spectrum of the set of coupling strength is calculated where the relative weight w_{rel} of each simulated spectrum is determined by the normal distribution. Then, using the mean and the standard deviation as only free parameters, the averaged spectrum is fitted to the experimental data. The resulting normal distribution is shown in Fig. 5.24 l).[22]

5.4.2 Magnetic field dependence of the vacuum-Rabi splitting

We have observed very different vacuum-Rabi spectra of the coupled atom–resonator system for TM and TE modes. The two dip structure in the spectrum of the E^{+}_{TM} mode is explained in our theoretical model by the almost perfectly σ_+ polarization of the mode which drives the cycling transition $|F = 3, m_F = +3\rangle \rightarrow |F' = 4, m_{F'} = +4\rangle$ and effectively decouples the atom from the counter-propagating mode. In order to verify that the atom is indeed in the extremal m_F-levels when it interacts with the resonator, we want to study the influence of an applied magnetic field on the vacuum-Rabi spectrum of the TM mode.

In the discussion of the atom lifetime in the evanescent field in section 5.3.3, it was already shown that the Zeeman shift of the hyperfine levels, originating from a magnetic field, changes the atomic transition frequencies and induces an atom–cavity detuning Δ_{ac}. Accordingly, one also expects an effect of the magnetic field in the vacuum-Rabi spectrum which should depend on the magnetic quantum numbers m_F and m'_F of the driven transition. To observe such effects, we measure the transmission spectrum of the same TM mode as in section 5.4.1 with identical experimental settings. The only difference is that now we set the TM mode resonant to the $|F = 3, m_F = 0\rangle \rightarrow |F' = 4, m_{F'} = 0\rangle$ transition which is not influenced by the magnetic field. Thus, atoms in a different Zeeman state ($m_F \neq 0$) should possess an atom–cavity detuning Δ_{ac} in the spectrum.

In a first set of experiments we send detection and probe light co-propagating through port 1 to the bottle resonator and detected at port 2 of the fiber network. Thus, mode E^{+}_{TM} is driven with σ_+ polarization is driven. For the first measurement of the transmission spectrum a magnetic field of $B_z = 4.5\,\text{G}$ is applied along the resonator axis. Thereafter, another spectrum with identical settings but with inverted magnetic field $B_z = -1.5\,\text{G}$ is measured. Note that the smaller amplitude of the magnetic field in this case originates from the residual stray fields in the chamber which create a positive magnetic offset field.

The spectra obtained from the measurements are shown in Fig. 5.25 a) and b). We observe for both cases a clear asymmetry of the spectrum which is, however, inverted when the sign of

---

[22] Note that the corresponding parameters μ_g and σ_μ of this continuous distribution are not the mean coupling strength $\bar{g}$ and the standard deviation σ_g of the discrete subset for which we calculated the spectra. These values can be obtained with the common definition for the mean value and the standard deviation for a discrete dataset where the weighting w_g of the considered values of g are given by the continuous distribution in Fig. 5.24 l).

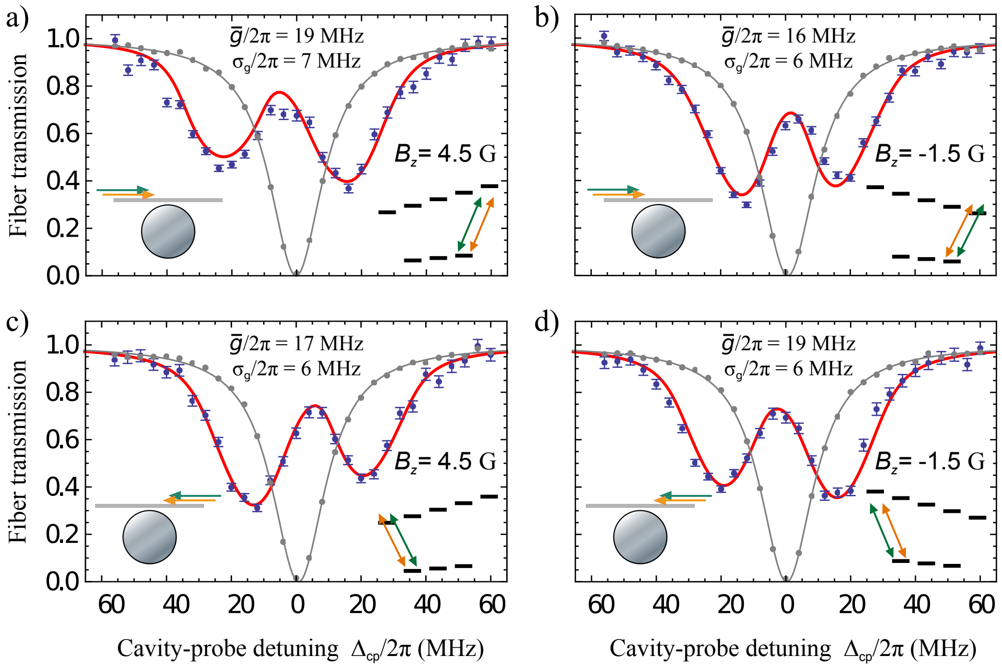

Figure 5.25: Vacuum-Rabi splitting of a TM-polarized mode coupled to single ^{85}Rb-atoms for different magnetic fields: Measured coupling fiber transmission (blue circles, error bars correspond to 1σ-statistical error) and simulated spectra (red lines) for a magnetic field of a) $B_z = 4.5\,\mathrm{G}$ and b) $B_z = -1.5\,\mathrm{G}$ along the resonator axis. The TM-mode is set resonant with the $|F=3, m_F=0\rangle \rightarrow |F'=4, m_{F'}=0\rangle$ transition. The inset show the propagation direction of detection (orange) and probing (green) field as well as an simplified atomic level scheme which indicates the driven transitions. c)-d) Same measurements but with detection and probe light propagating in opposite direction.

the magnetic field changes. The whole vacuum-Rabi spectrum is shifted to blue detuning for a positive magnetic field while a negative magnetic field induces a red-shift. This observation corresponds well to the Zeeman shift of the $|F=3, m_F=3\rangle \rightarrow |F'=4, m_{F'}=4\rangle$ transition which is 1.41 MHz/G for the ground state and 2.8 MHz/G for the excited state. As a consequence, the transition frequency becomes larger for positive and smaller for negative magnetic fields, as indicated in the insets of Fig. 5.25.

Thereafter, the same experiment is repeated, but with the detection and probe light send in from the opposite direction (through port 2 and detected at port 1 populating mode E^{-}_{TM}). The corresponding spectra are shown in Fig. 5.25 c) and d). Now, we find the asymmetry of the vacuum-Rabi spectra to be inverted compared to the case with the original probing direction in Fig. 5.25 a) and b). This observation qualitatively fits well to the predictions of our model, since for an inverse propagation of the detection and probe light fields the resonator mode E^{-}_{TM} is driven which has nearly σ_--polarization. Therefore, the atom is detected in the extremal state with $m_F = -3$ which has exactly the opposite magnetic field dependence than the $m_F = +3$

state.

For a quantitative comparison of the experimental results with our model we simulate and fit the transmission spectra with the method described in the preceding section. The simulated spectra are shown in Fig. 5.25 as red lines and agree well with the experimental data. In particular, the shift to positive and negative detuning for the corresponding magnetic field is correctly reproduced indicating that the atoms which interact with the resonator are indeed in the extremal $m_F = +3$ ($m_F = -3$) ground state when the mode E^+_{TM} (E^-_{TM}) is probed. For the situation in a) and b) we extract a mean coupling strength of $\bar{g}/2\pi = 19\,\text{MHz}$ with $\sigma_g/2\pi = 7\,\text{MHz}$ and $\bar{g}/2\pi = 16\,\text{MHz}$ with $\sigma_g/2\pi = 6\,\text{MHz}$ while for the case of c) and d) we obtain $\bar{g}/2\pi = 17\,\text{MHz}$ with $\sigma_g/2\pi = 6\,\text{MHz}$ and $\bar{g}/2\pi = 19\,\text{MHz}$ with $\sigma_g/2\pi = 6\,\text{MHz}$, respectively. The observed coupling strength are close to the one from the previous measurement such that we conclude that the detected atoms all follow a similar distribution of coupling strength. However, it is also interesting to note that we observe slightly higher coupling strengths for the case where the magnetic field increases the frequency of the closed cycling transition (see inset in Fig. 5.25 a) and d)). In this situation the detection light field is red-detuned to the atomic transition and one expects an attractive dipole force towards regions of higher fields strength as discussed in section 5.3.3. The opposite should be true for the blue-detuned detection field in Fig. 5.25 b) and c) which induces a repelling dipole force on the atoms and thus could lead to smaller coupling strengths. The observed difference in coupling strengths for red- and blue-detuned detection light is, however, rather small compared to the standard deviation $\sigma_g/2\pi = 6\,\text{MHz}$. Therefore, it is not possible to draw a definite conclusion whether the variation of $\bar{g}$ is induced by dipole forces or not. Nevertheless, taking into account as well the variations of the atom lifetime for red and blue detuning of the resonator field, investigated in section 5.3.3, this interpretation seems reasonable.

5.4.3 Suppression of coupling to the counter-propagating mode

The two dip structure of the experimental vacuum-Rabi spectrum of the TM mode and its dependence on the external magnetic field strongly indicate that the mode polarization of the evanescent field is close to circular, thereby driving coupled atoms on the cycling transition. What remains to be shown is that in this situation the counter-propagating mode should be practically decoupled from the atom, since it has nearly orthogonal polarization which couples to a much weaker atomic transition, as described in section 5.4.1.

In order to investigate this prediction, we next perform an experiment where atoms are detected with the E^+_{TM} (E^+_{TE}) mode and are then subsequently probed on the counter-propagating E^-_{TM} (E^-_{TE}) mode (compare Fig. 5.21 b-c)). For this purpose, we use the same TM and TE mode as in section 5.4.1 and send in detection light from port 1 of the fiber network under the same experimental conditions as in section 5.4.1, respectively. In contrast to the first measurements, this time the direction of the probing field is inverted relative to the detection field to drive the counter-propagating mode. In order to avoid any optical pumping effects, the duration of the probing phase is limited to 100 ns.

Figure 5.26 c) and d) show the transmission spectra which are measured for these conditions whereas a) and b) depict again the results from section 5.4.1 to allow comparison with the case where detection and probe light are send in from the same direction. While for the TE mode we observe the same spectrum as for the case of co-propagating probe and detection fields, the situation drastically changes for the TM mode, where an approximately empty resonator spectrum occurs. In order to compare these results with our theoretical model, we simulate the spectra according to the method described in section 5.4.1 with inverted probing direction. For the experiments with the TM mode in Fig. 5.26 a) and c) the coupling events are selected with the same trigger criterion and the only difference is the inversion of the probing direction. Thus, the distribution of the coupling strength g of the atoms should be identical for both cases. Likewise, for the TE mode the distribution of g obtained from the fit in Fig. 5.26 b) should also describe the situation in d). In order to test this hypothesis, we use the obtained fitting parameters from Fig. 5.26 a) for TM and b) for TE as input values for the simulations of the spectra in c) and d), respectively. Thus, the simulations for the inverted probing direction do not comprise any further fitting and are shown as red lines in the Fig. 5.26 c) and d).

Excellent agreement is found between the experimental data and the simulation. In the case of the TE modes the two identical spectra suggest that counter-propagating modes have indeed identical polarization. As a consequence, no matter which of the two running modes is probed, in both cases, the mode can be decomposed into the same two standing waves such that one standing wave has no intensity at the position of the atom. Thus, the uncoupled mode appears as central feature in the spectrum no matter which of the two running modes is driven.

In contrast, in the case of TM polarization the detection of an atom with one mode and the subsequent probing on the corresponding counter-propagating mode flips abruptly the polarization of the resonator light field to the orthogonal polarization. During the detection phase with nearly σ_+ polarized light with the mode E^+_{TM} the atom will be detected most likely in the extremal ground state $|F = 3, m_F = 3\rangle$ where it cycles on the closed $|F = 3, m_F = 3\rangle \rightarrow |F' = 4, m_{F'} = 4\rangle$ transition. When suddenly the probing field which couples to the counter-propagating resonator mode E^-_{TM} with nearly σ_- polarization is switched on, the transition $|F = 3, m_F = 3\rangle \rightarrow |F' = 4, m_{F'} = 2\rangle$ is driven. In this case, the level scheme in Fig. 5.21 a) shows that the transition strength is more than 1 order of magnitude smaller than the one for the closed cycling transition. Accordingly, the effect of the atom–light coupling on the spectrum is much weaker.

There is, however, a second effect which reduces the coupling of the E^-_{TM} mode to the atom which is illustrated in Fig. 5.27 b). Due to the multilevel structure of the atom the resonator field can interact with many transitions. In the discussion of the Jaynes-Cumming model it was shown that for strong coupling even an empty resonator mode leads to a vacuum-Rabi splitting of the energy levels. In our experiment this means that the E^+_{TM} mode not only couples to the cycling transition but also to all other $\Delta m_F = +1$ transitions, leading to the formation of dressed states even when the mode is not populated. Thus, the interaction with the $|F = 3, m_F = 1\rangle \rightarrow |F' = 4, m_{F'} = 2\rangle$ transition results in a vacuum Rabi-splitting of the $|F' = 4, m_{F'} = 2\rangle$. The coupling between the $|F = 3, m_F = 1\rangle \rightarrow |F' = 4, m_{F'} = 2\rangle$ transition and the E^+_{TM} is approximately 4 times stronger than the coupling between the $|F = 3, m_F = 3\rangle \rightarrow |F' = 4, m_{F'} = 2\rangle$ transition and the E^-_{TM} mode. As a consequence, the vacuum-Rabi splitting induces by the E^+_{TM} will dominate the $|F' = 4, m_{F'} = 2\rangle$ excited state and detune it relative to the resonance frequency of the E^-_{TM} mode. Thus, the counter-propagating mode has not only a much weaker coupling to the atom but is also off-resonant. Thereby the atom–light interaction is suppressed

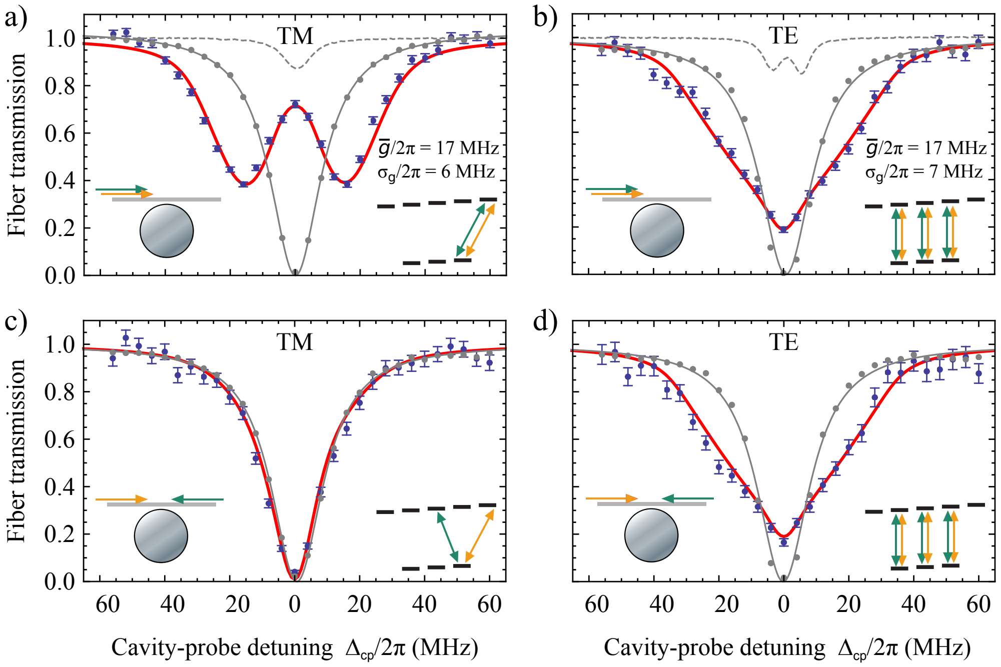

Figure 5.26: Experimental transmission spectra of a TM and a TE bottle mode for different probing directions: Coupling fiber transmission for the coupled atom–resonator system (blue points, error bars correspond to 1σ-statistical error) and the empty resonator (gray points). The plots in a) and b) are the same as in Fig. 5.23. For a)-b) the probing light (green) co-propagates with the detection light (orange) while for c)-d) the two light fields are counter-propagating as shown by the insets. The insets illustrate as well the dominant driven transitions in a simplified atomic level scheme. The gray line is a Lorentzian fit while the red lines corresponds to a simulated spectrum averaged over a distribution of g with a mean value $\bar{g}$ and a standard deviation σ_g. The parameters of the distribution are obtained from a fit of the simulated spectrum to the data in a) for TM and b) for TE which then enter as fixed parameters for the simulations in c)-d).

efficiently resulting in the appearance of the empty resonator spectrum in Fig. 5.26 c).

In order to estimate the contribution of the these two effect to the decoupling of the counter-propagating mode, we simulate a vacuum-Rabi spectrum where the atom exclusively couples to the $E^-_{\rm TM}$ mode and the interaction with the $E^+_{\rm TM}$ mode is switched off, as shown in Fig. 5.27 a). Similar to the analysis before, the coupling is average over the distribution of coupling strength g obtained from the fit in Fig. 5.26, however, reduced by a factor $1/\sqrt{28}$ corresponding to the ratio of g between the $|F=3, m_F=3\rangle \rightarrow |F'=4, m_{F'}=2\rangle$ and the cycling transition. Figure 5.27 c) shows the simulated spectrum of the fiber transmission when the interaction with the $E^-_{\rm TM}$ mode is exclusively taken into account as well as the result from the simulation with the full model. For the case where only the interaction with the $E^-_{\rm TM}$ mode is present, the spectrum is dominated by Lorentzian-like resonance. However, one finds also a small kink on the resonance at positive detuning which is a residual signature of the atom–light interaction. To obtain the

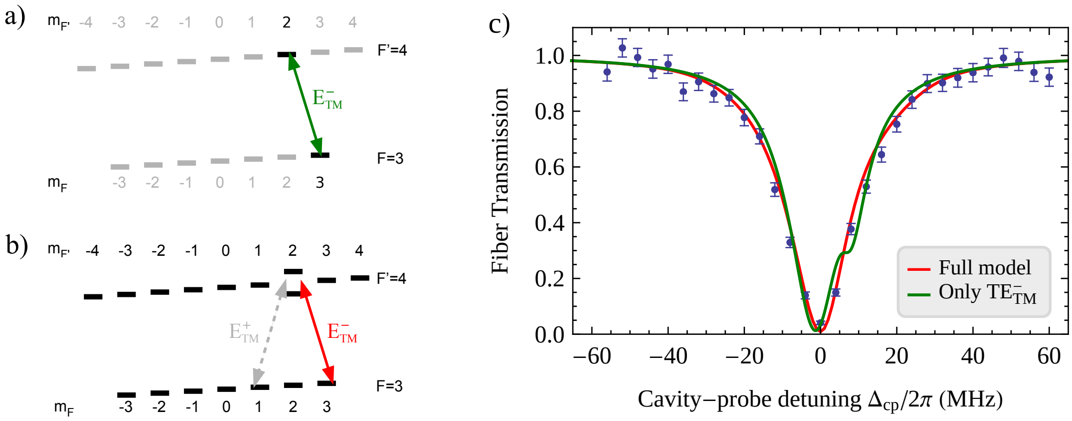

Figure 5.27: Modeling of the coupling between the E^-_{TM} mode and the atom in the $m_F = +3$ ground state. a) Level scheme of the ^{85}Rb D$_2$ line where only the levels $|F = 3, m_F = 3\rangle$ and $|F' = 4, m_{F'} = 2\rangle$ are taken into account for the modeling of the interaction between the E^-_{TM} mode and the atom. b) Taking into account the full multi-level structure of the atom for the modeling, the coupling to the empty E^+_{TM} mode induces a vacuum-Rabi splitting of the excited $m_F = +2$ state (Note that also all other excited state have a vacuum-Rabi splitting which is left out here for clarity). c) Data from Fig. 5.26 c) (blue points) and simulated spectra for the modeling in a) and b). The spectra are averaged over a distribution of the coupling strength g as explained in the text.

experimentally observed empty cavity resonance it is necessary to include also the interaction of the $|F = 3, m_F = 1\rangle \rightarrow |F' = 4, m_{F'} = 2\rangle$ transition with the E^+_{TM} mode into the modeling. As predicted by our model, both effects together result in an effective decoupling of the atom from the counter-propagating resonator mode. Therefore, an atom in the $|F = 3, m_F = 3\rangle$ state dominantly interacts with the E^+_{TM} mode on the cycling transition. Thus, despite the multi-level structure of the atom and the presence of two resonator modes, we actually encounter a situation close to the idealized scenario of the Jaynes-Cummings model in which a two-level atom couples to a single cavity mode.

5.5 Atomic state preparation via optical pumping

The experimental and theoretical study of vacuum-Rabi spectra for the TM mode in section 5.4.1, as well as the measurements of the atom lifetime in section 5.3.3, clearly indicate that at the end of the detection phase the atoms are in an extremal m_F state. So far we have, however, not addressed the question whether our detection scheme only reacts on atoms that are initially in this state, or if the state is actively prepared during detection. The latter option would require optical pumping of the atom from an arbitrary ground state of the $F = 3$ manifold to the outer m_F state. Since TM modes overlap almost perfectly with circular polarization, optical pumping should naturally occur in our system. If the atom is detected, e.g., with the E^+_{TM} in the $m_F = +3$ state, it should be possible, by exciting the counter-propagating E^-_{TM} mode with σ_--polarization,

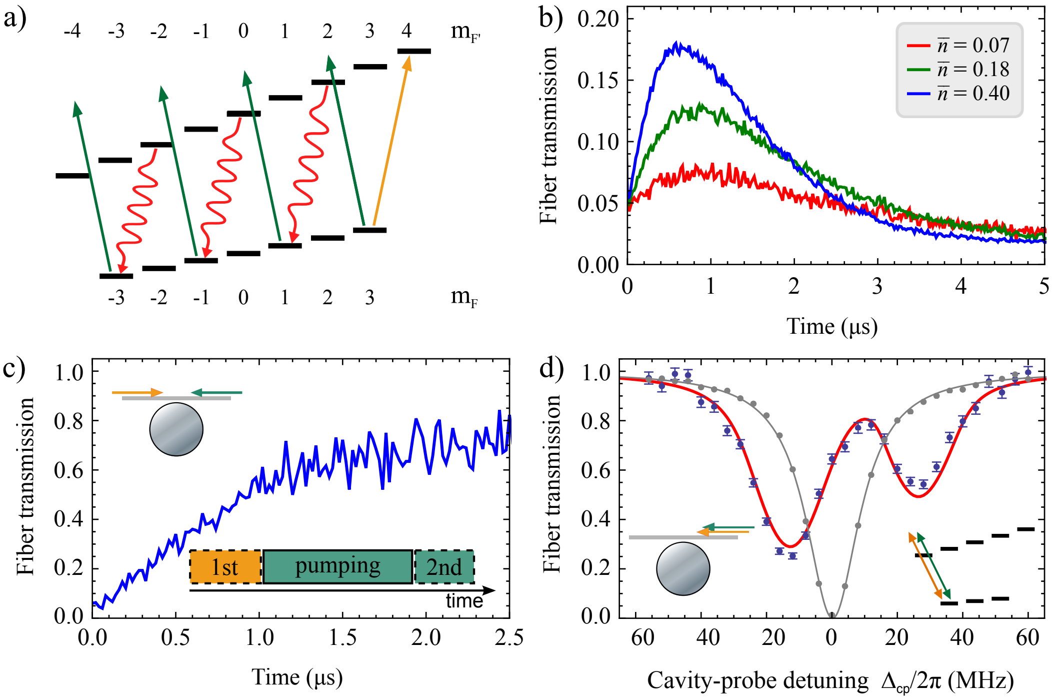

Figure 5.28: Observation of optical pumping in a TM mode: a) Level scheme illustrating the pumping process: The TM-mode, the detection light (orange) and the probe light (green) are resonant with the $|F = 3, m_F = 3\rangle \rightarrow |F' = 4, m_{F'} = 4\rangle$ transition. The probe field is send in with opposite direction, driving the counter propagating mode thereby inducing optical pumping to the $m_F = -3$ ground state. b) Averaged fiber transmission where after the atom detection, probe light is send in inverse direction to the detection field with three different powers corresponding to the denoted mean intra-cavity photon numbers $\bar{n}$ when no atom is present. c) Average fiber transmission for $\bar{n} = 0.4$ where after $2.5\,\mu$s the second trigger criterion is evaluated (see text). Insets illustrate the propagation direction of detection and probe light and the temporal scheme of the two detection and the probing phases where the colors indicate the involved light fields. d) Transmission spectrum corresponding to the situation where the atom has been pumped into the $m_F = -3$ state (for explanation of color codes and insets see Fig. 5.26).

to pump the atom to the opposite side of the atomic level scheme in the $m_F = -3$ state, as shown in Fig. 5.28 a). However, the coupling of an atom to the resonator field is limited to few microseconds. Here, we want to study if optical pumping occurs on this timescale, and if it is possible to manipulate the internal state of the atom.

We realize the desired experimental situation by tuning the $q \approx 3$ TM mode in resonance with the $|F = 3, m_F = 3\rangle \rightarrow |F' = 4, m_{F'} = 4\rangle$ transition taking into account the Zeeman shift of the guiding magnetic field with $B_z = 4.5\,$G. We critically couple coupling fiber 1 to the bottle resonator and send resonant detection light via port 1 into the fiber network. Thereby, the E^+_{TM} mode is populated with a mean intra-cavity photon number of $\bar{n} = 0.18$ when no atom is present. The first trigger criterion is evaluated with the standard settings of $\Delta t_{\text{trig1}} = 1.28\,\mu\text{s}$ and $N_{\text{tresh1}} = 6$ at the SPCMs at port 2 of the fiber network. Whenever an atom is detected in the evanescent resonator field the FPGA switches from the detection to the counter-propagating probe field which is sent in via port 2 to resonantly excite the E^{-}_{TM} mode. Afterwards, the probe light is detected at port 1 of the fiber network. In contrast to all preceding experiments, the probe light remains activated for 7 μs such that it is on during the whole remaining atom lifetime and only then we switch back to the detection beam. The measurement is performed for three different powers of the probing light field.

Figure 5.28 b) shows the average normalized transmission of coupling fiber 1 for the probe light after an atom detection. Initially, the transmission is very low and reproduces the measurement on-resonant value from the empty cavity spectrum in Fig. 5.26 c) where we concluded that the probed, σ_--polarized mode is practically uncoupled from the atom. However, for longer times we observe an increase of the transmission, where the timescale depends on the probing power. When no atom is present the probing powers correspond to intra-cavity photon numbers of $\bar{n} = 0.07$, $\bar{n} = 0.18$ and $\bar{n} = 0.4$. With a linear fit to the data we extract the initial slope of the transmission increase for the three probing powers to be $0.06\,\mu\text{s}^{-1}$, $0.18\,\mu\text{s}^{-1}$ and $0.37\,\mu\text{s}^{-1}$, respectively. Thus, there is a linear dependence between the photon flux and the rate of the initial transmission increase. For larger times the transmission drops exponentially which we attribute to the loss of the atoms from the evanescent field due to their motion.

In order to exclude these premature atom losses from the analysis, we perform an extensive analysis of the case $\bar{n} = 0.4$. For this purpose, we apply the second trigger criterion to the data thereby post-selecting only events where after $2.5\,\mu\text{s}$ the transmission has more than $N_{\text{tresh2}} = 6$ counts in a time window of $\Delta t_{\text{trig2}} = 1\,\mu\text{s}$. Note that in contrast to the other experiments we evaluate the second trigger using the probe transmission in reverse direction and that the threshold level has been adapted to the higher probing powers. In Fig. 5.28 c) the average normalized transmission of coupling fiber 1 is shown for $\bar{n} = 0.4$ when the second trigger criterion is applied. We now observe an linear increase of the transmission which saturates around 70 % to a stable value. This behavior is a strong indicator that we indeed observe optical pumping: Initially when the atom is detected in the $m_F = +3$ ground state and subsequently probed with σ_--polarized light, the driven $|F = 3, m_F = 3\rangle \rightarrow |F' = 4, m_{F'} = 2\rangle$ transition is only weakly coupled to the resonator (see level scheme in Fig. 5.28 a)) and we observe a transmission close to an empty cavity. However, when the probe light is applied long enough the atom eventually scatters a photon and is then transferred under the emission of an σ_+-photon to the $m_F = 1$ ground state. Therefore, after three such scattering events the atom ends up in the $m_F = -3$ ground-state on a closed cycling transition where it recovers the situation of a single cavity mode coupled strongly to a two-level atom. Moreover, our observation that the initial transmission increase scales linear with the incoming photon flux is in excellent agreement with the fact that at $t = 0$ the probability to scatter photons should depend linearly on the power of incoming light, if the emission into free space is negligible. Thus, the increase of the transmission over time in Fig. 5.28 b) and c) is a strong indication that the described scattering of photons and the thereby induced pumping actually takes place.

To verify that the final transmission of 70 % in Fig. 5.28 c) fits to the expected on-resonant transmission, we perform a measurement of the corresponding vacuum-Rabi spectrum. For this purpose, the propagation direction of the detection field is inverted to be identical to the probe field and the standard procedure for the measurement of a transmission spectrum is performed. The TM mode and the detection light are kept resonant to the $|F = 3, m_F = 3\rangle \rightarrow |F' = 4, m_{F'} = 4\rangle$ with $B_z = 4.5\,\mathrm{G}$. Upon an atom detection the probe light is switched on for $500\,\mathrm{ns}$ before we switch back to the detection light for the second trigger evaluation. Under these experimental condition the atom should be prepared during the detection phase in the $m_F = -3$ ground state and the measured spectrum should correspond well to the steady state which the system reaches after the optical pumping process shown in Fig. 5.28 c). The obtained vacuum-Rabi spectrum is depicted in Fig. 5.28 d) and shows a strong asymmetry which indicates that the probed atomic transition is red-shifted to the resonator light field. This behavior is expected as the cavity is resonant to the $|F = 3, m_F = 3\rangle \rightarrow |F' = 4, m_{F'} = 4\rangle$ transition whereas we detect and probe the atom on the $|F = 3, m_F = -3\rangle \rightarrow |F' = 4, m_{F'} = -4\rangle$ transition that has a 13 MHz smaller transition frequency which is due to Zeeman shift of the applied magnetic field. The simulated spectrum fitted to the data supports this interpretation. In particular, one finds an on-resonant transmission value of approximately $70\,\%$ which fits well to the final value of the fiber transmission in Fig. 5.28 c). We therefore conclude that the atom is indeed pumped from the $m_F = +3$ to the $m_F = -3$ ground state when the mode with σ_- polarization is driven.

To summarize, in this section we could not only gain another confirmation that our detection scheme triggers on atoms in an extremal m_F state, but also that it is possible to transfer the atom to the opposite extremal state of the level scheme with $-m_F$ by optical pumping. This process depends on the power of the pumping light and can be performed well during the lifetime of the atom in the evanescent field. It therefore seems reasonable that the detection mechanism not only reacts on atoms which are already initially driven on the cycling transition, but that also atoms in other ground states are pumped into these extremal m_F states states during the detection phase.

5.6 Summary of the experimental results

Within this chapter we experimentally studied the role of non-transversal polarization in light–matter interactions. The chapter started with an introduction to the CQED setup, describing the vacuum system, the atomic fountain as source of cold ^{85}Rb-atoms, and the bottle resonator coupling setup comprising nano-positioning units of two ultra-thin fibers and the fiber network.

Using this setup we have measured the signals of single atoms transiting the evanescent field of the bottle resonator in the coupling fiber transmission. Based on this effect, a real-time detection and probing system for the study of the transit events was developed. Thereby, we were able to measure vacuum-Rabi spectra of single atoms coupled to a WGM microresonator which clearly demonstrate strong coupling and a distinct vacuum-Rabi splitting.

We observed a fundamentally different vacuum-Rabi spectra for the case of TM and TE modes. The latter can be well described with the standard model of WGM microresonators of a two-mode ring cavity where the identical polarization of counter-propagating modes results in the formation of a standing wave which is uncoupled from the atom. For the TE mode, we found a clear indication for this uncoupled standing wave in the vacuum-Rabi spectrum which is dominated by a central resonance. This resonance limits the transmission change an atom can induce to 25 % and thereby effectively reduces the light-matter interaction strength of the system.

In contrast, for the TM mode, a vacuum-Rabi splitting into two distinct resonances is observed similar to the case of a Fabry-Pérot resonator. The spectrum gives clear evidence for the prediction of our theoretical model from chapter 4: The non-transversal polarization of TM modes results in nearly orthogonal polarization of counter-propagating modes such that no destructive interfere occurs between them. Moreover, the two mode polarizations overlap strongly with σ_+- and σ_--polarized light and therefore optical pumping between the internal states of the atom occurs. We quantitatively studied these effects in the vacuum-Rabi spectrum, in the dependence of the atomic lifetime in the resonator field on an external magnetic fields and as function of the propagation direction of the light in the resonator. Excellent qualitative and quantitative agreement was found between the experimental data and the theoretical predictions based on our model. In particular, in the case of TM polarization, the atom is already prepared during the detection process in a well defined extremal m_F level of the atomic ground state. In this situation the atom interacts on the closed cycling transition with the driven resonator mode, which has the strongest coupling strength. Simultaneously, the second, counter-propagating mode is only weakly coupled to the atom. As a consequence, despite the simultaneous existence of two degenerate resonator modes, this effectively results in the ideal situation of a two-level atom interacting with a single traveling-wave mode.

As we will see in the next chapter, the non-transversal polarization properties of WGMs allow one to realize powerful applications like a very efficient switch for light controlled by a single atom, and open up the routes towards the non-destructive detection of photons and the generation of optical Schrödinger-cat states.

CHAPTER 6

Switching Light with a Single Atom

The ability to control and manipulate optical signals has become the fundament of many applications affecting our daily life. To cite a view examples: the main part of today's worldwide communication over long distances relies on optical fiber networks which require the efficient routing of optical signals. Moreover, the trend in computer architecture to parallelize computation demands for increasing on-chip communication bandwidth between the processing units, which will be most likely realized in-next generation chips with the help of photonic technologies [131]. These applications require devices which are able to manipulate optical signals with high speed and efficiency and at the same time can be well integrated into existing architectures. In this context, optical resonators have proven to be reliable tools in order to combine and to separate different wavelength channels in so called "wavelength-division multiplexers". The basic element in theses devices is a waveguide switch which, depending on the wavelength, reroutes an optical signal to different output ports. Naturally, this can be performed with an optical resonator as wavelength selective element, which couples to one or more waveguides. Because of the highly efficient evanescent in- and out-coupling of light and the compatibility to existing silicon fabrication techniques, whispering-gallery-mode microresonators are ideal candidates to realize such optical switches.

The on-going miniaturization of computer architectures pushes the circuit size constantly closer to the quantum regime. As a consequence, it seems to be only a matter of time until single bits of information will be represented by individual quantum systems. As this trend towards quantum computation coincides with the progressive integration of photonics into computer architectures, it is of great relevance to develop devices which work at the interface of these technologies. In this context, scaling a waveguide-coupled optical switch into the quantum domain, where a single quantum system controls the flow of light, would be an important step towards the implementation of quantum communication and information protocols. Making use of the quantum nature of such a switch would also open up completely new applications as, e.g., the preparation of non-classical states of light for improved quantum metrology experiments [132, 133].

In this chapter a fiber-optical switch controlled by a single atom is demonstrated. We begin the chapter with an overview of classical optical switching devices which are based on WGM resonators and then show how such a switch can be realized with the bottle microresonator in the CQED experiment. Then, we analyze the performance of the switch according to classical criteria as well as in terms of quantum effects which arise due to the control by the single atom. Finally we discuss the perspective of possible applications which the switch could enable.

The results of this chapter were published in [111].

6.1 Overview of optical switching with WGM micro resonators

The optical routing capabilities of WGM microresonators have been investigated and demonstrated in numerous theoretical and experimental studies. The realized capabilities are well summarized in Ref. [41], and range from passive device like simple stop- and passband filters [134–136], over higher-order filters [137–139], to active devices based on non-linear effects in the resonator allowing all-optical switching [140–143].

In general all these approaches have in common that they rely on the frequency selective properties of the resonator spectrum to absorb or reroute an optical signal. To control the flux of light between different output ports with a WGM microresonator, several possible approaches exist. Technically, the straight forward solution is to couple a single waveguide to the resonator and to exploit the internal mode coupling. If the mode scattering rate is high enough, resonant light that couples into the resonator is scattered into the counter-propagating mode, from where it couples back into the waveguide. Thus, resonant light is reflected from the WGM resonator while off-resonant light is transmitted. This technique has been employed in several experiments and has proven to work with almost unity efficiency [29, 73, 89]. However, in this approach the light remains in the same waveguide and only the propagation direction is inverted. Thus, the reflected signal can not be accessed easily without affecting as well the incoming light.

Therefore, an alternative option is to operate the WGM resonator in the so called add-drop configuration which was introduced in section 2.4.6. In this scheme light is transferred between two waveguides which couple both to the resonator as shown in Fig. 6.1 a) for the case of our bottle resonator. The bus fiber is critically coupled to the combined resonator–drop fiber system so that resonant light is transferred completely into the resonator. When the coupling of the drop fiber dominates the intrinsic resonator losses light is preferentially transferred into the drop fiber. The transfer efficiency between the bus and drop fiber can reach values higher than 93 % [74,79]. Thus, the add-drop configuration actually realizes a real separation of resonant and off-resonant light into two independent output modes. Moreover, it was demonstrated that based on the Kerr effect, non-linear all optical switching can be realized with a bottle resonator in the add-drop configuration where the power of the incoming light determines the output channel [79].

The goal of the work presented in this chapter is to establish the add-drop configuration with a bottle microresonator in the quantum regime where the switching process is no longer controlled by classical effects like the Kerr-nonlinearity but instead by a single quantum system.

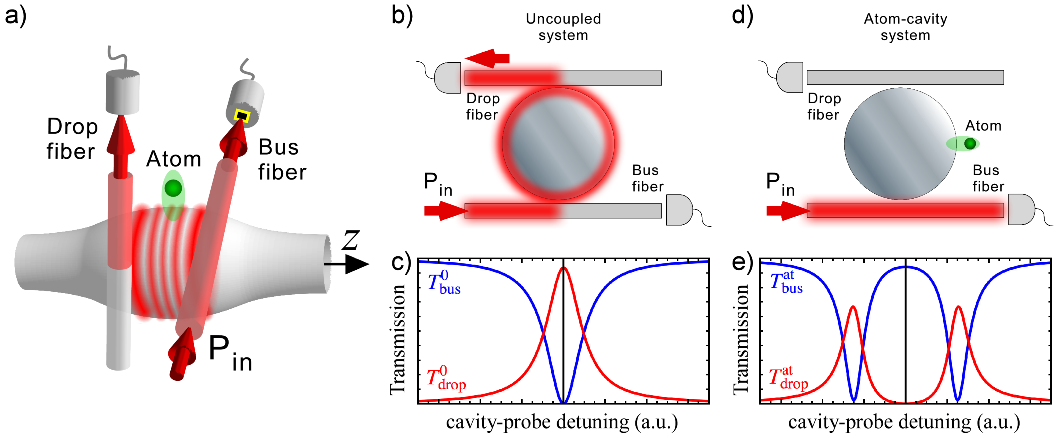
a)
Drop fiber
Atom
Bus fiber
Z
P_{in}
b)
Uncoupled system
Drop fiber
P_{in}
Bus fiber
c)
Transmission
T^0_{bus}
T^0_{drop}
cavity-probe detuning (a.u.)
d)
Atom-cavity system
Drop fiber
Atom
P_{in}
Bus fiber
e)
Transmission
$T^{\text{at}}_{\text{bus}}$
$T^{\text{at}}_{\text{drop}}$
cavity-probe detuning (a.u.)

Figure 6.1: Concept of the optical fiber switch based on the bottle resonator. a) Two fibers are coupled to the bottle resonator in add-drop configuration. To control the light flux between the bus and the drop fiber a single atom is broad in the evanescent resonator field. b) Uncoupled system: The bus fiber is critically coupled so that the complete incoming light power P_{in} is transferred into the resonator from where it couples to the drop fiber. c) Corresponding spectrum of the system with the bus and drop fiber transmissions T^0_{bus} (blue) and T^0_{drop} (red). d) Coupled system: The atom blocks the build-up of an intra-cavity field and the light remains in the bus fiber. e) Corresponding transmission spectrum showing the vacuum-Rabi splitting of $T^{\text{at}}_{\text{bus}}$ and $T^{\text{at}}_{\text{drop}}$ which prevents the build-up of an intra-cavity field on resonance. Figures appeared in Ref. [111].

6.2 Concept of an optical switch controlled by a single atom

When the bottle resonator is operated in the add-drop configuration the switching process of light between the bus and the drop depends on the resonance frequency of the resonator mode compared to the frequency of the incoming light. Thus, by controlling the resonance frequency of the resonator, light can be switched between the two output ports. In the switching scheme presented here the control should be realized with a single atom. For this purpose, we want to exploit the spectral change an atom induces to the system when it couples strongly to a TM polarized bottle mode.

In Fig. 6.1 a) the concept of the optical switch is illustrated. The resonator is coupled to the bus and drop fiber and the fiber separations are chosen such that the bus fiber critically couples the combined drop fiber–resonator system fulfilling the condition

$$\kappa_{\text{bus}} = \sqrt{(\kappa_0 + \kappa_{\text{drop}})^2 + h^2}\,. \tag{6.1}$$

According to chapter 2, κ_{bus} and κ_{drop} are the coupling rates between the corresponding fibers and the resonator mode, κ_0 represents the intrinsic resonator loss and h is the mode–mode scattering rate. In this situation, as depicted in Fig. 6.1 c) the transmission through the bus fiber T^0_{bus} drops on resonance to zero meaning that resonant light will be transferred completely into the resonator. Simultaneously, when $\kappa_{\text{drop}} \gg \kappa_0, h$ light in the resonator is preferentially coupled out into the drop fiber T^0_{drop}. This situation corresponds to the ON state of the switch.

In order to prepare the OFF state of the switch, an atom is introduced in the evanescent field of the bottle resonator. If the atom is in a state with a transition resonant to the cavity, the resonance condition of the system is modified drastically compared to the uncoupled case. This has been demonstrated in chapter 4 and 5, where we have found that for the case of a TM polarized mode the vacuum-Rabi splitting results in a large on resonant transmission change as shown in Fig. 6.1 e). Thus, the atom prevents the build-up of an intra-cavity field and as a consequence ideally no light is transferred from the bus into the drop fiber.

This application demonstrates the advantages of the light–matter interaction arising from non-transversal TM modes. As we have shown in chapter 5, the non-transversal field of TM modes can realize a situation where only a single resonator mode interacts strongly with a two-level atom. Thus, the vacuum-Rabi splitting has considerable influence on the system's spectrum resulting in a large extinction of light in the drop fiber. In contrast, for TE polarization the uncoupled standing wave mode will dominate the spectrum even when an atom couples strongly to the resonator, as shown in Fig. 5.22 b). As a consequence, only low switching contrasts can be expected in this case. Thus, efficient switching in the add-drop configuration by a single atom can is only possible with TM polarized bottle modes.

6.3 Experimental realization and characterization of the switch

6.3.1 Experimental setup

In order to realize the optical switch with the CQED setup, both ultra-thin fibers have to be coupled to the bottle resonator. For the experiment, we assign coupling fiber 1 as bus fiber whereas coupling fiber 2 serves as drop fiber (see overview of fiber network in Fig. 5.10). The simultaneous operation of two coupling fibers at the resonator requires very good stability of the resonator–fiber gaps. Although the coupling setup in the current experiment is well isolated from external mechanical vibrations and acoustic noise, there is a residual slow drift of the resonator–fiber gap during the measurements. We compensate for this drift approximately every 3 min with a procedure similar to the one for a single coupling fiber. More details on the drift compensation can be found in Ref. [60].

For the measurement, we select the TM mode with axial quantum number $q \approx 3$ and $\kappa_0/2\pi = 5\,\text{MHz}$ which has been already used for the experiments in chapter 5 and tune its resonance frequency to the $|F = 3, m_F = 0\rangle \rightarrow |F' = 4, m'_F = 0\rangle$ transition of the ^{85}Rb D$_2$-line. The fibers are aligned such that the bus fiber critically couples the drop fiber–resonator system according to Eq. (6.1). For the further analysis, we neglect the mode coupling rate which is $h/2\pi < 2\,\text{MHz}$ and therefore rather small compared to the other coupling rates of the system. Light is sent into the fiber network through port 1 along the bus fiber and detected at port 2 with two SPCMs. Light which couples from the resonator into the drop fiber is monitored at port 3 with two additional SPCMs.

Single atoms are delivered to the evanescent field of the bottle resonator by the atomic fountain which is operated according to the procedure described in chapter 5. In order to detect a single-atom coupling event, we send light resonant with the TM mode and a power of 15 to 20 photons$/\mu$s along the bus fiber. The transmission increase caused by the atom in the evanescent resonator field is detected with the FPGA which evaluates the first trigger criterion with the parameters $\Delta t_{\text{trig1}} = 1.28\,\mu$s and $N_{\text{trig1}} = 6$. If not stated otherwise in the text, we post-analyze the detected events with the second trigger criterion $1\,\mu$s after the detection with $\Delta t_{\text{trig2}} = 1\,\mu$s and $N_{\text{trig2}} = 2$.

6.3.2 Demonstration of optical switching with a single atom

In order to investigate the influence of the atom on the resonator in the add-drop configuration, we measure the spectrum of the coupled system. For this purpose, the same method as in section 5.4.1 is employed: Upon an atom trigger, the detection light is switched off and a probe field with equal power but variable detuning to the resonator mode is turned on for $1\,\mu$s. For the measurement, the bus fiber is critically coupled to the combined resonator–drop fiber system with the individual decay constants $\kappa_{\text{bus}}/2\pi = 11\,\text{MHz}$ and $\kappa_{\text{drop}}/2\pi = 6\,\text{MHz}$.

In Fig. 6.2, the transmission spectra of the bus and drop fiber are shown: If no atom is coupled to the bottle mode, we observe a clear drop of the bus fiber transmission for resonant light to $T^0_{\text{bus}} = 3\,\%$ while about $T^0_{\text{drop}} = 58\,\%$ of the incoming light is transferred into the drop fiber. The interaction with a single atom drastically changes the spectral properties of the system. As depicted in Fig. 6.2 a), the bus fiber transmission reveals a vacuum-Rabi splitting in this situation which results in an increase of the on-resonant transmission by 12 dB to $T^{\text{at}}_{\text{bus}} = 46\,\%$. Also the drop fiber transmission in Fig. 6.2 b) shows the signature of the vacuum-Rabi splitting which decreases the amount of transferred light on resonance to $T^{\text{at}}_{\text{drop}} = 12\,\%$ yielding an extinction of 7 dB.

The spectra of the bus and drop fiber clearly demonstrate the underlying physical effect of the optical switch: When a single atom interacts strongly enough with the bottle resonator, the dressed states of the coupled system emerge with new eigen-frequencies as is apparent from the vacuum-Rabi splitting. As a consequence, the atom prevents the build-up of the intra-cavity field and the transfer of light to the drop fiber is suppressed.

In order to verify this interpretation quantitatively, we simulated the spectra for the parameters of the experiment with our theoretical model from chapter 4. The coupling to the drop fiber can be treated in the model as an additional loss channel with rate κ_{drop}, yielding a transmission to the drop fiber of $T_{\text{drop}} = |\langle \hat{a} \rangle \sqrt{2\kappa_{\text{drop}}}/s_{\text{in}}|^2$, where $\langle \hat{a} \rangle$ is the expectation value of the resonator field and s_{in} is the amplitude of the incoming light field in the bus fiber. To account for the motion of the atom in the evanescent resonator field, we follow the procedure described in section 5.4.1 and calculate for both fibers an average spectrum of coupling strengths ranging from $g/2\pi = 7.5\,\text{MHz}$ to 30 MHz. Then, the spectra are fitted to the experimental data in Fig. 6.2 a) and b) assuming the same normal distribution of g for both spectra with the mean $\bar{g}$ and the standard deviation σ_g as fitting parameters. The obtained spectra are shown in Fig. 6.2 as solid lines and show good agreement with the experimental data. We attribute the residual deviation between theory and experiment to the small ill-defined magnetic off-set field in the science chamber. Note that at the time of the measurement, the external field coil that is described in section 5.1.5 was still not integrated into the setup.

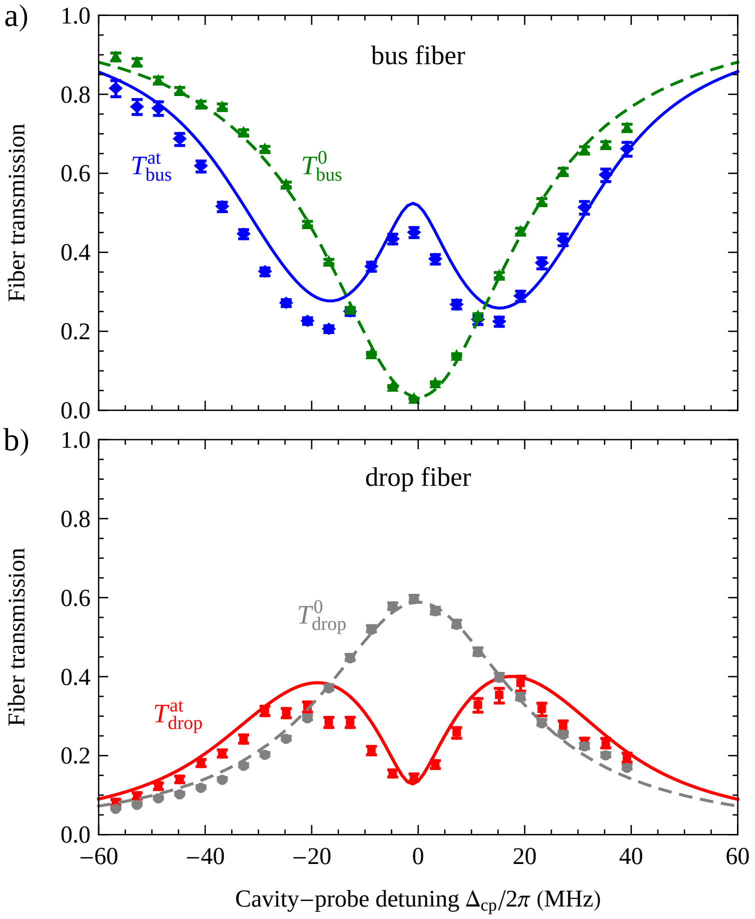

Figure 6.2: Normalized transmission spectra without and with atom coupled to the bottle resonator a) through the bus fiber $T_{\mathrm{bus}}^{0,\mathrm{at}}$ (green triangles, blue diamonds) and b) from the bus to the drop fiber $T_{\mathrm{drop}}^{0,\mathrm{at}}$ (grey points, red squares). The error bars indicate the $\pm 1\sigma$ statistical error while the dashed lines are Lorentzian fits. The solid lines are simulated spectra which are averaged over a distribution of the coupling strength g (see text). Figures appeared in Ref. [111].

From the simulation, we infer a distribution of the coupling strength with a mean of $\bar{g}/2\pi = 16\,\mathrm{MHz}$ and a standard deviation of $\sigma_g/2\pi = 9\,\mathrm{MHz}$. Taking into account the resonator decay rate for the specific coupling condition of the measurement of $\kappa/2\pi = 22\,\mathrm{MHz}$, we obtain a cooperativity of $C = 1.9$. Thus, the coupled system is at the edge of the strong coupling limit and enters the so called “fast cavity” regime. In this regime the resonator losses dominate over the coherent light–atom interaction strength which is, however, still larger then the spontaneous emission rate of the atom ($\kappa > g^2/\kappa > \gamma$).

The simultaneous coupling to two fibers considerably reduces the quality factor of the bottle resonator. For this reason, there is a trade-off between the transfer efficiency from the bus to the drop fiber and the relative strength of the light–matter interaction which determines the switching capability of the device. Therefore, in the following section, we will systematically study the performance of the switch for varying fiber–resonator separations.

6.3.3 Performance of the optical switch

In order to find the optimal working point of the optical switch, the coupling of the drop fiber to the resonator is varied while, simultaneously, the condition for critical coupling is maintained with the bus fiber. Thereby, the transfer efficiency between the two fibers changes according to Eq. (2.74) which reads

$$T^0_{\text{drop}} = \frac{\kappa_{\text{drop}}}{\kappa_0 + \kappa_{\text{drop}}} = 1 - 2\frac{\kappa_0}{\kappa} \,. \tag{6.2}$$

Thus, if the coupling to the drop fiber becomes stronger, the amount of transferred power increases as well. However, this gain in efficiency comes at the expense of shorter photon lifetimes in the resonator which reduces the relative light–matter coupling strength. This is well expressed by the critical atom number N_0 which scales with $N_0 \propto \kappa$ as defined in section 4.1.2.

We begin the measurement with a very weakly coupled drop fiber while the bus fiber is critically coupled to the system. Then, the drop fiber is brought stepwise closer to the bottle resonator. Simultaneously, the bus fiber is moved towards to the resonator to maintain the critical coupling condition. For each setting, the on-resonant transmissions of the bus and drop fiber are measured for the empty resonator (T^0_{bus} and T^0_{drop}) and directly after the detection of an atom in the resonator field ($T^{\text{at}}_{\text{bus}}$ and $T^{\text{at}}_{\text{drop}}$).

Figure 6.3 shows the averaged transmission values as a function of the total resonator decay rate $\kappa = \kappa_0 + \kappa_{\text{bus}} + \kappa_{\text{drop}}$. Without atom, we observe an increasing drop fiber transmission T^0_{drop} (gray circles) with κ which follows precisely the theoretical prediction from Eq. (6.2) (grey solid line). For the smallest fiber–resonator separation the maximal measured transfer efficiency reaches a value of $T^0_{\text{drop}} = 90\,\%$.

If an atom is present in the resonator field, the transmission through the bus fiber $T^{\text{at}}_{\text{bus}}$ increases while, at the same time, the transfer to the drop fiber $T^{\text{at}}_{\text{drop}}$ is suppressed. However, with increasing coupling rates of the two fibers, the influence of the atom on the system diminishes as expected due to the increase of the critical atom number N_0. This becomes apparent in $T^{\text{at}}_{\text{bus}}$ which decreases with a growing cavity decay rate while simultaneously the suppression of $T^{\text{at}}_{\text{drop}}$ becomes weaker.

In order to quantify the optimal working point of the switching process, we define the classical raw switching fidelity

$$\mathcal{F} = \frac{1}{2}\left(T^0_{\text{drop}} + T^{\text{at}}_{\text{bus}}\right) \,. \tag{6.3}$$

This quantity corresponds to the probability that a photon is routed to the intended output port of the switch without correction of photon loss and is plotted as a function of the cavity decay rate in Fig. 6.4. Moreover, to also quantify the total photon loss the probability to recovery an input photon is calculated according to

$$p_{\text{rec}} = \frac{1}{2}\left(T^0_{\text{bus}} + T^0_{\text{drop}} + T^{\text{at}}_{\text{bus}} + T^{\text{at}}_{\text{drop}}\right) \,, \tag{6.4}$$

which is shown as well in Fig. 6.4.

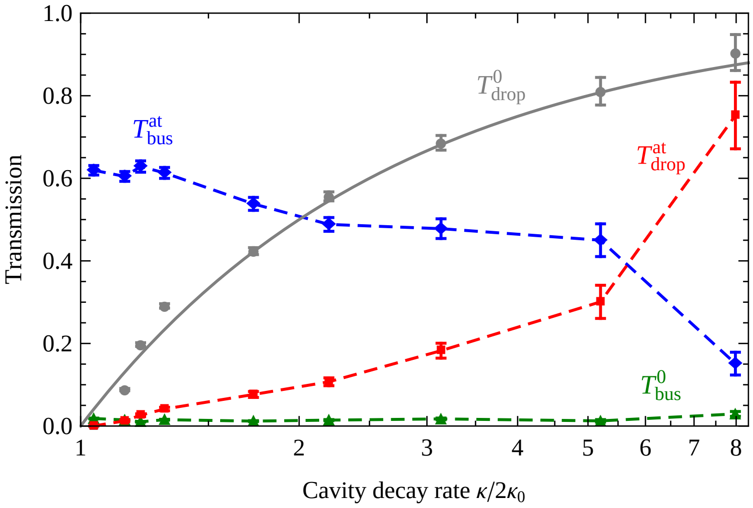

Figure 6.3: Normalized transmission with and without atom through the bus fiber $T^{0,\rm at}_{\rm bus}$ (green triangles, blue diamods) and b) from the bus to the drop fiber $T^{0,\rm at}_{\rm drop}$ (grey points, red squares) as a function of the cavity decay rate. The error bars indicate the $\pm 1\sigma$ statistical error, the grey solid line is the theoretically expected transfer efficiency according to Eq. (6.2) and the dashed lines are guides to the eye. Figure appeared in Ref. [111].

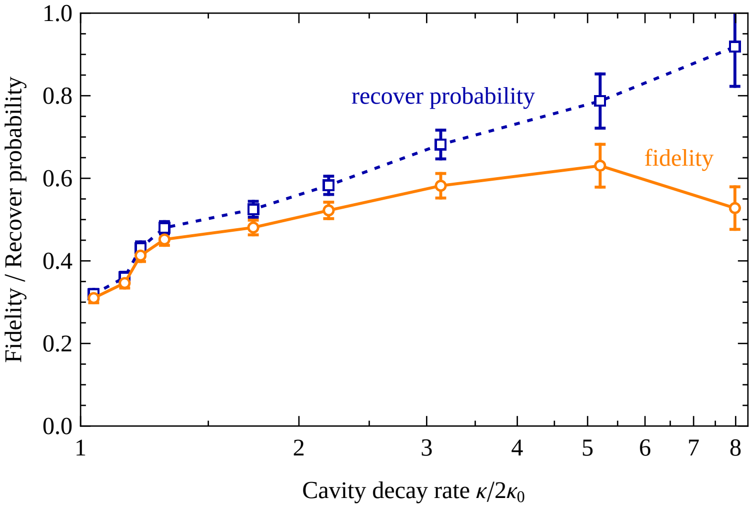

Figure 6.4: Classical fidelity (orange) and probability to recover an incoming photon (blue) as a function of the cavity decay rate κ evaluated for the data from Fig. 6.3. Lines are guides to the eye. Figure appeared in Ref. [111].

A maximal classical fidelity of $\mathcal{F} = 62\,\%$ is obtained together with a high photon recover probability of $p_{\text{rec}} = 79\,\%$ for a cavity decay rate of $\kappa/2\pi = 48.7\,\text{MHz}$. At this point, the critical atom number N_0 is still smaller than 1, but the system is already in the fast cavity regime, where the out-coupling to the fibers dominates over the atom–light interaction strength. However, in the regime of $\kappa/2\pi \simeq 30 - 50\,\text{MHz}$, the effect of the atom onto the bus fiber transmissions $T_{\text{bus}}^{\text{at}}$ is remarkably constant and the switching mechanism is thus robust against variations of κ. Moreover, in this parameter range, the intrinsic resonator losses become small compared to the coupling rates to the fibers. For instance, at the point of maximal classical fidelity, the coupling rates of add and drop fiber are $\kappa_{\text{bus}}/2\pi = 25\,\text{MHz}$ and $\kappa_{\text{drop}}/2\pi = 20\,\text{MHz}$, respectively, and the system is therefore almost symmetric such that a reversal of the roles of bus and drop fiber would yield a very similar performance.

The optimal working point of our optical switch is a compromise between a high transmission into the drop fiber in the ON-state and a good suppression of the in-coupling of light into the resonator in the OFF-state. A high coupling rate between the resonator and the drop fiber κ_{drop} (compared to the intrinsic resonator losses κ_0) is required to met the first condition. However, this relation leads to a broader resonator linewidth, which determines the suppression of the intra-cavity field build-up due to the vacuum-Rabi splitting of the coupled atom–resonator system. This tradeoff puts the optimal working point of the current setup in the fast cavity regime and limits the achievable fidelity. There are two options to increase the fidelity of the switch: One could either enhance the atom–resonator coupling or reduce the intrinsic resonator losses. The latter option corresponds to working with larger intrinsic quality factors. In the current experiment, the intrinsic quality factor is about $Q_0 = 8 \times 10^7$. Since bottle resonators with up to $Q_0 = 3.6 \times 10^8$ have been produced without further increase of the mode volume [58], significant improvements are within reach on this side. Using the model from chapter 4 and assuming the same distribution of coupling strength as in Fig. 5.24, we find that with the $Q_0 = 3.6 \times 10^8$ a fidelity of $\mathcal{F} = 81\,\%$ should be well realizable.

The enhancement of the atom–resonator coupling is much more difficult since it requires an improved localization of single atoms in the evanescent field. Several propositions exists to either trap an atom directly in the evanescent resonator field in a two-color trap configuration [97, 100, 144] or, alternatively, to use a similar, already demonstrated trap around an ultra-thin fiber [8, 121] close to the resonator. In such traps, the atoms would interact with the resonator field with a much better defined coupling strength g. Moreover, if the atom could be positioned close to the resonator surface, a considerably higher g should be attainable. For instance, from Fig. 5.13 in chapter 5 we found for the fundamental TM mode a maximal coupling strength of $g/2\pi = 55\,\text{MHz}$ at the surface of the resonator. Although, the shift of the atomic transition frequency close to the surface will prevent the realization of such strong light–matter coupling, a coupling strength of $g/2\pi \approx 40\,\text{MHz}$ should be realizable at distances of about 50 nm from the surface. Based on this value, combined with the ultra-high quality factor of $Q_0 = 3.6 \times 10^8$, fidelities of $\mathcal{F} > 91\,\%$ would come into reach. We note that for theses parameters, the system would be in the strong coupling regime which is in clear contrast to the current setup where we find a maximal fidelity in the fast cavity regime. Thus, the optical switch based on the bottle resonator is still far from fundamental limitations and holds great potential for further improvements.

6.4 Non-classical light from the switch

The internal dynamics of a single atom that controls the optical switch is governed by the laws of quantum mechanics. Therefore, it is interesting to investigate if any signature of this quantum nature is imprinted on the light which is routed by the switch. In our experiment, the incoming light field is an attenuated laser beam and can be interpreted as a coherent state following a Poisson photon statistic for which photons are temporally uncorrelated. However, the coupled atom–resonator system creates a strong optical nonlinearity at the single photon level which originates from the fact that a single atom can absorb only one photon at time. As a consequence, the behavior of the switch should be sensitive to the number of simultaneously incoming photons. It has been demonstrated that this nonlinearity in a strongly coupled atom–resonator system can give rise to a so called "photon blockade" where the presence of a single photon blocks the transport of a second photon through an optical system [30]. Based on a similar principle a photon turnstile [29] and routing of photons [89] have been demonstrated where an incoming light field was converted into a stream of single photons with the help of a WGM microresonator coupled to a single atom.

6.4.1 Measurement of the intensity auto-correlation function

In order to investigate if the performance of our optical switch is photon-number depended, the photon statistic of the light in the bus and drop fiber is analyzed with a Hanbury–Brown–Twiss setup at port 2 and 3 of the fiber network (compare Fig. 5.10). The experimental settings are identical to the measurement of the Rabi-spectra in section 6.3.2. The cavity–probe detuning is set to $\Delta_{\mathrm{cp}} = 0$ while, due to the residual magnetic field offset at the resonator, the atom–probe detuning is $\Delta_{\mathrm{ap}} = 1.1\,\mathrm{MHz}$. As before, the photons coming from the setup are detected with SPCMs and recorded with a FPGA with sub-nanosecond resolution.

As a measure of non-classical correlations of the light, the normalized intensity correlation function $g^{(2)}(\tau)$ can be evaluated. Experimentally, this quantity is determined by analyzing the photon arrival times between the two detectors of the Hanbury–Brown–Twiss setup. For this purpose, the time delays τ between photon events in a time window of 500 ns after the detection of an atom are plotted in a histogram which is normalized to $g^{(2)} = 1$ for long time delays. If the photons are completely uncorrelated and follow a Poisson statistic like, e.g., for a coherent state, one finds a flat intensity auto-correlation function $g^{(2)} = 1$, independent of the value of τ.

In Fig. 6.5 the experimental intensity auto-correlation functions for the bus and the drop fiber, $g^{(2)}_{\mathrm{b}}$ and $g^{(2)}_{\mathrm{d}}$, are shown. We note a clear deviation of $g^{(2)}$ from unity at small delays $|\tau| \lesssim 20\,\mathrm{ns}$ for the bus as well as for the drop fiber. Light in the bus fiber shows sub-Poisson statistic which reveals itself in the drop of the intensity correlation function at $\tau = 0$ to $g^{(2)}_{\mathrm{b}}(0) \approx 0.5$. This feature is also denoted as photon "anti-bunching" as it corresponds to a situation where the probability to detect simultaneously arriving photons is reduced considerably in the bus fiber. In contrast, the opposite effect, so-called photon "bunching", is observed in the drop fiber where for zero time delay we find $g^{(2)}_{\mathrm{d}}(0) \approx 2.5$. This result indicates that photon pairs are preferentially coupled into the drop fiber.[1] We therefore conclude that the presence of the

---

[1] The $g^{(2)}$-function does not allow to differentiate between two photon events and coincidences with even more

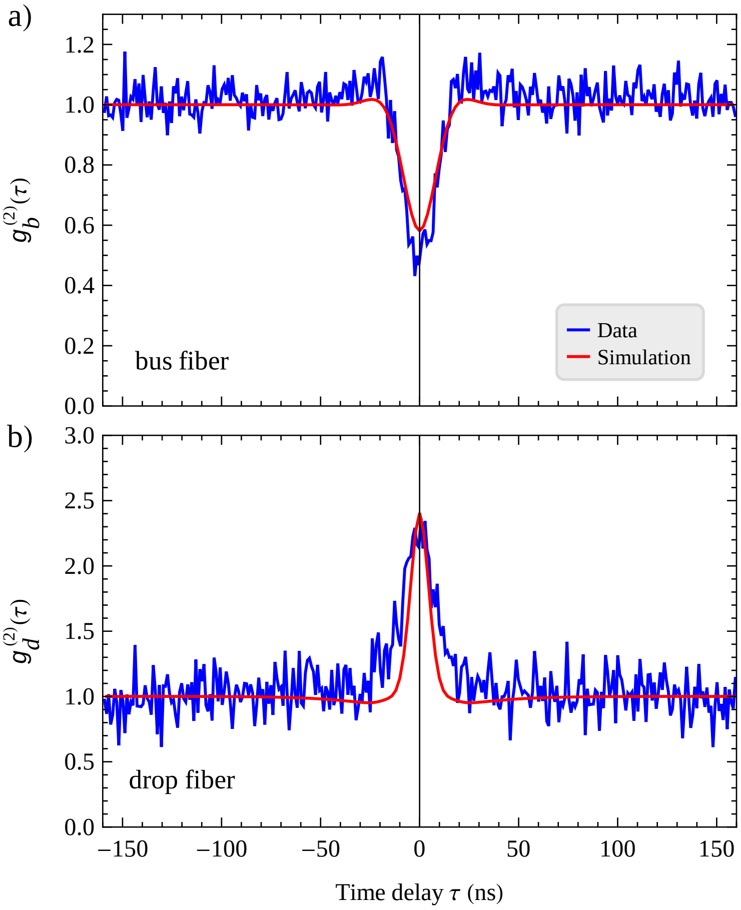

Figure 6.5: Intensity auto-correlation functions of light exiting a) the bus and b) the drop fiber for the coupled atom–resonator system as a function of the time delay τ. The measured data (blue lines) is plotted with a binning of 1 ns and normalized to unity for large τ. The simulations (red lines) are calculated for a single mode cavity coupled to a two-level atom with the parameters $\{\kappa_0, \kappa_{\text{bus}}, \kappa_{\text{drop}}, \gamma\} = 2\pi \cdot \{5, 11.25, 6.25, 3\}\,\text{MHz}$. The probe light is resonant to the cavity ($\Delta_{\text{cp}} = 0$) whereas the atom–probe detuning is $\Delta_{\text{ap}} = 1.1\,\text{MHz}$ due to residual magnetic fields. The coupling strength is assumed to lie between $g = 2.5$–$35\,\text{MHz}$ following the same distribution as for the vacuum-Rabi spectrum (see text for details). Figure appeared in Ref. [111].

atom in the evanescent field of the resonator indeed leads to non-classical features in the photon statistic.

---

photons. However, for the pump power in the experiment, these multi-photon events are very unlikely.

6.4.2 Simulation of the intensity correlation function

In order to facilitate the interpretation of the measured intensity auto-correlation, we have to simulate $g_{\mathrm{b}}^{(2)}(\tau)$ and $g_{\mathrm{d}}^{(2)}(\tau)$ for the parameters of our experiments. Formally the intensity auto-correlation function with time delay τ for a field operator $\hat{c}(t)$ is defined in the long-time limit of the steady state as [94]

$$g^{(2)}(\tau) = \lim_{t\to\infty} \frac{\langle \hat{c}^\dagger(t)\hat{c}^\dagger(t+\tau)\hat{c}(t+\tau)\hat{c}(t)\rangle}{\langle \hat{c}^\dagger(t)\hat{c}(t)\rangle\langle \hat{c}^\dagger(t+\tau)\hat{c}(t+\tau)\rangle}\,. \tag{6.5}$$

For the analysis, we are interested in the $g^{(2)}$ functions of the output field operators in the bus and drop fiber $\hat{s}_{\mathrm{bus}}$ and $\hat{s}_{\mathrm{drop}}$. In analogy to the classical field amplitudes from section 2.4.2, these operators can be defined as [145]

$$\hat{s}_{\mathrm{bus}} = \hat{s}_{\mathrm{in}} - c_{\mathrm{b}}\hat{a}(t)\,, \tag{6.6}$$

$$\hat{s}_{\mathrm{drop}} = -c_{\mathrm{d}}\hat{a}(t)\,, \tag{6.7}$$

where $\hat{a}$ is the annihilation operator of the resonator mode with the coefficients $c_{\mathrm{b}} = \sqrt{2\kappa_{\mathrm{bus}}}$ and $c_{\mathrm{d}} = \sqrt{2\kappa_{\mathrm{drop}}}$ and $\hat{s}_{\mathrm{in}}$ is the annihilation operator of the pump field in the bus fiber.

In order to derive the intensity auto-correlation function of the bus fiber $g_{\mathrm{b}}^{(2)}(\tau)$, we use Eq. 6.6 in combination with Eq. (6.5) and obtain

$$g_b^{(2)}(\tau) = \frac{\langle(\hat{s}_{\mathrm{in}}^\dagger - c_{\mathrm{b}}\hat{a}^\dagger)(\hat{s}_{\mathrm{in}}^\dagger - c_{\mathrm{b}}\hat{a}_\tau^\dagger)(\hat{s}_{\mathrm{in}} - c_{\mathrm{b}}\hat{a}_\tau)(\hat{s}_{\mathrm{in}} - c_{\mathrm{b}}\hat{a})\rangle}{\langle(\hat{s}_{\mathrm{in}}^\dagger - c_{\mathrm{b}}\hat{a}^\dagger)(\hat{s}_{\mathrm{in}} - c_{\mathrm{b}}\hat{a})\rangle\langle(\hat{s}_{\mathrm{in}}^\dagger - c_{\mathrm{b}}\hat{a}_\tau^\dagger)(\hat{s}_{\mathrm{in}} - c_{\mathrm{b}}\hat{a}_\tau)\rangle}\,, \tag{6.8}$$

where the time dependence is dropped for clarity following the replacements rules $\hat{a} = \hat{a}(t)$ and $\hat{a}_\tau = \hat{a}(t+\tau)$. If the incoming pump field in the bus fiber is a coherent state, which is a reasonable assumption for weak laser pulses, one can replace the pump field operators $\hat{s}_{\mathrm{in}}$ and $\hat{s}_{\mathrm{in}}^\dagger$ in Eq. 6.8 with their expectation values $s_{\mathrm{in}} = \langle\hat{s}_{\mathrm{in}}\rangle$ and $s_{\mathrm{in}}^* = \langle\hat{s}_{\mathrm{in}}^\dagger\rangle$ [145]. The intensity auto-correlation function then can be expanded to the expression

$$\begin{aligned} g_{\mathrm{b}}^{(2)}(\tau) = \; & \frac{1}{N}\Big[|s_{\mathrm{in}}|^4 \\ & - c_{\mathrm{b}}|s_{\mathrm{in}}|^2\left(s_{\mathrm{in}}^*\langle\hat{a}\rangle + s_{\mathrm{in}}\langle\hat{a}^\dagger\rangle + s_{\mathrm{in}}^*\langle\hat{a}_\tau\rangle + s_{\mathrm{in}}\langle\hat{a}_\tau^\dagger\rangle\right) \\ & + c_{\mathrm{b}}^2|s_{\mathrm{in}}|^2\left(\langle\hat{a}^\dagger\hat{a}\rangle + \langle\hat{a}^\dagger\hat{a}_\tau\rangle + \langle\hat{a}_\tau^\dagger\hat{a}\rangle + \langle\hat{a}_\tau^\dagger\hat{a}_\tau\rangle\right) \\ & + c_{\mathrm{b}}^2\left(s_{\mathrm{in}}^2\langle\hat{a}^\dagger a_\tau^\dagger\rangle + (s_{\mathrm{in}}^*)^2\langle\hat{a}_\tau a\rangle\right) \\ & - c_{\mathrm{b}}^3\left(s_{\mathrm{in}}\langle\hat{a}^\dagger\hat{a}_\tau^\dagger\hat{a}_\tau\rangle + s_{\mathrm{in}}^*\langle\hat{a}_\tau^\dagger\hat{a}_\tau\hat{a}\rangle + s_{\mathrm{in}}\langle\hat{a}^\dagger\hat{a}_\tau^\dagger\hat{a}\rangle + s_{\mathrm{in}}^*\langle\hat{a}^\dagger\hat{a}_\tau\hat{a}\rangle\right) \\ & + c_{\mathrm{b}}^4\langle\hat{a}^\dagger\hat{a}_\tau^\dagger\hat{a}_\tau\hat{a}\rangle\Big]\,, \end{aligned} \tag{6.9}$$

where the normalization factor N corresponds to the denominator of Eq. 6.8 and reads

$$\begin{aligned} N = \; & \left(|s_{\mathrm{in}}|^2 - s_{\mathrm{in}}^* c_{\mathrm{b}}\langle\hat{a}\rangle + s_{\mathrm{in}} c_{\mathrm{b}}\langle\hat{a}^\dagger\rangle + c_{\mathrm{b}}^2\langle\hat{a}^\dagger\hat{a}\rangle\right) \\ & \cdot\left(|s_{\mathrm{in}}|^2 - s_{\mathrm{in}}^* c_{\mathrm{b}}\langle\hat{a}_\tau\rangle + s_{\mathrm{in}} c_{\mathrm{b}}\langle\hat{a}_\tau^\dagger\rangle + c_{\mathrm{b}}^2\langle\hat{a}_\tau^\dagger\hat{a}_\tau\rangle\right)\,. \end{aligned} \tag{6.10}$$

The expectation values in Eq. (6.9) that involve only operators at one point in time are easy to calculate according to the Master equation formalism from section 4.1.2, yielding, e.g., $\langle \hat{a}(t) \rangle = \mathrm{tr}(\hat{a}\rho(t))$. However, when it comes to calculating expectation values of operator products at different times, this approach is no longer meaningful. In order to determine all other expectation values in Eq. (6.9) which contain products of $\hat{a}$ and $\hat{a}_\tau$ or their complex conjugates, one can apply the quantum regression formula introduced by Lax [146] which, following Ref. [94], takes the form

$$\langle \hat{O}_1(t)\hat{O}_2(t+\tau)\hat{O}_3(t) \rangle = \mathrm{tr}\left[\hat{O}_2(0)e^{\mathcal{L}\tau}\left(\hat{O}_3(0)\rho(t)\hat{O}_1(0)\right)\right] , \tag{6.11}$$

where $\hat{O}_i$ are arbitrary operators and $\mathcal{L}$ is the Liouvillian superoperator. Using this approach together with the cyclic property of the trace, we can evaluate the expectation values in Eq. (6.9).[2] The expectation value of the last term can be determined the same way although it involves four operators: To circumvent this problem, we simply define the photon number operator $\hat{n}_\tau = \hat{a}_\tau^\dagger \hat{a}_\tau$ such that $\langle \hat{a}^\dagger \hat{a}_\tau^\dagger \hat{a}_\tau \hat{a} \rangle = \langle \hat{a}^\dagger \hat{n}_\tau \hat{a} \rangle$ to which the quantum regression formula applies.

The calculation of the intensity auto-correlation function for light in the drop fiber $g^{(2)}_{\mathrm{d,d}}(\tau)$ is much easier. Since no additional pumping term occurs and therefore no interference with the resonator field takes place, the insertion of $\hat{s}_{\mathrm{drop}}$ into Eq. (6.5) simply yields

$$g^{(2)}_{\mathrm{d}}(\tau) = \frac{\langle \hat{a}^\dagger \hat{a}_\tau^\dagger \hat{a}_\tau \hat{a} \rangle}{\langle \hat{a}^\dagger \hat{a} \rangle \langle \hat{a}_\tau^\dagger \hat{a}_\tau \rangle} , \tag{6.12}$$

which is the intensity auto-correlation of the intra-cavity field. With help of the quantum regression formula, we can calculate this expression without further effort.

To facilitate the calculation of the density matrix $\rho(t)$ with the master equation formalism, we make use of our finding from chapter 5 that, effectively, the light–matter interaction can be described by a two-level atom interacting with a single resonator mode. In order to include multi photon effects into the simulation up to three intra-cavity photon states are taken into account. Then, we determine $\rho(t)$ numerically and subsequently calculate $g^{(2)}_{\mathrm{b}}(\tau)$ and $g^{(2)}_{\mathrm{d}}(\tau)$. In analogy to the simulations of the vacuum-Rabi spectrum in section 5.4.1, one has to take the motion of the atoms in the evanescent resonator field into account for the modeling. This is necessary since the measured intensity auto-correlation functions are averaged over many atoms with different coupling strength. Therefore, we calculate $g^{(2)}_{\mathrm{b}}(\tau)$ and $g^{(2)}_{\mathrm{d}}(\tau)$ for a set of different couping strength $g/2\pi$ ranging from 2.5 MHz to 35 MHz. The average $g^{(2)}$ is then determined according to

$$g^{(2)}(\tau) = \sum_g p_g \cdot g^{(2)}_g(\tau) , \tag{6.13}$$

where $g^{(2)}_g(\tau)$ is the intensity auto-correlation function for an individual value of the coupling strength g and p_g is the corresponding weighting factor which is determined by

$$p_g = \frac{(T^{\mathrm{at}}_g)^2 \cdot w_g}{\sum_g (T^{\mathrm{at}}_g)^2 \cdot w_g} , \tag{6.14}$$

---

[2] for the product of only two operators one choses $O_3(t)$ equal to the unity operator

where T_g^{at} is the transmission of either the bus or drop fiber while an atom couples. For the weighting, one not only hat to take into account the probability w_g for a certain coupling strength g to occur, but one also has to consider the transmission at this coupling strength. This is necessary since $g^{(2)}$ practically measures the probability of detecting two photons which scales with the intensity squared, and thus, is proportional to $(T_g^{\mathrm{at}})^2$.

Following this procedure, we calculate the $g^{(2)}$ functions where we use the values for w_g and $(T_g^{\mathrm{at}})^2$ which were obtained during simulations of the vacuum-Rabi spectrum of Fig. 6.2. In Fig. 6.5, $g_{\mathrm{b}}^{(2)}(\tau)$ and $g_{\mathrm{d}}^{(2)}(\tau)$ for the bus and drop fiber are shown as red lines. We observe excellent agreement between the experimental data and the simulated results. It should be especially emphasized that no direct fit to the experimental data of $g^{(2)}(\tau)$ is performed. The only fitted parameters stem from the distribution of the coupling strength g which was obtained from the simulation of the vacuum-Rabi spectrum in Fig. 6.2. Thus, our ansatz of treating the system as a two-level atom coupled to a single mode cavity turns out to be sufficient to reproduce all important features in the intensity auto-correlation functions.

6.4.3 Discussion of the photon-number-dependent routing capability

One can interpret the measured intensity auto-correlation functions in the simplified picture of a two level atom interacting with a single cavity mode. As long as no atom is present in the evanescent field, a resonant photon in the bus fiber is transferred with unity efficiency into the resonator due to the critical coupling condition. This situation changes when the coupling to the atom leads to the formation of the dressed states with a shift of the eigenenergies $\Delta E_\pm = \pm\hbar g$. As a consequence, an incoming photon is no longer resonant with the system and remains in the bus fiber with high probability. This effect can be interpreted as an induced under-coupling of the system which can be seen from the expression of bus fiber transmission in the steady state which is given according to Eq. 4.12 by[3]

$$T_{\mathrm{bus}} = \left| \frac{g^2/\gamma + \kappa_0 + \kappa_{\mathrm{drop}} - \kappa_{\mathrm{bus}}}{g^2/\gamma + \kappa_0 + \kappa_{\mathrm{drop}} + \kappa_{\mathrm{bus}}} \right|^2 . \tag{6.15}$$

Formally the effect of the atom is to add an additional decay channel to the resonator which is given by g^2/γ. This term reflects the losses of photons due to scattering of the atom which weakens the intra-cavity field and therefore under-couples the system. As a consequence, the build-up of an intra-cavity field is suppressed by the presence of the atom.

However, this picture is only valid for a single incoming photon. Given that a single photon is already enough to saturate the atom, the system will respond in a highly nonlinear way depending on the number of incoming photons. For instance, let us assume that two photons in the bus fiber arrives at the same time at the resonator. Since the atom can only scatter one photon at time, it cannot inhibit the build-up of an intra-cavity field as efficiently as for a single incoming photon. This fact is also reflected in the spectral properties of the system. The energy shift of the dressed states compared to the unperturbed system is a function of the intra-cavity

---

[3] To extend the expression to the case of the add-drop configuration we apply the replacements $\kappa_{\mathrm{ext}} \rightarrow \kappa_{\mathrm{bus}}$ and $\kappa_0 \rightarrow \kappa_0 + \kappa_{\mathrm{bus}}$

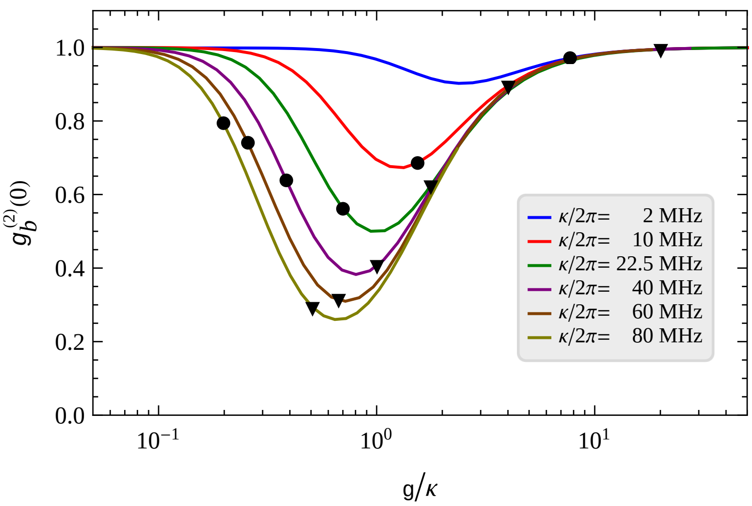

Figure 6.6: Calculated intensity auto correlation $g_\mathrm{b}^{(2)}(0)$ of light transmitted through the bus fiber as a function of g/κ for different cavity decay rates κ. The black points indicate the values which are expected for the current setup with $g/2\pi = 16\,\mathrm{MHz}$, while the black triangles illustrate values which could be reached under optimal atom–light coupling with $g/2\pi = 40\,\mathrm{MHz}$. For the calculation, the bus fiber is assumed to be critically coupled ($\kappa_\mathrm{bus} = \kappa/2$).

photon number n and scales with $\Delta E_\pm(n) = \pm\hbar\sqrt{n}g$. Thus, the energy shift per photon is $g/\sqrt{n}$, meaning that with increasing photon number the resonance of the dressed states in the spectrum are closer to the cavity resonance of the unperturbed system [147]. As a consequence, for increasing photon number, the incoming photons are closer resonant to the dressed states of the system. The measured intensity auto-correlation functions $g_\mathrm{b}^{(2)}(\tau)$ and $g_\mathrm{d}^{(2)}(\tau)$ reflect this qualitative description: The anti-bunching in the bus fiber together with the bunching in the drop fiber suggests that simultaneously arriving photons couple more efficiently into the resonator than if they arrive individually. Thus, we observe photon-number-dependent routing of the optical switch.

This can be an useful property to produce non-classical states of light. For instance, in Ref. [29] a similar approach with a WGM microresonator coupled to a single atom was used to realize a photon turnstile. This device was able to produce a stream of single photons in transmission with strong anti-bunching of $g^{(2)}(0) \approx 0.1$, while all additional incoming photons were reflected. In this context, it is interesting to investigate if similar results can be obtained with our system and how the photon-number-dependent routing capability scales with the key parameters, the coupling strength g and the resonant decay rate κ, of the optical switch. In section 6.3, we found that the switching performance is mainly influenced by the intrinsic quality factor and the coupling strength. Ideally, the system should be in the strong coupling regime to realize optimal switching between the two fibers with a single atom. In order to verify if the switch would also create non-classical photon statistics under these optimal conditions, we calculate $g_\mathrm{b}^{(2)}(0)$ as a function of the coupling strength g for several values of the resonator decay rate κ, where we assume critical coupling ($\kappa_{\text{bus}} = \kappa/2$). The results are shown in Fig. 6.6 where we plot $g_{\text{b}}^{(2)}(0)$ over g/κ. From the calculations, it is evident that the intensity auto-correlation functions measurements were already performed close to the optimal point for achieving the minimal value of $g_{\text{b}}^{(2)}(0) \approx 0.5$ for our current experimental parameters with $g/2\pi = 16\,\text{MHz}$ (black points). By increasing simultaneously the atom–light coupling strength g and the cavity decay rate κ one can reach in principle even stronger anti-bunching resulting in a value of $g_{\text{b}}^{(2)}(0) \approx 0.25$ under ideal conditions with $g/2\pi = 40\,\text{MHz}$ (black triangles). For even larger decay rates κ, values of $g_{\text{b}}^{(2)}(0)$ close to zero would be in principle possible. However, they require unrealistically high coupling strength and are therefore not shown.

We note that the minimum of $g_{\text{b}}^{(2)}(0)$ is always reached in the regime where $\kappa > g^2/\kappa > \gamma$ while $g_{\text{b}}^{(2)}(0)$ approaches unity if the system is in the strong coupling regime ($g \gg \kappa$). The latter finding is qualitatively well explained by the energies of the dressed states. If the coupling strength is much larger than the resonator linewidth, the two-photon dressed states are also far off-resonant. Accordingly, pairs of photons will also remain in the bus fiber, if an atom is coupled to the resonator, yielding practically the same behavior as for one photon. As we will discuss in the next section, this is an important feature of the optical switch. Under optimal operation conditions with strong light–matter coupling and small resonator losses, the routing capability of the switch would become almost photon-number-independent.

6.5 Outlook on deterministic generation of atom–light entanglement and optical Schrödinger cat states

So far, we analyzed the performance of the optical switch mostly according to classical efficiency considerations. However, the atom which triggers the switching process is a quantum system and, thus, can be prepared in a superposition of its internal states. Thereby entanglement between the atom and an incoming light field could be created which would allow one to realize highly non-classical states of light which are, e.g., of great interest for applications in quantum metrology.

6.5.1 Creation of atom–photon entanglement

In order to generate entanglement between an incoming photon and an atom which is coupled to the resonator, control over the atomic hyperfine states is required. Then, one could prepare a ^{85}Rb atom either in the $|F = 2\rangle$ or in the $|F = 3\rangle$ ground state where the latter couples via the $|F = 3\rangle \rightarrow |F' = 4\rangle$ transition to the cavity mode, as shown in Fig. 6.7 a). If the atom is in state $|F = 2\rangle$, all possible transitions are far off-resonant with respect th to the resonator mode. As a consequence, the atom–resonator interaction is negligible and an ideal optical switch directs an incoming single photon to the drop port. This corresponds to the photonic state $|0_{\text{b}}, 1_{\text{d}}\rangle$ having zero photons in the outgoing bus fiber mode and 1 photon in the drop fiber mode, as depicted in Fig. 6.7 b). In contrast, an atom in the $|F = 3\rangle$ state ideally blocks the build-up of an intra-cavity field and the photon is routed to the bus port ending up in the state $|1_{\text{b}}, 0_{\text{d}}\rangle$, illustrated in Fig. 6.7 c). In this way the internal state of the atom defines the output port for light. If the atom is

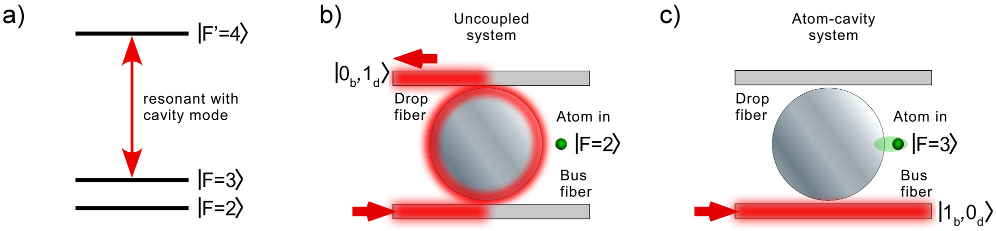

Figure 6.7: Concept of the optical switch controlled by the internal state of the atom. a) Relevant states of a three-level atom where only one of the two possible transitions is resonant with the cavity mode. b) Since the $|F=2\rangle \to |F'=4\rangle$ transition is off-resonant the presence of the atom does not alter the resonance condition of the optical switch and a single photon is transferred to the drop fiber ending up in the state $|0_\mathrm{b}, 1_\mathrm{d}\rangle$. c) An atom in the $|F=3\rangle$ state couples to the resonator and thereby blocks the build-up of an intra cavity field leaving an incoming photon in the state $|1_\mathrm{b}, 0_\mathrm{d}\rangle$.

prepared in a quantum mechanical superposition of the two ground states, the final state of the combined atomic and photonic subsystems then reads

$$|\Phi\rangle = \frac{1}{\sqrt{2}} \left(|F=2\rangle\, |0_\mathrm{b}, 1_\mathrm{d}\rangle + |F=3\rangle\, |1_\mathrm{b}, 0_\mathrm{d}\rangle \right) , \tag{6.16}$$

which is a maximally entangled Bell state [148]. Thus, one could deterministically generate entanglement between the atom and an incoming freely propagating photon if the atom is prepared in a superposition state.

The real switch, characterized in the preceding sections, deviates from this ideal picture in two important points: First of all, it does not have unit routing efficiency since it incorporates internal resonator losses and the switching is not performed with full contrast (compare Fig. 6.3). Secondly, so far, the switch is controlled by the presence of an atom and not by its internal state. However, it is interesting to quantify the degree of entanglement which could be reached with the current optical switch if control over the internal atomic states was available. For the analysis, we assume that the optical switching using the internal state of the atom would yield the same transmission values as measured in Fig. 6.3. This assumption seems reasonable since for the ON state of the switch an atom in the level $|F=2\rangle$ is far off-resonant to the resonator such that the situation is comparable to the case where the atom is not present. Furthermore, in this scenario, the OFF state of the switch, i.e., the state for which the atom couples to the resonator, is identical to the one which we already investigated experimentally.

In order to quantify the capacity of the switch to generate atom–photon entanglement, we assume the atom to be in an equal superposition such that the combined state of the system reads

$$\begin{aligned} |\Psi\rangle = &\frac{1}{\sqrt{2}}(\alpha_2\, |F=2\rangle\, |0_\mathrm{b}, 1_\mathrm{d}\rangle + \alpha_3\, |F=3\rangle\, |0_\mathrm{b}, 1_\mathrm{d}\rangle \\ &+ \beta_2\, |F=2\rangle\, |1_\mathrm{b}, 0_\mathrm{d}\rangle + \beta_3\, |F=3\rangle\, |1_\mathrm{b}, 0_\mathrm{d}\rangle) \, . \end{aligned} \tag{6.17}$$

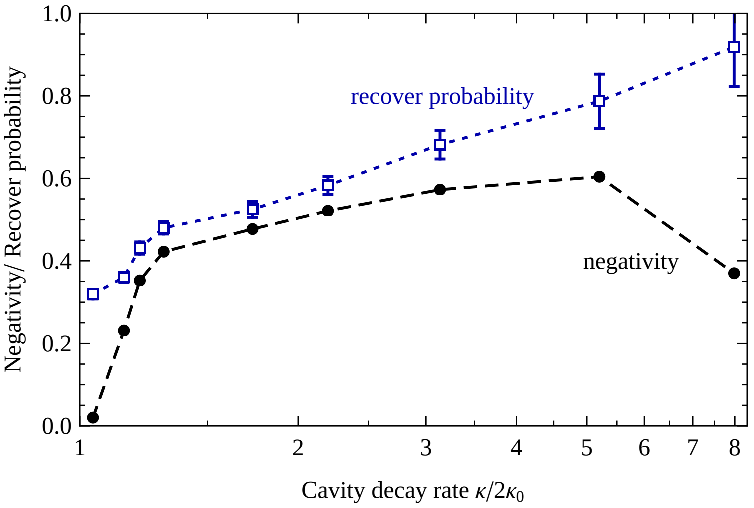

Figure 6.8: Expected negativity (black) and probability of recovering an incoming photon (blue) as a function of the cavity decay rate κ evaluated for the data from Fig. 6.3. The negativity illustrates the degree of entanglement the optical switch could reach when the atom is prepared in a superposition state (see text). Lines are guides to the eye. Figure appeared in Ref. [111].

The modulus of the coefficients can be obtained according to

$$\begin{aligned} |\alpha_2| &= \sqrt{T^0_{\text{drop}}}\,, \\ |\alpha_3| &= \sqrt{T^{\text{at}}_{\text{drop}}}\,, \\ |\beta_2| &= \sqrt{T^0_{\text{bus}}}\,, \\ |\beta_3| &= \sqrt{T^{\text{at}}_{\text{bus}}}\,, \end{aligned} \tag{6.18}$$

from the experimental data in Fig. 6.3. Note that, due to the resonator losses, we find $T^0_{\text{drop}} + T^0_{\text{bus}} < 1$ and $T^{\text{at}}_{\text{drop}} + T^{\text{at}}_{\text{bus}} < 1$ and as a consequence the $|\Psi\rangle$ is not normalized.

In order to characterize the entanglement of the this state, we employ the definition of the negativity [149, 150] which measures the degree of entanglement of a state with the density matrix ρ and can be computed according to

$$\mathcal{N}(\rho) = \sum_i |\lambda_i| - \lambda_i\,. \tag{6.19}$$

where λ_i are the eigenvalues of the partially transposed density matrix ρ^{T_2} [151]. For a separable state all eigenvalues λ_i are positive and the negativity evaluates to $\mathcal{N} = 0$. In contrast, entanglement results in some negative eigenvalues and a maximally entangled state, like, e.g., the Bell state $|\Phi\rangle$, would yield $\mathcal{N} = 1$.

Figure 6.8 presents the results of the calculation[4] of the negativity $\mathcal{N}(|\Psi\rangle\langle\Psi|)$. If the current bottle resonator in the add-drop configuration was coupled to an atom in an equal superposition state one would obtain a maximal negativity of $\mathcal{N} = 0.6$. This is a highly entangled state which demonstrates the potential of our optical switch to create non-classical states of light. Moreover, taking into account the predicted fidelities from section 6.3.3 for improvements of the quality factor Q_0 and trapping of atoms, even higher negativities would be achievable.

A possible application of the described entanglement operation would be the realization of a controlled NOT (C-NOT) quantum gate [148] between a propagating photon and an atom. Therein, the atom would play the role of the control qubit which determines whether the photonic qubit state $|1_\mathrm{b}, 0_\mathrm{d}\rangle$ flips to $|0_\mathrm{b}, 1_\mathrm{d}\rangle$ or not. To be fully operational, the inverse transfer from the drop to the bus fiber would also have to be possible with identical efficiency. For this, the switching process needs to be symmetric. This condition is fulfilled in good approximation if the intrinsic resonator decay rate κ_0 is small compared to the out-coupling to the fibers. In this case at critical coupling of the bus, fiber $\kappa_\mathrm{bus} = \kappa_0 + \kappa_\mathrm{drop} \approx \kappa_\mathrm{drop}$ is fulfilled.

6.5.2 Deterministic generation of Schrödinger cat states

The above described scheme for the generation of atom–photon entanglement could be even extended to more incoming photons in order to create so-called optical "Schrödinger cat"-states. Following the gedankenexperiment by Erwin Schrödinger, the concept of this kind of states is to entangle a single quantum system like, e.g., a two level atom with a more "macroscopic" system. The latter can be, e.g., a coherent state $|\alpha\rangle$ of a light field with a macroscopic amplitude α. Schrödinger cat states hold great potential for many applications comprising fundamental test in quantum theory [152–154], improved schemes in quantum computing [155, 156] and communication [157–159] and quantum metrology [160].

Schrödinger cat states have been realized in various systems like, e.g., in CQED with microwave cavities [161, 162], with trapped ions [163, 164] and more recently also with super conducting qubits coupled to a resonator [165] (for an overview see Ref. [166]). All of the cited examples describe the generation of Schrödinger cat states in bound systems. However, for many possible applications like in quantum communication and metrology, cat states in freely propagating optical fields are required. Their generation is extremely challenging since the smallest photon loss will destroy the coherence of the state. As a consequence only few experiments have been reported so far which succeeded in creating freely propagating optical cat states [167–171]. These schemes are based on optical parametric amplification processes leading to spontaneous creation of cat states and are therefore non-deterministic.

Here, we are going to discuss the possibility of deterministically creating freely propagating optical cat states with our fiber optical switch. The proposed scheme follows in some points Ref. [172] where a coherent pulse $|\alpha\rangle$ is reflected from a single mode cavity containing a three-level atom in a superposition of its two ground states. Thereby, a cat state $|\alpha\rangle + e^{i\Theta}|-\alpha\rangle$ composed out of two coherent states with equal amplitude but opposite phase is created. In contrast to this scheme where the cat state is encoded in the phase of a single mode, we want to create the cat state between two different spatial fiber modes in our approach. For this purpose, let us reconsider the situation from section 6.3.3 where we assumed that we can prepare the atom in the evanescent resonator field in a superposition of its two ground states $|F=2\rangle$ and $|F=3\rangle$ with only the transition $|F=3\rangle \rightarrow |F'=4\rangle$ being resonant to the cavity. For an ideal switch with a fidelity of $\mathcal{F} \approx 1$, an incoming coherent light pulse $|\alpha\rangle$ would then be entangled with the atom yielding the state

---

[4] In the calculation, we verified that the negativity of the unnormalized state $|\Phi\rangle$ yields the same result as the full calculations treating the resonator losses as an additional incoherent output channel.

$$|\Phi\rangle = \frac{1}{\sqrt{2}} \left(|F=2\rangle \, |\alpha_\mathrm{b}, 0_\mathrm{d}\rangle + |F=3\rangle \, |0_\mathrm{b}, \alpha_\mathrm{d}\rangle \right) . \tag{6.20}$$

where $|\alpha_\mathrm{b}, 0_\mathrm{d}\rangle$ and $|0_\mathrm{b}, \alpha_\mathrm{d}\rangle$ represent the states with the coherent pulse being either in the drop or in the bus fiber. If the amplitude of the coherent state is large enough, the state $|\Phi\rangle$ represents a superposition of a quantum and a “macroscopic” system and is in this sense a Schrödinger cat state. After the entanglement operation with the switch, one can follow the procedure in Ref. [161] and apply a rotation of the atomic state on the Bloch sphere with a $\pi/2$-pulse which performs the transformation

$$\begin{aligned} |F=2\rangle &\rightarrow \frac{1}{\sqrt{2}} \left(|F=2\rangle + |F=3\rangle \right) , \\ |F=3\rangle &\rightarrow \frac{1}{\sqrt{2}} \left(|F=2\rangle - |F=3\rangle \right) , \end{aligned} \tag{6.21}$$

preparing thereby the state

$$|\Phi'\rangle = \frac{1}{2} \left[|F=2\rangle \left(|0_\mathrm{b}, \alpha_\mathrm{d}\rangle + |\alpha_\mathrm{b}, 0_\mathrm{d}\rangle \right) + |F=3\rangle \left(|0_\mathrm{b}, \alpha_\mathrm{d}\rangle - |\alpha_\mathrm{b}, 0_\mathrm{d}\rangle \right) \right] . \tag{6.22}$$

A subsequent measurement of the atomic state would then project the light field into one of the Schrödinger cat states $|\Psi^\pm_\text{cat}\rangle = \frac{1}{\sqrt{2}}(|0_\mathrm{b}, \alpha_\mathrm{d}\rangle \pm |\alpha_\mathrm{b}, 0_\mathrm{d}\rangle)$. Thus, upon the input of a photon pulse the scheme would allow to deterministically create a freely propagating, optical Schrödinger cat state. Moreover, in contrast to cat states constructed from two coherent states with opposite phases, the outcome of the proposed procedure would be a superposition state between two spatially separated modes. This is favorable for two reasons: First, coherent states with opposite phase need a large amplitude α to be approximately orthogonal. In contrast, the two fiber modes represent real orthogonal states. Second, since the cat state is created between two distinct optical fibers, it is directly ready-to-use for all kind of interferometric applications where the first beam splitter of the interferometer is represented by the optical switch.

Instead of using a coherent pulse as input state of the optical switch, one could also send in a photon Fock state. Then the final state of the described scheme would be a so-called “N00N state” [173, 174] which is defined as a superposition between N particles in one mode and the vacuum state in the other one and vice versa, reading

$$|\Psi^\pm_\text{N00N}\rangle = \frac{1}{\sqrt{2}}(|N_\mathrm{b}, 0_\mathrm{d}\rangle \pm |0_\mathrm{b}, N_\mathrm{d}\rangle) . \tag{6.23}$$

Optical N00N states are even more challenging to create than optical cat states since as input photon Fock states are required which so far cannot be produced deterministically with arbitrary photon numbers N. Similar to cat states, N00N states are of particular interest for the use in interferometers, since they enable precise measurements of the phase at the Heisenberg limit [174]. Moreover, novel applications in quantum imaging were proposed with N00N states [175].

Prospects for the realization of the entanglement protocol

In order to realize the described protocol, several challenging requirements have to be fulfilled. First of all, the efficiency of the system has to be extremely high since already the loss of a single photon destroys the coherence of the cat state. This renders our optical switch an ideal candidate to realize the protocol, since WGM microresonators enable very high in- and out-coupling efficiencies and a created cat state would be directly fiber-coupled. In this context, the high photon survival probability of 79 % of our current optical switch is already very promising. However, in order to prepare maximally entangled states, a higher fidelity close to unity is required. In section 6.3.3 we discussed prospects how fidelities up to 91 % could be realized with state of the art improvements of the quality factor and trapping of atoms close to the resonator surface. Trapped atoms would also simplify the coherent manipulation of the internal atomic states. Without trapping extremely short and intense $\pi/2$-pulses would be required for the atomic state preparation and manipulation within the interaction time of the atom. Such pulses are very hard to achieve with realistic microwave powers [128].

Apart from theses technical challenges, there is also another important requirement which is related to the strong single photon nonlinearity of the switch. From the discussion of the intensity auto correlation functions, we found that depending on the number of incoming photons the switching properties can be very different. This limits the use for the creation of cat states: With increasing photon number of the pulse, the switch will start to deviate from its intended behavior. Fortunately, we found that for two incoming photons this effect should be relatively small because for optimal operation condition of the switch $g^{(2)}(0)$ is close to unity and, therefore, no difference to the single photon case should occur. However, for larger photon numbers, the corresponding dressed state of the coupled atom–resonator system will become more resonant, reducing thereby the switching fidelity. A solution of this problem is to stretch the duration T_{pulse} of the incoming multi-photon pulse such that it is much longer than the decay time of the resonator field fulling the condition $T_{\text{pulse}} \gg 1/\kappa$ [172]. Then, the probability of coupling simultaneously several photons into the resonator is small and the switch behaves according to the single photon case.

Thus, despite the demanding technical requirements which have to be fulfilled, the optical switch clearly has the potential of enabling a deterministic generation of freely propagating, optical Schrödinger cat states. This would be a important step towards the implementation of many important applications in quantum communication and metrology.

6.6 Conclusion

In this chapter we discussed the concept and the realization of a fiber-integrated optical switch which is controlled by a single atom. The switch consists of an atom that is coupled to the bottle resonator which is interfaced by two fibers in the add-drop configuration. The underlying principle of the switch is directly related to our finding, that with the help of the non-transversal polarization of TM modes, a situation close to the ideal one of a two-level atom coupled to a single resonator mode can be realized. We experimentally verified that, as predicted by this analogy, the presence of an atom in the evanescent resonator field leads to distinct two peak vacuum-Rabi spectrum and triggers the switching of light between the two fibers. In a parameter scan of the resonator–fiber coupling rate, we identified the optimal working point of the switch to lie in the transition from the strong coupling to the fast cavity regime where the condition $\kappa > g^2/\kappa > \gamma$ is fullfilled. At this point the switching process reaches a classical fidelity of 62 % in conjunction with a high photon survival probability of 79 %.

We also analyzed the light from the optical switch and found a modification of the photon statistics showing photon bunching in the drop and anti-bunching in the bus fiber. This photon-number-depended routing capacity is most pronounced in the fast cavity regime and leads to a preferential coupling of two photon states into the resonator from where they can exit through the drop fiber, while single photons remain with higher probability in the bus fiber.

Moreover, we theoretically investigated the possibility fo creating atom–photon entanglement with our optical switch. Assuming that coherent manipulation of the atom is possible, one could reach, for the current experimental parameters, a final entangled state with a negativity of 0.6 . This high degree of entanglement clearly demonstrates the potential of the switch for future applications in quantum information and metrology. In a next generation setup, state-of-the-art improvements of the resonator quality factor should allow one to reach much higher fidelities of the switching operation. In addition, the concept will profit enormously if trapping of atoms close to the resonator surface becomes available. Then, much stronger atom–light coupling could be realized. Based on these improvements, we proposed a scheme for the deterministic creation of freely propagating optical Schrödinger cat and N00N states. These state would have great potential for applications in the field of quantum communication, computation and metrology.

CHAPTER 7

Summary

In this thesis, strong coupling between single atoms and non-transversally polarized photons was investigated. It was demonstrated that non-transversal light fields possess intriguing properties compared to transversal fields, that can lead to quantitatively different light–matter interaction. The system under study was a whispering-gallery-mode (WGM) bottle microresonator to which single laser-cooled ^{85}Rb atoms were coupled using an atomic fountain. The bottle resonator combines in the same system an ultra-high quality factor, a small mode volume and in- and out-coupling of light with near unity efficiency via ultra-thin fibers. For this reasons, it is an ideal tool to enable strong light–matter interaction and high photon-survival probabilities.

In the present work, it was demonstrated, that in the evanescent field of WGM microresonators a non-transversal polarization components occur. A detailed analysis of the evanescent field for the general case of total internal reflection at a silica–vacuum interface, as well as for the specific field equations of the bottle resonator was performed. The results showed that while TE modes are fully transversally polarized, for TM modes, a strong longitudinal field component arises which can reach for glass up 73 % of the transversal field. Moreover, the transversal and the longitudinal fields oscillate out of phase by $\pi/2$ resulting in elliptical polarization, where the field vector rotates in the plane of propagation. Due to the large ratio between the longitudinal and the transversal component, the overlap with circular polarization is up to 96 %. Astonishingly, the rotation sense of the polarization is tagged to the propagation direction of the light, meaning that counter-propagating TM modes have almost orthogonal polarization. These properties deviate fundamentally from transversal light fields and, therefore, one expects very different light–matter interaction for TE and TM modes. However, so far, the non-transversal polarization has not been taken into account for the description of light–matter interactions with WGM microresonators. Instead, the model of a conventional ring resonator, which sustains a pair of counter-propagating, degenerate modes with identical polarization, has been used. As a consequence, counter-propagating modes interfere destructively and can be described by fully intensity modulated standing waves. The analysis in the present thesis showed that this model is in general inadequate. Actually, in the case of counter-propagating TM modes the interference is suppressed, due to their almost orthogonal polarization resulting in a fundamentally different physical situation. Within the thesis, a new model of light–matter interaction in WGMs was developed to take into account the non-transversal field properties. The novel model describes modes with arbitrary polarization, in particular, the exact field properties of TM resonator modes and considers also the full magnetic sub-structure of the involved atomic transition.

In order to verify the theoretical results, the system was also investigated experimentally by coupling of single ^{85}Rb atoms to a bottle resonator. This cavity quantum electrodynamics (CQED) experiment comprised an atomic fountain which delivered laser-cooled atoms into the evanescent field of the resonator and a vacuum-compatible setup to interface the resonator with two ultra-thin fibers. Using this setup, the vacuum-Rabi spectra of the coupled atom–resonator system were measured for the the case of TE and TM polarization. The experimental results were quantitatively compared to the theoretical predictions and excellent agreement was found. While the transversally polarized TE mode showed a vacuum-Rabi spectrum that was dominated by a central resonance, which is the signature of the interference of counter-propagating resonator modes, the non-transversally polarized TM mode featured a vacuum-Rabi spectrum with two distinct resonance, similar to the one of a Fabry-Pérot resonator strongly coupled to an atom. The analysis showed that despite the simultaneous existence of two degenerate resonator modes, the presence of the non-transversal polarization effectively led to the ideal case of a two-level atom that only interacts with a single resonator mode.

Based on theses findings, the distinct vacuum-Rabi splitting of TM modes was exploited to realize a highly efficient optical switch controlled by a single atom. For this purpose, the bottle resonator was interfaced with two ultra-thin fibers. Then the presence of a single ^{85}Rb atom in the evanescent resonator field was able to switch light efficiently between the two fibers. The optical switch was characterized for different coupling rates to the two ultra-thin fibers and including all losses a classical fidelity of 62 % was found in conjunction with a high photon survival probability of 79 %. Based on these results, the potential of the switch for the deterministic creation of atom–light entanglement was investigated: With full control over the internal atomic states available, it should be possible to create entanglement between an atom coupled to the bottle resonator and a freely propagating photon with a negativity of 0.6 . The degree of entanglement could be further increased in a next generation experiment employing state-of-the-art improvements of the quality factor of the bottle resonator. Then, by scaling up the number of photons sent onto the switch, the creation of freely propagating optical Schrödinger cat states would come into reach.

In summary, the studies presented in this thesis demonstrate that due to non-transversal polarization components, light–matter interaction can be drastically modified. In the context of WGM microresonators, one has to carefully differentiate between transversal TE modes, for which a WGM resonator behaves like a conventional ring resonator, and non-transversal TM modes with fundamentally different field properties. For the case of strong interaction of a single atom and the resonator, the presence of the longitudinal field effectively leads to the ideal situation of a two-level atom that only interacts with a single resonator mode. This allows one to combine, the advantages of Fabry-Pérot resonator with the high in- and out-coupling efficiencies of WGM microresonators and their intrinsic fiber-coupled design. This opens up a great perspective towards new powerful applications in CQED, as it is apparent from the demonstration of a highly efficient optical fiber switch controlled by a single atom.

Moreover, the findings in this thesis demonstrate that WGM microresonators have to be seen as a completely new class of optical resonators which possess an intrinsic correlation between the propagation direction and the polarization of TM modes. Since transversal TE modes are complemented by a pair of counter-propagating TM modes with almost orthogonal polarization, three mutually nearly orthogonal polarizations are simultaneously supported in the resonator. This is an unique situation not encountered in other types of resonators.

The presented results have also implications in a broader context. In all situations, where transversal field gradients on a scale on the order of the wavelength occur, strong longitudinal polarization components are present. For instance, this is the case in tightly focussed laser beams, plasmonic devices and all kinds of photonic micro- and nanostructures. Due to the longitudinal component, the light field will be elliptically polarized in the plane of propagation and gives rise to the described correlation between propagation direction and polarization [12]. As in the case of a WGM microresonator, this implies that in a superposition of counter-propagating, non-traversal fields, no full destructive interference can occur. Moreover, when it comes to light–matter interactions, the correlation between polarization and propagation direction can favor the directional emission of photons. The non-transversal polarization of light allows to address these directional coupling effects and gives rise to a new degree of freedom in the control of light–matter interaction.

Bibliography

[1] M. Lax, W. H. Louisell, and W. B. McKnight. From maxwell to paraxial wave optics. *Phys. Rev. A*, 11:1365–1370, Apr 1975.

[2] M. O. Scully and M. S. Zubairy. Simple laser accelerator: Optics and particle dynamics. *Phys. Rev. A*, 44:2656–2663, Aug 1991.

[3] L. Cicchitelli, H. Hora, and R. Postle. Longitudinal field components for laser beams in vacuum. *Phys. Rev. A*, 41:3727–3732, Apr 1990.

[4] L. Novotny, M. R. Beversluis, K. S. Youngworth, and T. G. Brown. Longitudinal field modes probed by single molecules. *Phys. Rev. Lett.*, 86:5251–5254, Jun 2001.

[5] K. S. Youngworth and T. G. Brown. Focusing of high numerical aperture cylindrical-vector beams. *Opt. Express*, 7(2):77–87, Jul 2000.

[6] H. P. Urbach and S. F. Pereira. Field in focus with a maximum longitudinal electric component. *Phys. Rev. Lett.*, 100:123904, Mar 2008.

[7] F. Warken, E. Vetsch, D. Meschede, M. Sokolowski, and A. Rauschenbeutel. Ultra-sensitive surface absorption spectroscopy using sub-wavelength diameter optical fibers. *Opt. Express*, 15(19):11952–11958, Sep 2007.

[8] E. Vetsch, D. Reitz, G. Sagué, R. Schmidt, S. T. Dawkins, and A. Rauschenbeutel. Optical interface created by laser-cooled atoms trapped in the evanescent field surrounding an optical nanofiber. *Phys. Rev. Lett.*, 104(20):203603, 2010.

[9] K. J. Vahala. Optical microcavities. *Nature*, 424(6950):839–846, 2003.

[10] E. Ozbay. Plasmonics: Merging photonics and electronics at nanoscale dimensions. *Science*, 311(5758):189–193, 2006.

[11] D. Axelrod, T. P. Burghardt, and N. L. Thompson. Total internal reflection fluorescence. *Annu. Rev. Biophys. Bio.*, 13(1):247–268, 1984.

[12] K. Y. Bliokh and F. Nori. Transverse spin of a surface polariton. *Phys. Rev. A*, 85:061801, Jun 2012.

[13] S. Quabis, R. Dorn, M. Eberler, O. Glöckl, and G. Leuchs. Focusing light to a tighter spot. *Opt. Commun.*, 179(1–6):1 – 7, 2000.

[14] R. Dorn, S. Quabis, and G. Leuchs. Sharper focus for a radially polarized light beam. *Phys. Rev. Lett.*, 91:233901, Dec 2003.

[15] L. Novotny, E. J. Sánchez, and X. S. Xie. Near-field optical imaging using metal tips illuminated by higher-order Hermite–Gaussian beams. *Ultramicroscopy*, 71(1–4):21 – 29, 1998.

[16] M. K. Tey, Z. Chen, S. A. Aljunid, B. Chng, F. Huber, G. Maslennikov, and C. Kurtsiefer. Strong interaction between light and a single trapped atom without the need for a cavity. *Nat. Phys.*, 4(12):924–927, 12 2008.

[17] K. G. Lee, X. W. Chen, H. Eghlidi, P. Kukura, R. Lettow, A. Renn, V. Sandoghdar, and S Götzinger. A planar dielectric antenna for directional single-photon emission and near-unity collection efficiency. *Nat. Photon.*, 5(3):166–169, 2011.

[18] R. Maiwald, A. Golla, M. Fischer, M. Bader, S. Heugel, B. Chalopin, M. Sondermann, and G. Leuchs. Collecting more than half the fluorescence photons from a single ion. *Phys. Rev. A*, 86:043431, Oct 2012.

[19] P. R. Berman. *Cavity quantum electrodynamics*. Academic Press, 1994.

[20] A. Rauschenbeutel, G. Nogues, S. Osnaghi, P. Bertet, M. Brune, J.-M. Raimond, and S. Haroche. Step-by-step engineered multiparticle entanglement. *Science*, 288(5473):2024–2028, 2000.

[21] J.-M. Raimond, M. Brune, and S. Haroche. Manipulating quantum entanglement with atoms and photons in a cavity. *Rev. Mod. Phys.*, 73:565–582, Aug 2001.

[22] C. Sayrin, I. Dotsenko, X. Zhou, B. Peaudecerf, T. Rybarczyk, S. Gleyzes, P. Rouchon, Mirrahimi. M., H. Amini, M. Brune, J. M. Raimond, and S. Haroche. Real-time quantum feedback prepares and stabilizes photon number states. *Nature*, 477(7362):73–77, 09 2011.

[23] G. Nogues, A. Rauschenbeutel, S. Osnaghi, M. Brune, J. M. Raimond, and S. Haroche. Seeing a single photon without destroying it. *Nature*, 400(6741):239–242, 07 1999.

[24] A. Reiserer, S. Ritter, and G. Rempe. Nondestructive detection of an optical photon. *Science*, 2013.

[25] A. Kuhn, M. Hennrich, and G. Rempe. Deterministic single-photon source for distributed quantum networking. *Phys. Rev. Lett.*, 89:067901, Jul 2002.

[26] A. D. Boozer, A. Boca, R. Miller, T. E. Northup, and H. J. Kimble. Reversible state transfer between light and a single trapped atom. *Phys. Rev. Lett.*, 98:193601, May 2007.

[27] S. Ritter, C. Nolleke, C. Hahn, A. Reiserer, A. Neuzner, M. Uphoff, M. Mucke, E. Figueroa, J. Bochmann, and G. Rempe. An elementary quantum network of single atoms in optical cavities. *Nature*, 484(7393):195–200, 04 2012.

[28] W. Chen, K. M. Beck, R. Bücker, M. Gullans, M. D. Lukin, H. Tanji-Suzuki, and V. Vuletić. All-optical switch and transistor gated by one stored photon. *Science*, 341(6147):768–770, 2013.

[29] B. Dayan, A. S. Parkins, T. Aoki, E. P. Ostby, K. J. Vahala, and H. J. Kimble. A photon turnstile dynamically regulated by one atom. *Science*, 319(5866):1062, 2008.

[30] K. M. Birnbaum, A. Boca, R. Miller, A. D. Boozer, T. E. Northup, and H. J. Kimble. Photon blockade in an optical cavity with one trapped atom. *Nature*, 436(7047):87–90, 07 2005.

[31] Royal Swedish Academy of Sciences. The nobel prize in physics 2012. Press release, 2012.

[32] H. Mabuchi, Q. A. Turchette, M. S. Chapman, and H. J. Kimble. Real-time detection of individual atoms falling through a high-finesse optical cavity. *Opt. Lett.*, 21(17):1393–1395, Sep 1996.

[33] D. Hunger, T. Steinmetz, Y. Colombe, C. Deutsch, T. W. Hänsch, and J. Reichel. A fiber fabry–perot cavity with high finesse. *New J. Phys.*, 12(6):065038, 2010.

[34] J. M. Gérard, D. Barrier, J. Y. Marzin, R. Kuszelewicz, L. Manin, E. Costard, V. Thierry-Mieg, and T. Rivera. Quantum boxes as active probes for photonic microstructures: The pillar microcavity case. *Appl. Phys. Lett*, 69(4):449–451, 1996.

[35] S. Reitzenstein and A. Forchel. Quantum dot micropillars. *J. Phys. D Appl. Phys.*, 43(3):033001, 2010.

[36] C. Wuttke, M. Becker, S. Brückner, M. Rothhardt, and A. Rauschenbeutel. Nanofiber Fabry–Perot microresonator for nonlinear optics and cavity quantum electrodynamics. *Opt. Lett.*, 37(11):1949–1951, Jun 2012.

[37] T. Yoshie, A. Scherer, J. Hendrickson, G. Khitrova, H. M. Gibbs, G. Rupper, C. Ell, O. B. Shchekin, and D. G. Deppe. Vacuum Rabi splitting with a single quantum dot in a photonic crystal nanocavity. *Nature*, 432(7014):200–203, 11 2004.

[38] J. D. Thompson, T. G. Tiecke, N. P. de Leon, J. Feist, A. V. Akimov, M. Gullans, A. S. Zibrov, V. Vuletić, and M. D. Lukin. Coupling a single trapped atom to a nanoscale optical cavity. *Science*, 340(6137):1202–1205, 2013.

[39] A. B. Matsko and V. S. Ilchenko. Optical resonators with whispering-gallery modes—part I: basics. *IEEE J. Sel. Top. Quant.*, 12(1):3–14, 2006.

[40] T. J. Kippenberg, S. M. Spillane, and K. J. Vahala. Demonstration of ultra-high-Q small mode volume toroid microcavities on a chip. *Appl. Phys. Lett*, 85(25):6113–6115, 2004.

[41] V. S. Ilchenko and A. B. Matsko. Optical resonators with whispering-gallery modes—part II: applications. *IEEE J. Sel. Top. Quant.*, 12(1):15–32, 2006.

[42] B. E. A. Saleh and M. C. Teich. *Fundamentals of photonics*, volume 22. Wiley New York, 1991.

[43] T. J. Kippenberg. *Nonlinear Optics in Ultra-high-Q Whispering-Gallery Optical Microcavities*. PhD thesis, California Institute of Technology, 2004.

[44] Y. Louyer, D. Meschede, and A. Rauschenbeutel. Tunable whispering-gallery-mode resonators for cavity quantum electrodynamics. *Phys. Rev. A*, 72(3):031801, 2005.

[45] J. W. S. Rayleigh. *The theory of sound*, volume 2. Macmillan and Co., London, 1878.

[46] Lord Rayleigh. The problem of the whispering gallery. *Phil. Mag.*, 20(120):1001–1004, 1910.

[47] Lord Rayleigh. Further applications of Bessel's functions of high order to the whispering gallery and allied problems. *Phil. Mag.*, 27(157):100–109, 1914.

[48] T. Kawalec, L. Józefowski, J. Fiutowski, MJ Kasprowicz, and T. Dohnalik. Spectroscopic measurements of the evanescent wave polarization state. *Opt. Commun.*, 274(2):341–346, 2007.

[49] R. Symes, R. M. Sayer, and Jonathan P. Reid. Cavity enhanced droplet spectroscopy: Principles, perspectives and prospects. *Phys. Chem. Chem. Phys.*, 6:474–487, 2004.

[50] V. B. Braginsky, M. L. Gorodetsky, and V. S. Ilchenko. Quality-factor and nonlinear properties of optical whispering-gallery modes. *Phys. Lett. A*, 137(7):393–397, 1989.

[51] M. L. Gorodetsky, A. A. Savchenkov, and V. S. Ilchenko. Ultimate Q of optical microsphere resonators. *Opt. Lett.*, 21(7):453–455, 1996.

[52] T. J. Kippenberg, S. M. Spillane, D. K. Armani, and K. J. Vahala. Fabrication and coupling to planar high-Q silica disk microcavities. *Appl. Phys. Lett*, 83(4):797–799, 2003.

[53] M. Pöllinger. *Bottle microresonators for applications in quantum optics and all-optical signal processing*. PhD thesis, Johannes Gutenberg-Universität Mainz, 2010.

[54] D. Armani, B. Min, A. Martin, and K. J. Vahala. Electrical thermo-optic tuning of ultrahigh Q microtoroid resonators. *Appl. Phys. Lett*, 85(22):5439–5441, 2004.

[55] W. von Klitzing, R. Long, V. S. Ilchenko, J. Hare, and V. Lefèvre-Seguin. Frequency tuning of the whispering-gallery modes of silica microspheres for cavity quantum electrodynamics and spectroscopy. *Opt. Lett.*, 26(3):166–168, 2001.

[56] M. Sumetsky. Whispering-gallery-bottle microcavities: the three-dimensional etalon. *Opt. Lett.*, 29(1):8–10, 2004.

[57] F. Warken. *Ultradünne Glasfasern als Werkzeug zur Kopplung von Licht und Materie*. PhD thesis, Rheinische Friedrich-Wilhelms-Universität Bonn, 2007.

[58] M. Pöllinger, D. O'Shea, F. Warken, and A. Rauschenbeutel. Ultrahigh-Q tunable whispering-gallery-mode microresonator. *Phys. Rev. Lett.*, 103(5):053901, 2009.

[59] D. O'Shea, A. Rettenmaier, and A. Rauschenbeutel. Active frequency stabilization of an ultra-high Q whispering-gallery-mode microresonator. *Appl. Phys. B-Lasers O.*, 99(4):623–627, 2010.

[60] D. O'Shea. *Cavity QED experiments with a whispering-gallery-mode bottle resonator*. PhD thesis, Vienna University of Technology, 2013.

[61] D. R. Rowland and J. D. Love. Evanescent wave coupling of whispering gallery modes of a dielectric cylinder. In *IEE Proc.-J*, volume 140, pages 177–188. IET, 1993.

[62] S. Schiller and R. L. Byer. High-resolution spectroscopy of whispering gallery modes in large dielectric spheres. *Opt. Lett.*, 16(15):1138–1140, Aug 1991.

[63] A. Serpengüzel, G. Griffel, and S. Arnold. Excitation of resonances of microspheres on an optical fiber. *Opt. Lett.*, 20(7):654–656, Apr 1995.

[64] N. Dubreuil, J. C. Knight, D. K. Leventhal, V. Sandoghdar, J. Hare, and V. Lefèvre. Eroded monomode optical fiber for whispering-gallery mode excitation in fused-silica microspheres. *Opt. Lett.*, 20(8):813–815, Apr 1995.

[65] G. Griffel, J. Connolly, N. Morris, S. Arnold, D. Taskent, and A. Serpengüzel. Morphology-dependent resonances of a microsphere–optical fiber system. *Opt. Lett.*, 21(10):695–697, May 1996.

[66] S. M. Spillane. *Fiber-coupled Ultra-high-Q Microresonators for Nonlinear and Quantum Optics*. PhD thesis, California Institute of Technology, 2004.

[67] J. C. Knight, G. Cheung, F. Jacques, and T. A. Birks. Phase-matched excitation of whispering-gallery-mode resonances by a fiber taper. *Opt. Lett.*, 22(15):1129–1131, 1997.

[68] A. Yariv. *Optical Electronics in Modern Communications*. Oxford University Press, New York, Oxford, 1997.

[69] G. Sagué. *Cold atom physics using ultra-thin optical fibres*. PhD thesis, Rheinischen Friedrich-Wilhelms-Universität Bonn, 2008.

[70] E. Snitzer. Cylindrical dielectric waveguide modes. *J. Opt. Soc. Am.*, 51(5):491–498, May 1961.

[71] S. M. Spillane, T. J. Kippenberg, O. J. Painter, and K. J. Vahala. Ideality in a fiber-taper-coupled microresonator system for application to cavity quantum electrodynamics. *Phys. Rev. Lett.*, 91(4):043902, 2003.

[72] H. A. Haus. *Waves and fields in optoelectronics*, volume 1. Prentice-Hall Englewood Cliffs, NJ, 1984.

[73] T. J. Kippenberg, S. M. Spillane, and K. J. Vahala. Modal coupling in traveling-wave resonators. *Opt. Lett.*, 27(19):1669–1671, 2002.

[74] H. Rokhsari and K. J. Vahala. Ultralow loss, high Q, four port resonant couplers for quantum optics and photonics. *Phys. Rev. Lett.*, 92(25):253905, Jun 2004.

[75] C. Junge, S. Nickel, D. O'Shea, and A. Rauschenbeutel. Bottle microresonator with actively stabilized evanescent coupling. *Opt. Lett.*, 36(17):3488–3490, 2011.

[76] R. W. P. Drever, J. L. Hall, F. V. Kowalski, J. Hough, G. M. Ford, A. J. Munley, and H. Ward. Laser phase and frequency stabilization using an optical resonator. *Appl. Phys. B-Lasers O.*, 31(2):97–105, 1983.

[77] E. D. Black. An introduction to Pound–Drever–Hall laser frequency stabilization. *Am. J. Phys.*, 69:79, 2001.

[78] A. Rettenmaier. Aktive Frequenzstabilisierung eines durchstimmbaren Flüstergaleriemoden-Mikroresonators ultrahoher Güte. Diplomarbeit, Johannes Gutenberg-Universität Mainz, 2009.

[79] M. Pöllinger and A. Rauschenbeutel. All-optical signal processing at ultra-lowpowers in bottle microresonators usingthe kerr effect. *Opt. Express*, 18(17):17764–17775, Aug 2010.

[80] T. Aoki, B. Dayan, E Wilcut, W. P. Bowen, A. S. Parkins, T. J. Kippenberg, K. J. Vahala, and H. J. Kimble. Observation of strong coupling between one atom and a monolithic microresonator. *Nature*, 443(7112):671–674, 2006.

[81] F. Vollmer and S. Arnold. Whispering-gallery-mode biosensing: label-free detection down to single molecules. *Nat. Meth.*, 5(7):591–596, 07 2008.

[82] J. Zhu, S. K. Ozdemir, Y.-F. Xiao, L. Li, L. He, D.-R. Chen, and L. Yang. On-chip single nanoparticle detection and sizing by mode splitting in an ultrahigh-q microresonator. *Nat. Photon.*, 4(1):46–49, 01 2010.

[83] P. Del'Haye, A. Schliesser, O. Arcizet, T. Wilken, R. Holzwarth, and T. J. Kippenberg. Optical frequency comb generation from a monolithic microresonator. *Nature*, 450(7173):1214–1217, 12 2007.

[84] V. Sandoghdar, F. Treussart, J. Hare, V. Lefèvre-Seguin, J. M. Raimond, and S. Haroche. Very low threshold whispering-gallery-mode microsphere laser. *Phys. Rev. A*, 54:R1777–R1780, Sep 1996.

[85] M. Cai, O. Painter, K. J. Vahala, and P. C. Sercel. Fiber-coupled microsphere laser. *Opt. Lett.*, 25(19):1430–1432, 2000.

[86] W. von Klitzing, E Jahier, R. Long, F. Lissillour, V. Lefèvre-Seguin, J. Hare, J.-M. Raimond, and S. Haroche. Very low threshold green lasing in microspheres by up-conversion of IR photons. *J. Opt. B*, 2(2):204, 2000.

[87] D. S. Rabeling, J. H. Chow, M. B. Gray, and D. E. McClelland. Experimental demonstration of impedance match locking and control for coupled resonators. *Opt. Express*, 18(9):9314–9323, 2010.

[88] E.T. Jaynes and F. W. Cummings. Comparison of quantum and semiclassical radiation theories with application to the beam maser. *P. IEEE*, 51(1):89–109, 1963.

[89] T. Aoki, A. S. Parkins, D. J. Alton, C. A. Regal, B. Dayan, E. Ostby, K. J. Vahala, and H. J. Kimble. Efficient routing of single photons by one atom and a microtoroidal cavity. *Phys. Rev. Lett.*, 102(8):083601, 2009.

[90] C. Junge, D. O'Shea, J. Volz, and A. Rauschenbeutel. Strong coupling between single atoms and nontransversal photons. *Phys. Rev. Lett.*, 110:213604, May 2013.

[91] C. C. Gerry and P. L. Knight. *Introductory quantum optics*. Cambridge university press, 2005.

[92] J. J. Sanchez-Mondragon, N. B. Narozhny, and J. H. Eberly. Theory of spontaneous-emission line shape in an ideal cavity. *Phys. Rev. Lett.*, 51:550–553, Aug 1983.

[93] V. Peano and M. Thorwart. Quasienergy description of the driven Jaynes-Cummings model. *Phys. Rev. B*, 82:155129, Oct 2010.

[94] H. J. Carmichael. *Statistical Methods in Quantum Optics 1: Master Equations and Fokker-Planck Equations*, volume 1. Springer, 2002.

[95] K. M. Birnbaum, A. S. Parkins, and H. J. Kimble. Cavity QED with multiple hyperfine levels. *Phys. Rev. A*, 74:063802, Dec 2006.

[96] M. Rosenblit, P. Horak, S. Helsby, and R. Folman. Single-atom detection using whispering-gallery modes of microdisk resonators. *Phys. Rev. A*, 70:053808, Nov 2004.

[97] M. Rosenblit, Y. Japha, P. Horak, and R. Folman. Simultaneous optical trapping and detection of atoms by microdisk resonators. *Phys. Rev. A*, 73:063805, Jun 2006.

[98] J.T. Shen and S. Fan. Theory of single-photon transport in a single-mode waveguide. II. coupling to a whispering-gallery resonator containing a two-level atom. *Phys. Rev. A*, 79(2):23838, 2009.

[99] D. J. Alton, N. P. Stern, T. Aoki, H. Lee, E. Ostby, K. J. Vahala, and H. J. Kimble. Strong interactions of single atoms and photons near a dielectric boundary. *Nat. Phys.*, 7(2):159–165, 2010.

[100] N. P. Stern, D. J. Alton, and H. J. Kimble. Simulations of atomic trajectories near a dielectric surface. *New J. Phys.*, 13(8):085004, 2011.

[101] K. Srinivasan and O. Painter. Linear and nonlinear optical spectroscopy of a strongly coupled microdisk-quantum dot system. *Nature*, 450(7171):862–865, 12 2007.

[102] P. Domokos, M. Gangl, and H. Ritsch. Single-atom detection in high-Q multimode cavities. *Opt. Express*, 185(1):115–123, 2000.

[103] Q. A. Turchette, C. J. Hood, W. Lange, H. Mabuchi, and H. J. Kimble. Measurement of conditional phase shifts for quantum logic. *Phys. Rev. Lett.*, 75(25):4710–4713, 1995.

[104] L.-M. Duan and H. J. Kimble. Scalable photonic quantum computation through cavity-assisted interactions. *Phys. Rev. Lett.*, 92(12):127902, 2004.

[105] M. Soljačić, E. Lidorikis, J. D. Joannopoulos, and L. V. Hau. Ultralow-power all-optical switching. *Appl. Phys. Lett*, 86(17):–, 2005.

[106] E. Waks and J. Vuckovic. Dipole induced transparency in drop-filter cavity-waveguide systems. *Phys. Rev. Lett.*, 96:153601, Apr 2006.

[107] P. Bermel, A. Rodriguez, S. G. Johnson, J. D. Joannopoulos, and M. Soljačić. Single-photon all-optical switching using waveguide-cavity quantum electrodynamics. *Phys. Rev. A*, 74(4):043818, 2006.

[108] I. Fushman, D. Englund, A. Faraon, N. Stoltz, P. Petroff, and J. Vučković. Controlled phase shifts with a single quantum dot. *Science*, 320(5877):769–772, 2008.

[109] T. Kampschulte, W. Alt, S. Brakhane, M. Eckstein, R. Reimann, A. Widera, and D. Meschede. Optical control of the refractive index of a single atom. *Phys. Rev. Lett.*, 105:153603, Oct 2010.

[110] A. E. B. Nielsen and J. Kerckhoff. Efficient all-optical switch using a Λ atom in a cavity QED system. *Phys. Rev. A*, 84:043821, Oct 2011.

[111] D. O'Shea, C. Junge, J. Volz, and A. Rauschenbeutel. Fiber-optical switch controlled by a single atom. *Phys. Rev. Lett.*, 111:193601, Nov 2013.

[112] F. de Fornel. *Evanescent Waves: From Newtonian Optics To Atomic Optics*. Springer, Berlin, 2000.

[113] F. Goos and H. Hänchen. Ein neuer und fundamentaler Versuch zur Totalreflexion. *Ann. Phys.*, 436(7-8):333–346, 1947.

[114] K. Artmann. Berechnung der Seitenversetzung des totalreflektierten Strahles. *Ann. Phys.*, 437(1-2):87–102, 1948.

[115] D. A. Steck. Rubidium 85 D line data, 2012.

[116] K. Srinivasan and O. Painter. Mode coupling and cavity–quantum-dot interactions in a fiber-coupled microdisk cavity. *Phys. Rev. A*, 75(2):023814, Feb 2007.

[117] C. Hauswald. Aufbau und Charakterisierung eines Atom-springbrunnens für ein Resonator-QED-Experiment mit Flüstergaleriemoden-Mikroresonatoren. Diplomarbeit, Johannes Gutenberg-Universität Mainz, 2010.

[118] E. L. Raab, M. Prentiss, A. Cable, S. Chu, and D. E. Pritchard. Trapping of neutral sodium atoms with radiation pressure. *Phys. Rev. Lett.*, 59(23):2631–2634, Dec 1987.

[119] J. Ye, D. W. Vernooy, and H. J. Kimble. Trapping of single atoms in cavity QED. *Phys. Rev. Lett.*, 83(24):4987–4990, 1999.

[120] P. W. H. Pinkse, T. Fischer, P. Maunz, and G. Rempe. Trapping an atom with single photons. *Nature*, 404(6776):365–368, 2000.

[121] A. Goban, K. S. Choi, D. J. Alton, D. Ding, C. Lacroûte, M. Pototschnig, T. Thiele, N. P. Stern, and H. J. Kimble. Demonstration of a state-insensitive, compensated nanofiber trap. *Phys. Rev. Lett.*, 109:033603, Jul 2012.

[122] M. A. Kasevich, E. Riis, S. Chu, and R. G. DeVoe. rf spectroscopy in an atomic fountain. *Phys. Rev. Lett.*, 63:612–615, Aug 1989.

[123] P. Münstermann, T. Fischer, P. W. H. Pinkse, and G. Rempe. Single slow atoms from an atomic fountain observed in a high-finesse optical cavity. *Opt. Commun.*, 159(1-3):63 – 67, 1999.

[124] C. J. Bordé. Atomic clocks and inertial sensors. *Metrologia*, 39(5):435, 2002.

[125] J. Dalibard and C. Cohen-Tannoudji. Laser cooling below the Doppler limit by polarization gradients: simple theoretical models. *J. Opt. Soc. Am. B*, 6(11):2023–2045, 1989.

[126] G. Lamporesi. Realizzazione di una fontana di atomi di rubidio per un interferometro atomico. Master's thesis, Università di Firenze, 2003.

[127] S. Nickel. Kopplung, Charakterisierung und aktive Frequenzstabilisierung von Flaschenresonatoren ultrahoher güte innerhalb einer Ultrahochvakuum-Apparatur. Diplomarbeit, Johannes Gutenberg-Universität Mainz, 2010.

[128] M. Scheucher. Towards a quantum switch for light. Master's thesis, Technische Universität Wien, 2013.

[129] K. Friebe. Strong coupling of single atoms to a whispering-gallery-mode resonator of ultrahigh quality. Diplomarbeit, Johannes Gutenberg-Universität Mainz, 2011.

[130] B. Schlederer. Description of a bottle resonator evanescently coupled to a waveguide. Master's thesis, Technische Universität Wien, 2013.

[131] M. Asghari and Ashok V. Krishnamoorthy. Silicon photonics: Energy-efficient communication. *Nat. Phys.*, 5(5):268–270, 05 2011.

[132] V. Giovannetti, S. Lloyd, and L. Maccone. Quantum-enhanced measurements: Beating the standard quantum limit. *Science*, 306(5700):1330–1336, 2004.

[133] V. Giovannetti, S. Lloyd, and L. Maccone. Advances in quantum metrology. *Nat. Photon.*, 5(4):222–229, 04 2011.

[134] P. P. Absil, J. V. Hryniewicz, B. E. Little, R. A. Wilson, L. G. Joneckis, and P.-T. Ho. Compact microring notch filters. *IEEE Photon. Technol. Lett.*, 12(4):398–400, 2000.

[135] F. C. Blom, H. Kelderman, H. J. W. M. Hoekstra, A. Driessen, Th. J. A. Popma, S. T. Chu, and B. E. Little. A single channel dropping filter based on a cylindrical microresonator. *Opt. Commun.*, 167(1–6):77 – 82, 1999.

[136] T. Bilici, S. Isci, A. Kurt, and A. Serpenguzel. Microsphere-based channel dropping filter with an integrated photodetector. *IEEE Photon. Technol. Lett.*, 16(2):476–478, 2004.

[137] J. V. Hryniewicz, P. P. Absil, B. E. Little, R. A. Wilson, and P.-T. Ho. Higher order filter response in coupled microring resonators. *IEEE Photon. Technol. Lett.*, 12(3):320–322, 2000.

[138] S.-T. Chu, B. E. Little, Wugen Pan, T. Kaneko, and Y. Kokubun. Second-order filter response from parallel coupled glass microring resonators. *IEEE Photon. Technol. Lett.*, 11(11):1426–1428, 1999.

[139] S.-T. Chu, B. E. Little, Wugen Pan, T. Kaneko, and Y. Kokubun. Cascaded microring resonators for crosstalk reduction and spectrum cleanup in add-drop filters. *IEEE Photon. Technol. Lett.*, 11(11):1423–1425, 1999.

[140] J. Popp, M. H. Fields, and R. K. Chang. Q switching by saturable absorption in microdroplets: elastic scattering and laser emission. *Opt. Lett.*, 22(17):1296–1298, Sep 1997.

[141] V. Van, T. A. Ibrahim, K. Ritter, P. P. Absil, F. G. Johnson, R. Grover, J. Goldhar, and P.-T. Ho. All-optical nonlinear switching in GaAs-AlGaAs microring resonators. *IEEE Photon. Technol. Lett.*, 14(1):74–76, 2002.

[142] M. T. Hill, H. J. S. Dorren, T. de Vries, X. J. M. Leijtens, J. H. den Besten, B. Smalbrugge, Y.-S. Oei, H. Binsma, G.-D. Khoe, and M. K. Smit. A fast low-power optical memory based on coupled micro-ring lasers. *Nature*, 432(7014):206–209, 11 2004.

[143] H. C. Tapalian, J.-P. Laine, and P. A. Lane. Thermooptical switches using coated microsphere resonators. *IEEE Photon. Technol. Lett.*, 14(8):1118 – 1120, Aug 2002.

[144] D. W. Vernooy and H. J. Kimble. Quantum structure and dynamics for atom galleries. *Phys. Rev. A*, 55(2):1239, 1997.

[145] C. W. Gardiner and M. J. Collett. Input and output in damped quantum systems: Quantum stochastic differential equations and the master equation. *Phys. Rev. A*, 31:3761–3774, Jun 1985.

[146] M. Lax. Formal theory of quantum fluctuations from a driven state. *Phys. Rev.*, 129:2342–2348, Mar 1963.

[147] S. S. Shamailov, A. S. Parkins, M. J. Collett, and H. J. Carmichael. Multi-photon blockade and dressing of the dressed states. *Opt. Commun.*, 283(5):766 – 772, 2010. <ce:title>Quo vadis Quantum Optics?</ce:title>.

[148] M. A. Nielsen, I. Chuang, and L. K. Grover. *Quantum computation and quantum information*. Cambridge University Press, 2000.

[149] K. Życzkowski, P. Horodecki, A. Sanpera, and M. Lewenstein. Volume of the set of separable states. *Phys. Rev. A*, 58:883–892, Aug 1998.

[150] G. Vidal and R. F. Werner. Computable measure of entanglement. *Phys. Rev. A*, 65:032314, Feb 2002.

[151] A. Peres. Separability criterion for density matrices. *Phys. Rev. Lett.*, 77:1413–1415, Aug 1996.

[152] Barry C. Sanders. Entangled coherent states. *Phys. Rev. A*, 45:6811–6815, May 1992.

[153] J. Wenger, M. Hafezi, F. Grosshans, R. Tualle-Brouri, and P. Grangier. Maximal violation of Bell inequalities using continuous-variable measurements. *Phys. Rev. A*, 67:012105, Jan 2003.

[154] H. Jeong, W. Son, M. S. Kim, D. Ahn, and Č. Brukner. Quantum nonlocality test for continuous-variable states with dichotomic observables. *Phys. Rev. A*, 67:012106, Jan 2003.

[155] T. C. Ralph, A. Gilchrist, G. J. Milburn, W. J. Munro, and S. Glancy. Quantum computation with optical coherent states. *Phys. Rev. A*, 68:042319, Oct 2003.

[156] E. Knill. Quantum computing with realistically noisy devices. *Nature*, 434(7029):39–44, 03 2005.

[157] S. J. van Enk and O. Hirota. Entangled coherent states: Teleportation and decoherence. *Phys. Rev. A*, 64:022313, Jul 2001.

[158] H. Jeong, M. S. Kim, and J. Lee. Quantum-information processing for a coherent superposition state via a mixedentangled coherent channel. *Phys. Rev. A*, 64:052308, Oct 2001.

[159] M. Hillery, V. Bužek, and A. Berthiaume. Quantum secret sharing. *Phys. Rev. A*, 59:1829–1834, Mar 1999.

[160] H. Jeong, M. S. Kim, and J. Lee. Quantum-information processing for a coherent superposition state via a mixedentangled coherent channel. *Phys. Rev. A*, 64:052308, Oct 2001.

[161] M. Brune, E. Hagley, J. Dreyer, X. Maître, A. Maali, C. Wunderlich, J.-M. Raimond, and S. Haroche. Observing the progressive decoherence of the “meter” in a quantum measurement. *Phys. Rev. Lett.*, 77:4887–4890, Dec 1996.

[162] S. Deleglise, I. Dotsenko, C. Sayrin, J. Bernu, M. Brune, J.-M. Raimond, and S. Haroche. Reconstruction of non-classical cavity field states with snapshots of their decoherence. *Nature*, 455(7212):510–514, 09 2008.

[163] C. Monroe, D. M. Meekhof, B. E. King, and D. J. Wineland. A “Schrödinger” cat superposition state of an atom. *Science*, 272(5265):1131–1136, 1996.

[164] D. Leibfried, E. Knill, S. Seidelin, J. Britton, R. B. Blakestad, J. Chiaverini, D. B. Hume, W. M. Itano, J. D. Jost, C. Langer, R. Ozeri, R. Reichle, and D. J. Wineland. Creation of a six-atom ‘Schrodinger cat’ state. *Nature*, 438(7068):639–642, 12 2005.

[165] B. Vlastakis, G. Kirchmair, Z. Leghtas, S. E. Nigg, L. Frunzio, S. M. Girvin, M. Mirrahimi, M. H. Devoret, and R. J. Schoelkopf. Deterministically encoding quantum information using 100-photon Schrödinger cat states. *Science*, 2013.

[166] B. C. Sanders. Review of entangled coherent states. *J. Phys. A*, 45(24):244002, 2012.

[167] A. Ourjoumtsev, H. Jeong, R. Tualle-Brouri, and P. Grangier. Generation of optical Schrödinger cats from photon number states. *Nature*, 448(7155):784–786, 08 2007.

[168] A. Ourjoumtsev, F. Ferreyrol, R. Tualle-Brouri, and P. Grangier. Preparation of non-local superpositions of quasi-classical light states. *Nat. Phys.*, 5(3):189–192, 03 2009.

[169] T. Gerrits, S. Glancy, T. S. Clement, B. Calkins, A. E. Lita, A. J. Miller, A. L. Migdall, S. W. Nam, R. P. Mirin, and E. Knill. Generation of optical coherent-state superpositions by number-resolved photon subtraction from the squeezed vacuum. *Phys. Rev. A*, 82:031802, Sep 2010.

[170] A. I. Lvovsky, R. Ghobadi, A. Chandra, A. S. Prasad, and C. Simon. Observation of micro-macro entanglement of light. *Nat. Phys.*, 9(9):541–544, 09 2013.

[171] N. Bruno, A. Martin, P. Sekatski, N. Sangouard, R. T. Thew, and N. Gisin. Displacement of entanglement back and forth between the micro and macro domains. *Nat. Phys.*, 9(9):545–548, 09 2013.

[172] B. Wang and L.-M. Duan. Engineering superpositions of coherent states in coherent optical pulses through cavity-assisted interaction. *Phys. Rev. A*, 72:022320, Aug 2005.

[173] B. C. Sanders. Quantum dynamics of the nonlinear rotator and the effects of continual spin measurement. *Phys. Rev. A*, 40:2417–2427, Sep 1989.

[174] J. P. Dowling. Quantum optical metrology–the lowdown on high-N00N states. *Contemp. Phys.*, 49(2):125–143, 2008.

[175] A. N. Boto, P. Kok, D. S. Abrams, S. L. Braunstein, C. P. Williams, and J. P. Dowling. Quantum interferometric optical lithography: Exploiting entanglement to beat the diffraction limit. *Phys. Rev. Lett.*, 85:2733–2736, Sep 2000.

Danksagung

An erster Stelle möchte ich mich bei Professor Arno Rauschenbeutel für die persönliche Betreuung und das entgegengebrachte Vertrauen bedanken. Ich hatte großen Spaß daran, in dem offenen und internationalen Umfeld seiner Arbeitsgruppe, an solch einem interessanten und vielseitigen Projekt zu forschen.

Ich danke Professor Stefan Rotter für die anregende Kooperation, die mir immer wieder neue Einsichten und Denkanstöße geliefert hat.

Ganz besonders danken möchte ich allen Mitgliedern der Arbeitsgruppe, für die hervorragende Atmosphäre, den Zusammenhalt, die große Hilfsbereitschaft und allgemein für eine schöne Zeit im Institut und darüber hinaus.

Dr. Jürgen Volz danke ich für die großartige Unterstützung während dieser Arbeit, für die spannenden Diskussionen und die vielen erhellenden Momenten.

Ein besonderer Dank geht an Dr. Danny O'Shea für die unzähligen kreativen Stunden im Labor, die gute Zusammenarbeit und die exzellente Planung des Experiments. Außerdem danke ich den ehemaligen Diplomanden Christian Hauswald, Sebastian Nickel, Konstantin Friebe und Michael Scheucher, die mit großer Tatkraft und guter Laune zum Gelingen des CQED Experiments beigetragen haben.

Mein Dank gilt Dr. Johannes Majer und Dr. Tobias Nöbauer für die lehrreiche Unterweisung in der Programmierung von FPGAs. Heinz Lenk und Michael Boeßenecker danke ich für die vielfältige Unterstützung in Elektronikfragen aller Art.

Ein großes Dankeschön geht außerdem an Dr. Jürgen Volz, Dr. Danny O'Shea, Michael Scheucher und Kathrin Markert für die wertvollen Anregungen und das unermüdliche Korrekturlesen dieser Arbeit.

Rudolf Mitsch möchte ich für seine Freundschaft, die vielen aufbauenden Gespräche und eine tolle Zeit in Wien danken.

Ganz besonders möchte ich meiner Freundin Sabine und meiner Familie für das Vertrauen, die Geduld und den Zuspruch danken, ohne die diese Arbeit nicht möglich gewesen wäre.

Mein Dank gilt der Studienstiftung des Deutschen Volkes, die diese Arbeit im Rahmen eines Stipendiums finanziell unterstützt hat.

LEBENSLAUF

Christian Junge
Hießgasse 2 / 9
1030 Wien
Österreich

Persönliche Daten

Geburtsdatum: 16. August 1982
Geburtsort: Saarbrücken
Staatsangehörigkeit: deutsch

Ausbildung

seit 05/2009	Technische Universität Wien und Johannes Gutenberg-Universität Mainz Doktorand in Technischer Physik
10/2006 – 02/2009	Technischen Universität Darmstadt und Ecole Polytechnique Fédérale de Lausanne, Schweiz Master of Science in Physik
10/2003 – 09/2006	Technischen Universität Darmstadt, Bachelor of Science in Physik
08/1993 – 06/2002	Georg Büchner Gymnasium, Bad Vilbel
08/1989 – 07/1993	Stadtschule, Bad Vilbel